

234p.

646
N64-19926

CODE-1

NASA CB-53924

FINAL REPORT

INTEGRATED ENGINE FOR SPACECRAFT

REPORT NO. SGC 206 FR-1

OTS PRICE

XEROX

\$

15.50 *pk*

MICROFILM

\$

2.22 *rf.*




INTEGRATED ENGINE FOR SPACECRAFT
FINAL REPORT ON CONTRACT NAS 7-140

Research Study Covering the Period
18 April 1962 to 18 September 1963

Report No. 206 FR-1

Prepared for the
National Aeronautics and Space Administration

by


R.L. Border
Project Engineer


C.A. Lysdale, Manager
Advanced Technology Department

SPACE OPERATIONS DIVISION
SPACE-GENERAL CORPORATION

FOREWORD

The final report is submitted in compliance with the requirements of the National Aeronautics and Space Administration Contract NAS 7-140.

ABSTRACT

19926

A

This report summarizes the studies conducted to determine the feasibility of employing a portion of the spacecraft structure for nozzle surfaces to provide high nozzle area ratio and minimum structure weight. A wide array of integrated concepts is presented and two concepts are evaluated in detail to determine their relative payload capability with that of a reference conventional vehicle. Nozzle frictional drag was found to be a critical factor, and an experimental study was performed to determine frictional drag losses in two- and three-dimensional type nozzles.

Author

CONTENTS

	<u>Page</u>
SECTION I - INTRODUCTION	1
SECTION II - SUMMARY	3
2.1 Objectives	3
2.2 Conceptual Study	3
2.3 Selection of Concepts for Detailed Evaluation	9
2.4 Detailed Evaluation of the Selected Concepts	9
2.4.1 Liquid Oxygen/Liquid Hydrogen Propellants	10
2.4.2 Hydrogen Peroxide/Diborane Propellants	21
2.4.3 Effects of the Third Stage Configuration on First and Second Stage Structure Weight	25
2.4.4 Payload Comparison of the Evaluated Vehicles	27
2.5 Results of the Experimental Program	30
2.6 Conclusions and Recommendations	33
SECTION III - VEHICLE CONCEPTUAL STUDY	35
3.1 Method of Evolving Concepts	35
3.1.1 Matrix Construction	36
3.2 Qualitative Evaluation of Concepts	36
3.3 Preliminary Evaluation of Most Promising Concepts	38
3.3.1 Promising Concepts	38
3.3.2 Preliminary Weight and Performance Analysis	44
3.4 Selection of Vehicles for Detailed Evaluation	49
3.4.1 Integrated Nozzle/Tankhead Configuration	49
3.4.2 Small Throat Concept	53
3.4.3 Factors Critical to Feasibility of Selected Concepts	53
SECTION IV - DETAILED EVALUATION OF THE SELECTED VEHICLES	54
4.1 Important Ground Rules	54
4.1.1 Mission	54
4.1.2 Loads	55
4.1.3 Structural Materials	55
4.1.4 Additional Assumptions	56
4.2 Propulsion and Performance Analysis	56
4.2.1 Propellant Performance	56
4.2.2 Heat Transfer	65

CONTENTS - Cont'd.

	<u>Page</u>
4.2.3	Nozzle Losses 75
4.2.4	Flow Divergence Losses 80
4.2.5	Cycle Losses 88
4.3	Engine Weights 92
4.3.1	Turbopumps 92
4.3.2	Gas Generators 93
4.3.3	Conventional Engine Weights 93
4.3.4	Forced-Deflection Engine Weights 95
4.3.5	Small Nozzle Concept - Engine Weights 95
4.3.6	Trajectory Considerations 95
4.4	Vehicle Structural and Weight Analysis 98
4.4.1	Sizing 98
4.4.2	Structural Design 98
4.5	Conventional Vehicle (Liquid Oxygen/Liquid Hydrogen) Propellants 110
4.5.1	General Description 110
4.5.2	Propulsion Analysis 110
4.5.3	Effect of Changing Assumptions on Optimum Engine 111
4.5.4	Selected Engine Configuration 121
4.5.5	Vehicle Analysis 121
4.5.6	Vehicle Payload 123
4.6	Conventional Vehicle (Hydrogen Peroxide/Diborane) Propellants 124
4.6.1	Engine Configuration 124
4.6.2	Conventional Vehicle Weight Breakdown (Wt. in Pounds) . . . 126
4.7	Integrated Nozzle/Tankhead Vehicle (Liquid Oxygen/Liquid Hydrogen) Propellants 126
4.7.1	General Description 126
4.7.2	Propulsion 128
4.7.3	Engine Configuration 128
4.7.4	Integrated Vehicle Weight Breakdown 132
4.7.5	Pressurized Tankage Design 132
4.7.6	Relative Payload 133
4.8	Small Nozzle Engine Concept (Liquid Oxygen/Liquid Hydrogen) Propellants 133
4.8.1	Propulsion Analysis 135
4.8.2	Chamber and Manifold Sizing 138
4.8.3	Stress Analysis 140

CONTENTS - Cont'd.

	<u>Page</u>
4.8.4	Weight Analysis 154
4.8.5	Engine Configuration 158
4.8.6	Vehicle Analysis 162
4.8.7	Vehicle Payload 164
4.9	Small Throat Engine Concept (Hydrogen Peroxide/Diborane) Propellants 164
4.9.1	Engine Configurations 164
4.9.2	Vehicle Weight Breakdown (Weight in Pounds) 164
4.10	Effects of the Third Stage Configuration on First and Second Stage Structure Weight 167
4.11	Payload Comparison of the Evaluated Vehicles 173
4.11.1	Liquid Oxygen/Liquid Hydrogen Propellants 173
4.11.2	Hydrogen Peroxide/Diborane Propellants 174
SECTION V - EXPERIMENTAL PROGRAM 175	
5.1	Discussion of Test Program 178
5.2	Facility and Model Description 179
5.2.1	Facility Description 179
5.2.2	Model Description 184
5.3	Data Analysis Procedures 191
5.3.1	Thrust Coefficient and Friction Loss 191
5.3.2	Discharge Coefficient 198
5.3.3	Balance Calibration 198
5.4	Discussion of Results 202
5.4.1	15° Conical Nozzle 202
5.4.2	Two-Dimensional Forced-Deflection Nozzle 211

ILLUSTRATIONS

<u>Figure No.</u>		<u>Page</u>
1	Most Promising Integrated Concepts	4
2	Nozzle Frictional Drag Loss Predicted by Modified Frankl-Voishel Equation	8
3	Configurations of the Evaluated Vehicles	12
4	Effect of Chamber Pressure and Expansion Ratio on Performance of the Conventional Vehicle	13
5	Effect of Engine Parameters on Payload Capability of a Forced-Deflection Engine/Vehicle	15
6	Effect of Expansion Ratio on Payload Capability Using a Constant Nozzle Exit Diameter Equal to Tank Diameter . . .	16
7	Integrated Vehicle Design	18
8	Small Nozzle Concept - Geometry of Engine System	19
9	Manifold Configurations	20
10	Evaluated Vehicle Configurations	22
11	Effect of Area Ratio and Mixture Ratio on Specific Impulse of H_2O_2/B_2H_6	23
12	Effect of Chamber Pressure and Mixture Ratio on Combustion Temperature of H_2O_2/B_2H_6	24
13	Effect of Bending Moment and Cone Angle on Interstage Weight	26
14	Effect of Bending Moment on Tankage and Structure Weight .	28
15	Concepts Evolved from Morphological Construction	39
16	Concepts Evolved from Morphological Construction	40
17	Brainstormed Concepts	41
18	Brainstormed Concepts	42
19	Most Promising Integrated Concepts	43
20	Frictional Drag Loss in Conical Nozzles Predicted by Modified Frankl-Voishel Equation	48
21	Small Nozzle Concepts	50
22	Small Nozzle Concept Using Two-Dimensional Forced- Deflection Nozzle	51
23	Preliminary Optimization of the Two-Dimensional Nozzle . .	52
24	Shifting Impulse Performance of LO_2/LH_2	58

ILLUSTRATIONS - Cont'd.

<u>Figure</u>		<u>Page</u>
25	Shifting Impulse Performance of LO_2/LH_2	59
26	Combustion Temperature of LO_2/LH_2 (Shifting Performance) .	60
27	Frozen Impulse Performance of LO_2/LH_2	61
28	Frozen Impulse Performance of LO_2/LH_2	62
29	Combustion Temperature of LO_2/LH_2 (Frozen Performance) . .	63
30	Actual vs Theoretical Performance for LO_2/LH_2	64
31	Theoretical Chemical Composition of $\text{H}_2\text{O}_2/\text{B}_2\text{H}_6$	66
32	Effect of Area Ratio and Mixture Ratio on Specific Impulse of $\text{H}_2\text{O}_2/\text{B}_2\text{H}_6$	67
33	Effect of Chamber Pressure and Mixture Ratio on Combustion Temperature of $\text{H}_2\text{O}_2/\text{B}_2\text{H}_6$	68
34	Wall Temperature vs Heat Flux in Forced-Deflection Nozzle ($X = .01$)	70
35	Wall Temperature vs Heat Flux in Forced-Deflection Nozzle ($X = .1$)	71
36	Wall Temperature vs Heat Flux in Forced-Deflection Nozzle ($X = 1.0$)	72
37	Wall Temperature vs Heat Flux in Forced-Deflection Nozzle ($X = 1.0$, $K = 20$)	73
38	Effect of Nozzle Wall Thickness on Heat Flux	74
39	Nozzle Frictional Drag Loss Predicted by Modified Frankl-Voishel Equation	78
40	Comparison of Prediction Techniques for Computing Nozzle Friction Losses	79
41	Drag Losses in Conical Nozzles	81
42	Drag Losses in Bell Nozzles	82
43	Drag Losses in Forced-Deflection Nozzles	83
44	Effect of Length on Efficiency of Forced-Deflection Two- Dimensional Nozzles	87
45	Nozzle Exit Mach Number	89
46	Nozzle Exit Wall Angle	90
47	Geometrical Losses of Bell Nozzles	91
48	Conventional Engine Weight	94

ILLUSTRATIONS - Cont'd.

<u>Figure</u>		<u>Page</u>
73	Buckling Coefficient of a Compressed Cone (NACA TN 3783)	149
74	Buckling Coefficient	150
75	Two-Dimensional Nozzle Contour	155
76	Properties of Rene 41 Skirt Material	157
77	Manifold Configuration I	159
78	Manifold Configuration II	160
79	Small Nozzle Concept - Thrust Structure	161
80	Small Nozzle Concept Vehicle (LO_2/LH_2)	163
81	Small Nozzle Concept Vehicle ($\text{H}_2\text{O}_2/\text{B}_2\text{H}_6$)	165
82	Configurations of the Evaluated Vehicles	169
83	Effect of Bending Moment and Cone Angle on Interstage Weight	171
84	Effect of Bending Moment on Tankage and Structure Weight .	172
85	High Area Ratio Nozzle Test Facility	180
86	Photographs of Test Area and Installed Models	181
87	Station Definition for Channel 8 Static Thrust Facility .	182
88	Assembly of Space-General Conical Nozzle in FluidDyne Channel 8	183
89	15° Conical Nozzle	185
90	15° Conical Nozzle - Pressure Tap Locations	186
91	Assembly of 2-D Forced-Deflection Nozzle in FluidDyne Channel 8	187
92	Two-Dimensional Forced-Deflection Nozzle Inlet and Shroud	188
93	Two-Dimensional Forced-Deflection Nozzle Centerbody . . .	189
94	Two-Dimensional Forced-Deflection Nozzle Total and Boundary Layer Pressure Tap Locations	190
95	Photographs of Two-Dimensional Forced-Deflection Nozzle .	192
96	Boundary Layer Probe	193
97	Sample Thrust Calculations	194
98	Inlet Momentum Integration, 15° Conical Nozzle	196

ILLUSTRATIONS - Cont'd.

<u>Figure</u>		<u>Page</u>
49	Forced-Deflection Engine Weight	96
50	Change in Velocity Requirement due to Gravitational Effects	97
51	Vehicle Nomenclature	99
52	Design Column Curves for Extruded Shapes	102
53	Tankhead Surface Area	107
54	Effect of Engine Parameters on Performance of Conventional Vehicle	112
55	Effect of Engine Parameters on Performance of Conventional Vehicle	113
56	Effect of Engine Parameters on Performance of Conventional Vehicle	114
57	Effect of Thrust on Performance of Conventional Vehicle.	115
58	Effect of Velocity Increment on Selection of Engine Parameters	116
59	Effect of Cycle Losses on Selection of Engine Parameters	118
60	Effect of Equilibrium Performance on Selection of Engine Parameters	119
61	Effect of Nozzle Extension Thickness on Selection of Engine Parameters	120
62	Conventional LO_2/LH_2 Vehicle	122
63	Conventional H_2O_2/B_2H_6 Vehicle	125
64	Separation Technique for the Integrated Vehicle	127
65	Effect of Forced-Deflection Engine Parameters on Payload Performance	129
66	Integrated LO_2/LH_2 Vehicle	130
67	Structural Details of Integrated Vehicle	131
68	Small Nozzle Concept - Geometry of Engine System	134
69	Nozzle Frictional Drag Losses	136
70	Effect of Percent Length on Efficiency of Forced-Deflection Nozzle	137
71	Strength Properties of Manifold Material	141
72	Stress Model and Free Body Diagrams for Manifold Configurations	142

ILLUSTRATIONS - Cont'd.

<u>Figure</u>		<u>Page</u>
99	Static Thrust Coefficients, 15° Conical Nozzle	203
100	Channel 8 Test Schedule	205
101	Discharge Coefficients, 15° Conical Nozzle	206
102	Conical Nozzle Pressure Distribution	207
103	Conical Nozzle Pressure Distribution	208
104	Conical Nozzle Pressure Distribution	209
105	Boundary Layer Surveys	210
106	Static Thrust Coefficients, Two-Dimensional Nozzle	212
107	Centerbody Base Pressures, Two-Dimensional Nozzle	213
108	Discharge Coefficients, Two-Dimensional Nozzle	215
109	Inlet Pressure Distribution, Two-Dimensional Nozzle	216
110	Shroud Pressure Distribution, Two-Dimensional Nozzle	217
111	Shroud Pressure Distribution, Two-Dimensional Nozzle	218
112	Shroud Pressure Distribution, Two-Dimensional Nozzle	219
113	Shroud Pressure Distribution, Two-Dimensional Nozzle	220
114	Boundary Layer Survey, Two-Dimensional Nozzle	221

TABLES

<u>Table No.</u>		<u>Page</u>
I	Restrictions and Potential Problem Areas	6
II	Summary of Evaluated Vehicles	11
III	Restrictions and Potential Problem Areas	45
IV	Summary of Evaluated Vehicles	168
V	Performance Summary	204

Section 1
INTRODUCTION

This study program was conducted to establish if a method exists for integrating the nozzle expansion surfaces and structural or tankage surfaces of space vehicles which will provide significant advantage over present conventional vehicle designs. For any promising integration concepts, the objectives of the study were to include:

1. Detailed design of the engine-vehicle concept to determine relative payload advantages.
2. Experimental or feasibility investigation to support analytical studies of features critical to the concept.

During the first portion of the study, integration concepts were generated assuming no restrictions as to earth or space construction of the spacecraft or the reorientation of vehicle components while in space. Propellants studied included both liquid oxygen/liquid hydrogen and storables, and velocity increments of 4000 to 15,000 feet per second were considered. In the latter portion of the study, selected configurations were evaluated for an earth-escape mission assuming earth construction and structural loadings dictated by the boost trajectory. Evaluation of the concepts was performed with both high energy cryogenic (LO_2/LH_2) and storable propellants ($\text{H}_2\text{O}_2/\text{B}_2\text{H}_6$).

The payload achieved through the application of these concepts in a specified mission must be measured against the payload delivered by a reference conventional system. Since no truly optimum "conventional" engine-vehicle system has been designed and built to date, comparison of the integrated schemes to on-the-shelf systems was not considered equitable, and freedom exists to select a reference vehicle against which to measure the merits of the new concepts. Obviously, the selection of this reference system is a critical factor in this study since the reference level can make new concepts appear either poor or promising.

The reference "conventional" vehicle was therefore defined as being conventional in the respect that the nozzle it employs has not been integrated with tankage or structure, but the system has been optimized to achieve maximum payload using conventional non-integrated structure.

Review of current state-of-the-art of liquid chemical propulsion and vehicle systems shows that cycle efficiencies, thrust coefficients, propellant fractions, and reliabilities are high. Years of continuous development have brought the conventional systems near their maximum potential. Thus, it is apparent that if significant improvements are to be achieved, new or unique methods, such as dual usage of components or integration of engine and vehicle surfaces, should be investigated.

Major goals of this study were, then, to generate as many integration schemes as possible, such that promising schemes are not overlooked, to determine which of these concepts appear to provide advantages, and to evaluate by more detailed investigation the most promising of these concepts. In addition, the study will point out novel concepts which, although not competitive with the conventional system in payload performance, may have advantages for specialized applications.

Section 2

SUMMARY

2.1 OBJECTIVES

The purpose of this program was to investigate the possibility and feasibility of employing spacecraft structure to provide expansion surfaces in place of a conventional nozzle. To accomplish the program objectives, the effort was broken into two major tasks:

1. Investigation of integrated vehicle concepts and selection of promising configurations for further study.
2. Detailed design of the selected concepts to establish relative payload advantages, and experimental investigation of features critical to the concept.

2.2 CONCEPTUAL STUDY

During the first portion of the study, morphological construction and "brainstorming" techniques were used to evolve integration concepts, (Refer to Section 3). Approximately 200 configurations were generated, of which 100 have been presented in this report. A qualitative rating system was devised to evaluate the potential advantages of these concepts on the basis of engine performance, structural weight, engine weight, potential heat transfer problems, and payload restrictions. Finally, an over-all rating was given to each concept. The concepts which appeared to have payload advantage over the "conventional" reference vehicle, or which appeared to provide advantages for special applications, are presented in Figure 1. In these vehicles, structure or engine weight has been reduced by one or more of the following means:

- a) Dual usage of structure
- b) Shortened load paths to the payload
- c) Reduction or elimination of interstage structure

Legend:

1 = Apparent advantage over "Conventional"

2 = Same as Conventional

3 = Apparent disadvantage compared to Conventional

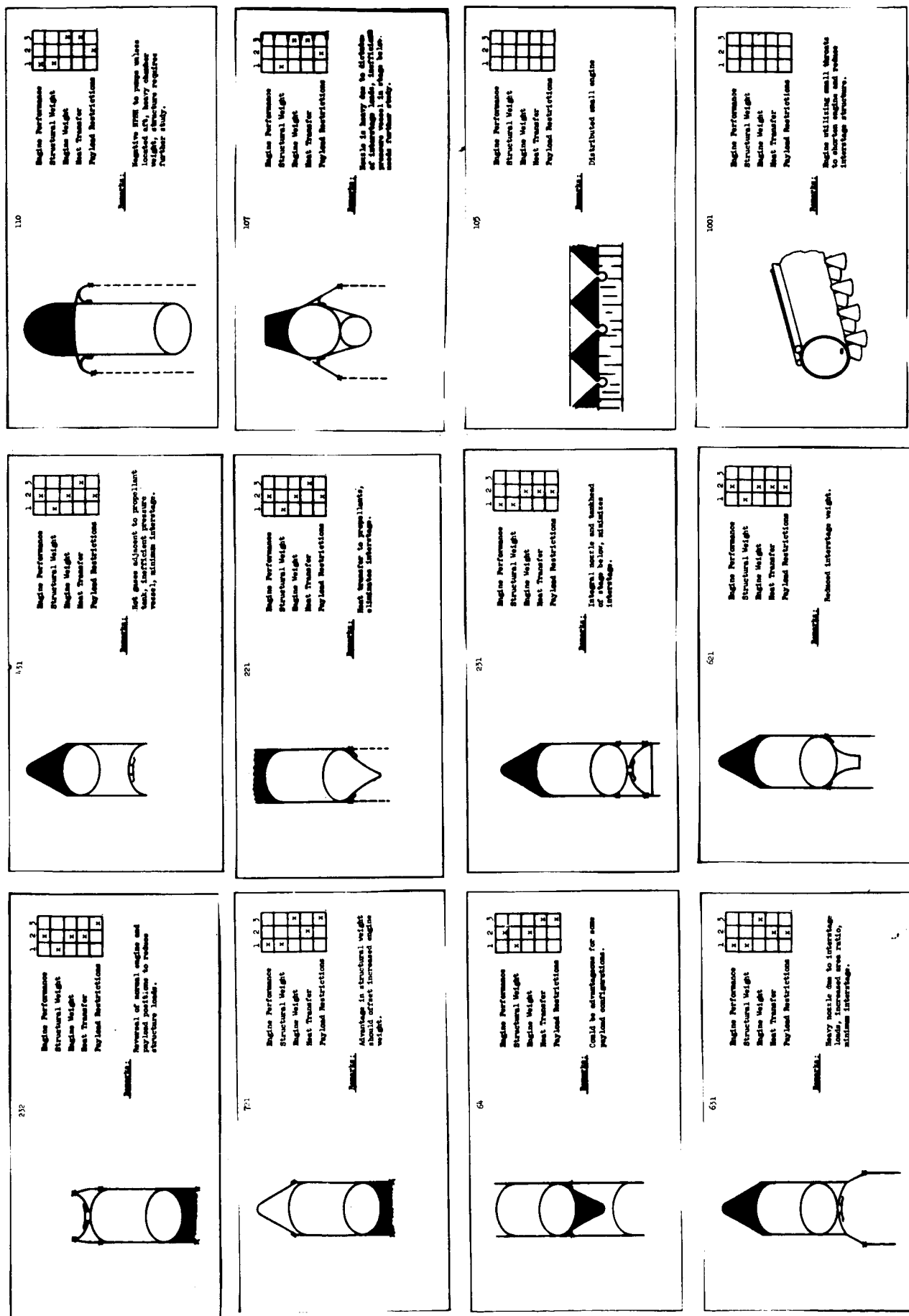


FIGURE 1. Most Promising Integrated Vehicle Concepts

The concepts (Figure 1) are self explanatory except for the small engine concept, number 105 and 1001 in Figure 1.. This concept takes the form of many very-small-throat, high-area-ratio nozzles distributed over tankage structure or other surfaces on the vehicle. The concept appeared to merit further evaluation due to potential gains from utilizing high area ratio and yet retaining minimum nozzle and interstage length.

All of the concepts in Figure 1 appear to provide payload gains, however each configuration must be analyzed as to possible restrictions or potential problem areas. In the past, vehicles capable of a wide range of applications have been built economically by use of several basic engines (sometimes in clusters) and staging the vehicles according to the desired payload and application. Obviously, some of the proposed integrated concepts in this report limit this type of flexibility. Several of the concepts require reorientation of the vehicle after separation, or they restrict payload envelope. These factors become very important when cost in dollars per pound of payload is considered. Table 1 summarizes the restrictions and potential development and operational problems for each of the concepts.

The concepts which restrict payload envelope (64, 232, 721), and those which limit the usage of both the second and third stage and third stage propulsion system (107, 110) were considered to be promising for specialized applications only. Concept 631, which appeared to offer an advantage over the conventional vehicle after the initial qualitative examination, was eliminated later because of payload penalties resulting from the vehicle having to carry the heavy interstage/nozzle after separation from the lower stage. The remaining concepts, 621, 231, 431, 221, and the small nozzle concepts (105, 1001) were selected for preliminary weight and performance analysis.

Relative payloads of the vehicle concepts were determined for a 300 n.m. earth-orbit escape maneuver. The integrated concepts were compared with two unintegrated "conventional" vehicles, one utilizing a bell type nozzle, and the other using a forced-deflection nozzle. Results of the preliminary study, indicating relative payload gains of the configurations, are given in the table below.

TABLE I

Restrictions and Potential Problem Areas

Configuration (Refer to Figure 1)	64	107	110	221	231	232	431	621	631	721	105 and 1001
Restrictions											
Payload Envelope	X					X				X	
Third Stage Use		X	X								-
Third Stage Engine Use	X	X	X	X	X		X		X		-
Second Stage Use	X	X	X	X	X			X	X		
Potential Problem Areas											
Heat Transfer	X	X	X	X			X		X		X
Reorientation of Vehicle After Separation						X				X	

X means the configuration has the given restriction or problem area

- means the restriction is dependent on the way in which the engine is integrated with the vehicle.

<u>Configuration</u>	<u>Conventional</u>		<u>221</u>	<u>231</u>	<u>431</u>	<u>621</u>
	<u>Bell</u>	<u>Forced-Deflection</u>				
Relative Payload (percent)	100.0	103.0	102.5	103.5	103.0	102.0

All of the concepts have a relative payload gain over the conventional bell nozzle configuration, but the integrated nozzle/tankhead concept (231) was the only configuration showing higher payload than the conventional forced-deflection engine/vehicle.

The small nozzle concept, when taking the form of small nozzles distributed over large areas of tankage structure, showed a three percent payload loss even though interstage structure length due to nozzle length was essentially eliminated. This result was partly due to the predicted high frictional drag losses in the very small nozzles (throat diameter in the order of .05 to .10 inches for a structure thickness of 1 to 2 inches). Secondly the concept requires a distributed thrust chamber or feed system supplying a large area. Therefore, regenerative cooling was considered impractical and off (low) mixture ratio operation to reduce combustion temperature to 4000°F was investigated with the use of refractory metals for the high temperature engine components.

A second configuration utilized the small nozzle concept as a means to reduce interstage length and weight and decrease bending moments in the boost stages. A preliminary study of this concept indicated that an annular two-dimensional forced deflection nozzle with throat width in the order of .125 inches (for the vehicle evaluated in this study) would eliminate the portion of interstage normally required for the nozzle. Again, the relative payload afforded by the concept was dependent on the predicted nozzle frictional drag losses and strength to density ratio of the high temperature metals. Magnitude of the predicted nozzle drag losses can be seen in Figure 2. Obviously, both the absolute magnitude of the drag for the two nozzles, and it's trend with throat size (i.e., changing Reynold's number) are critical to the relative performance of the concept.

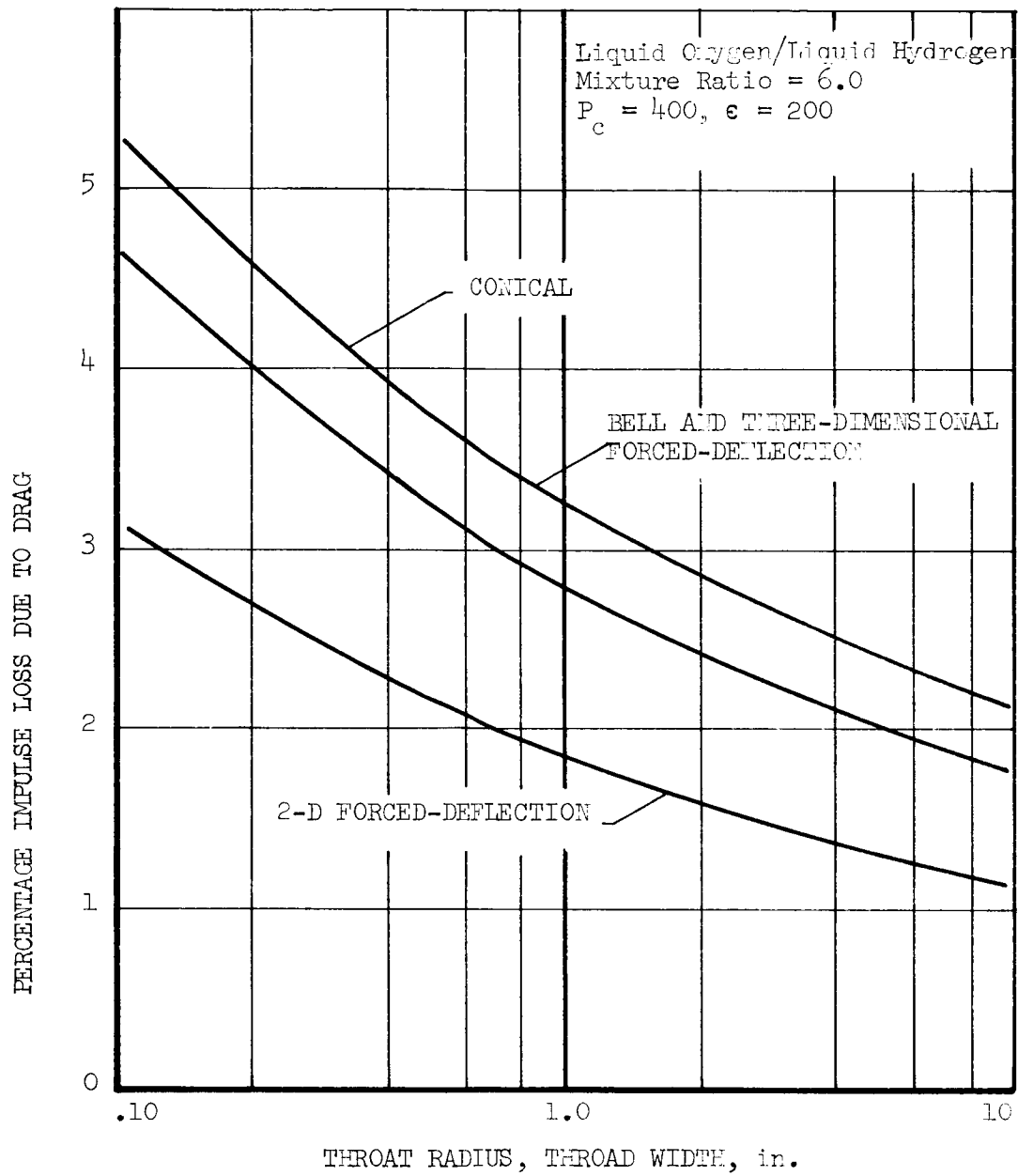


FIGURE 2. Nozzle Frictional Drag Loss Predicted by
Modified Frankl-Voishel Equation

2.3 SELECTION OF CONCEPTS FOR DETAILED EVALUATION

The integrated nozzle/tankhead vehicle was selected for further evaluation since this concept exhibited the highest potential payload of the evaluated vehicles. The configuration reduces vehicle length, and decreases bending moments in the boost stages.

The small nozzle concept was chosen for further study for its advantages of reduced vehicle length and bending moments and the fact that the engine configuration is amenable to unconventional engine envelope restrictions which are imposed in many advanced-mission vehicles, i.e., Apollo Service Module and Transtage.

At this point in the program, the two selected concepts were reviewed to determine if feasibility demonstration or experimental evaluation of any critical features was necessary to establish potential performance gains for the concepts. Verification of predicted values of nozzle frictional drag losses was selected as the most critical feature for experimental investigation. Aside from establishing the geometry-drag performance trade-off for the evaluated concepts in this study, the results of the investigation of frictional losses in nozzles would be useful to the general technology of nozzle performance prediction.

2.4 DETAILED EVALUATION OF THE SELECTED CONCEPTS

The objectives of this effort were to obtain more accurate comparative payload evaluations of the vehicles and to establish practical design considerations of the integrated concepts which had not been recognized in the initial evaluation phase.

The spacecraft used for comparing the concepts has a gross weight of 240,000 pounds and performs an escape maneuver from a 300 n.m. orbit. The critical structural loads for the vehicle were assumed to be dictated by the boost trajectory of the two succeeding stages. Both storable and high energy cryogenic propellants are used in the evaluation.

Impulse performance of the engine systems was determined from detailed studies of nozzle and cycle (pumping) losses, and from theoretical vacuum specific impulse of the propellant combinations at various chamber pressures and expansion ratios (See Sections 4.2.1 & 4.2.3). A structural design and weight breakdown analysis was conducted for each vehicle (see Section 4.4). This structural analysis was carried through to the first stage to insure the determination of changes in bending moments and weights in the first two stages caused by variations in the configuration of the third stage.

Data from the propulsion and structure analysis were used in optimizing thrust, chamber pressure, and expansion ratio of the engine systems, and optimum stringer-frame-skin design criteria were utilized in the vehicle designs. Table II summarizes the propulsion and structural characteristics of the evaluated vehicles. The vehicle configurations are shown in Figure 3. The following paragraphs briefly describe the characteristics of the third (integrated stage) of the vehicle, and discuss the effects of changing the configuration of this stage on the structure and weight of the two boost stages.

2.4.1 LIQUID OXYGEN/LIQUID HYDROGEN PROPELLANTS

2.4.1.1 CONVENTIONAL (REFERENCE) VEHICLE

Obviously, the selection of the reference system is a critical factor in this study since the reference system is used for screening and rating the new concepts. The "conventional" vehicle was therefore defined as being conventional in the respect that the nozzle it employs has not been integrated with tankage or structure, but the system has been optimized (Figure 3) to achieve maximum payload using conventional non-integrated structure.

The engine is regeneratively-cooled to expansion ratio of 15 and utilizes a radiation-cooled extension to an expansion ratio of 220. Optimum thrust-to-weight ratio for this vehicle (escape mission) was 0.52 which corresponded to a thrust of 125,000 pounds.

TABLE II
SUMMARY OF EVALUATED VEHICLES

CONFIGURATION	CONVENTIONAL LO_2/LH_2	SMALL NOZZLE LO_2/LH_2	INTEGRATED LO_2/LH_2	CONVENTIONAL H_2O_2/B_2H_6	SMALL NOZZLE H_2O_2/B_2H_6
Thrust	lbs	90,000	125,000	125,000	90,000
Chamber Pressure	psia	520	500	525	400
Expansion Ratio		220	440	220	220
Nozzle Exit Radius	in.	87	150	88	54 (width)
Nozzle Length	in.	260	244	246	58
\dot{W}_{ex} , Bulk Density		6, 22.4	6, 22.4	1.83, 48.2	1.83, 48.2
\dot{W}_{fuel} lbs/ft ³					
Engine Impulse	sec*	462	468	419	414
Velocity Increment	ft/sec	10,065	10,065	10,065	10,140
Propellant Weight	lbs	117,900	116,700	126,100	127,600
Vehicle Length	in.	2646	2471	2524	2294
ΔW_{pl3} First Stage Tankage			249	76	254
Contributed from First stage		133	155	43	149
Second Stage Structure elements		94	1830	302	1050
Second Inter-stage		537	461	438	2065
TOTAL	lbs	1940	2695	859	3518
Third Stage Tank, Structure, Insul., Press., Mount		9807	7091	3650	4163
Inert Weight		7018	3346	1516	
Engine System		1494	10,437	5166	
TOTAL	lbs	8512	115,558	109,593	
Third Stage Payload	lbs	113588			
Relative Payload	% *	100.0	102.0	96.6	96.5
Relative Payload	***	95.1	95.0		

* 100% shifting equilibrium propellant performance

*** 100% frozen propellant performance

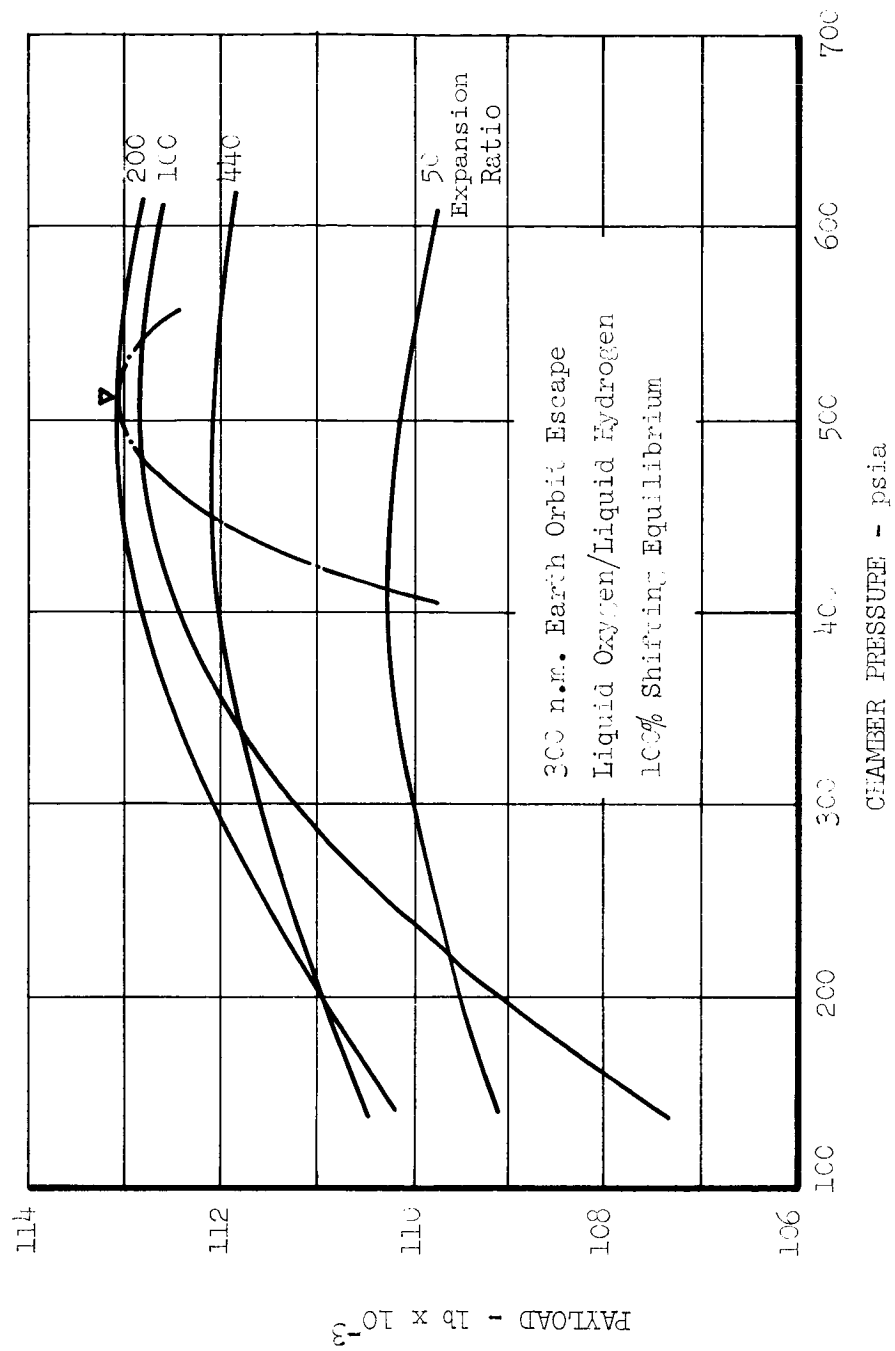


FIGURE 4. Effect of Chamber Pressure and Expansion Ratio on Performance of Conventional Vehicle

This study of the conventional vehicle showed that the effect of changing the cycle (i.e., gas-generator cycle to "topping cycle") or cycle losses has only a very small effect upon the selection of the chamber pressure and expansion ratio of the spacecraft engine. This has not been found to be the case with booster stage propulsion systems. The engine was also optimized for several velocity increments. It was found that exchange factors of structure weight for impulse shifts from favoring impulse for high ΔV missions to favoring structure weights for moderate or low ΔV missions.

2.4.1.2 INTEGRATED NOZZLE/TANKHEAD VEHICLE

Several interesting design considerations of this concept were brought out in the detailed study. Initially, the thrust, chamber pressure, and expansion ratio of the forced-deflection nozzle were optimized (Figure 5) exclusive of first and second stage structure weights except for consideration of second stage interstage structure weight. This optimized nozzle (Figure 5) was then used to size the second stage vehicle diameter (since the nozzle serves as the fuel tank head). The resulting first and second stage structure was excessively heavy due to high second stage tank $\frac{L}{D}$ ratio and attendant high bending moments in the first and second stages. A second vehicle was designed by setting the second stage diameter for minimum structure weight and letting the nozzle exit diameter be dictated by the vehicle diameter. Expansion ratio of the forced-deflection nozzle was then varied by changing the base or lip radius. The resulting optimum expansion ratio is 440:1 as shown in Figure 6. . It can be seen that to obtain the optimum integrated design, both structure and performance would have to be compromised to some extent. However, the optimum structural design point (Figure 6) and the optimum engine design point (Figure 5) are within 0.6 percent payload.

Another consideration brought out in the detailed study was the materials compatibility requirement between the second stage tankage and the integrated nozzle/tankhead. Since welded joints must exist between the tank and the tankhead, the materials cannot be selected independently as would normally be desirable; i.e., aluminum would probably be the most economical

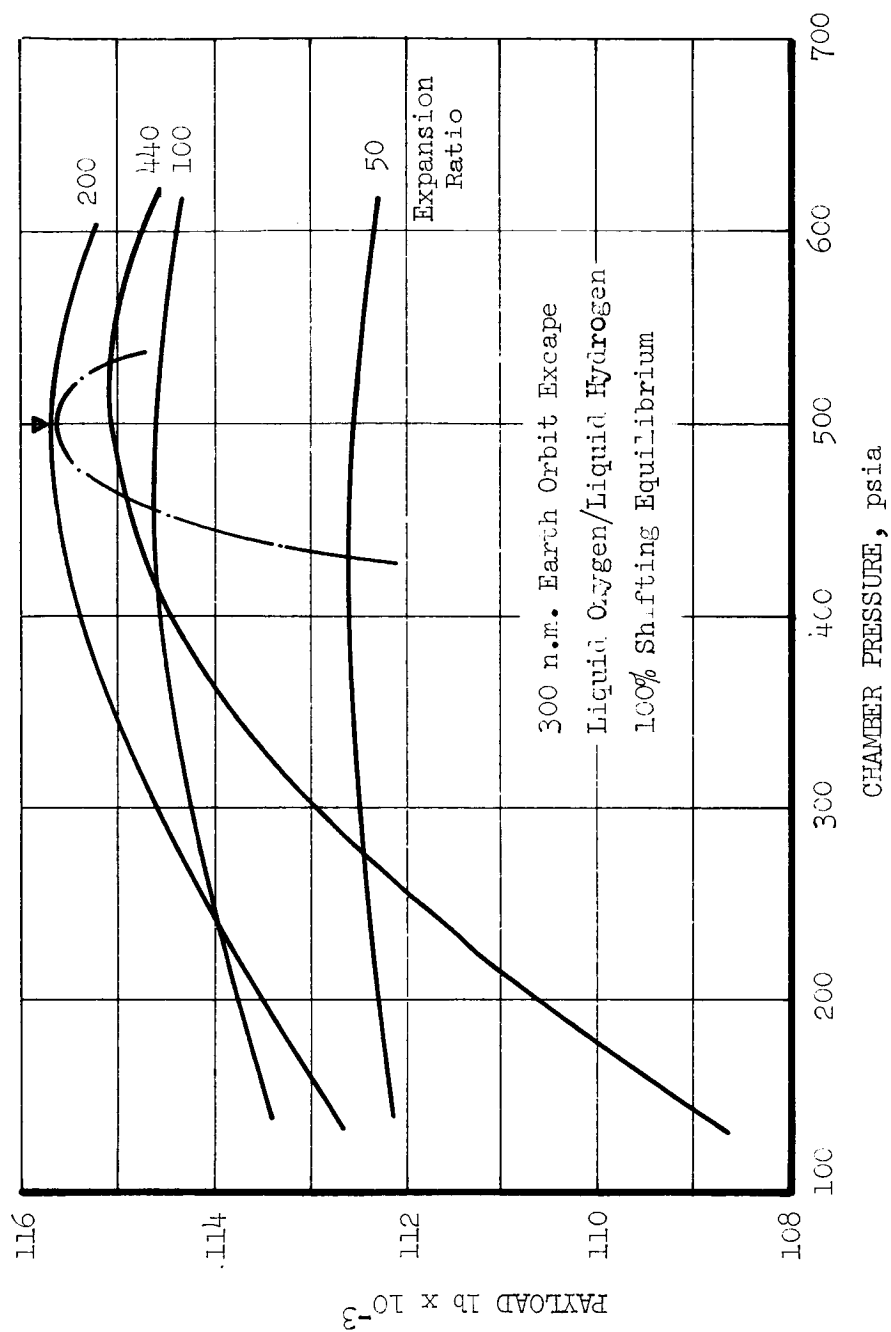


FIGURE 5. Effect of Engine Parameters on Payload Capability of a Forced-Deflection Engine/Vehicle

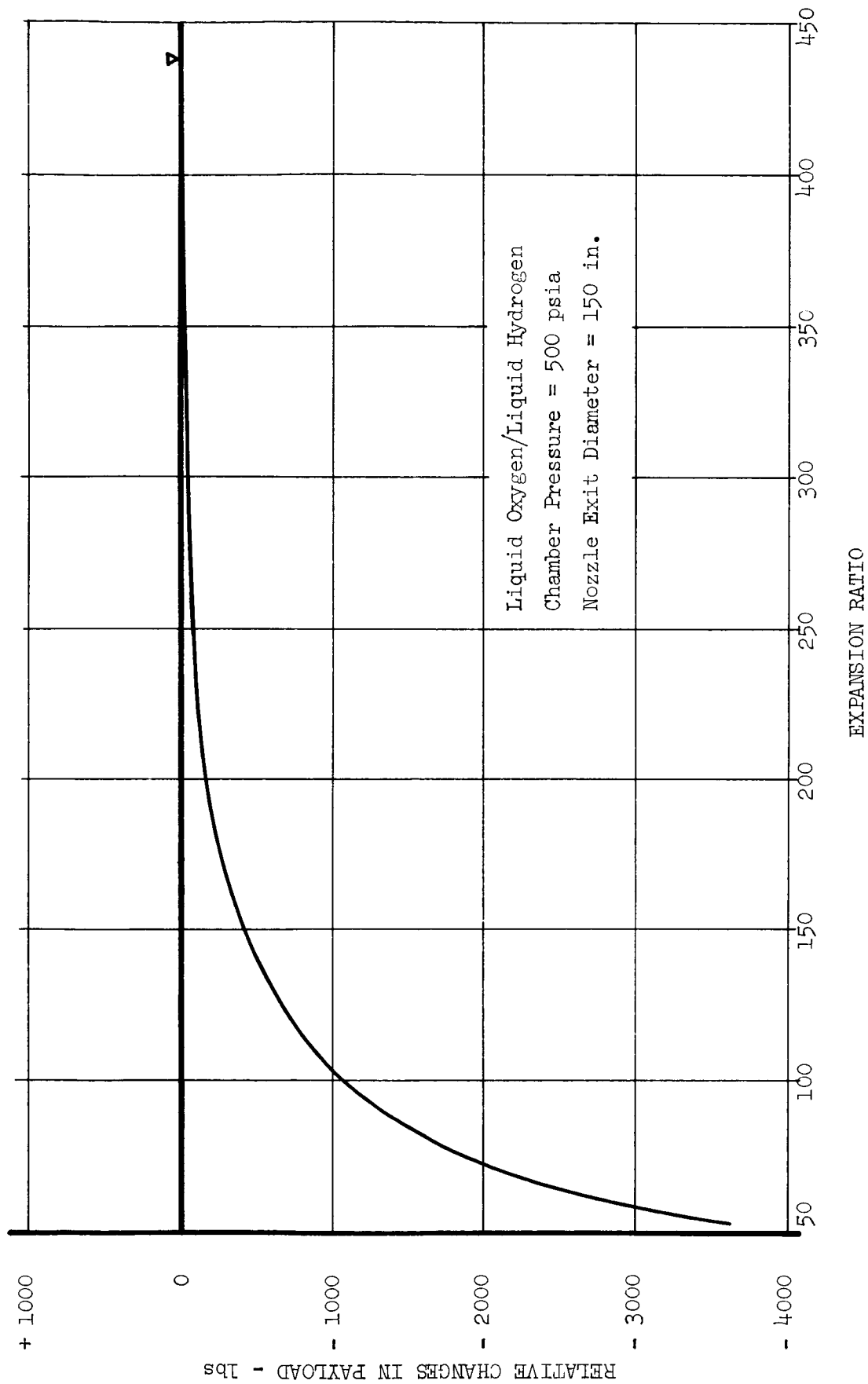


FIGURE 6. Effect of Expansion Ratio on Payload Capability Using
A Constant Nozzle Exit Diameter Equal to Tank Diameter

tankage material and Rene 41 or titanium would be used for the radiation-cooled nozzle extension. Titanium was selected as the best material for the tankage and nozzle in the integrated application. The vehicle configuration is presented in Figure 7 .

Structure weight of the integrated third stage is essentially the same as the weight for the conventional third stage since performance and propellant requirement are almost equal for the two stages (Table II).

2.4.1.3 SMALL NOZZLE CONCEPT

During the early efforts of the program it was concluded that the original concept of integrating many very small axisymmetrical nozzles with tankage or vehicle structure was not competitive with the conventional vehicle from the performance standpoint, however it may be worthwhile for specialized applications. This integration concept appeared to be more competitive when using large diameter annular two-dimensional nozzles. This second concept requires the use of very narrow throat widths which are probably impractical with ablative or regenerative cooling methods, therefore the engine was designed for 4000°F wall temperatures (off optimum mixture ratio) in the chamber and manifolds to permit the use of refractory type materials.

The geometrical configuration of this engine concept is presented in Figure 8 . It has a central turbopump which feeds toroidal distribution manifolds. Eight sets of propellant lines come from this manifold to uncooled chambers and manifolds which feed the two-dimensional forced-deflection nozzle.

A detailed stress and weight analysis was conducted for two configurations of the hot gas manifold (Figure 9). One configuration takes the thrust loads from the nozzle, through the manifold, and into a single shell thrust structure. In the second configuration, thrust loads are taken out at the flange on each side of the two-dimensional annular nozzle, and into a double-sided thrust structure. For the engine parameters evaluated, the second configuration is 19 percent lighter using the current materials technology of tungsten, and therefore the second configuration was used in determining payload capability of this concept. The tankage and structure weight of this

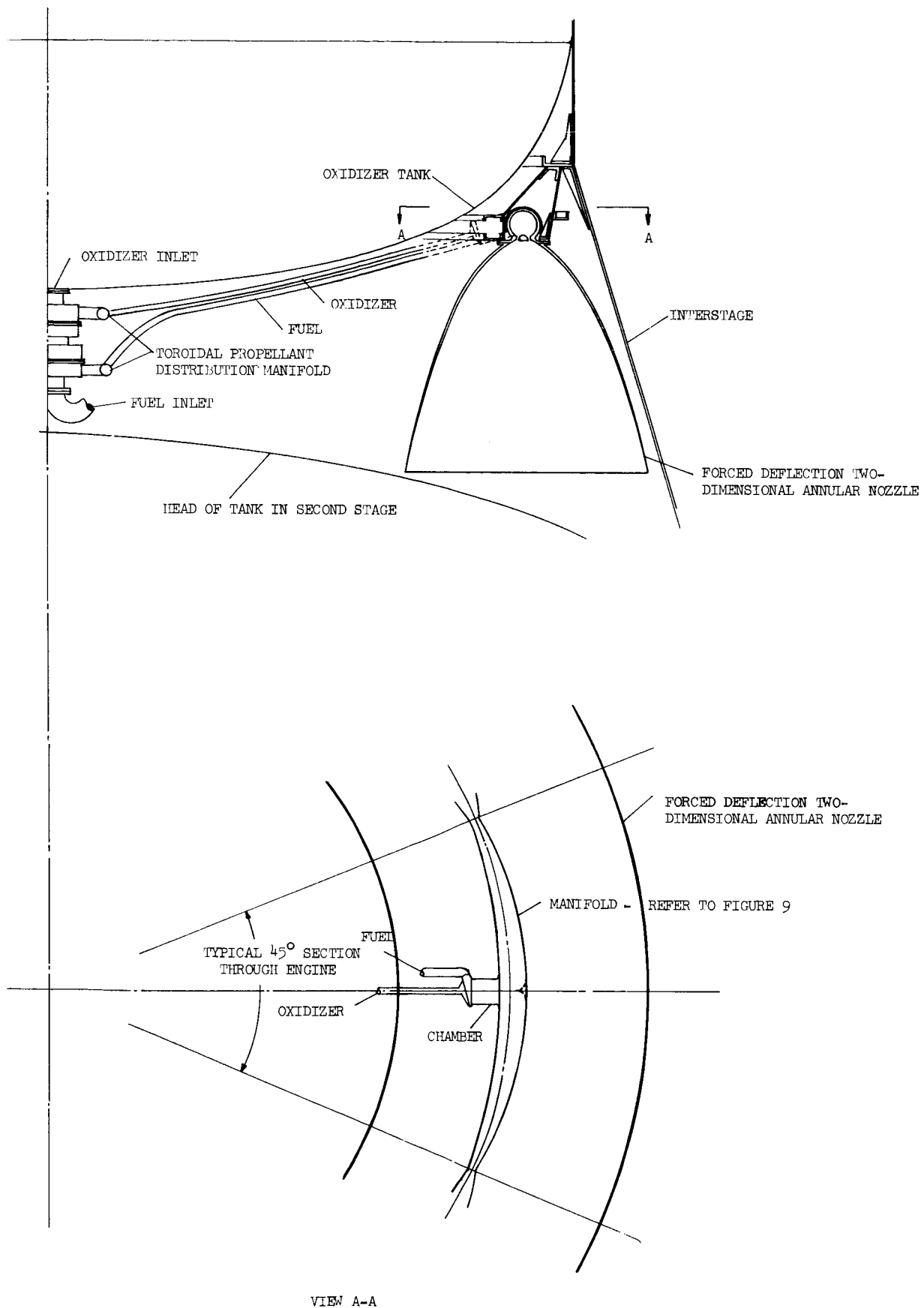
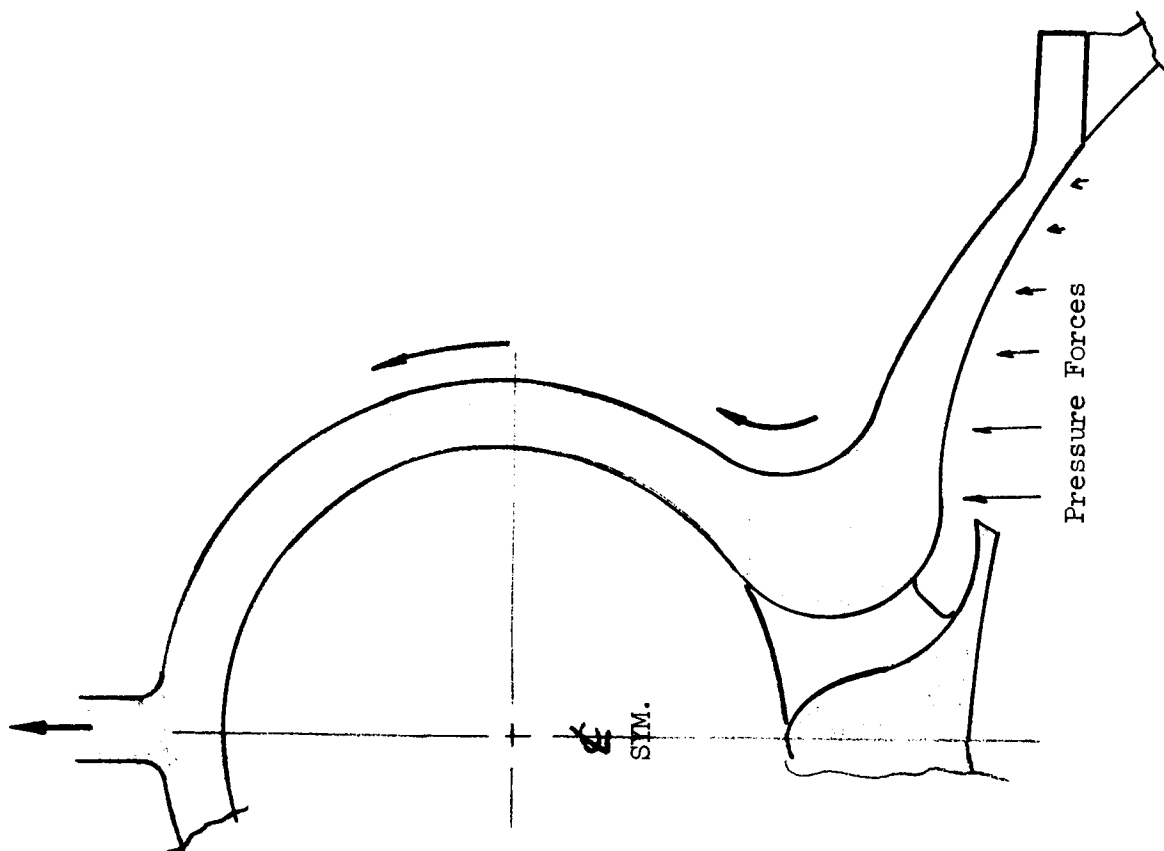


FIGURE 8. Small Nozzle Concept - Geometry of Engine System

I. Thrust forces taken through manifold to thrust structure



II. Thrust forces taken out at flanges on both sides of two-dimensional nozzle

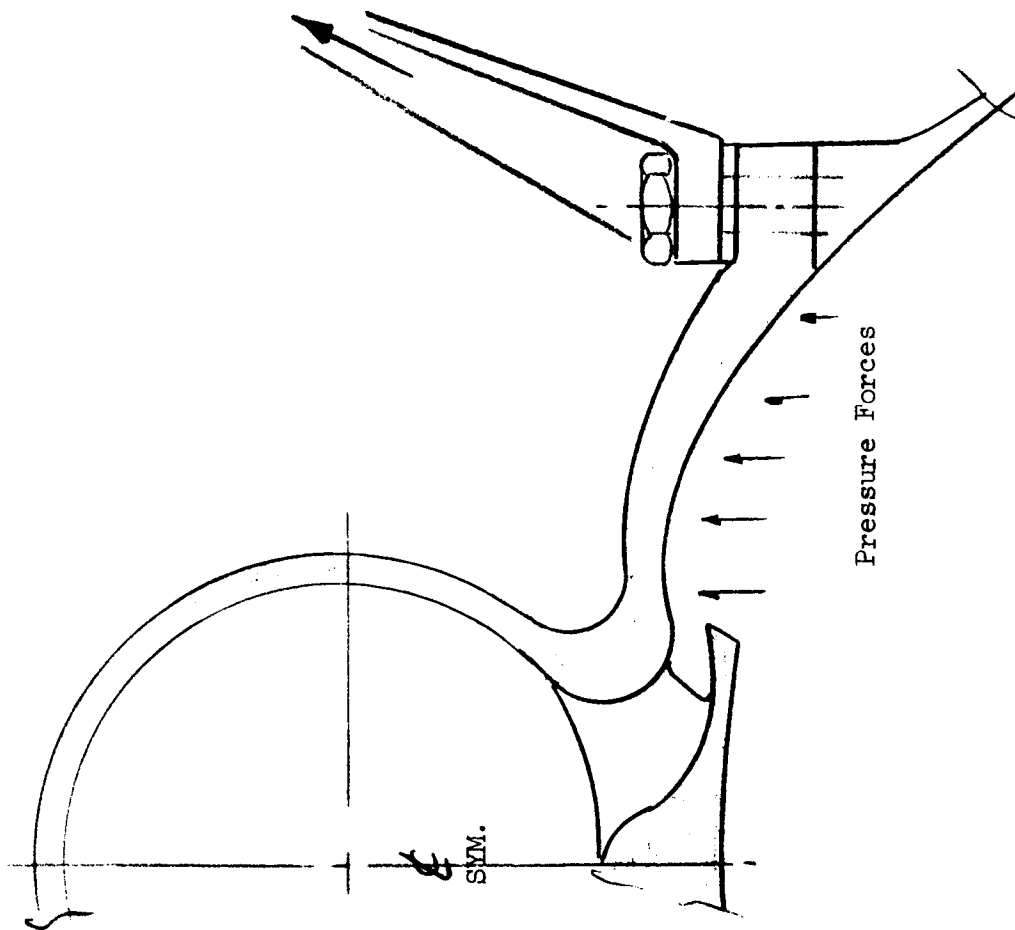


FIGURE 9. Manifold Configurations

third stage is increased considerably over the conventional third stage (Table II) due to the decreased impulse performance and lower propellant bulk density associated with the lower mixture ratio. Therefore the bending moment at base of the third stage is larger than for the integrated or conventional vehicles (Figure 10). However, due to the minimized interstage length, the bending moment at the base of the second interstage is smaller than it is for the other two vehicles.

2.4.2 HYDROGEN PEROXIDE/DIBORANE PROPELLANTS

The potential payload capability of the small nozzle concept was evaluated with storable propellants. Since the small nozzle concept utilizes low mixture ratio to provide reduced combustion temperature, a search for a storable propellant combination exhibiting more optimum impulse at around the selected 4000°F combustion temperature was conducted. The combination of hydrogen peroxide/diborane appears to come closest to this optimum impulse/temperature requirement. Very near optimum impulse is obtained at a mixture ratio of 1.86 (Figure 11) and the combustion temperature at this mixture ratio is 4200°F (Figure 12, $P_c = 500$ psia). Additional characteristics of the propellant combination are listed below.

	100 % Hydrogen <u>Peroxide</u>	<u>Diborane</u>
Freezing point °F	11	-265
Boiling point °F	286	-135
Density lb/ft ³	86.7 (68°F)	29.3
Vapor pressure, psia	.8 (160°F)	30
Bulk Density at Mixture	48.2	
Ratio of 1.86		

A mixture ratio of 1.86 was selected for use in the detailed design of both the conventional and the small nozzle concept vehicles.

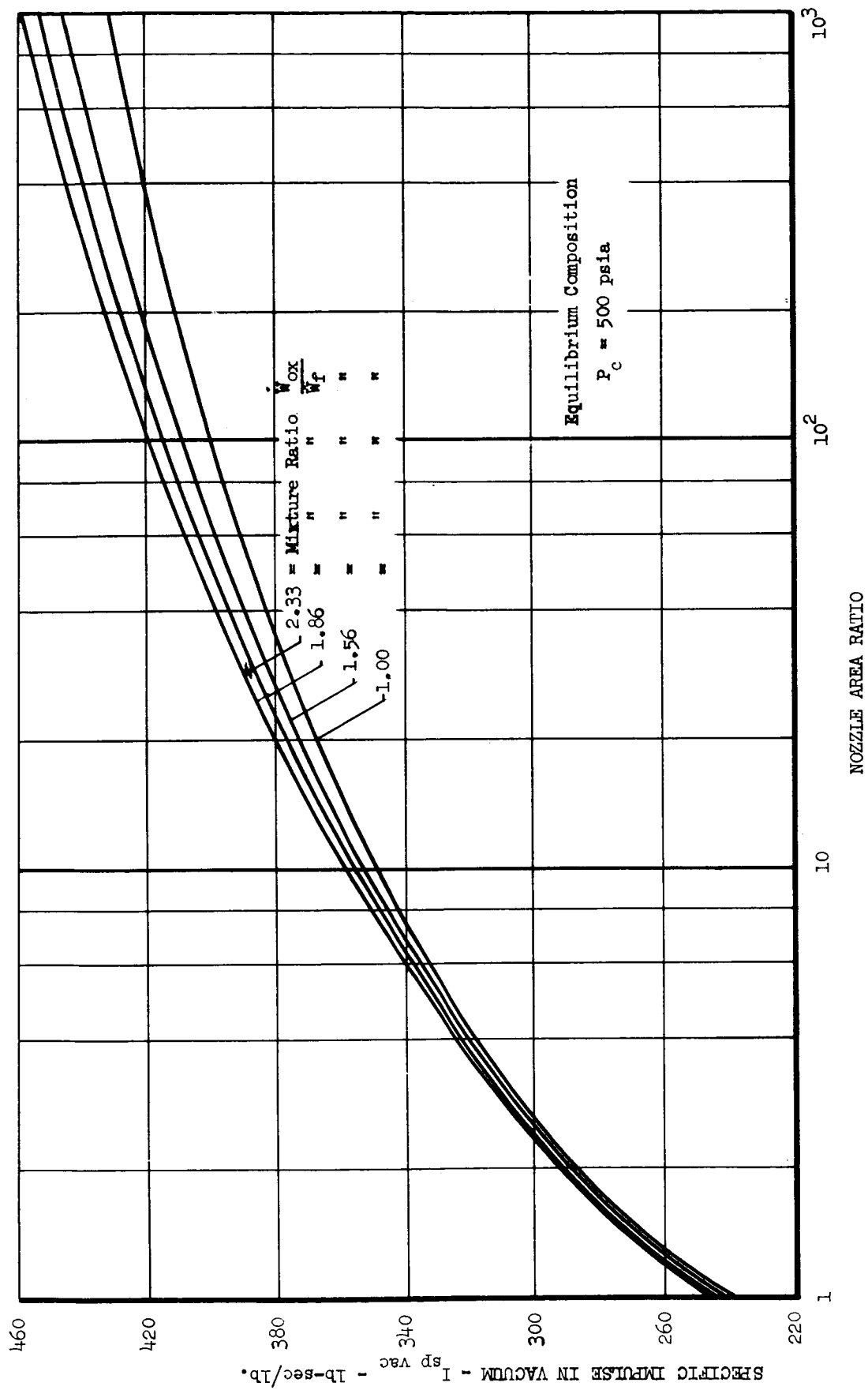


FIGURE 11. Effect of Area Ratio and Mixture Ratio on Specific Impulse of H_2O_2/B_2H_6

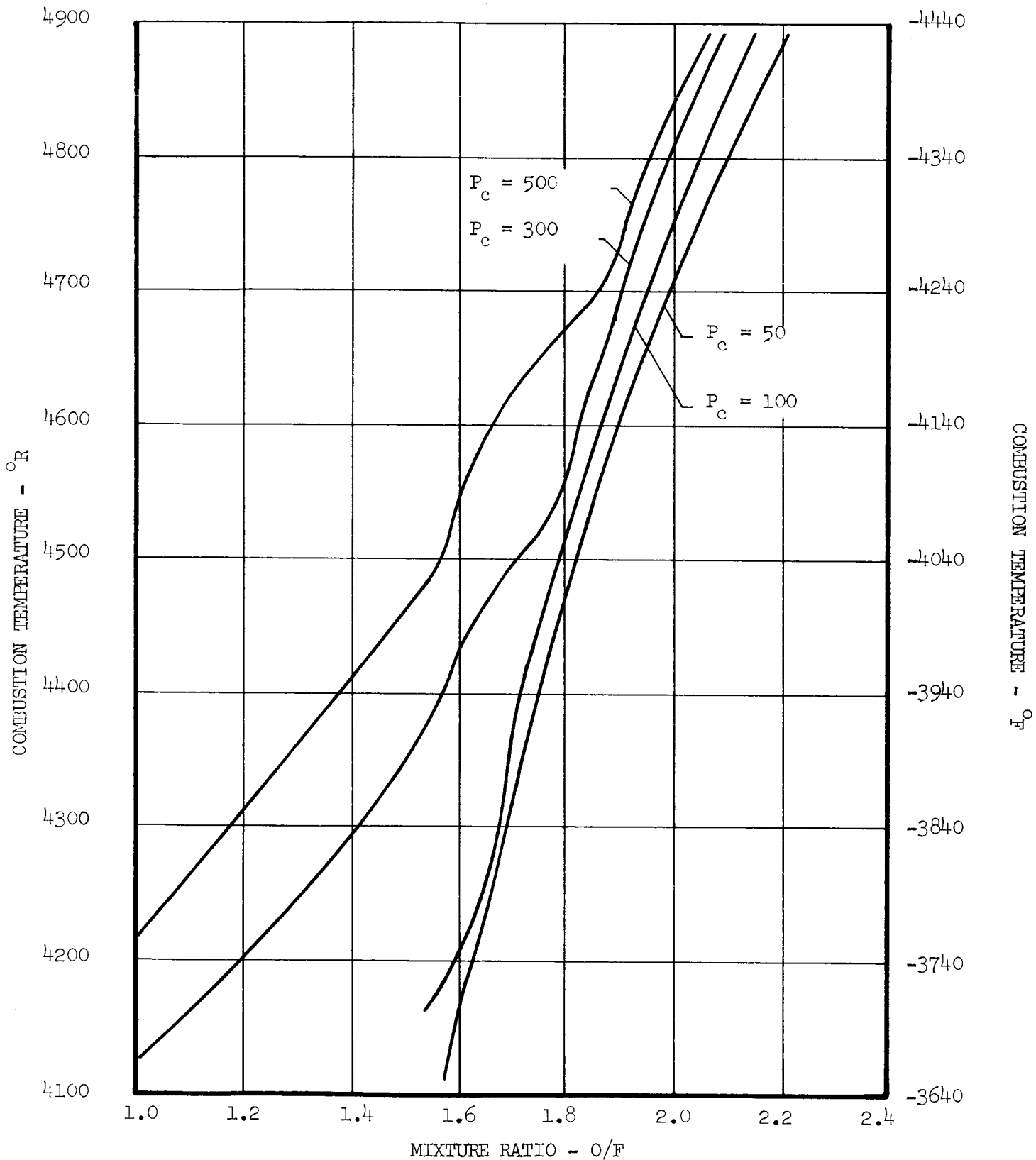


FIGURE 12. Effect of Chamber Pressure and Mixture Ratio on Combustion Temperature of H_2O_2/B_2H_6

The design techniques used in the structural and propulsion elements in the storable conventional and small nozzle concept vehicle is similar to that discussed for the cryogenic propellants. . A design study of the integrated vehicle with storable propellants was not completed since it was felt that the payload capability and design problems associated with the integrated concept had been sufficiently delineated with the cryogenic propellant design.

2.4.3 EFFECTS OF THE THIRD STAGE CONFIGURATION ON FIRST AND SECOND STAGE STRUCTURE WEIGHT

The effects of changing the third stage configurations (i.e., going from conventional to the integrated concept) on the structural loads in the boost stages of the vehicles was very important to the relative advantages of the evaluated concepts. Bending and axial load determination and structure weight calculations were completed for the boost stages of each vehicle. These results are presented in Table II and Figure 10. For the purposes of payload comparison, the first and second stage structure and interstage weights of the conventional liquid oxygen/liquid hydrogen vehicle were used as a reference, and differences between the weights of this configuration and the other configurations, ΔW structure, were used to calculate the ΔW_{pl} which is presented in Table II. The term ΔW_{pl} is the ΔW structure of the particular element divided by the appropriate mass ratio(s) to correct it to third stage payload weight. The following trends were results of the detailed structural and weight analysis (see Section 4.4).

- Varying the third stage engine length not only changes interstage length, but also changes the bending loads and frustrum cone angle of the interstage structure (Figure 13). Weight per axial length of the second interstage was plotted in Figure 13 for the different vehicles. It can be seen that if the forward and aft diameters of the two joined stages are held constant to minimize tankage structure, a reduction in length does not bring the interstage weight down proportionately with this length change since the cone angle increases as the length is decreased.

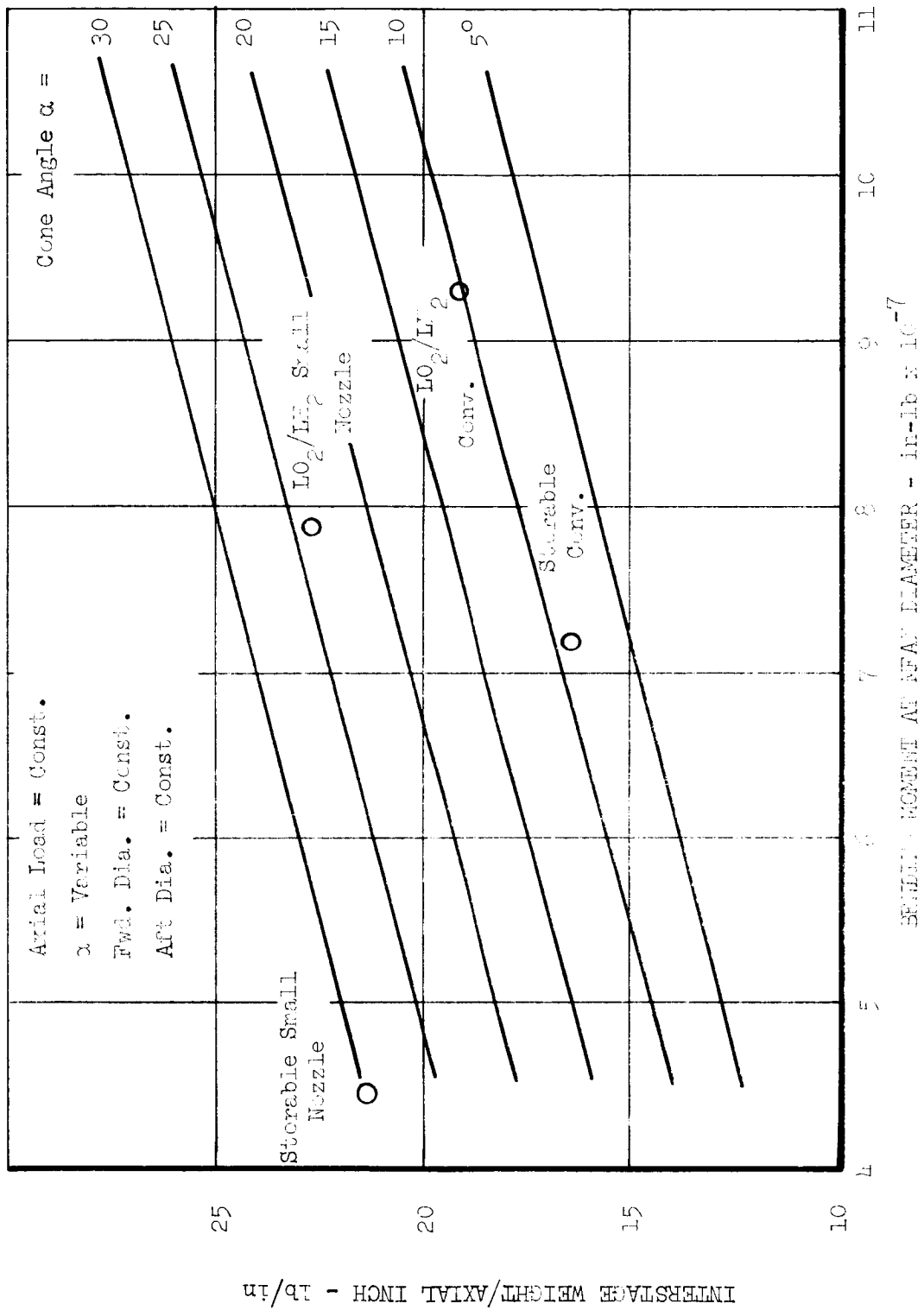


FIGURE 13. Effect of Bending Moment and Cone Angle on Interstage Weight

Another interesting factor brought out by the structural analysis and detailed design study was the relationship between the bending loads imposed on the stage, and the stage weight. Percent of the reference stage weight was plotted versus percent of the reference bending moment calculated at the base of the fuel tank. It was determined from the detailed design study that approximately sixty percent of the vehicle tankage and structural weight is contributed by elements dependent on bending loads and that the bending load is approximately sixty percent of the total load imposed on these structural elements. Therefore, as the curve in Figure 14 indicates, a decrease in bending moment, (related to changes in the third stage configuration in this case) of ten percent brings about a decrease in tankage and structural weight of about 3.6 percent.

It can be seen from Table II that differences in second stage tankage and structure weights are significant for some of the configurations and must be included in determining the payload capability of the vehicles.

However, changes in bending moment in the first stage due to changes in third stage geometrical configuration are very small (Figure 10) and the corresponding payload contributions from these changes are also small (Table II).

2.4.4 PAYLOAD COMPARISON OF THE EVALUATED VEHICLES

Payload for the reference and integrated vehicle configurations is summarized in the table below.

Configuration	Conventional LO ₂ /LH ₂	Small Nozzle Concept LO ₂ /LH ₂	Integrated Nozzle/Tank LO ₂ /LH ₂	Conven- tional H ₂ O ₂ /B ₂ H ₆	Small Nozzle Concept H ₂ O ₂ /B ₂ H ₆
Payload - lb 100% Shifting	113,588	108,184	115,558	109,593	109,334
Relative Payload-% 100% Shifting	100.0	95.3	102.0	96.6	96.5
Relative Payload 100% Frozen	95.1	95.0			

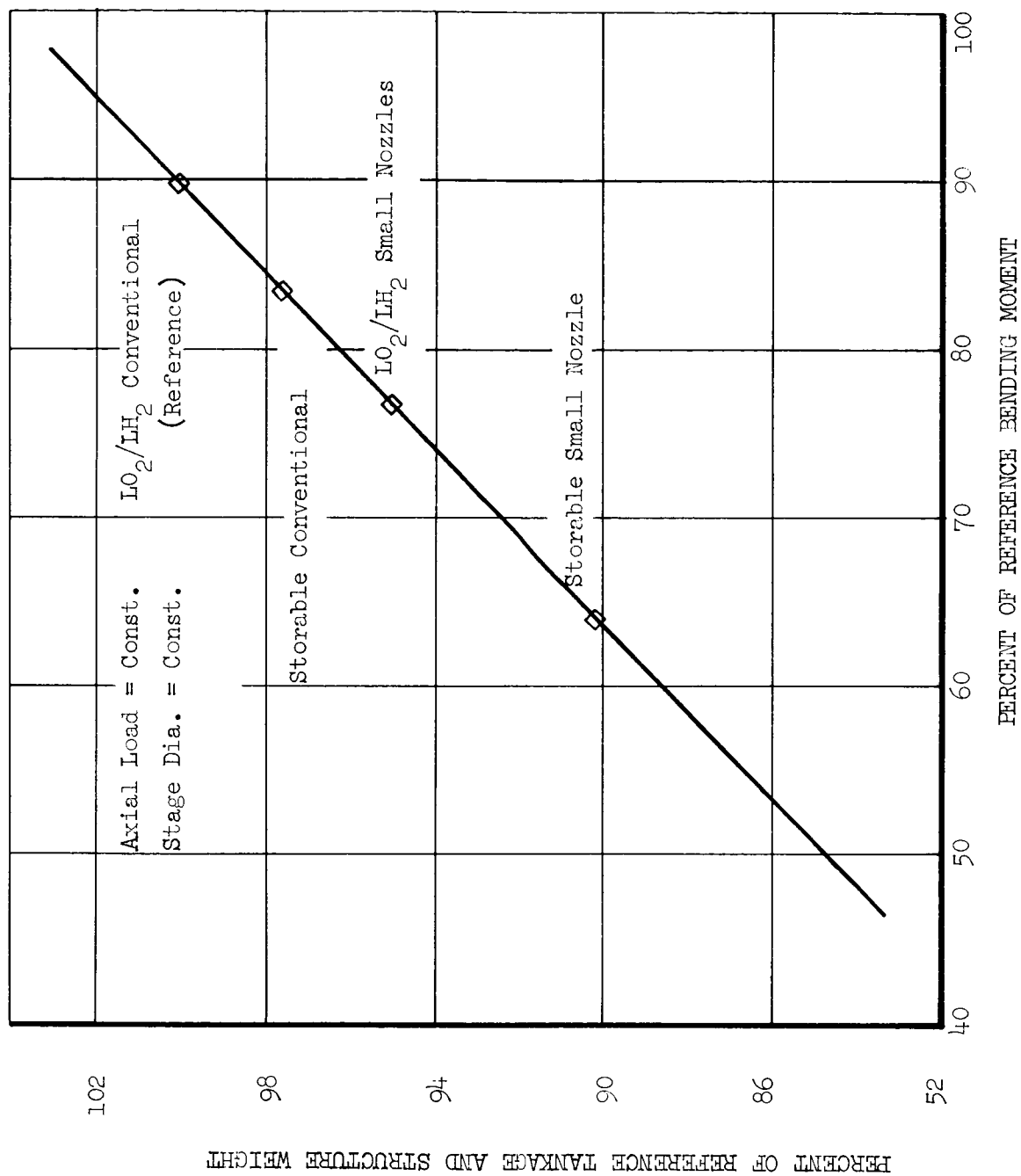


FIGURE 14. Effect of Bending Moment on Tankage and Structure Weight

2.4.4.1 LIQUID OXYGEN/LIQUID HYDROGEN PROPELLANTS

2.4.4.1.1 INTEGRATED VEHICLE

The integrated nozzle/tankhead vehicle has a two percent payload advantage over the conventional vehicle. Although the gross payload increase due to higher specific impulse and savings in first and second stage structure weights amounted to about 4000 pounds, a much heavier integrated tankhead/nozzle now carried with the third stage makes the propulsion system about 1800 pounds heavier than the conventional propulsion system. The net payload advantage is therefore limited to about 2200 pounds or two percent.

2.4.4.1.2 SMALL NOZZLE CONCEPT

The small nozzle concept/vehicle has limited payload capability with this propellant combination due to the non-optimum mixture ratio for shifting equilibrium performance. In going from mixture ratio of 6.0 to 3.0, the propellant weight is increased 3600 pounds and the propellant bulk density is decreased considerably. In addition, the propulsion system weight is 1300 pounds higher than for the conventional system. These disadvantages are partially offset by decreased first and second stage weights, however the net payload for the concept is 96 percent of the conventional vehicle payload.

When 100 percent frozen equilibrium performance is assumed, the mixture ratio is not as "off-optimum" and payload is nearly equal for the conventional and small nozzle vehicles.

2.4.4.2 HYDROGEN PEROXIDE/DIBORANE PROPELLANTS

2.4.4.2.1 CONVENTIONAL VEHICLE

A very interesting point brought out by the study was the payload capability of this propellant combination relative to the high energy cryogenic system. Even if some reasonable estimates of combustion efficiency are introduced, the payload capability of this storable combination merits further investigation.

2.4.4.2.2 SMALL NOZZLE VEHICLE

The small nozzle vehicle configuration has lower specific impulse than the conventional vehicle and a heavier engine; however, reductions on first and second stage tankage, structure, and interstage weights bring the net payload to very near that provided by the conventional vehicle. In addition, the length of this vehicle is 20 feet shorter than the conventional vehicle length.

2.5 RESULTS OF THE EXPERIMENTAL PROGRAM (Refer to Section 5)

Objectives of the experimental program were;

1. To determine nozzle drag losses at two Reynolds Numbers, therefore making possible the correlation of measured losses with the theoretical methods of prediction.
2. To substantiate the predicted difference in drag for two-dimensional and three-dimensional nozzles.

These test objectives were selected as being the most meaningful to the evaluation of the small nozzle concept, and valuable to the general technology of nozzle performance prediction.

Two test nozzles were fabricated and cold flow tested at the facilities of the Fluidyne Engineering Corporation. One nozzle was a 15° half-angle conical nozzle and the other was a two-dimensional forced-deflection nozzle with throat width of .054 inches. Both models had an expansion ratio of 65:1 and throat area of 1.0 square inch. The nozzles were run at various pressure ratios and at two different chamber pressures (i.e., two different Reynolds Numbers). Each model had over 100 static pressure taps downstream of the throat. The frictional force in the nozzle was calculated from the thrust coefficient determined from force balance readings and the thrust coefficient obtained from the integral of wall pressure and area. Results of the experimental study are summarized in the following table.

Configuration	Throat Reynolds Number/ft	Chamber Pressure psia	Static Thrust Coefficient C_{T_F}	Measured Drag Loss ΔC_{T_a}	Predicted Drag Loss ΔC_{T_p}	Computed Experimental Error ΔC_{T_e}
15° Conical Nozzle	4.2×10^7	135	0.974	0.004	.015	$\pm .001$
	1.46×10^7	45	0.974	0.005	.019	$\pm .001$
2-D Forced- Deflection Nozzle	4.22×10^7	135	0.972	0.028	.014	$\pm .0035$
	1.47×10^7	45	0.971	0.022	.017	$\pm .0035$

Since, theoretically, nozzle frictional drag is inversely proportional to the Reynolds Number, nozzle drag should increase as Reynolds Number (or chamber pressure) is decreased. The data indicate that for the forced-deflection nozzle, the measured drag does not show this predicted trend with Reynolds Number. However, there was evidence during the test that unanticipated flow variations were obtained in the two-dimensional nozzle when the chamber pressure was varied from 45 to 135 psia (at the same pressure ratio) and this phenomenon might possibly have caused the drag to differ from the expected trend. Magnitude of the measured drag for this nozzle was found to be about 20 to 80 percent higher than the predicted value for the high and low Reynolds Numbers, respectively.

The measured drag data for the conical nozzle exhibits the predicted trend with Reynolds Number, but the drag is only about 25 percent of the predicted drag at each Reynolds Number.

Since the same equations were used for predicting the drag for each nozzle, and assuming the same flow phenomenon is being dealt with, it seems unlikely that the equations would predict drag values four times too high for the conical nozzle and half the correct value for the two-dimensional nozzle.* It appears to be more probable that the errors in instrumentation,

* Spalding and Chi, AIAA Journal, pg 2160, 1963, show the root mean square of $\frac{C_{f \text{ experimental}}}{C_{f \text{ theoretical}}} - 1$ for 22 data sources, as calculated by the Frankl-Voishel Equation, to be 28 percent.

recording, data reduction, and analysis may have reduced the accuracy of determining the actual frictional forces in the nozzle below that predicted by error analysis and below the accuracy which might be expected from a review of the excellent reproducibility of data evidenced in the test program. This conclusion is further supported by the boundary layer probe data which were obtained for each nozzle in the test program. Predicted boundary layer thickness for the two nozzles is shown below.

Configuration	Throat Reynolds Number/foot	Predicted Exit B.L. Thickness, δ in.
15° Conical Nozzle	4.2×10^7	.27
	1.46×10^7	.34
2-d Forced-Deflection Nozzle	4.22×10^7	.25
	1.47×10^7	.31

The rake data indicated that free stream total pressure was obtained at .30 to .40 inches from the wall for the conical nozzle, and .25 to .35 inches for the forced deflection nozzle, and the boundary layer was thicker at the low chamber pressures as would be expected from the theory. The fact that the measured boundary layer was even thicker for the conical nozzle than for the two-dimensional nozzle is further evidence that the measured nozzle frictional losses should be suspected.

Although painstaking efforts were put forth under this program to insure sufficient accuracy in the instrumentation and reduction of data, it appears that additional experimental effort is necessary (preferably after further refinement of techniques and facilities) before sound conclusions can be drawn concerning correlation of theoretical and experimental frictional losses in nozzles.

2.6 CONCLUSIONS AND RECOMMENDATIONS

A wide array of vehicles utilizing integrated nozzle/structure configurations have been qualitatively and quantitatively evaluated in this study. It should be emphasized that the conventional stages against which these concepts were compared had both optimized engine performance and very high propellant fractions:

- Conventional (Liquid Oxygen/Liquid Hydrogen)

Specific impulse = 462 ($P_c = 520$ psia, $\epsilon = 220$)

Propellant fraction = .910 including jettisoned interstage

- Conventional (Hydrogen Peroxide/Diborane)

Specific impulse = 419 ($P_c = 525$ psia, $\epsilon = 220$)

Propellant fraction = .939 including jettisoned interstage

These "conventional" stages were intended to represent the maximum payload capability available from present technology, non-integrated, vehicles. Promising integrated concepts evolved in this study cannot be expected to provide large* payload advantages relative to these reference stages. Thus factors other than payload improvement become important to the results of the study.

The integrated nozzle/tankhead concept affords a gain in payload of two percent and reduces vehicle length by 112 inches (for the stage evaluated in this study). However, these advantages could very easily be offset by the restricted usage of the second stage imposed by the integrated tankhead. Recommended usage of this stage would be dependent on a study of

* If a hypothetical integrated stage were devised which eliminated 30 percent of the total inert weight of the conventional H_2O_2/B_2H_6 stage and the specific impulse increased simultaneously by increasing the nozzle expansion ratio to 400:1 (without added weight), the payload of this hypothetical stage would be 4 percent greater than that of the conventional H_2O_2/B_2H_6 stage. Since engine weight for the conventional stage is only about 15 percent of the total inert weight of that vehicle, the goals set for this hypothetical stage are obviously high and the seemingly "small" improvement in payload of 4 percent would be a significant gain and difficult to obtain with integration or other unconventional schemes.

the cost per pound of delivered payload for a given mission (i.e., the penalty of restricted usage may be insignificant for military or tactical applications where a large number of vehicles would be required, but could be very important in the selection of a stage for space applications where the stage has to be used with several booster vehicle combinations for maximum economy).

The small nozzle concept decreases over-all vehicle length significantly (242 inches for the stage evaluated). This reduction in length offers important fabrication and operational advantages, especially for the very large vehicles anticipated for interplanetary manned missions. The relative payload advantages of vehicles using either small throated two-dimensional nozzles, or very small distributed nozzles integrated with tankage or other surfaces of the vehicle is dependent on more conclusive determination of actual nozzle drag losses. However, small nozzles, distributed or two-dimensional, lend themselves to unconventional envelope requirements and should be considered for applications where minimum engine lengths are required and high area ratio is necessary for the desired performance.

In general, the results of this study show that only small payload advantages can be expected from integrated propulsion and structural elements due to resultant compromises in expansion performance and/or structural weights. In addition, the integration schemes tend to restrict the flexibility of multiple usage in both the propulsion and structural elements, thus making the integrated schemes unattractive from the cost standpoint.

Section 3
VEHICLE CONCEPTUAL STUDY

The first task in the program was to evolve as many means of integrating engine and vehicle surfaces as possible. Obvious advantages of producing a large number of configurations for evaluation are that;

- (1) Some apparently unpromising or impractical designs might suggest other designs which are more feasible,
- (2) The greater the number of configurations which are considered, the smaller the chance that promising concepts have been overlooked.

After the concept formulation phase of the study, a qualitative analysis was made of each configuration such that the most promising of the designs could be evaluated in more detail. Finally, two configurations were selected for detailed evaluation in order to determine potential payload capability and to bring out considerations not recognized in the initial evaluation.

3.1 METHOD OF EVOLVING CONCEPTS

Several means of evolving integration concepts are available, among them systematized methods such as morphological construction, and unordered methods such as "brainstorming" or collecting "pet" ideas from project personnel. In the systematic method, integration techniques can be evolved without the chance of leaving out promising combinations (within the matrix considered). However, this system does lack the freedom of thought inherent in the brainstorming technique.

Therefore, since the methods actually complement each other, both were used in evolving vehicle configurations.

3.1.1 MATRIX CONSTRUCTION

Examination of upper stage vehicles indicated that the following components might possibly be acceptable as expansion surfaces:

- (1) Payload shroud
- (2) Payload
- (3) Forward tank closure
- (4) Tank trunk
- (5) Aft tank closure
- (6) Interstage
- (7) Stage below

These surfaces, which comprise the major portion of the vehicle inert weight, were then combined with four different types of nozzles; bell, forced-deflection, plug, and two-dimensional. The different nozzle configurations can be mounted on the vehicle elements either internally or externally. Thus, the matrix becomes a $7 \times 4 \times 2$ construction providing 56 integrated configurations. The matrix order is shown below.

I	II	III
1. Payload	1. Bell	1. Internal
2. Forward tank closure	2. Plug	2. External
3. Tank trunk	3. Forced-deflection	
4. Aft tank closure	4. Two-dimensional	
5. Interstage structure		
6. Stage below		
7. Payload shroud		

3.2 QUALITATIVE EVALUATION OF CONCEPTS

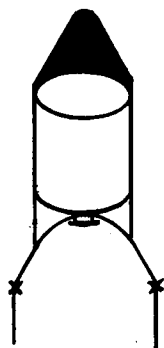
Since the large number of concepts generated (approximately 200) would have taken excessive time to quantitatively evaluate either in a preliminary or detailed manner, a qualitative rating system was devised to separate the more promising configurations. Concepts were rated on apparent

advantages or disadvantages in the areas of engine performance, structure weight, engine weight, possible heat transfer problems, and payload restrictions.

- (1) Engine performance - includes available expansion ratio gas-dynamic contour, and obstructions in the nozzle flow.
- (2) Tankage and Structure weight - includes pressure vessel shape, total inert weight, load paths, general simplicity, and propellant outage.
- (3) Engine weight - includes compromise due to shape, integration with very heavy structure usually jettisoned, NPSH considerations.
- (4) Heat transfer - includes consideration of propellant boiloff due to proximity of hot gases or hot surfaces to liquid propellants, and inert weight of potential insulation requirements.
- (5) Payload restrictions - includes compromise of payload envelope, or requirement of payload reorientation.

Ratings of 1, 2, or 3 were given for each of the five areas of evaluation listed above. A rating of one means that the configuration appears to be better than the conventional (non-integrated) vehicle in that particular category; a rating of two denotes no apparent advantage or disadvantage; and a rating of three means the design is not as good as the conventional vehicle. Some categories were indeterminate without further study and were not rated. A sample of the rating chart is shown below.

531



	1	2	3
Engine Performance	x		
Structural Weight		x	
Engine Weight			x
Heat Transfer		x	
Payload Restrictions		x	

Remarks:

Increased area ratio, nozzle wall heavy due to interstage design loads.

Rating B

The remarks area includes explanation of a given rating, or comments on factors such as compromise in vehicle aerodynamic shape, stability and control, and so on. Finally, a grade of A, B, or C was given to the configuration which takes into account all of the above considerations. The grade of A denotes a potential advantage, B means the configuration is probably only competitive with conventional vehicles, and C indicates that the concept does not appear to be competitive with conventional vehicles. The number adjacent to the vehicle configuration shows the combination of elements taken from the $7 \times 4 \times 2$ matrix. For example, the concept given above has the number 531 which means the interstage has been integrated with a forced-deflection type nozzle internally. Numbers on the brainstormed concepts are arbitrary and are included for convenience purposes when referring back to these concepts in the text. The -x- marks shown on the concepts indicate stage separation points or planes, and the shaded area in each configuration shows the envelope available for payload.

The concepts evolved from the morphological construction are shown in Figures 15 and 16, and the concepts which resulted from brainstorming techniques are given in Figures 17 and 18. A total of 107 vehicle concepts are presented, of these 9 have been given a rating of A, 24 a rating of B, and the remainder are rated as C or indeterminate.

3.3 PRELIMINARY EVALUATION OF MOST PROMISING CONCEPTS

3.3.1 PROMISING CONCEPTS

The most promising of the vehicle concepts (those rated as A) can be divided into configurations which (1) appear to have potential payload advantage for conventional applications, and (2) those which appear to have an advantage for special applications. These configurations are shown in Figure 19.

The distributed, or small throated engines (Nos. 105 and 1001, Figure 19) appeared to merit further evaluation at this stage of the study due to potential gains from high area ratios with minimum nozzle and interstage length.

45		<p>Engine Performance</p> <p>Structural Weight</p> <p>Engine Weight</p> <p>Heat Transfer</p> <p>Payload Restrictions</p>	<p>1 2 3</p> <table border="1"> <tr><td></td><td></td><td></td></tr> <tr><td></td><td></td><td></td></tr> <tr><td></td><td></td><td></td></tr> <tr><td></td><td></td><td></td></tr> <tr><td></td><td></td><td></td></tr> </table>																<p>Remarks:</p> <p>Inefficient tankage, outgase and structural problems inherent in area ratio, but saves adjacent to propellants.</p>	<p>Rating</p> <p><input type="checkbox"/> C</p>	<p>50</p>		<p>Engine Performance</p> <p>Structural Weight</p> <p>Engine Weight</p> <p>Heat Transfer</p> <p>Payload Restrictions</p>	<p>1 2 3</p> <table border="1"> <tr><td></td><td></td><td></td></tr> <tr><td></td><td></td><td></td></tr> <tr><td></td><td></td><td></td></tr> <tr><td></td><td></td><td></td></tr> <tr><td></td><td></td><td></td></tr> </table>																<p>Remarks:</p> <p>Poor load carrying structure, inefficient pressure vessel, propellant heating.</p>	<p>Rating</p> <p><input type="checkbox"/> U</p>	<p>55</p>		<p>Engine Performance</p> <p>Structural Weight</p> <p>Engine Weight</p> <p>Heat Transfer</p> <p>Payload Restrictions</p>	<p>1 2 3</p> <table border="1"> <tr><td></td><td></td><td></td></tr> <tr><td></td><td></td><td></td></tr> <tr><td></td><td></td><td></td></tr> <tr><td></td><td></td><td></td></tr> <tr><td></td><td></td><td></td></tr> </table>																<p>Remarks:</p> <p>Many disadvantages including control and outgase problems.</p>	<p>Rating</p> <p><input type="checkbox"/> C</p>	<p>60</p>		<p>Engine Performance</p> <p>Structural Weight</p> <p>Engine Weight</p> <p>Heat Transfer</p> <p>Payload Restrictions</p>	<p>1 2 3</p> <table border="1"> <tr><td></td><td></td><td></td></tr> <tr><td></td><td></td><td></td></tr> <tr><td></td><td></td><td></td></tr> <tr><td></td><td></td><td></td></tr> <tr><td></td><td></td><td></td></tr> </table>																<p>Remarks:</p> <p>Severe payload restriction, expandable nozzle requires further study.</p>	<p>Rating</p> <p><input type="checkbox"/> B</p>	<p>72</p>		<p>Engine Performance</p> <p>Structural Weight</p> <p>Engine Weight</p> <p>Heat Transfer</p> <p>Payload Restrictions</p>	<p>1 2 3</p> <table border="1"> <tr><td></td><td></td><td></td></tr> <tr><td></td><td></td><td></td></tr> <tr><td></td><td></td><td></td></tr> <tr><td></td><td></td><td></td></tr> <tr><td></td><td></td><td></td></tr> </table>																<p>Remarks:</p> <p>Severe payload restriction, expandable nozzle requires further study.</p>	<p>Rating</p> <p><input type="checkbox"/> B</p>
46		<p>Engine Performance</p> <p>Structural Weight</p> <p>Engine Weight</p> <p>Heat Transfer</p> <p>Payload Restrictions</p>	<p>1 2 3</p> <table border="1"> <tr><td></td><td></td><td></td></tr> <tr><td></td><td></td><td></td></tr> <tr><td></td><td></td><td></td></tr> <tr><td></td><td></td><td></td></tr> <tr><td></td><td></td><td></td></tr> </table>																<p>Remarks:</p> <p>Eliminates interstage, heat transfer to payload and separation of payload a problem.</p>	<p>Rating</p> <p><input type="checkbox"/> B</p>	<p>51</p>		<p>Engine Performance</p> <p>Structural Weight</p> <p>Engine Weight</p> <p>Heat Transfer</p> <p>Payload Restrictions</p>	<p>1 2 3</p> <table border="1"> <tr><td></td><td></td><td></td></tr> <tr><td></td><td></td><td></td></tr> <tr><td></td><td></td><td></td></tr> <tr><td></td><td></td><td></td></tr> <tr><td></td><td></td><td></td></tr> </table>																<p>Remarks:</p> <p>Poor load carrying structure, inefficient pressure vessel, propellant heating.</p>	<p>Rating</p> <p><input type="checkbox"/> C</p>	<p>56</p>		<p>Engine Performance</p> <p>Structural Weight</p> <p>Engine Weight</p> <p>Heat Transfer</p> <p>Payload Restrictions</p>	<p>1 2 3</p> <table border="1"> <tr><td></td><td></td><td></td></tr> <tr><td></td><td></td><td></td></tr> <tr><td></td><td></td><td></td></tr> <tr><td></td><td></td><td></td></tr> <tr><td></td><td></td><td></td></tr> </table>																<p>Remarks:</p> <p>Many disadvantages including control and outgase problems.</p>	<p>Rating</p> <p><input type="checkbox"/> C</p>	<p>61</p>		<p>Engine Performance</p> <p>Structural Weight</p> <p>Engine Weight</p> <p>Heat Transfer</p> <p>Payload Restrictions</p>	<p>1 2 3</p> <table border="1"> <tr><td></td><td></td><td></td></tr> <tr><td></td><td></td><td></td></tr> <tr><td></td><td></td><td></td></tr> <tr><td></td><td></td><td></td></tr> <tr><td></td><td></td><td></td></tr> </table>																<p>Remarks:</p> <p>Nozzle is stored over payload and rotated into position.</p>	<p>Rating</p> <p><input type="checkbox"/> X</p>																					
47		<p>Engine Performance</p> <p>Structural Weight</p> <p>Engine Weight</p> <p>Heat Transfer</p> <p>Payload Restrictions</p>	<p>1 2 3</p> <table border="1"> <tr><td></td><td></td><td></td></tr> <tr><td></td><td></td><td></td></tr> <tr><td></td><td></td><td></td></tr> <tr><td></td><td></td><td></td></tr> <tr><td></td><td></td><td></td></tr> </table>																<p>Remarks:</p> <p>Engine is two dimensional with chamber between tanks, heat transfer between tanks, but saves adjacent to propellant tanks.</p>	<p>Rating</p> <p><input type="checkbox"/> C</p>	<p>52</p>		<p>Engine Performance</p> <p>Structural Weight</p> <p>Engine Weight</p> <p>Heat Transfer</p> <p>Payload Restrictions</p>	<p>1 2 3</p> <table border="1"> <tr><td></td><td></td><td></td></tr> <tr><td></td><td></td><td></td></tr> <tr><td></td><td></td><td></td></tr> <tr><td></td><td></td><td></td></tr> <tr><td></td><td></td><td></td></tr> </table>																<p>Remarks:</p> <p>Expandable nozzle.</p>	<p>Rating</p> <p><input type="checkbox"/> X</p>	<p>57</p>		<p>Engine Performance</p> <p>Structural Weight</p> <p>Engine Weight</p> <p>Heat Transfer</p> <p>Payload Restrictions</p>	<p>1 2 3</p> <table border="1"> <tr><td></td><td></td><td></td></tr> <tr><td></td><td></td><td></td></tr> <tr><td></td><td></td><td></td></tr> <tr><td></td><td></td><td></td></tr> <tr><td></td><td></td><td></td></tr> </table>																<p>Remarks:</p> <p>Propellant heating, inefficient pressure vessel.</p>	<p>Rating</p> <p><input type="checkbox"/> C</p>	<p>64</p>		<p>Engine Performance</p> <p>Structural Weight</p> <p>Engine Weight</p> <p>Heat Transfer</p> <p>Payload Restrictions</p>	<p>1 2 3</p> <table border="1"> <tr><td></td><td></td><td></td></tr> <tr><td></td><td></td><td></td></tr> <tr><td></td><td></td><td></td></tr> <tr><td></td><td></td><td></td></tr> <tr><td></td><td></td><td></td></tr> </table>																<p>Remarks:</p> <p>Could be advantageous for some payload configurations.</p>	<p>Rating</p> <p><input type="checkbox"/> A</p>	<p>77</p>		<p>Engine Performance</p> <p>Structural Weight</p> <p>Engine Weight</p> <p>Heat Transfer</p> <p>Payload Restrictions</p>	<p>1 2 3</p> <table border="1"> <tr><td></td><td></td><td></td></tr> <tr><td></td><td></td><td></td></tr> <tr><td></td><td></td><td></td></tr> <tr><td></td><td></td><td></td></tr> <tr><td></td><td></td><td></td></tr> </table>																<p>Remarks:</p> <p>Severe payload restriction, expandable nozzle requires further study.</p>	<p>Rating</p> <p><input type="checkbox"/> B</p>
48		<p>Engine Performance</p> <p>Structural Weight</p> <p>Engine Weight</p> <p>Heat Transfer</p> <p>Payload Restrictions</p>	<p>1 2 3</p> <table border="1"> <tr><td></td><td></td><td></td></tr> <tr><td></td><td></td><td></td></tr> <tr><td></td><td></td><td></td></tr> <tr><td></td><td></td><td></td></tr> <tr><td></td><td></td><td></td></tr> </table>																<p>Remarks:</p> <p>Expandable plug nozzle, design would require further study.</p>	<p>Rating</p> <p><input type="checkbox"/> X</p>	<p>53</p>		<p>Engine Performance</p> <p>Structural Weight</p> <p>Engine Weight</p> <p>Heat Transfer</p> <p>Payload Restrictions</p>	<p>1 2 3</p> <table border="1"> <tr><td></td><td></td><td></td></tr> <tr><td></td><td></td><td></td></tr> <tr><td></td><td></td><td></td></tr> <tr><td></td><td></td><td></td></tr> <tr><td></td><td></td><td></td></tr> </table>																<p>Remarks:</p> <p>Large area ratio, poor pressure between tanks, heat transfer between tanks adjacent to propellant tanks.</p>	<p>Rating</p> <p><input type="checkbox"/> C</p>	<p>58</p>		<p>Engine Performance</p> <p>Structural Weight</p> <p>Engine Weight</p> <p>Heat Transfer</p> <p>Payload Restrictions</p>	<p>1 2 3</p> <table border="1"> <tr><td></td><td></td><td></td></tr> <tr><td></td><td></td><td></td></tr> <tr><td></td><td></td><td></td></tr> <tr><td></td><td></td><td></td></tr> <tr><td></td><td></td><td></td></tr> </table>																<p>Remarks:</p> <p>Many disadvantages.</p>	<p>Rating</p> <p><input type="checkbox"/> C</p>	<p>69</p>		<p>Engine Performance</p> <p>Structural Weight</p> <p>Engine Weight</p> <p>Heat Transfer</p> <p>Payload Restrictions</p>	<p>1 2 3</p> <table border="1"> <tr><td></td><td></td><td></td></tr> <tr><td></td><td></td><td></td></tr> <tr><td></td><td></td><td></td></tr> <tr><td></td><td></td><td></td></tr> <tr><td></td><td></td><td></td></tr> </table>																<p>Remarks:</p> <p>Severe payload restriction, expandable nozzle requires further study.</p>	<p>Rating</p> <p><input type="checkbox"/> B</p>																					
49		<p>Engine Performance</p> <p>Structural Weight</p> <p>Engine Weight</p> <p>Heat Transfer</p> <p>Payload Restrictions</p>	<p>1 2 3</p> <table border="1"> <tr><td></td><td></td><td></td></tr> <tr><td></td><td></td><td></td></tr> <tr><td></td><td></td><td></td></tr> <tr><td></td><td></td><td></td></tr> <tr><td></td><td></td><td></td></tr> </table>																<p>Remarks:</p> <p>Expandable plug, payload chamber weight but reduces structure loads in tank.</p>	<p>Rating</p> <p><input type="checkbox"/> X</p>	<p>54</p>		<p>Engine Performance</p> <p>Structural Weight</p> <p>Engine Weight</p> <p>Heat Transfer</p> <p>Payload Restrictions</p>	<p>1 2 3</p> <table border="1"> <tr><td></td><td></td><td></td></tr> <tr><td></td><td></td><td></td></tr> <tr><td></td><td></td><td></td></tr> <tr><td></td><td></td><td></td></tr> <tr><td></td><td></td><td></td></tr> </table>																<p>Remarks:</p> <p>Heavy tankage and combustion chamber weight but saves adjacent to propellant tanks.</p>	<p>Rating</p> <p><input type="checkbox"/> C</p>	<p>71</p>		<p>Engine Performance</p> <p>Structural Weight</p> <p>Engine Weight</p> <p>Heat Transfer</p> <p>Payload Restrictions</p>	<p>1 2 3</p> <table border="1"> <tr><td></td><td></td><td></td></tr> <tr><td></td><td></td><td></td></tr> <tr><td></td><td></td><td></td></tr> <tr><td></td><td></td><td></td></tr> <tr><td></td><td></td><td></td></tr> </table>																<p>Remarks:</p> <p>Severe payload restriction, expandable nozzle requires further study.</p>	<p>Rating</p> <p><input type="checkbox"/> B</p>	<p>77a</p>		<p>Engine Performance</p> <p>Structural Weight</p> <p>Engine Weight</p> <p>Heat Transfer</p> <p>Payload Restrictions</p>	<p>1 2 3</p> <table border="1"> <tr><td></td><td></td><td></td></tr> <tr><td></td><td></td><td></td></tr> <tr><td></td><td></td><td></td></tr> <tr><td></td><td></td><td></td></tr> <tr><td></td><td></td><td></td></tr> </table>																<p>Remarks:</p> <p>Nozzle is stored over payload and rotated into position.</p>	<p>Rating</p> <p><input type="checkbox"/> X</p>																					

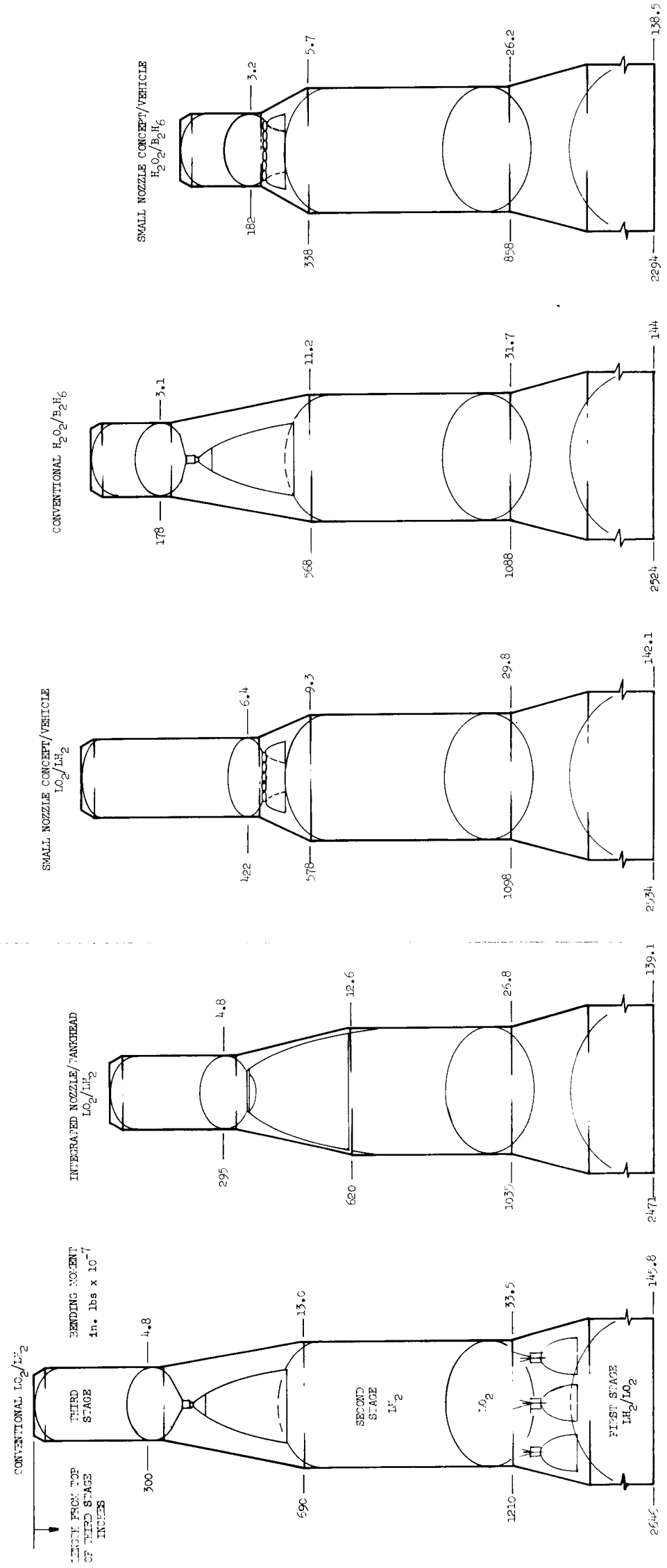


FIGURE 10. Evaluated Vehicle Configurations

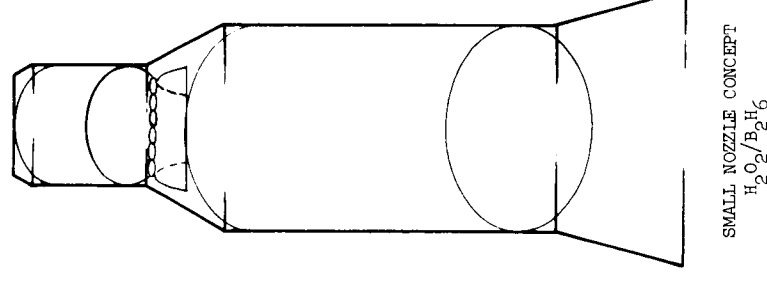
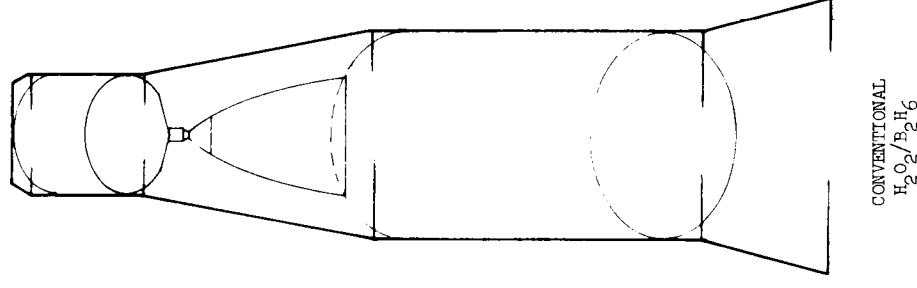
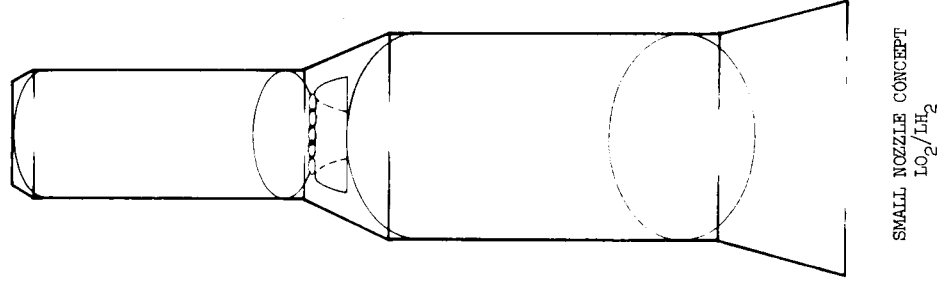
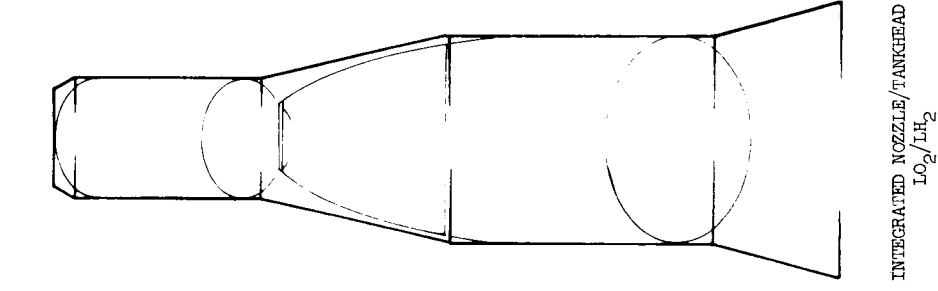
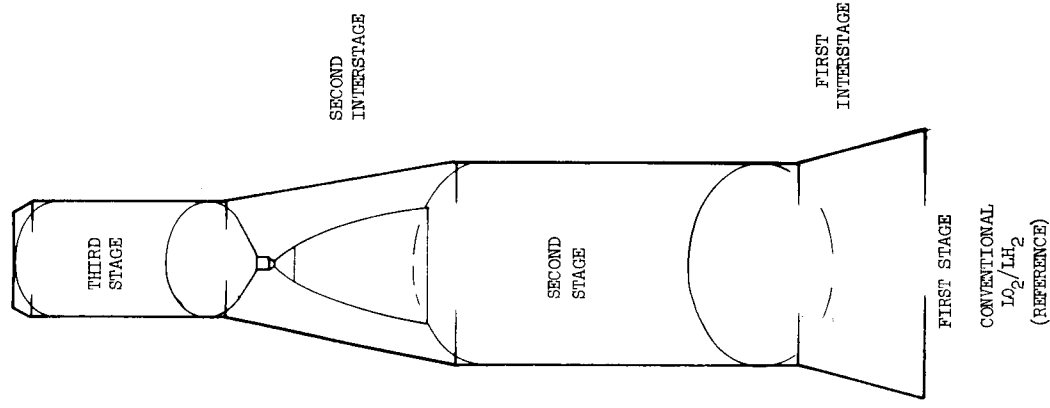


FIGURE 3. Configurations of the Evaluated Vehicles

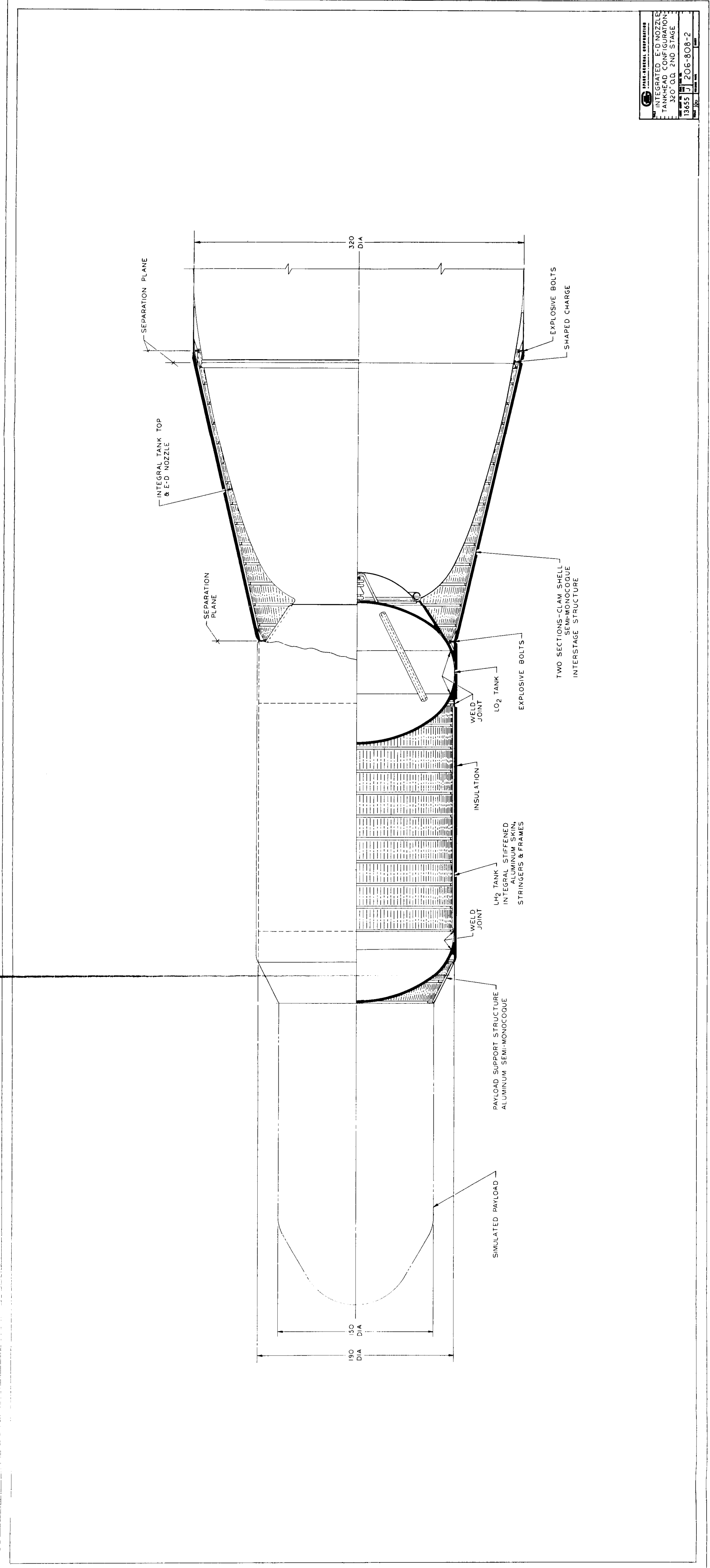


FIGURE 7. Integrated Vehicle Design

Legend:

- 1 = Apparent advantage over "Conventional"
- 2 = Same as Conventional
- 3 = Apparent disadvantage compared to Conventional

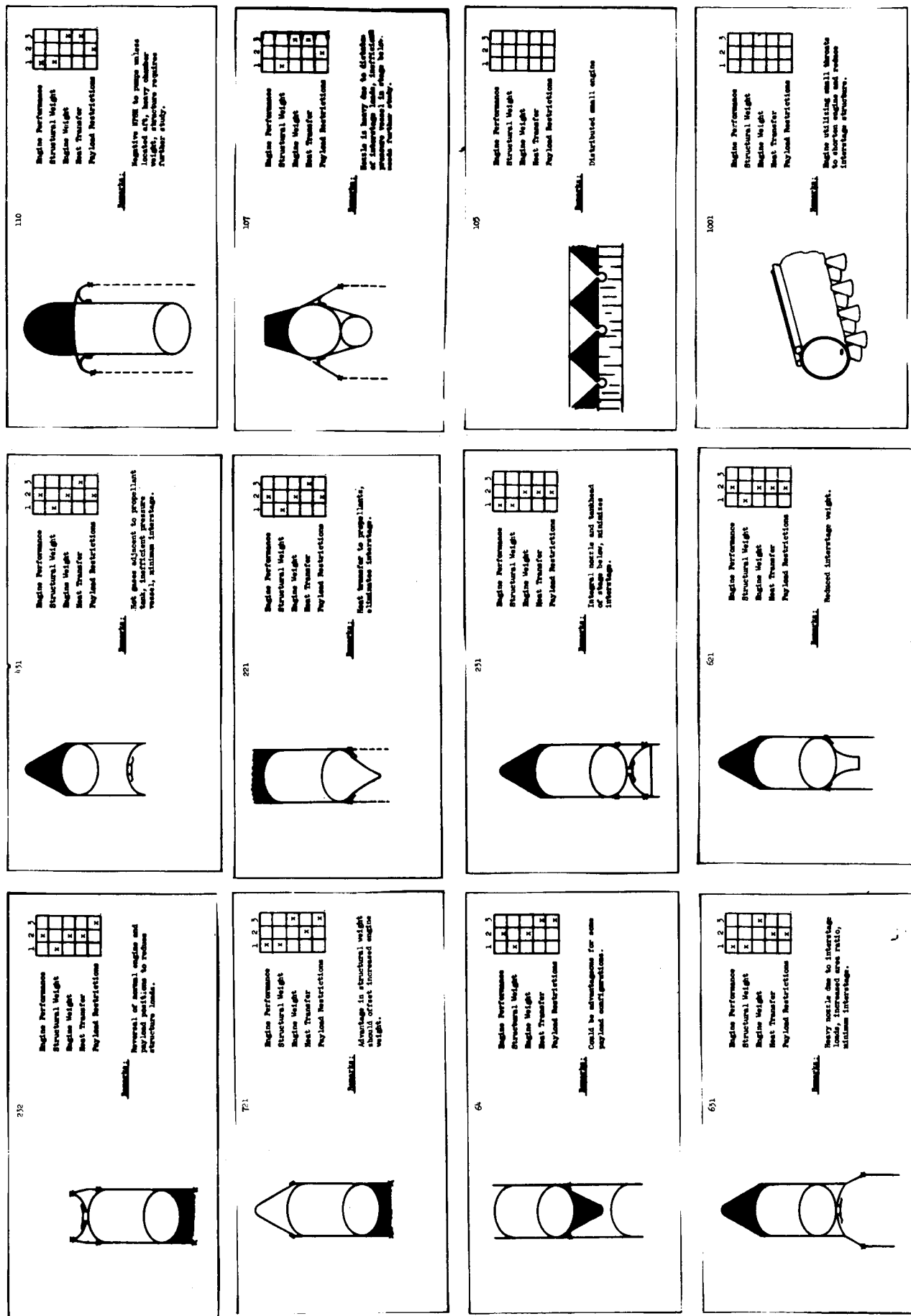


FIGURE 19. Most Promising Vehicle Concepts

Qualitative evaluation showed potential payload gains due to either (or a combination of) structural weight decrease or engine performance increase for all of the vehicles in Figure 19. However, each configuration has restrictions or potential problem areas resulting from the integration of vehicle elements. These considerations are summarized in Table III.

The concepts which restrict payload envelope (64, 232, 721), and those which limit the useage of both the second and third stage structure and third stage propulsion system (107, 110) were considered to be promising for specialized applications only. Concept 631, which appeared to offer an advantage over the conventional vehicle after the initial qualitative examination, was eliminated later because of payload penalties resulting from the vehicle having to carry the heavy interstage/nozzle after separation from the lower stage. The remaining concepts, 621, 231, 431, 221, and the small nozzle concepts (105, 1001) were selected for preliminary weight and performance analysis.

3.3.2 PRELIMINARY WEIGHT AND PERFORMANCE ANALYSIS

The following assumptions were used in the comparative analysis of the vehicle concepts:

- (1) Escape from earth orbit mission - $\Delta V = 10,000$ fps. The vehicle studied performs the escape maneuver from a 300 n.m. orbit and is boosted to orbit by two liquid hydrogen/liquid oxygen stages.
- (2) Gross weight of the third stage is 240,000 pounds.
- (3) The evaluated stage utilizes liquid oxygen/liquid hydrogen, a pumped feed system, propellant mixture ratio of 6.0, and 100 percent shifting combustion performance.
- (4) Third stage design loads which were assumed to be dictated by the boost trajectory, were calculated from accelerations of 4 "g's" axial and 1 "g" transverse. Aluminum with strength/density ratio of 470,000 in. was used for tankage and structure. In this preliminary evaluation the effect of changes in bending moments in the first and second stages resulting from the different integrated configurations was neglected.

TABLE III
RESTRICTIONS AND POTENTIAL PROBLEM AREAS

Configuration (Refer to Figure 19)	221	621	231	431	631	232	721	64	107	110	105 and 1001
Restrictions											
Payload Envelope						X	X	X			
Third Stage Use									X	X	-
Third Stage Engine Use	X		X	X	X			X	X	X	-
Second Stage Use	X	X	X		X			X	X	X	
Potential Problem Areas											
Heat Transfer	X			X	X			X	X	X	X
Reorientation of Vehicle After Separation						X	X				

X means the configuration has the given restriction or problem area

- means the restriction is dependent on the way in which the engine is integrated with the vehicle.

3.3.2.1 INTEGRATED CONCEPTS 621, 231, 431, 221

The integrated concepts were compared with two unintegrated "conventional" vehicles; one utilizing a bell-type nozzle, and the other using a forced-deflection nozzle. Results of the preliminary study, indicating relative payloads of the configurations, are given in the table below.

Configuration	Conventional		621	231	431	221
	Bell (412)	Forced- Deflection (432)				
Relative Payload (Percent)	100.0	103.0	102.0	103.5	103.0	102.5

Each of the integrated configurations appear to have a relative payload gain over the conventional bell nozzle configuration; however, the integrated nozzle/tankhead concept (231) was the only configuration showing higher payload than the conventional forced-deflection engine/vehicle.

The forced-deflection nozzle (432) provides high area ratio with a nozzle length of 40 percent of the bell (412) nozzle length, thus reducing engine weight and interstage length and weight. At first glance, one would expect that utilizing this nozzle as the tankhead of the stage below (231) would greatly increase the payload of the vehicle system; however, as seen in the table this increase is on the order of a half percent. Although integration of the nozzle and tankhead essentially eliminates the tankhead weight, the nozzle has to be designed to withstand the tank pressure of the stage below and in addition the geometry of the nozzle and tank may be compromised. Similarly, compromises due to integration of elements reduces some of the potential in all of the concepts.

3.3.2.2 SMALL NOZZLE CONCEPT

The small nozzle concept was originally envisioned as a large number of very small throat, high area ratio nozzles distributed over tank or structure surfaces with the integrated combination having the strength characteristics of sandwich type structure. In this way, it appeared that

large areas could be made available for nozzle expansion and that possibly the integrated nozzle and structure weight would be about the same as the total weight of the separate elements. Regenerative cooling of the distributed very small nozzles appeared to be impractical, and operation at reduced (fuel rich) mixture ratio was investigated. Based on current and extrapolated high temperature materials technology, 4000°F appeared to be a reasonable upper limit for combustion temperature. Tungsten has a yield stress of 7000 psi at this temperature although to date no surface coating to prevent oxidation is available for this material.* The strength/weight characteristics of tungsten were used in the study to determine weights of the uncooled structural elements. Obviously any state-of-the-art advances in high temperature materials will make the concept more promising.

Another critical factor in evaluating the potential of this concept was the frictional drag associated with small throat radius (low Reynold's number), high area ratio, and reasonably low chamber pressures. Percentage impulse loss due to friction in conical nozzles is presented in Figure 20. It can be seen that the nozzle drag loss for typical boosters or possibly second stage applications (low area ratio, large thrust or throat radius, and high chamber pressure) is not significant; in the order of one-half to one percent. Nozzle length has also been plotted on Figure 20 to give a feeling for the thickness of integral nozzle/structure required for a given throat radius and expansion ratio. As throat radius is decreased, nozzle length (approximately equal to integrated structure thickness) is decreased, and impulse losses due to drag increase. These are conflicting trends from the design standpoint since tankage or structure weight would probably be excessive if it exceeded one inch in thickness over a large area. Impulse loss with area ratio of 200, chamber pressure of 200, and one inch nozzle length, is about 8 percent (Figure 20). Results of a study of a distributed nozzle vehicle configuration indicated that even though interstage due to nozzle length is eliminated, and available nozzle exit

* However, it was reported in the '63-'64 Space Aeronautics R and D Handbook that from tests, at NASA Materials Research Division, coatings protected pure tungsten for 10 hours at 3450°F and 30 hours at 3000°F.

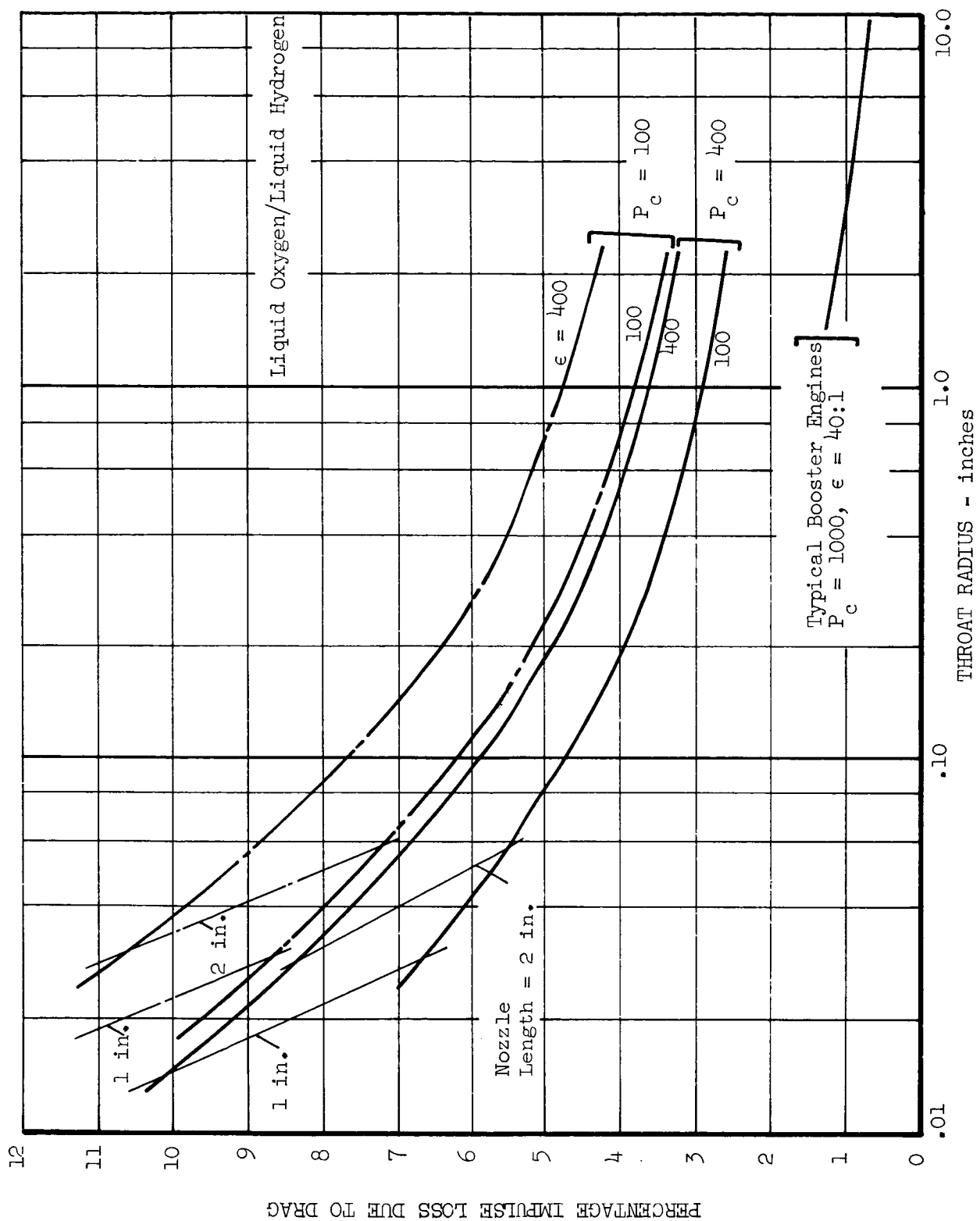


FIGURE 20. Frictional Drag Loss in Conical Nozzles
Predicted by Modified Frankl-Voishel Equation

area and area ratio are increased, the relative payload capability of this concept is two to three percent less than a conventional vehicle. This result is primarily due to:

- (1) loss in impulse due to frictional drag in the nozzles,
- (2) excessive weight of the distributed uncooled thrust chamber.

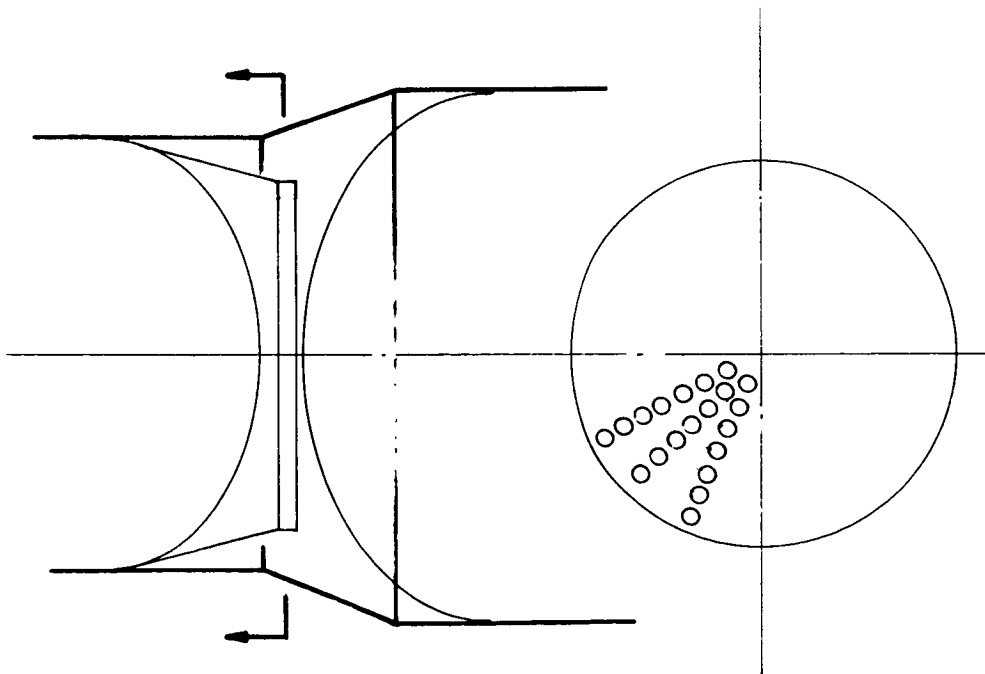
A second configuration utilized the small nozzle concept as a means to reduce interstage weight and decrease bending moments in the boost stages. The engine for this configuration could consist of clusters of bell nozzles, or rings of two-dimensional nozzles at the base of the aft tank as represented in Figure 21. Evaluation of these configurations showed that the two-dimensional forced-deflection nozzle with a single toroidal chamber (Figure 22) provided a higher payload capability than a large number of distributed three-dimensional nozzles or a series of rings of two-dimensional nozzles. The assumptions and ground rules used in the study were the same as discussed previously in this section. Results of the optimization of the two-dimensional nozzle are shown in Figure 23. Pertinent conclusions derived from the study were that frictional drag loss in the nozzle is both critical to the payload capability of the vehicle, and that trends in frictional drag with throat radius (or Reynold's Number) and nozzle geometry are important in establishing the best engine configuration.

3.4 SELECTION OF VEHICLES FOR DETAILED EVALUATION

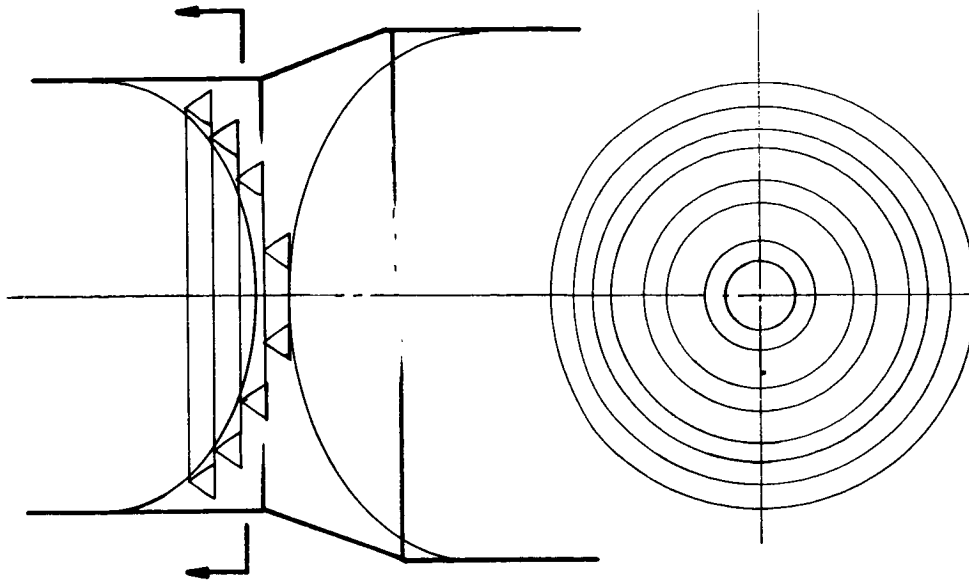
The following two concepts were selected for detailed evaluation as to performance, structure, weight, and payload capability to be performed during the second phase of the contract.

3.4.1 INTEGRATED NOZZLE/TANKHEAD CONFIGURATION

The integrated nozzle/tankhead vehicle exhibited the highest potential payload advantage of the integrated vehicles. This configuration reduces vehicle length, decreases bending moments in the boost stages, and has no apparently overwhelming problem areas.



CLUSTER OF SMALL CONICAL OR BELL
NOZZLES FED BY CENTRAL CHAMBER
AND RADIAL MANIFOLDS



RINGS OF TWO-DIMENSIONAL NOZZLES
WITH TOROIDAL CHAMBERS

FIGURE 21. Small Nozzle Concepts

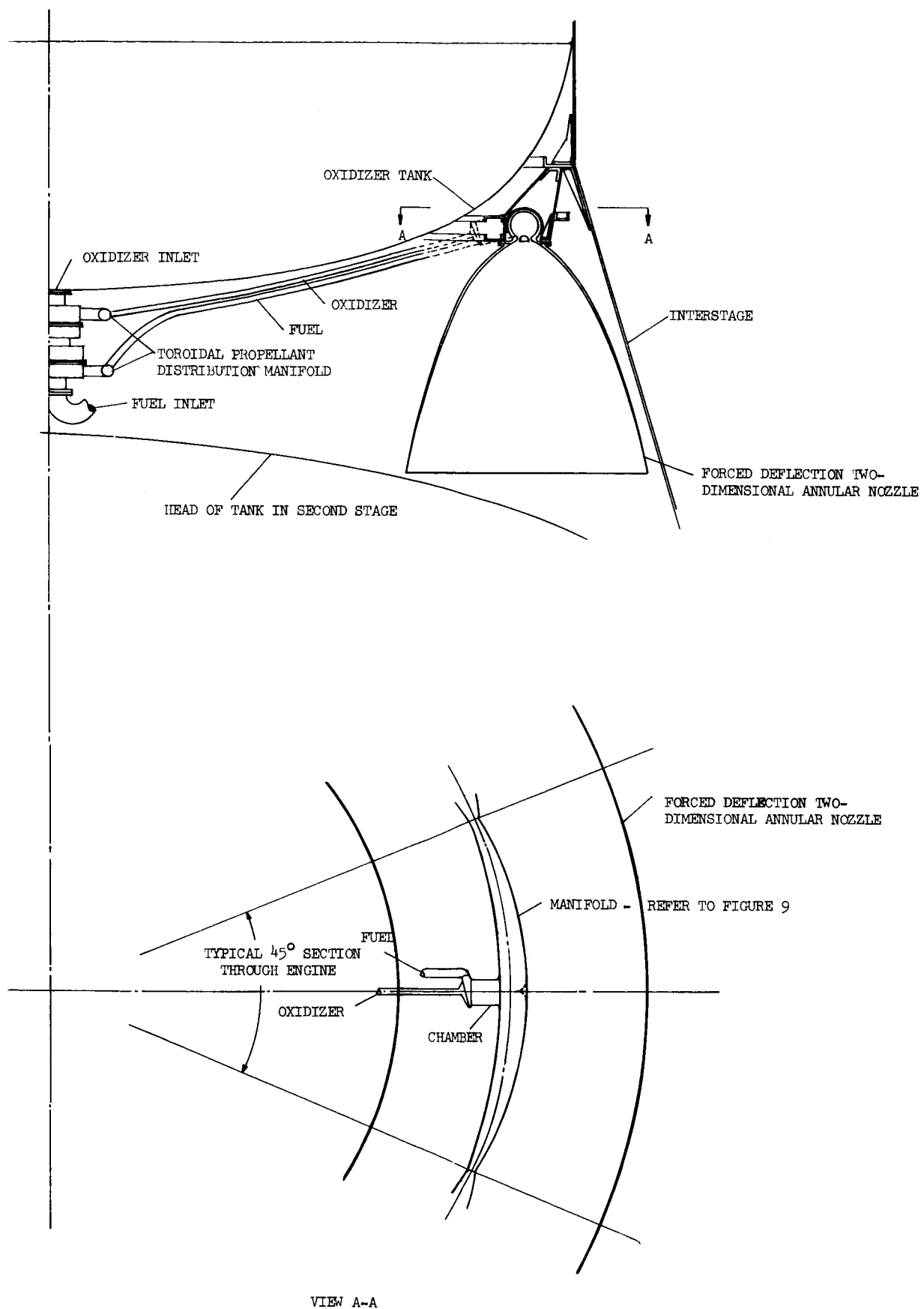


FIGURE 22. Small Nozzle Concept Using Two-Dimensional Forced-Deflection Nozzle

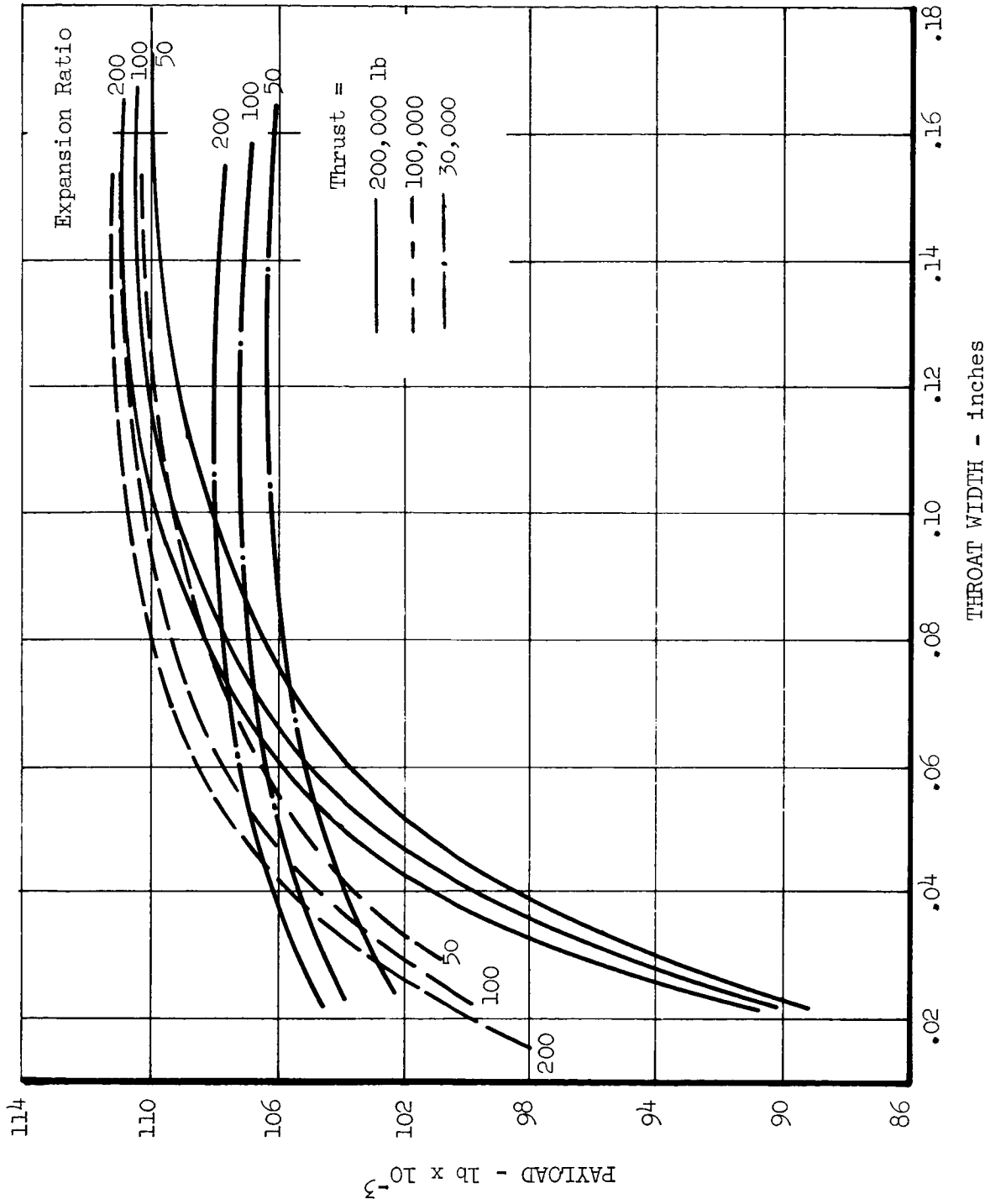


FIGURE 23. Preliminary Optimization of the Two-Dimensional Nozzle

3.4.2 SMALL THROAT CONCEPT

The potential promise of the small throat concept is dependent on high temperature material technology and actual versus predicted nozzle drag losses. The advantages of the concept are minimum nozzle and vehicle length, reduced bending moments, and the fact that the configuration is amenable to unconventional engine envelope restrictions.

3.4.3 FACTORS CRITICAL TO FEASIBILITY OF SELECTED CONCEPTS

At this point in the program, the concepts were reviewed to determine if feasibility demonstration or experimental evaluation of any critical features was necessary to establish potential performance of the concepts. Items listed below were among the features considered critical:

Small Throat Concept

- (a) Actual versus predicted nozzle frictional drag losses.
- (b) Availability, fabricability, and cost of high temperature materials.
- (c) Feasibility of structural integration of very hot and very cold components.

Integrated Nozzle/Tankhead Concept

- (d) Double separation technique, i.e., separating the nozzle from the cylindrical tank section, and inter-stage from second and third stages.
- (e) Operational or contractual complications arising from the integration of two stages.
- (f) "Blow-out" seal on throat to prevent propellant leakage from lower stage to upper stage.

The investigation of nozzle frictional drag was selected as the most critical feature lending to experimental demonstration. In addition to establishing the geometry-drag performance tradeoff for the evaluated concept, the investigation of frictional losses in nozzles should improve the general technology of nozzle performance prediction.

10,000 feet per second, and utilize both (1) liquid oxygen and liquid hydrogen (LO_2/LH_2) propellants, and (2) hydrogen peroxide and diborane ($\text{H}_2\text{O}_2/\text{B}_2\text{H}_6$) propellants.

The velocity increment, which corresponds to a 300 n.m. orbit escape mission, is typical of the initial maneuver required for spacecraft leaving the earth's gravitational field, and was selected for this reason.

The payload is between the capability of the Saturn and NOVA class vehicles for the same mission, and therefore is typical of payloads for the present and next generation of large boosters. Liquid oxygen and liquid hydrogen propellants are typical of existing high-energy chemical propellants, and both theoretical and limited experimental performance data are readily available for this combination. Hydrogen peroxide/diborane, which is described later in this section, appears to be a very promising storable propellant combination.

4.1.2 LOADS

It was assumed that the maximum loading condition for the stage considered (third stage of a three-stage-to-escape vehicle) would occur at burnout of the second stage. This is a reasonable assumption since from past experience the launch loads, free standing loads, and aerodynamic loads at maximum dynamic pressure are consistently smaller in magnitude than the axial load experienced at burnout plus a one "g" side load for the stage we are considering.

Aeroelastic and acoustic loads were not considered in the design study.

4.1.3 STRUCTURAL MATERIALS

The three materials which were considered in the tank design are 2014 Al, Titanium, and 301 stainless. The 2014 aluminum, which was used wherever possible for tank material, has the properties,

$$F_{ty} = 59,000 \text{ psi}$$

$$F_{tu} = 66,000 \text{ psi}$$

in accordance with Mil HDBK-5.

Section 4

DETAILED EVALUATION OF THE SELECTED VEHICLES

In the previous section a large number of vehicle configurations were qualitatively rated, the most promising of these were evaluated as to relative payload capabilities, and the integrated nozzle/tankhead and small nozzle engine concepts were selected for more detailed evaluation. In this section, important ground rules of the study, the performance and structural analysis involved, and the detailed analysis of the two concepts will be described. The objectives of this effort are: (1) to obtain more accurate comparative payload evaluations of the vehicles and (2) to bring out practical design considerations of the integrated concepts which have not been recognized in the initial evaluation phase.

4.1 IMPORTANT GROUND RULES

Several of the assumptions used to set the vehicle configurations are critical to the results of the study. Among these are mission, payload or stage gross weight, design loads, selected materials and safety factors, and general design philosophy. For example, the assumed loading condition can easily slant the results in favor of one concept or another. High loads or boost phase accelerations would favor a concept exhibiting reduced inter-stage or tankage. Similarly, use of a high ΔV will favor concepts with relative gains in performance.

Obviously, the vehicle designs could not be completed in as much detail for a range in ΔV or loading conditions as they could for a single ΔV and one loading criteria. Therefore, a single mission, and assumptions of 4 "g"s axial load and 1 "g" transverse load during boost were selected for design purposes. However, results of the study are perturbed to determine the effects of some of the more critical assumptions.

4.1.1 MISSION

The vehicles evaluated in the design study have a gross weight of 240,000 pounds (100,000 pound nominal payload), a velocity increment of

4.1.4 ADDITIONAL ASSUMPTIONS ARE:

LH_2 density = 4.36 lb/ft³

B_2H_6 density = 92 lb/ft³

LO_2 density = 71.2 lb/ft³

H_2O_2 density = 29 lb/ft³

Propellant mixture ratio for LO_2/LH_2

= 6.0 for conventional and integrated nozzle/tankhead vehicles

= 3.0 for the uncooled engine vehicle

Propellant mixture ratio for $\text{H}_2\text{O}_2/\text{B}_2\text{H}_6 = 1.86$ for both vehicles

Payload density = 50 lb/ft³

Tank Pressure:

Limit Pressure = 30 psi

Proof Pressure = 1.15 x limit pressure = 34.5 psi

Burst Pressure = 1.4 x limit pressure = 42 psi

Design Pressure = $f \frac{\text{Proof Pressure}}{F_{t_{\text{yield}}}}$ or $f \frac{\text{Burst Pressure}}{F_{t_{\text{ultimate}}}}$
(whichever is greater)

Payload was estimated for load purposes utilizing a propellant fraction of 0.90; this assumption was subsequently checked upon determination of actual payload weight.

4.2 PROPULSION AND PERFORMANCE ANALYSIS

4.2.1 PROPELLANT PERFORMANCE

Impulse performance for the two propellant combinations was assumed to be 100 percent of theoretical shifting equilibrium for the relative system comparisons, except as noted in the discussion. (Since the small nozzle concept (uncooled system) operates at a lower mixture ratio than the conventional system when using liquid oxygen/liquid hydrogen propellants, these two configurations were evaluated at both 100 percent frozen and 100 percent shifting performance.)

4.2.1.1 LIQUID OXYGEN/LIQUID HYDROGEN

Theoretical performance of liquid oxygen/liquid hydrogen was taken from Reference 1. Shifting performance curves with varying chamber pressure,

expansion ratio, and percent fuel (by weight) are shown in Figures 24 and 25. It can be seen that at chamber pressures and ϵ in the order of 400 and 200, respectively, the maximum specific impulse is obtained at about 16 percent fuel. Since hydrogen has such a low density, smaller percentages of fuel than this become more optimum in vehicle applications (i.e., mixture ratios of 6 to 7 which correspond to fuel percentages of 14.3 to 12.5). Note that at MR = 3, impulse increases 13 seconds from $\epsilon = 50$ to $\epsilon = 200$, and only 4.5 seconds from $\epsilon = 200$ to $\epsilon = 350$. In these same intervals at MR = 6, impulse increases 22 seconds and 5.5 seconds, respectively. Therefore, one would expect greater payload gains with increased ϵ at the higher mixture ratio, and that the vehicle system would optimize at lower expansion ratio with the low mixture ratio. Temperature versus percent fuel is shown in Figure 26. In order to achieve combustion temperatures in the order of 4000°F , percentage of fuel must be increased to approximately 25 percent. Frozen performance curves presented in Figures 27, 28 and 29, indicate optimum impulse for $400 P_c$ and $\epsilon = 200$ at about 22 percent fuel and that performance at mixture ratio of 3 ($\epsilon = 200$) is about 15 seconds higher than at mixture ratio of 6 ($\epsilon = 200$). This trend with mixture ratio is reversed with theoretical shifting performance.

Obviously, when systems utilizing different mixture ratio are compared, vastly different results will be obtained depending on the choice of shifting or frozen equilibrium. A limited amount of data has been published on actual nozzle performance with liquid oxygen/liquid hydrogen. Figure 30 reproduced from Reference 2, indicates the amount of recombination obtained in a series of hot firing tests. Zero and 100 percent equilibrium performance from Reference 1 has been superimposed in the original curve. The shifted experimental data indicates that as percentage fuel is increased, impulse performance greater than that theoretically predicted is achieved, which if true, certainly makes lower mixture ratios more desirable than theoretically predicted. However, there is enough question as to η_c^* as mixture ratio is changed to shift this curve appreciably. Recombination level predicted in Reference 3 by use of the Brae Analysis (Reference 4) has been plotted in Figure 30 for comparison with the actual data. The data also indicate that as percentage fuel is increased a greater percentage of theoretically predicted shifting performance is achieved.

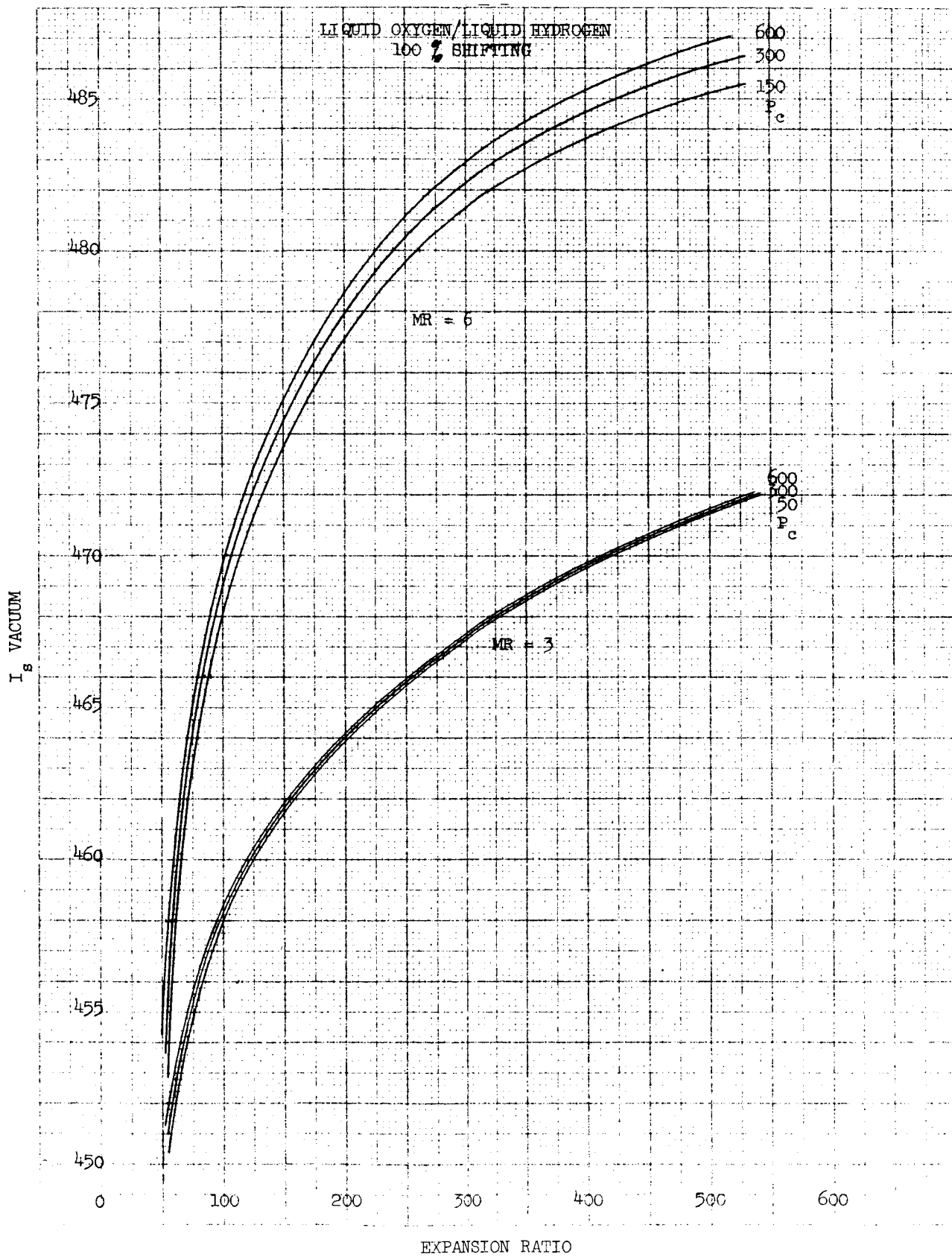


FIGURE 25. Shifting Impulse Performance of LO₂/LH₂

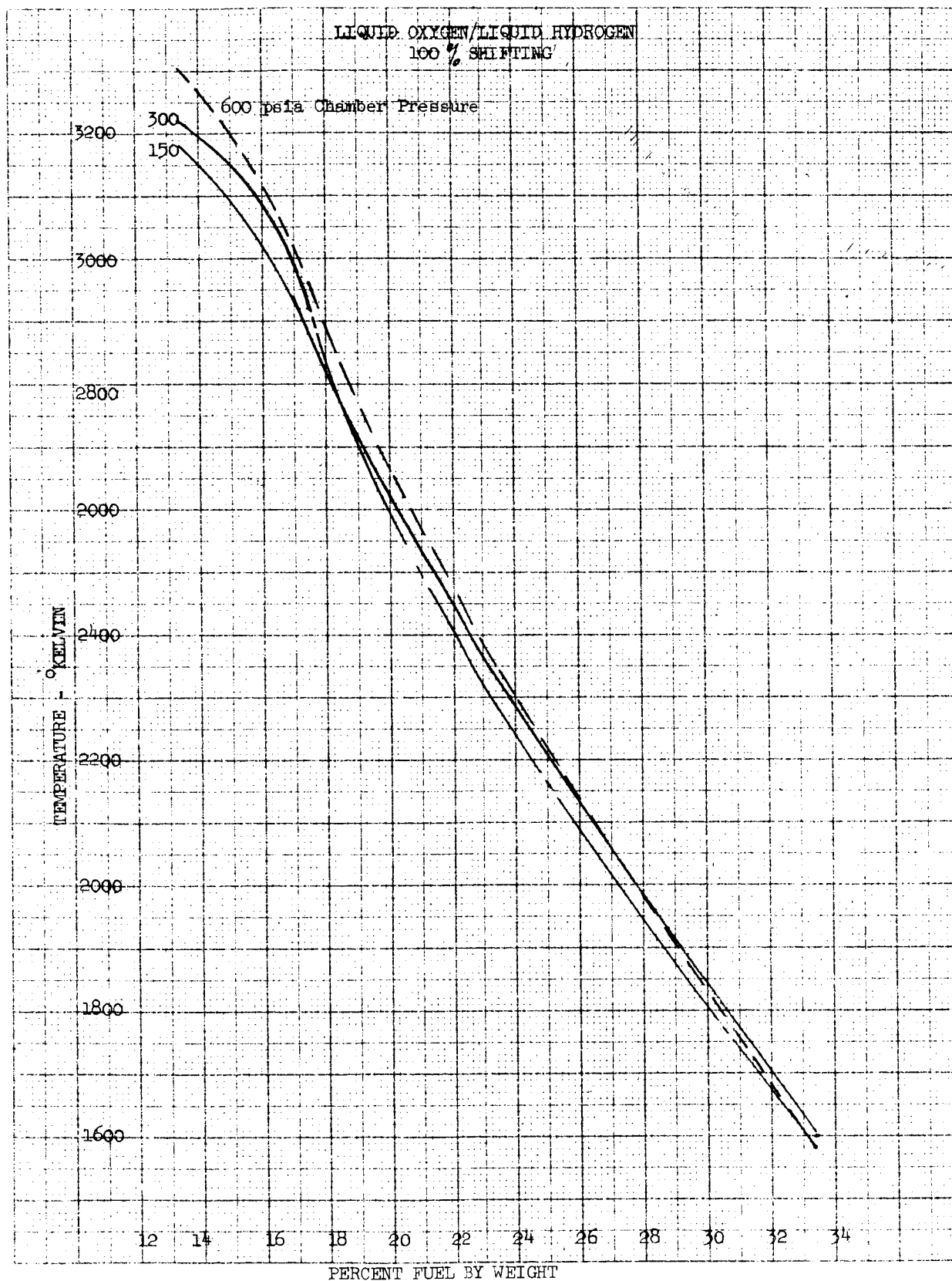


FIGURE 26. Combustion Temperature of LO_2/LH_2 (Shifting Performance)

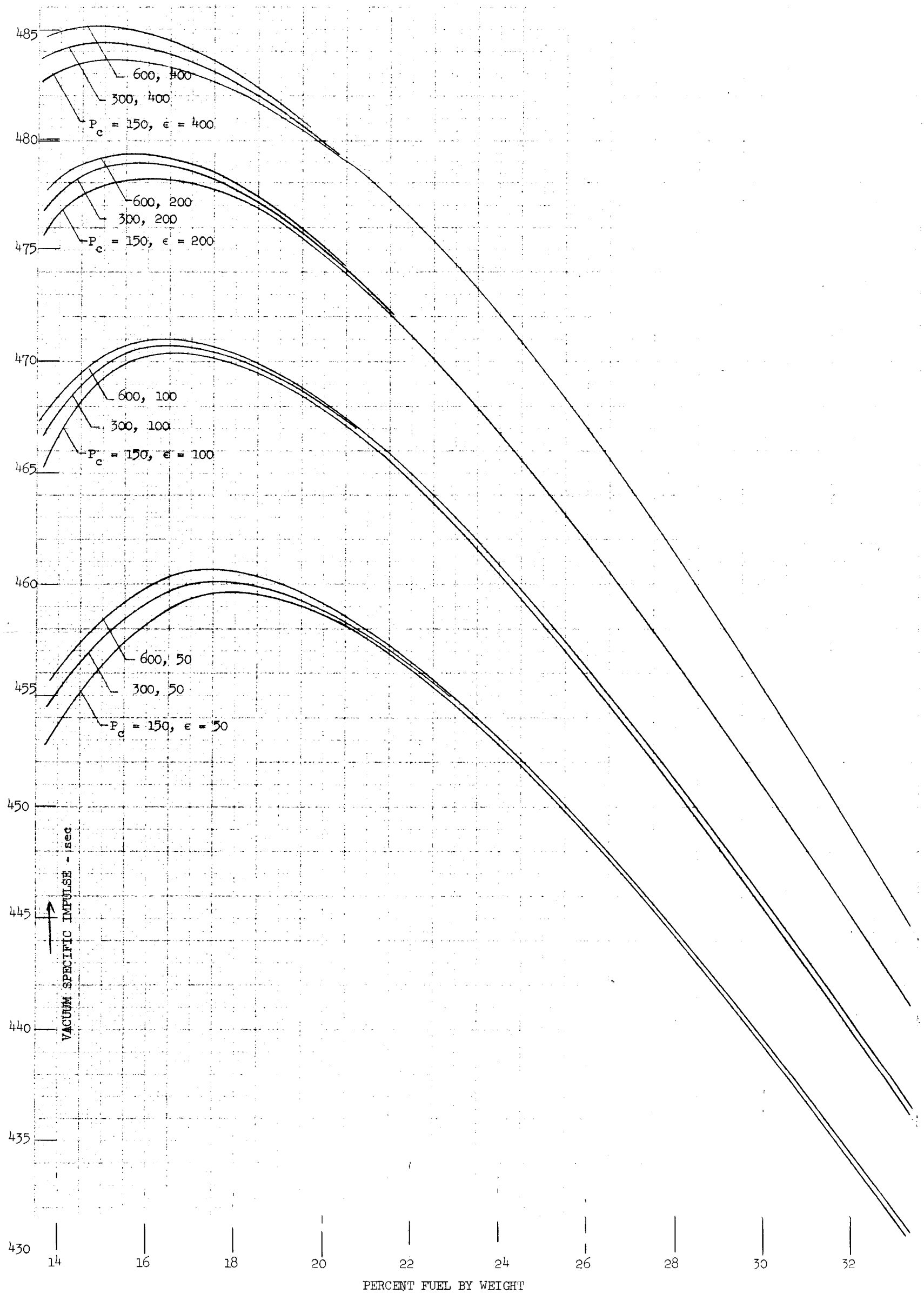


FIGURE 24. Shifting Impulse Performance of LO_2/LH_2

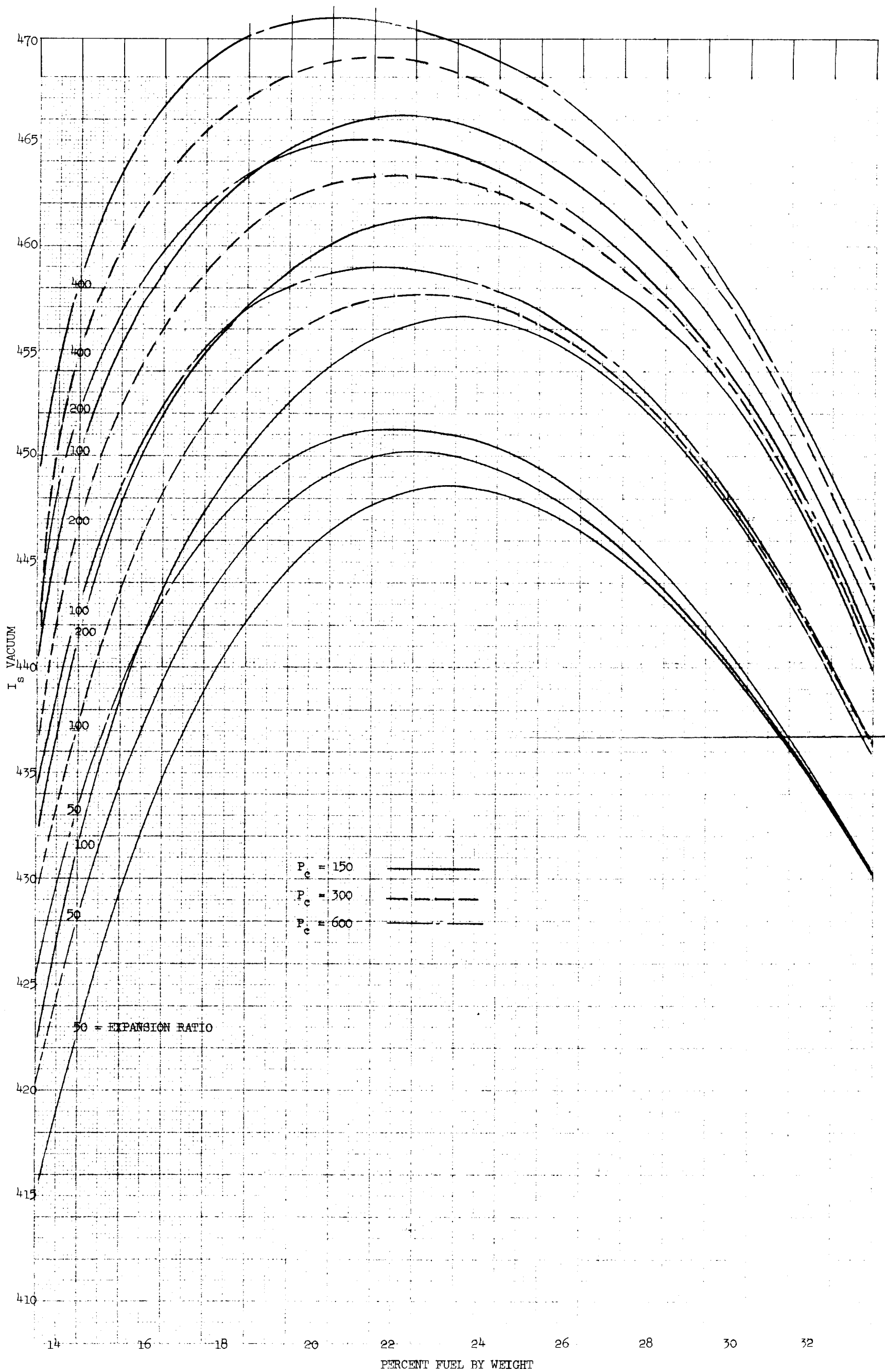


FIGURE 27. Frozen Impulse Performance of LO_2/LH_2

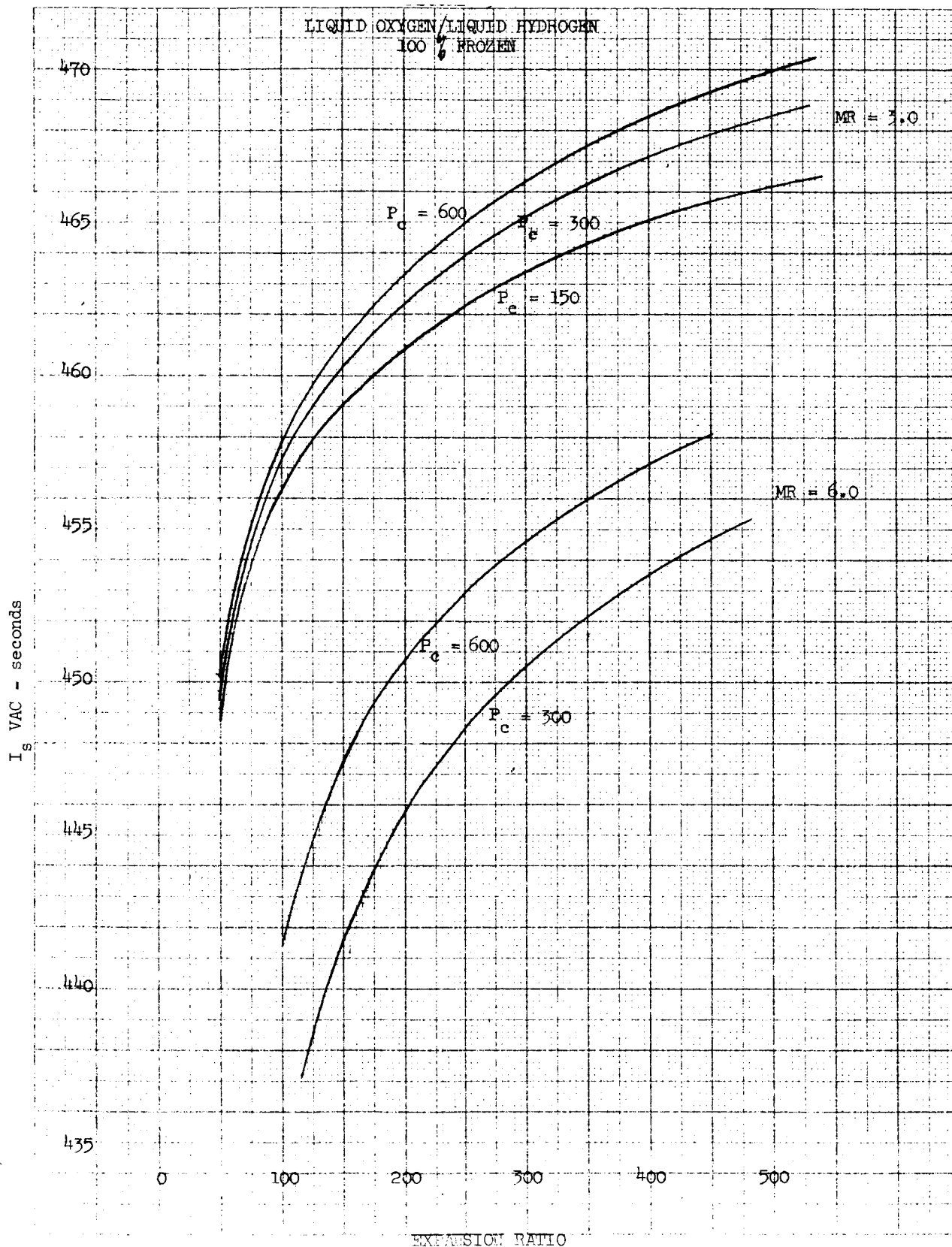


FIGURE 28. Frozen Impulse Performance of LO₂/LH₂

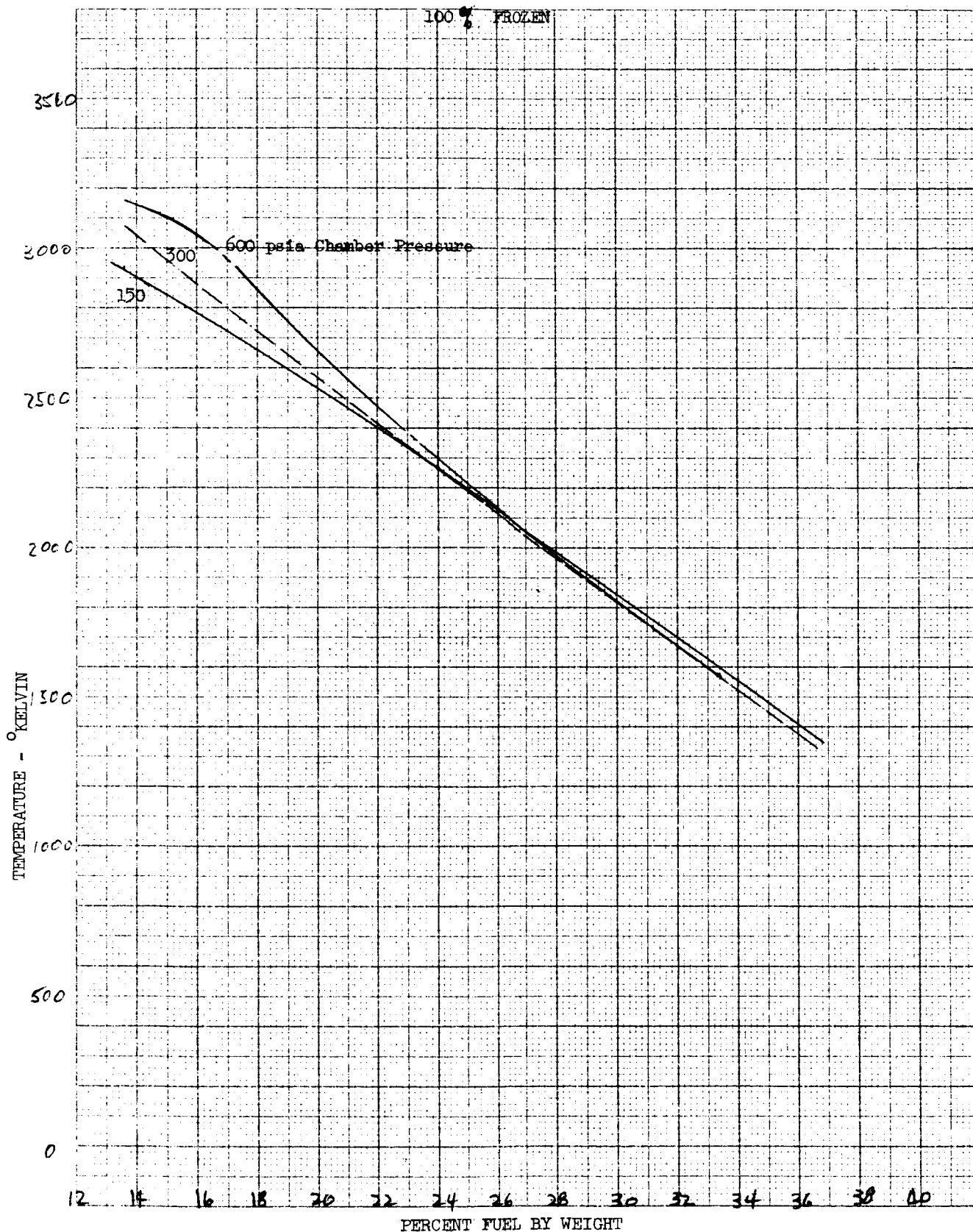


FIGURE 29. Combustion Temperature of LO_2/LH_2 (Frozen Performance)

Area Ratio = 100
 $P_c = 150$ psia
 25° Cone

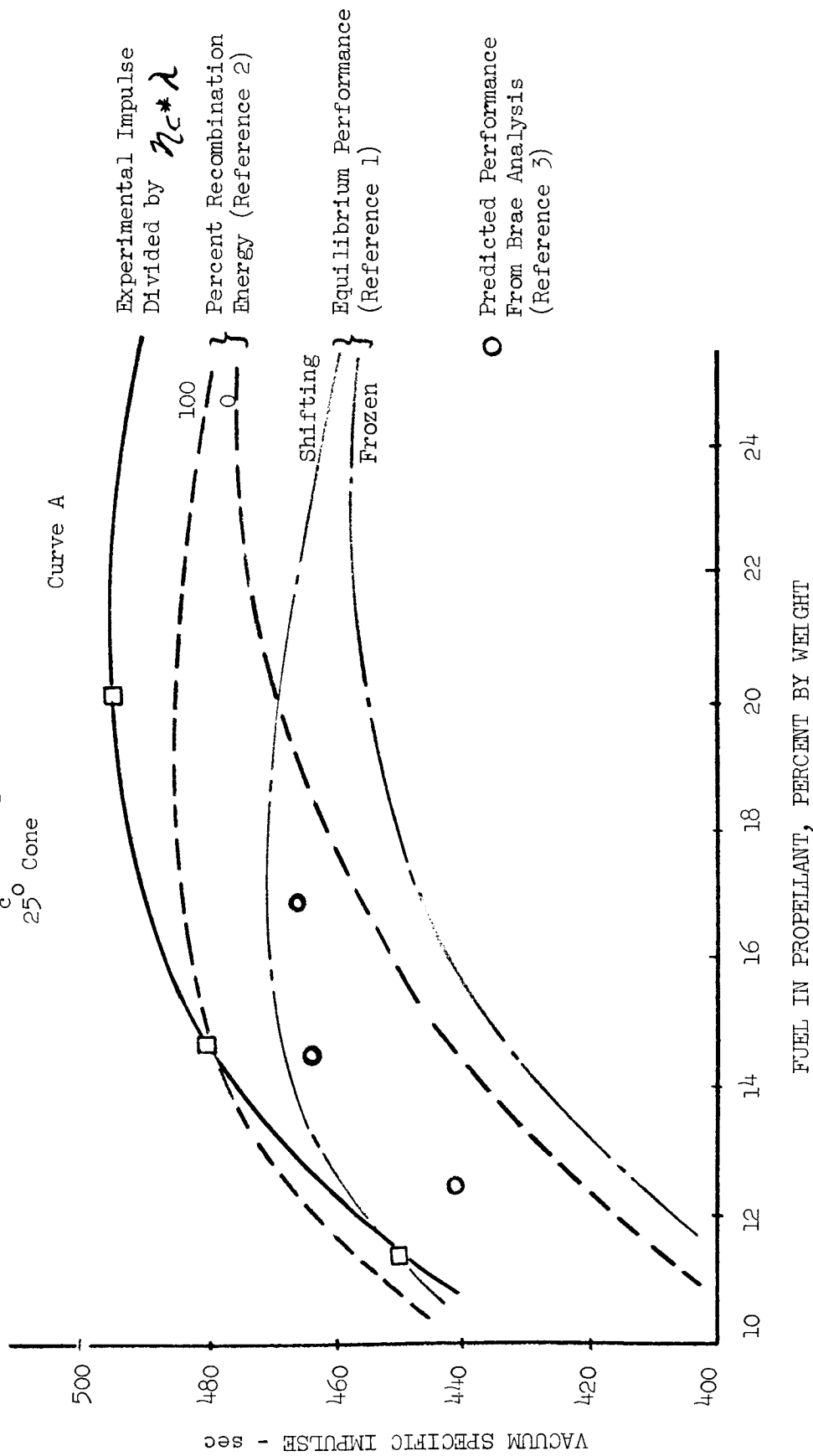


FIGURE 30. Actual vs Theoretical Performance for LO_2/LH_2

Since there is still sufficient question as to exactly what percentage of shifting performance will be achieved, the assumptions stated at the beginning of this paragraph were used in the analysis.

4.2.1.2 HYDROGEN PEROXIDE/DIBORANE

Due to the type of study involved, it was decided not to limit the analysis to present-day storable propellants. In addition to high theoretical performance, the characteristic of low combustion temperature at maximum I_{sp} was also desirable in the storable combination which was to be used in the evaluation of the selected concepts.

Several propellant combinations were investigated; hydrogen peroxide/diborane demonstrated low combustion temperature and high bulk density with satisfactory space storage characteristics. Figures 31, 32, and 33 show constituents, impulse, and temperature versus mixture ratio. It can be seen that the mole fraction of liquid/solid phase of B_2O_3 increases rapidly as mixture ratio goes below 1.86 and mole fraction of solid borane increases rapidly as mixture ratio decreases from 1.5. It would be desirable to stay out of the region where solid phase products exist, therefore a mixture ratio of 1.86 was chosen as the minimum which would be considered.

Impulse (Figure 32) is near optimum at mixture ratio of 1.86 and temperature (Figure 33) is tolerable for the uncooled engine concept (4150°F). A mixture ratio of 1.86 was selected for use in the performance analysis since all the required properties were available from IBM computer runs at that value of mixture ratio.

4.2.2 HEAT TRANSFER

A heat transfer analysis was conducted in parametric form on radiation-cooled nozzle extensions for the two- and three-dimensional, forced-deflection engines.

The possibility of using radiation-cooled extensions for the small nozzle concept-engine from a section downstream of the nozzle throat to the nozzle exit was investigated. Objectives were to determine equilibrium wall

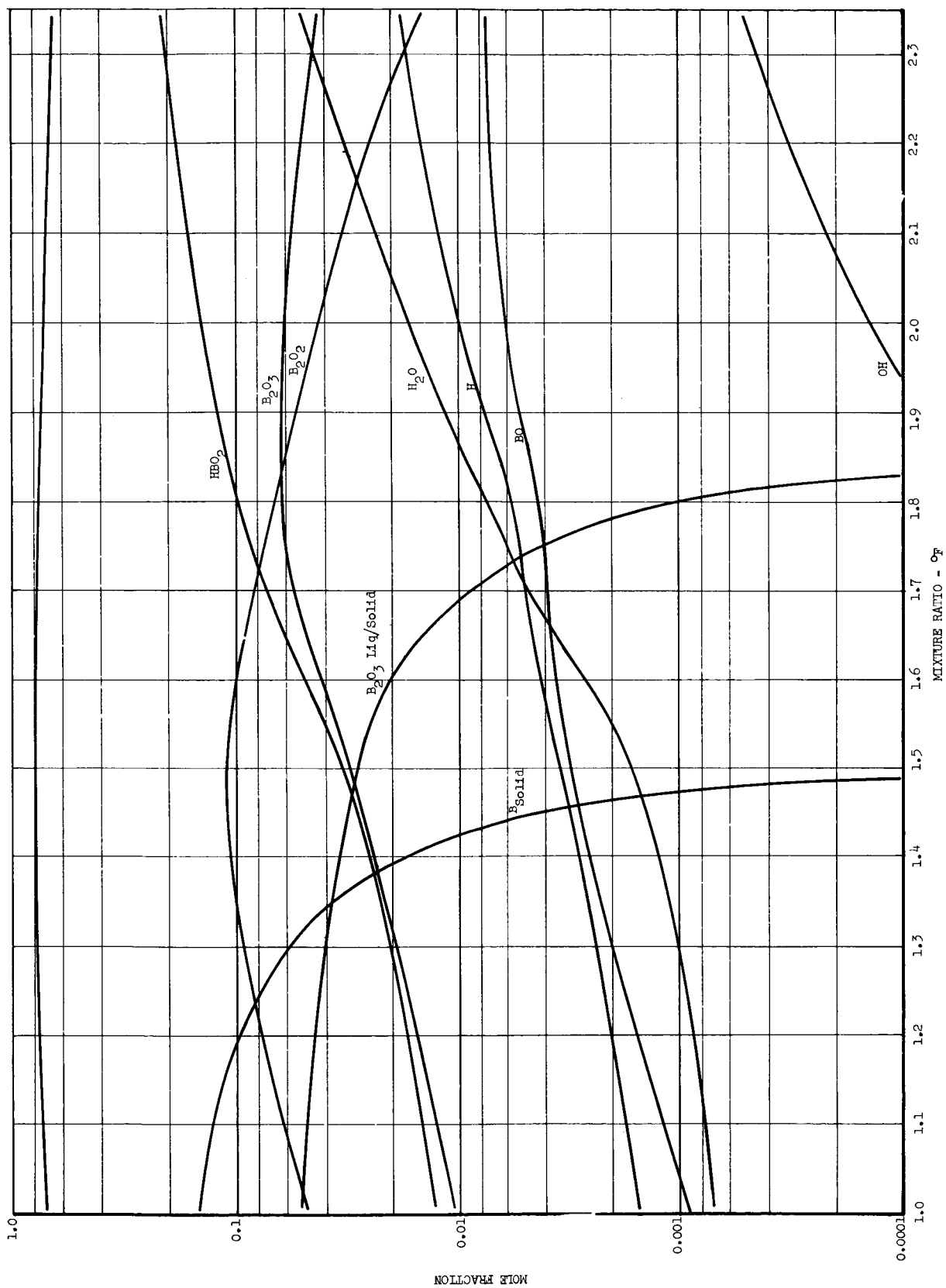


FIGURE 31. Theoretical Chemical Composition of $\text{H}_2\text{O}_2/\text{B}_2\text{H}_6$

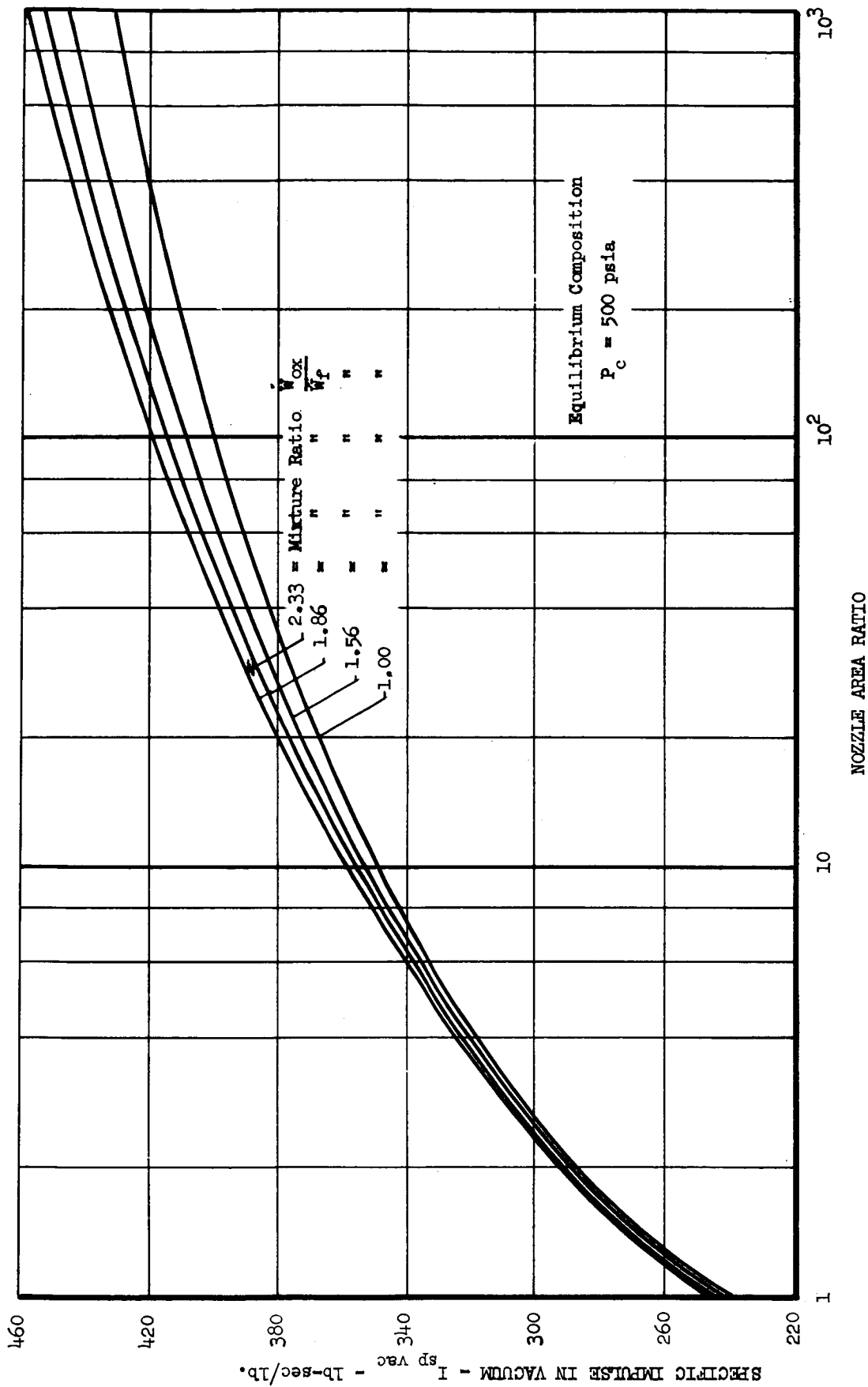


FIGURE 32. Effect of Area Ratio and Mixture Ratio on Specific Impulse of H_2O_2/B_2H_6

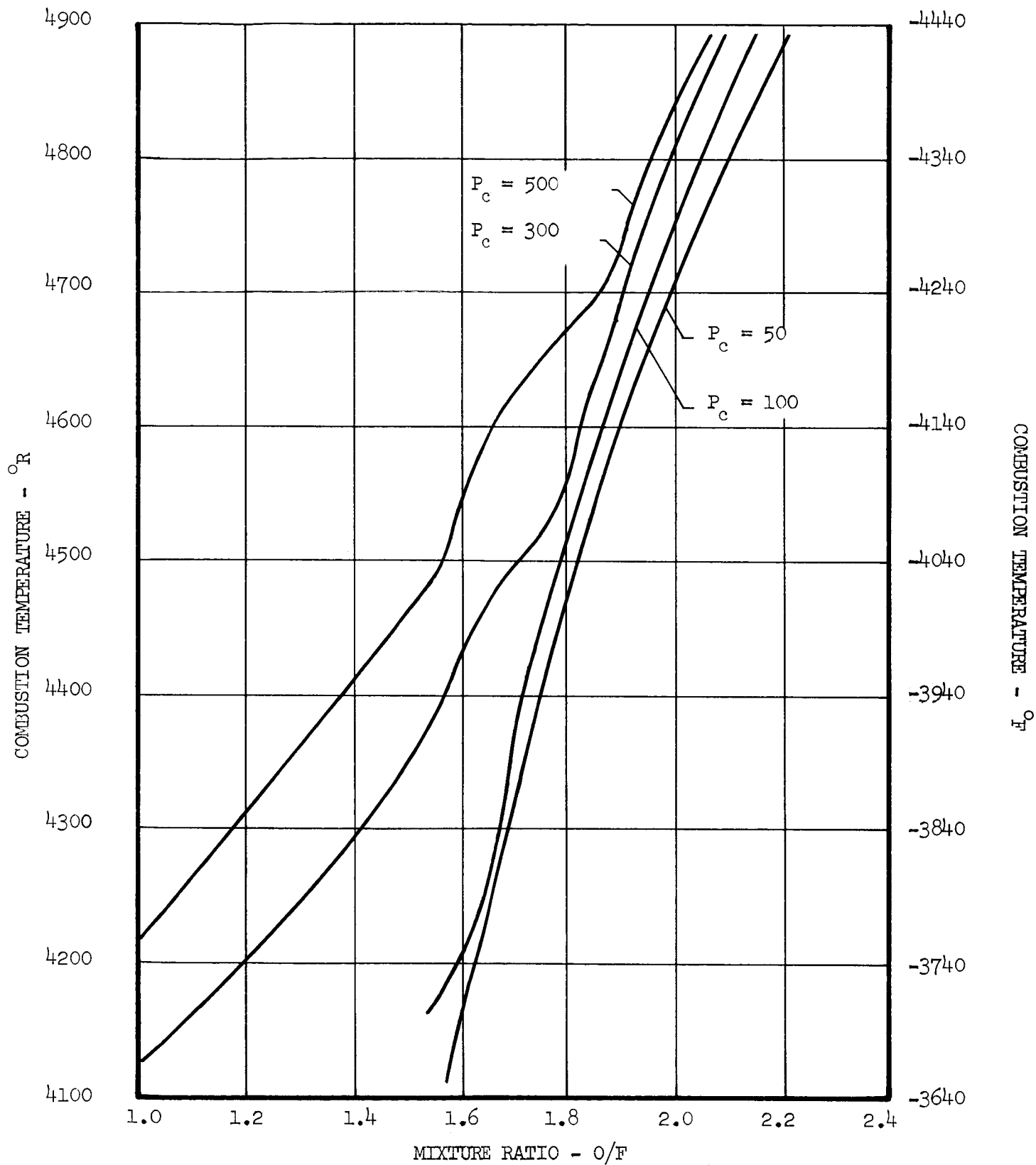


FIGURE 33. Effect of Chamber Pressure and Mixture Ratio on Combustion Temperature of H_2O_2/B_2H_6

temperatures and effect of wall thickness and emissivity on the wall temperature. A 200:1 area ratio nozzle, operating at a chamber pressure of 500 psia, thrust of 110,000 pounds, and using liquid oxygen/liquid hydrogen propellants, was selected as representative of the engines under consideration.

Propellant transport properties were taken from IBM computer programs and the film coefficient, h_g , derived versus area ratio from the equation:

$$h_g (\ell)^{.2} = [DB] k \left(\frac{\mu c_p}{k} \right)^{1/3} \left(\frac{V \rho}{\mu} \right)^{0.8}$$

where

ℓ = wall length from throat

k = thermal conductivity

DB = constant

μ = viscosity

c_p = specific heat

V = velocity

ρ = density

Consideration of the heat flux and heat balance equations (from the gas side, through the wall, and to space) resulted in the following equation:

$$\begin{aligned} \text{Heat flux}_{\text{conduction}} &= \frac{h_g k}{k + h_g x} (T_g - T_2) = .1713 \epsilon_w F_s \left(\frac{T_2}{1000} \right)^4 \\ &= \text{Heat flux}_{\text{radiation}} \end{aligned}$$

where

x = wall thickness

T_g = gas temperature (bulk)

T_2 = outside wall temperature

ϵ_w = emissivity

F_s = shape factor

With the assumption of $F_s = 1$, taking ϵ_w , k , and x as variables, and T_g known as a function of area ratio, T_2 was determined versus area ratio and heat flux. Plots of T_2 with variable wall thickness, conductivity, and emissivity are presented in Figures 34 through 37. It is seen that

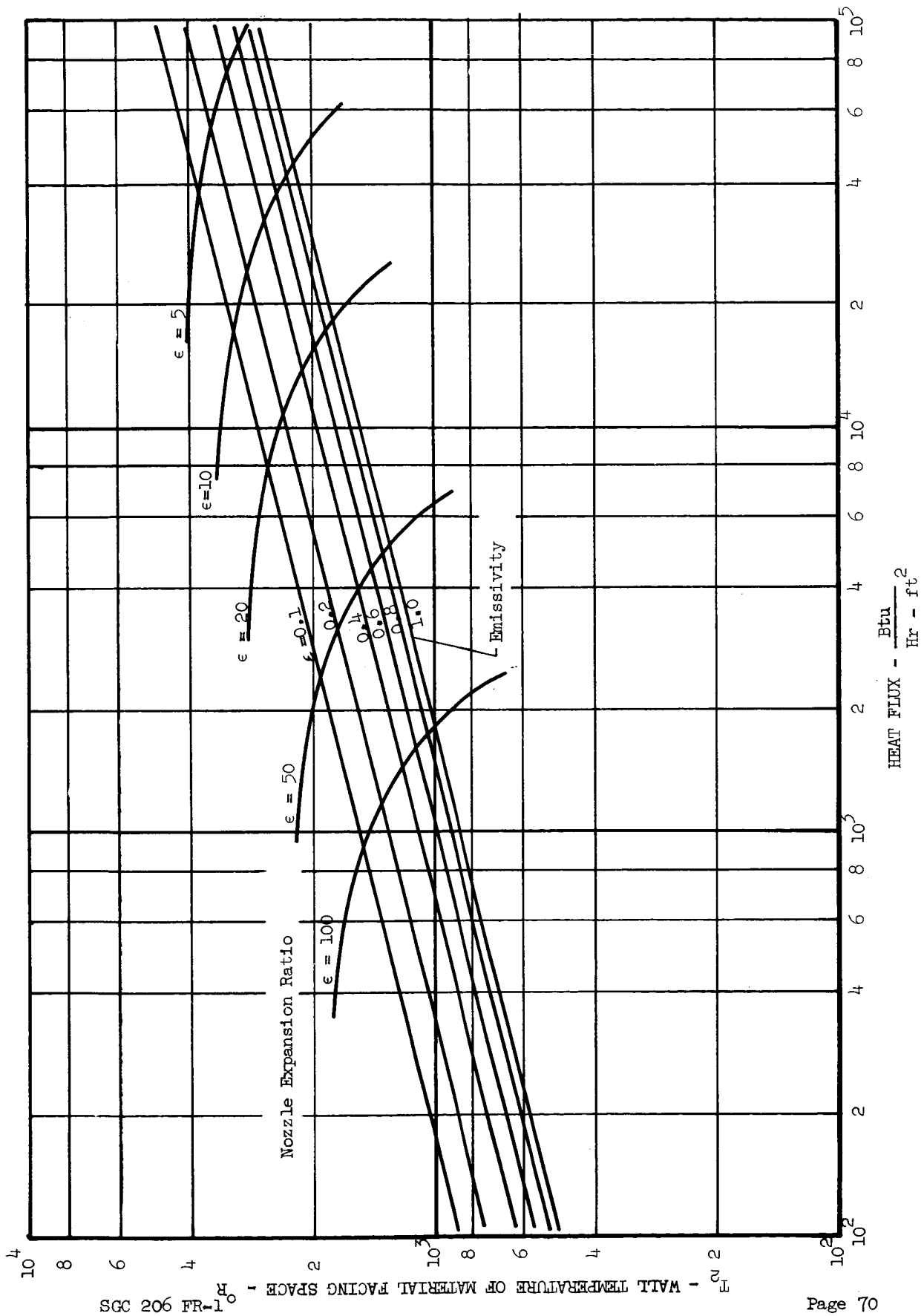


FIGURE 34. Wall Temperature vs Heat Flux in F-D Nozzle ($X = .01$)

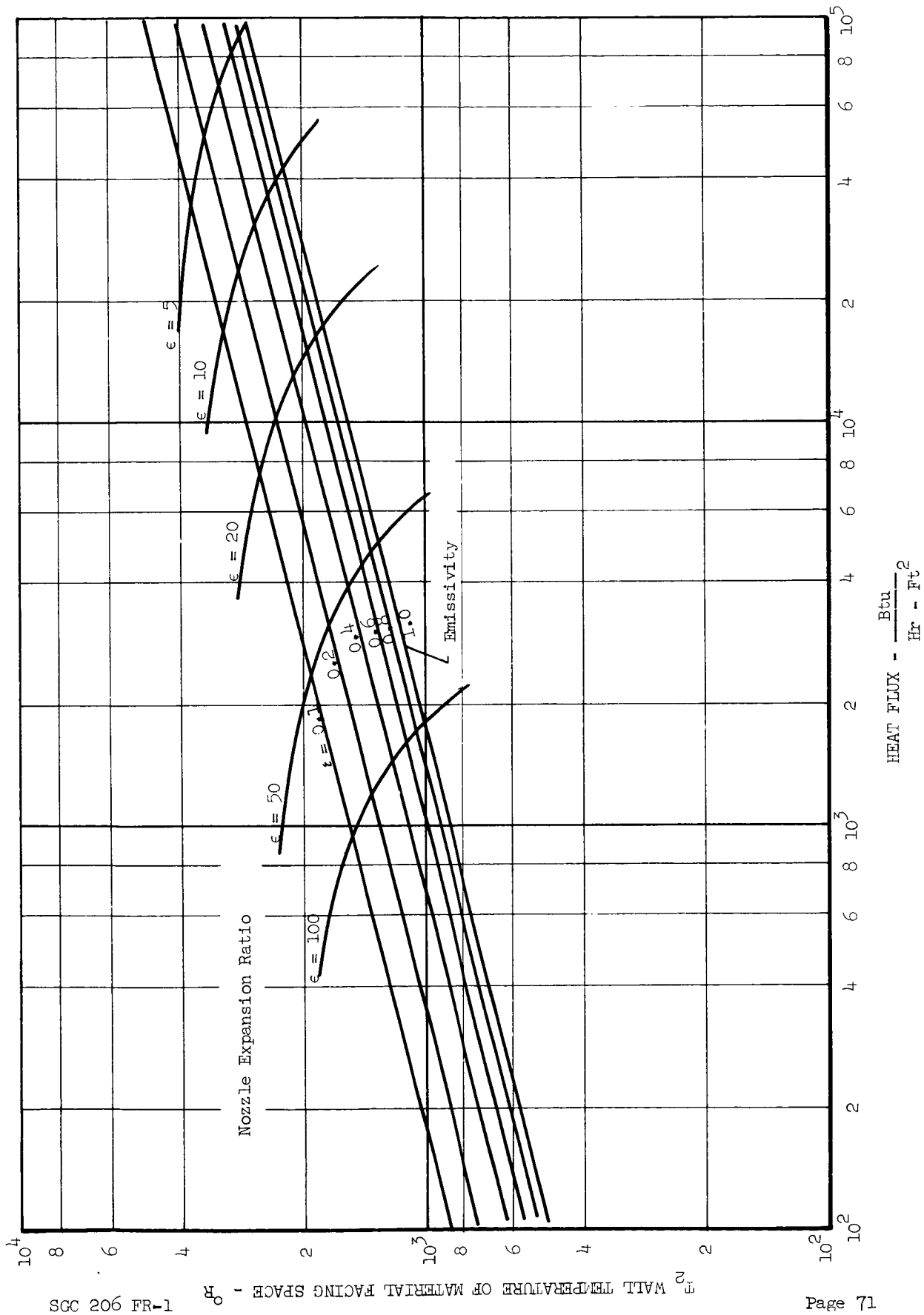


FIGURE 35. Wall Temperature vs Heat Flux in F-D Nozzle (X = .1)

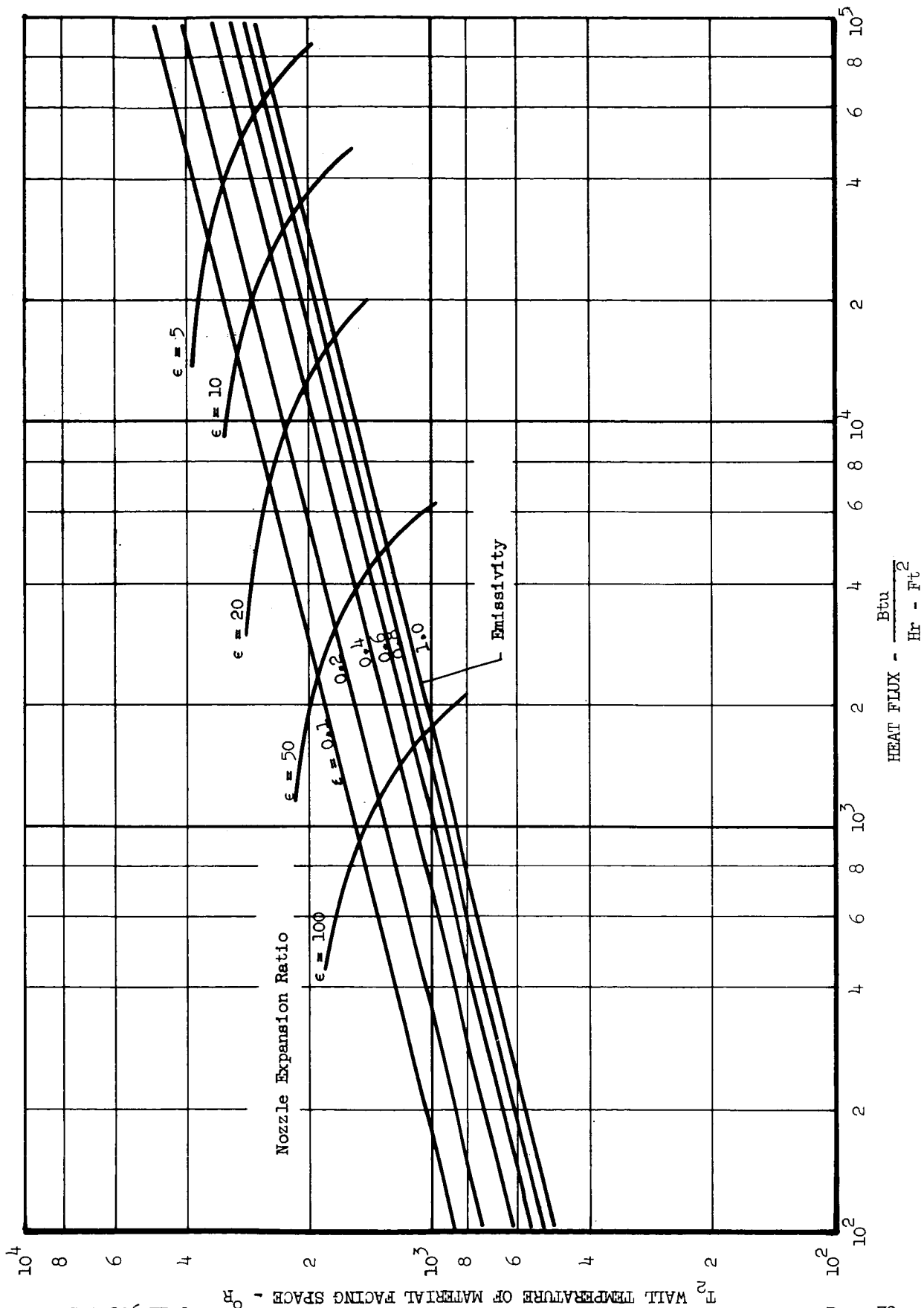


FIGURE 36. Wall Temperature vs Heat Flux in F-D Nozzle ($X = 1.0$)

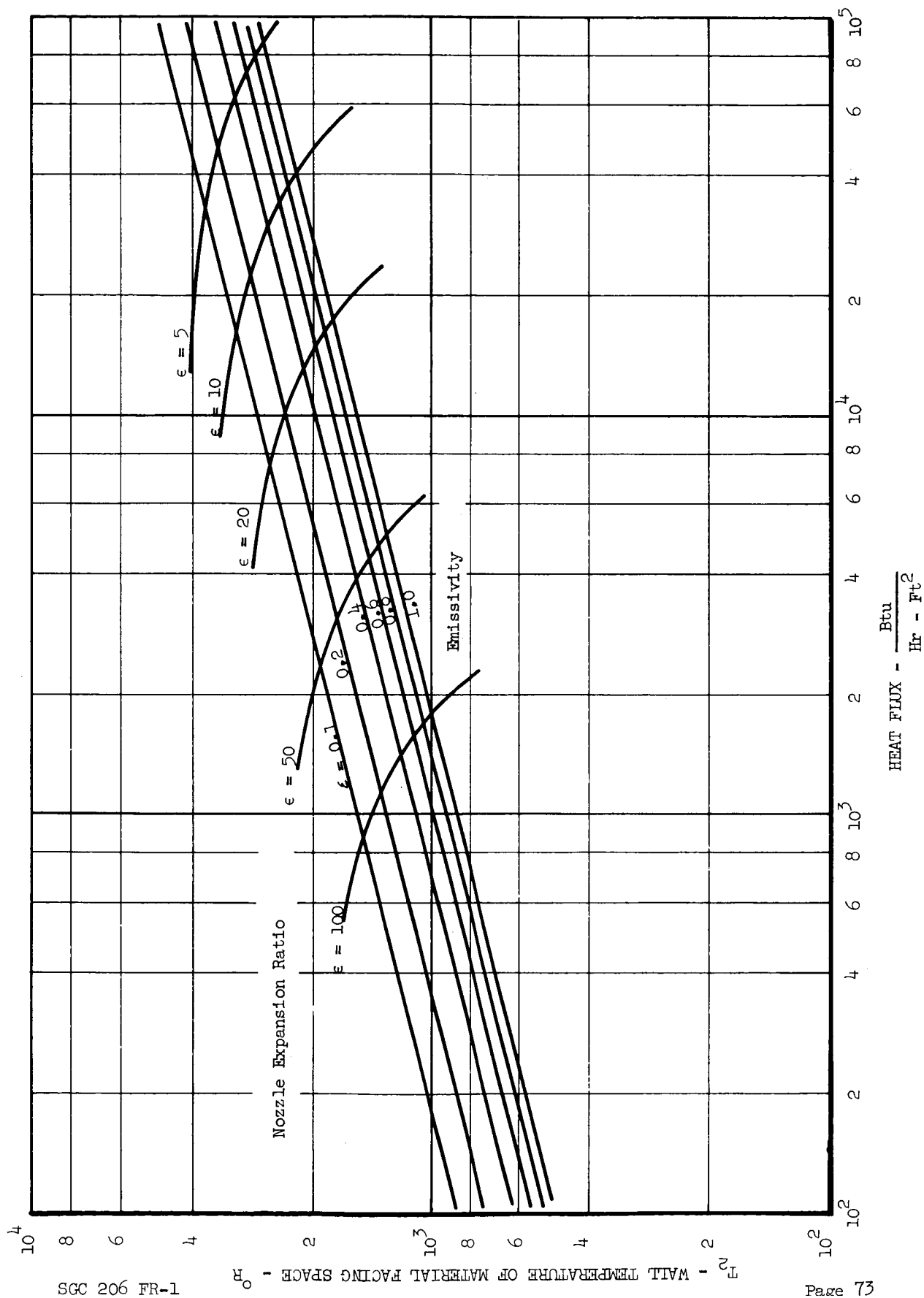


FIGURE 37. Wall Temperature vs Heat Flux in F-D Nozzle ($X = 1.0$, $K = 20$)

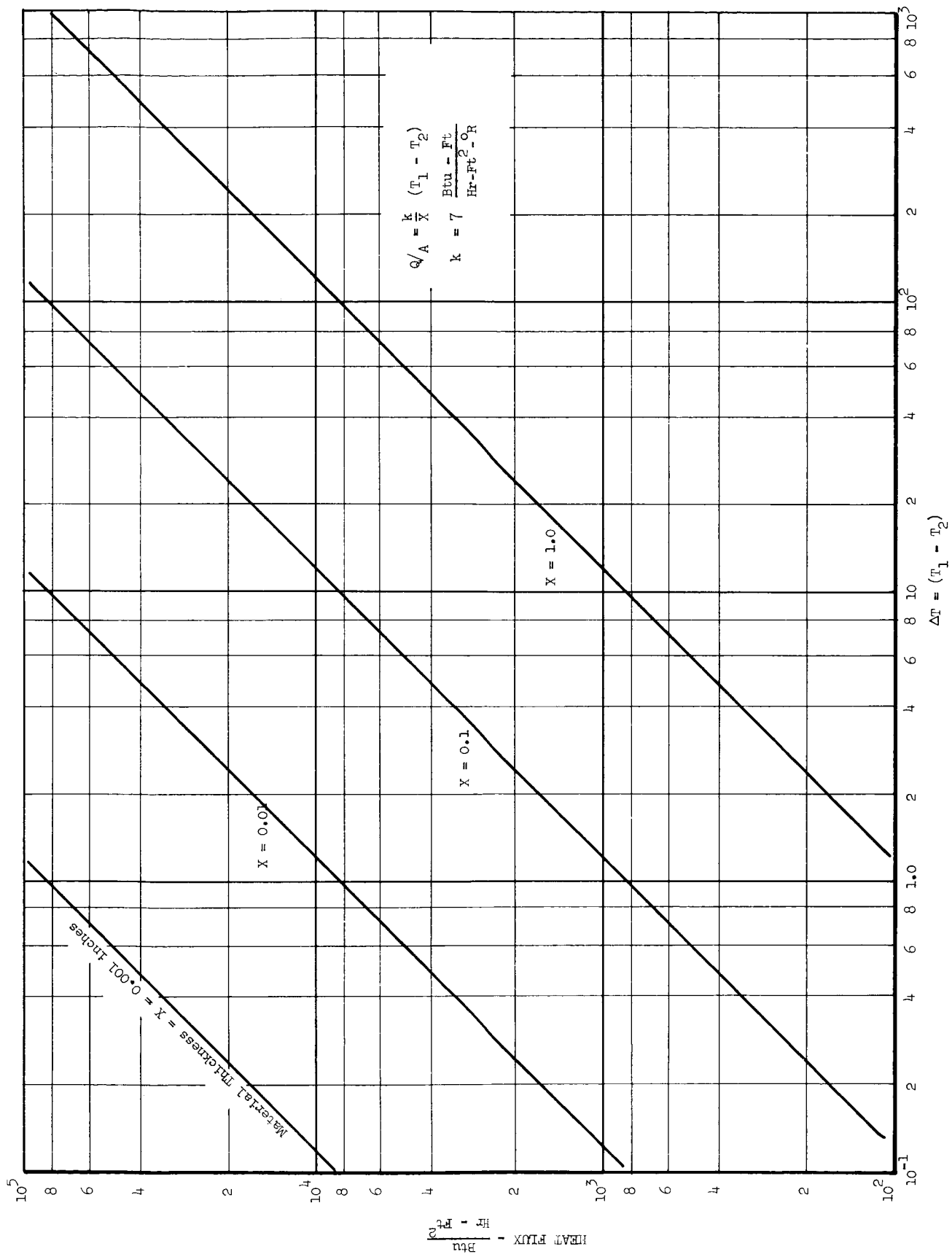


FIGURE 38. Effect of Nozzle Wall Thickness on Heat Flux

- 1) Wall thickness, x , has negligible effect on T_2
- 2) Thermal conductivity, k , has negligible effect on T_2
- 3) Emissivity, ϵ_w , has a significant effect on wall temperature over a wide range, however, considering typical emissivity of a polished metal surface as .8 to 1.0, this parameter also has only a small effect on T_2 .

Typical materials used in radiation-cooled nozzle extensions, such as Rene 41 or Titanium, exhibit good structural characteristics at temperatures in the order of 1500°F. Results in Figure 35 indicate that for T_2 of 1500°F (1960°R), and assuming $\epsilon_w = .8$, nozzle expansion ratio is about 19:1. Note from Figure 38 that inside and outside wall temperatures, T_1 and T_2 , are very close together. Thus, for this particular application it appears that a radiation-cooled extension is practical from an expansion ratio of 19:1 to the exit of the nozzle. Other means of cooling, (regenerative or otherwise) can be used from the throat to this section.

4.2.3 NOZZLE LOSSES

4.2.3.1 FRICTIONAL DRAG LOSSES

Nozzles of typical main spacecraft propulsion systems have large expansion ratios, relatively low chamber pressures, and relatively small throat radii. It can be seen from equations for friction coefficient, such as the following equation from Reference 5,

$$C_f = \frac{.273}{[Re]^{.2}} = f \left[\frac{.1}{PR} \right]^{.2}$$

where: Re = Reynolds No.

P = Chamber Pressure

R = Throat Radius

that as Reynolds Number decreases (i.e., P and R decrease), the friction coefficient increases. Also, it is obvious that as the surface area increases (expansion ratio increases) the total drag increases. Therefore, frictional drag becomes much more important in spacecraft applications than it has been in large booster applications.

Several methods of computing frictional drag losses have been published. Typical methods are those using nonintegral relationships (Reference 5) and those utilizing the integration of the characteristic boundary layer parameters, momentum thickness and boundary layer thickness (Ref. 6, 7, 8).

The modified Frankl-Voishel equation (Reference 5) turns out to be a very convenient method for calculating drag by IBM computer, or by hand calculations. This equation has been presented in Reference 3 in the form

$$df_w = \frac{.472 \rho V^2 dA}{2 (\log_{10} Re)^{2.5} (1 + \frac{\gamma-1}{2} M^2)^{.467}} \quad (1)$$

where df_w is the incremental drag force over area dA

$$Re = \frac{\rho Vx}{\mu}$$

ρ , V , μ , γ , M are free stream flow properties

x is the axial distance from the convergent section of the nozzle

Using the isentropic flow relationships, this equation was converted to a form more useable for nozzle drag calculations. The resulting equation is

$$df_{axial} = \frac{.236 (\gamma-1) \rho_o T_o M^2 c_p (1 + \frac{\gamma-1}{2} M^2)^{-\left[\frac{\gamma}{\gamma-1} + .467\right]} dA}{\left[\log_{10} \left\{ \rho_o \sqrt{g(\gamma-1)T_o} \frac{M \sqrt{c_p}}{\mu} (1 + \frac{\gamma-1}{2} M^2)^{-\left[\frac{1}{\gamma-1} + \frac{1}{2}\right]} x \right\} \right]^{2.58}} \quad (2)$$

where x = distance from initiation of boundary layer growth

$dA = 2\pi R dx$ for 3-d nozzles

$\gamma = L dx$ for 2-d nozzles

L = 2-d nozzle length

Subscript o denotes chamber stagnation conditions

The quantities c_p , μ , and M vary with expansion ratio or length along the nozzle and can be taken from typical computer printouts of nozzle designs. Thus, the incremental drag can easily be integrated over the nozzle length to determine total nozzle drag losses.

The Frankl-Voishel equation (Equation 2) was used to determine the frictional drag on a 1000:1 area ratio nozzle having a throat radius of 0.10 inches and using nitrogen at $p_c = 100$ psia and $T_c = 70^\circ\text{F}$. Results are shown in Figure 39. Cumulative percentage loss in thrust coefficient is 0.6 percent at the throat and increases to about 3.15 percent at the exit of the nozzle. One of the techniques, which utilized integration of momentum thickness to calculate the skin friction coefficient, (Reference 6), was also used to determine drag losses for this nozzle in order to compare the two types of calculation techniques mentioned earlier in this section. Results from the integral equation from Reference 6 indicated a total drag at the exit of 3.0 percent, which was considered very good agreement for the compared calculation techniques. The two methods also show good agreement in percentage of total drag loss distribution through the nozzle (Figure 40).

In general, the techniques employing integration of the momentum thickness are more cumbersome to use than the Frankl-Voishel Method shown here, however they may be more useful in some cases since, by a few more calculations, heat transfer coefficients can also be obtained through integration of the boundary layer parameters (References 6, 7 and 8).

It is not readily seen from Equation 2 how drag loss is affected by throat radius or chamber pressure, however, results of calculations of drag for several sizes of nozzles at various chamber pressures indicate the following approximate correlation for this method:

$$C_D = f \left\{ \frac{1}{P_c A_{R_{th}} B} \right\}$$

$$A = .20 \text{ to } .23$$

$$B = .20 \text{ to } .23$$

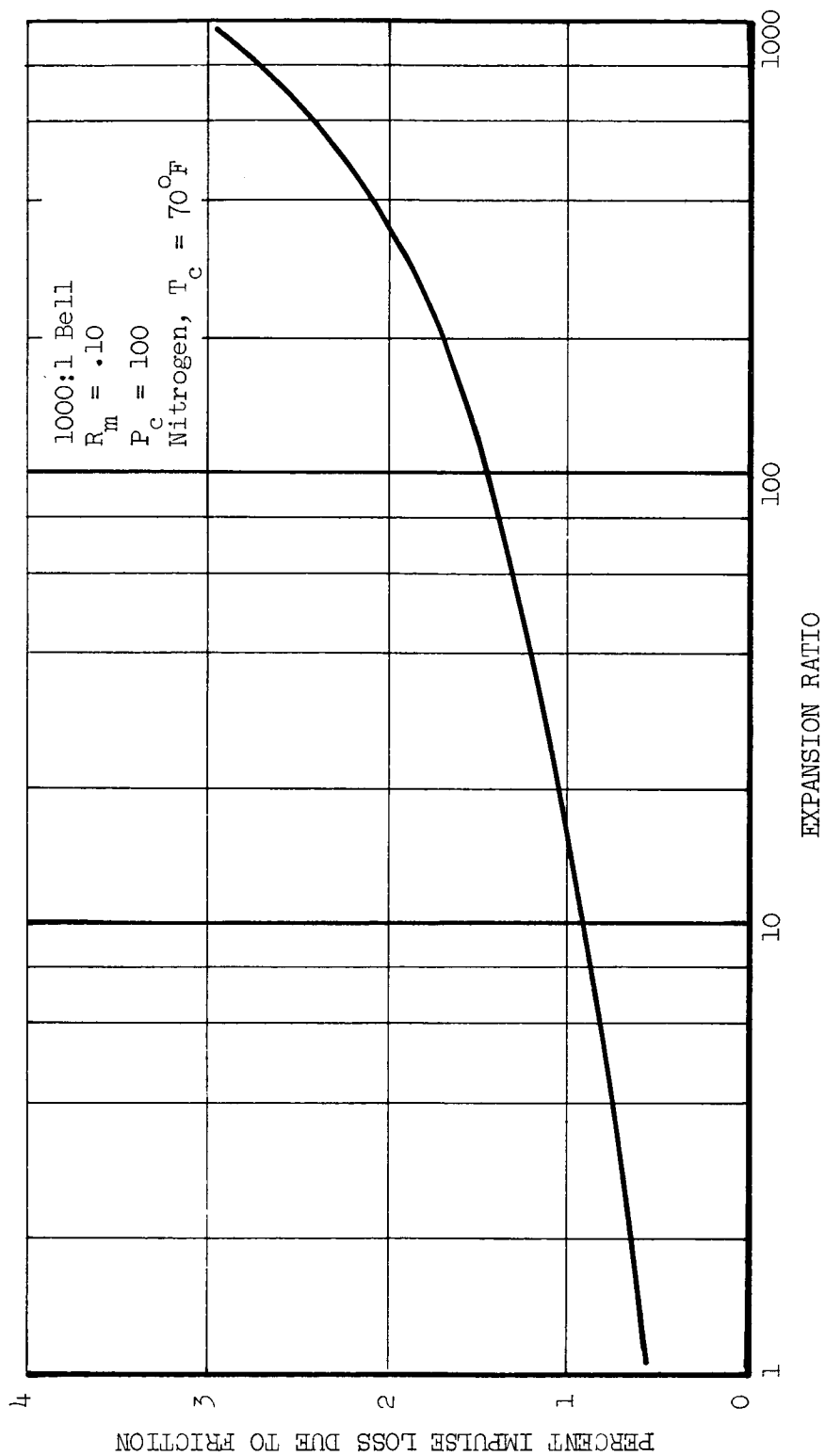


FIGURE 39. Nozzle Frictional Drag Loss Predicted by Modified Frankl-Voishel Equation

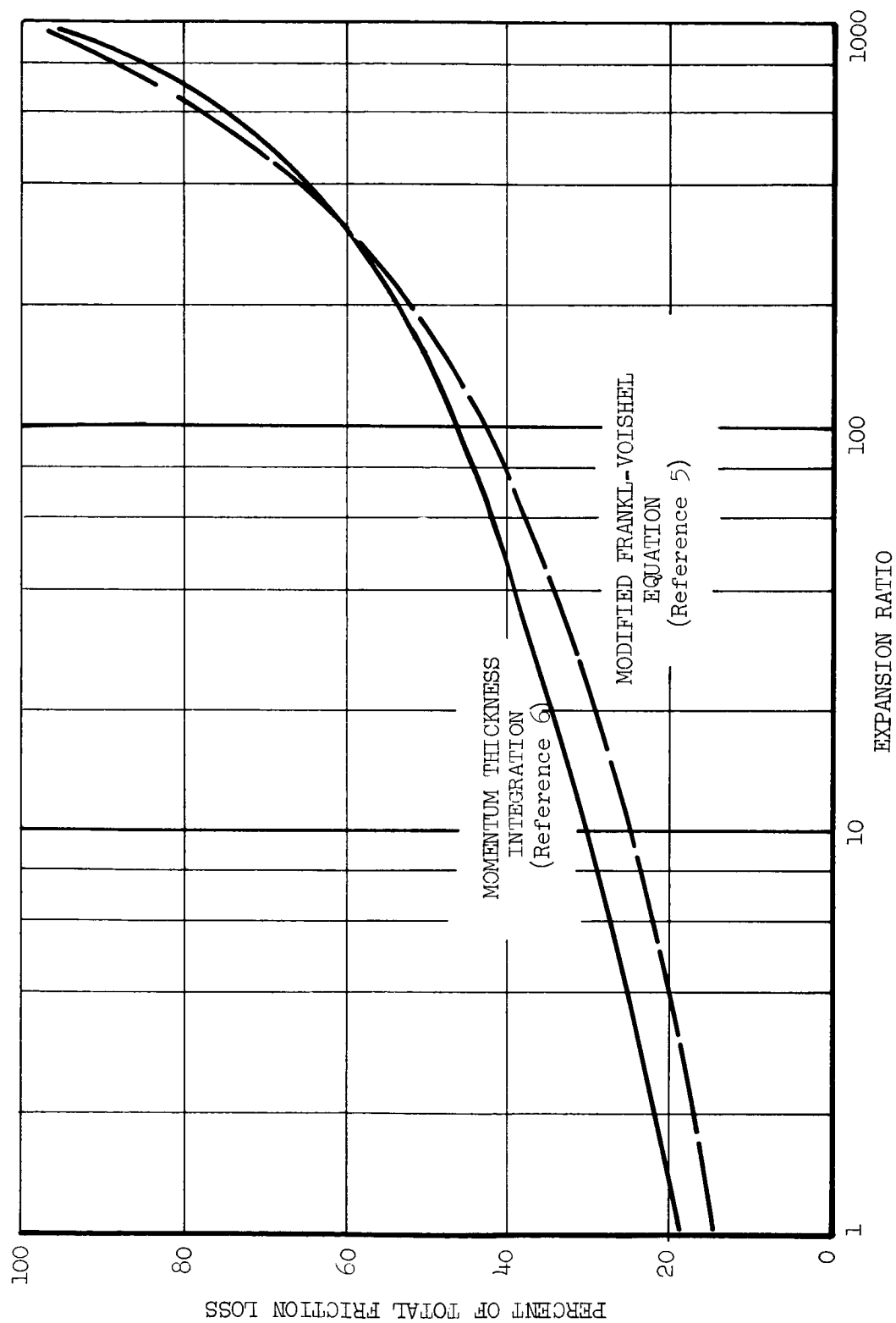


FIGURE 40. Comparison of Prediction Techniques for Computing Nozzle Friction Losses

Drag coefficient from Reference 6 is of the form,

$$C_D = f \left\{ \frac{1}{P_c \cdot .2 R_{th} \cdot .2} \right\}$$

Therefore, the two methods will show essentially the same effect of chamber pressure and R_{th} .

Reference 3 presents curves of percentage drag losses which have been computed from the Frankl-Voishel Equation using the IBM computer. These results are presented in Figures 41, 42, and 43 for the conical, bell, and forced deflection nozzles. Effect of mixture ratio for the range considered is small.

Further discussion of the effects of throat size and drag for two-dimensional type nozzles is presented in the section on the small nozzle concept.

4.2.4. FLOW DIVERGENCE LOSSES

Losses associated with the turning efficiency of the nozzle, or capability of the nozzle to discharge the exhaust gases in an axial direction, were calculated for the conical and forced deflection nozzles and taken from Reference 3 for the bell nozzle.

4.2.4.1 THREE-DIMENSIONAL FORCED-DEFLECTION NOZZLES

Taking a two-dimensional section through the nozzle contour and using the geometrical and flow parameters as shown below, the mass flow

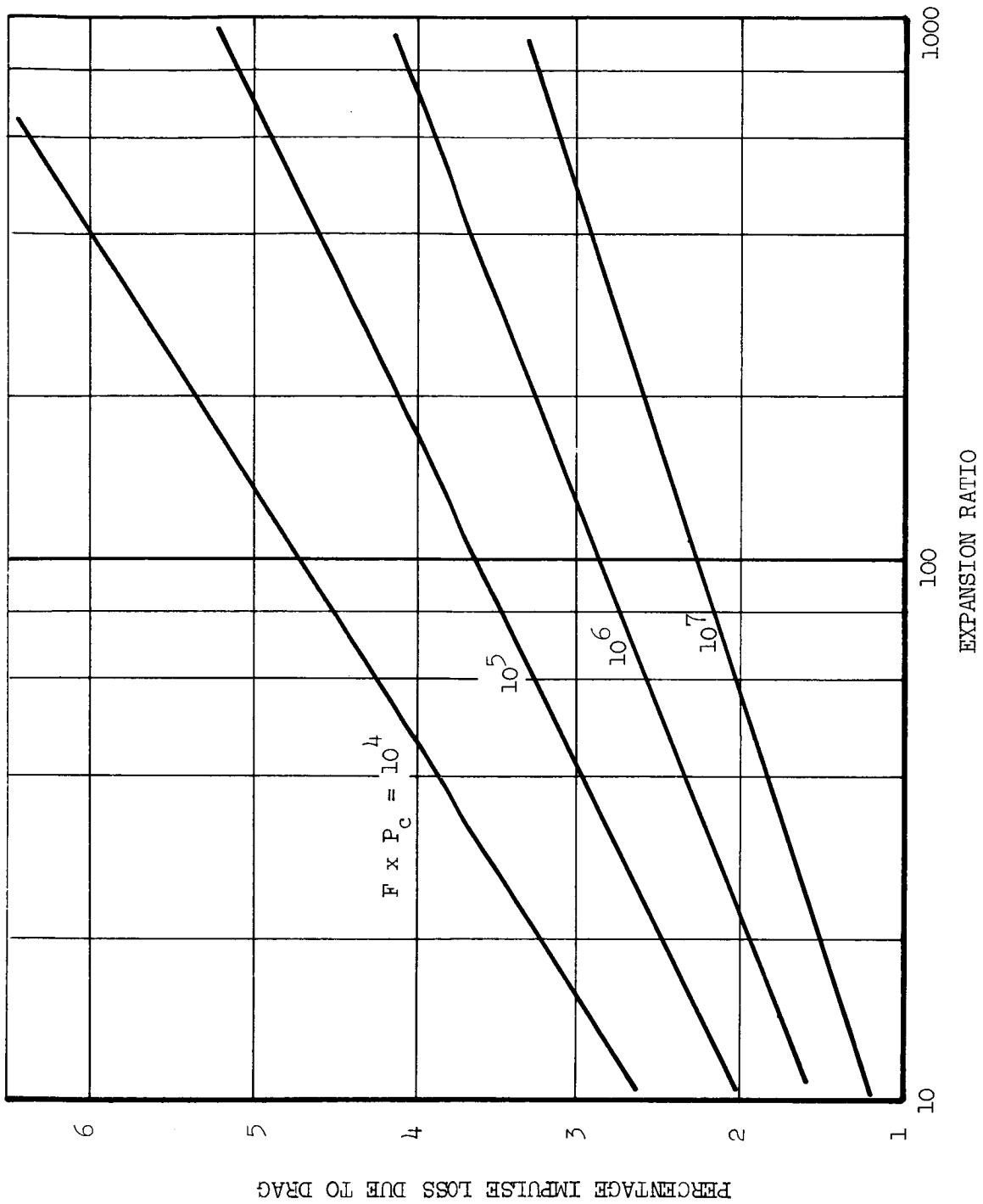


FIGURE 41. Drag Losses in Conical Nozzles

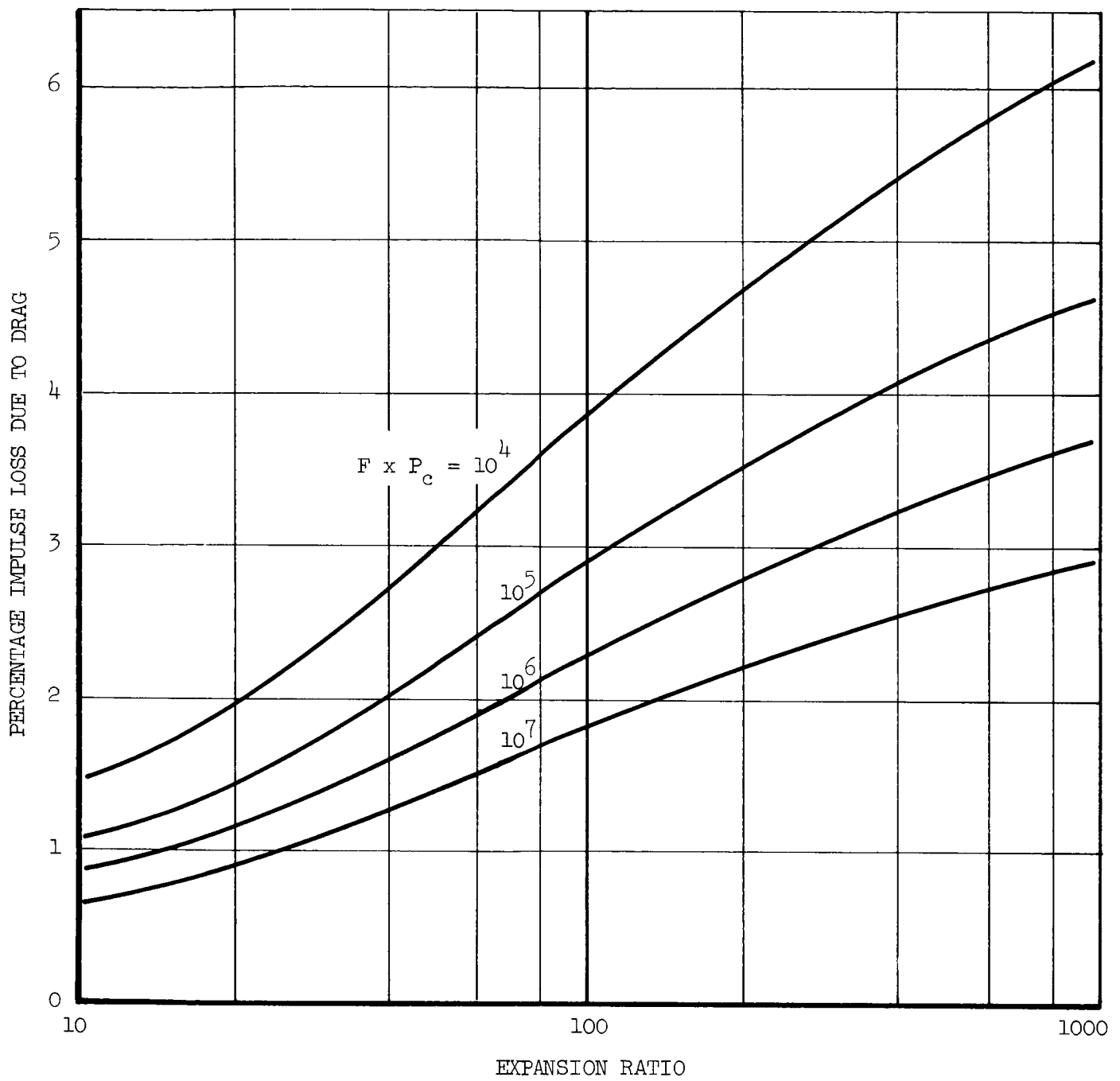


FIGURE 42. Drag Losses in Bell Nozzles

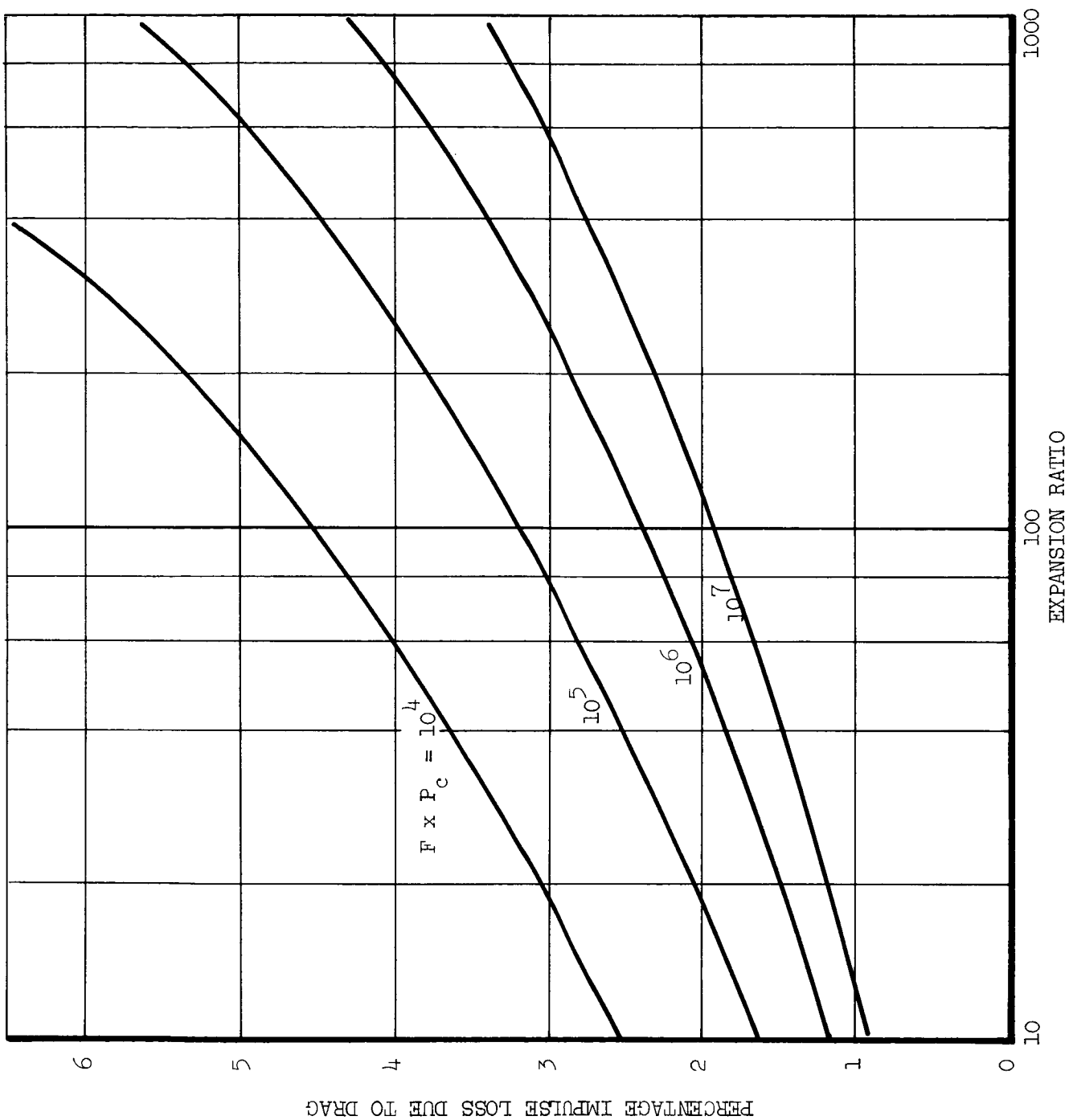
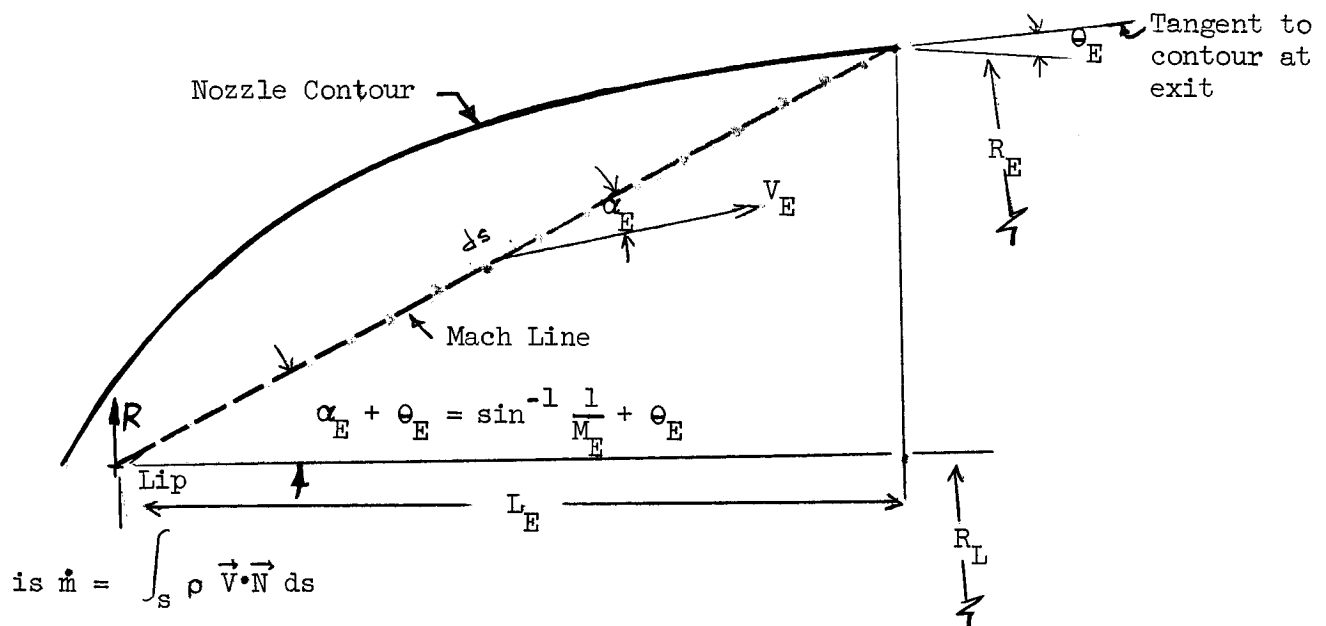


FIGURE 43. Drag Loss in Forced-Deflection Nozzles



where s is the control surface which will be defined as the Mach line from the lip to the exit

ρ density

\vec{V} velocity of gas

\vec{N} unit vector normal to control surface

Considering an elemental volume of mass across the control surface ds , the mass flow at the exit becomes

$$\dot{m}_E = \int_{R_L}^{R_E} \frac{\rho_E V_E \sin \alpha_E 2\pi R}{\sin (\theta_E + \alpha_E)} dR \text{ which also equals}$$

$$\dot{m}_i = \int_{R_L}^{R_i} \frac{\rho_i V_i \sin \alpha_i 2\pi R}{\sin (\theta_i + \alpha_i)} dR, \text{ where } i \text{ is any control surface along}$$

the contour. Equating \dot{m}_i to the mass flow at the throat and using the isentropic Mach No. and density relationships for supersonic flow, the equation giving the Mach No. at any point along the contour can be derived as,

$$\left(\frac{R_i}{r_t}\right)^2 - \left(\frac{R_L}{r_t}\right)^2 = \left[\frac{2}{\gamma+1} \left(1 + \frac{\gamma-1}{2} M_i^2\right) \right]^{\frac{\gamma+1}{2(\gamma-1)}} \sin(\theta_i + \alpha_i) \quad (1)$$

where $r_t = \sqrt{\frac{\text{Throat Area}}{\pi}}$

The thrust can be derived from

$$F = \int_s \left[\frac{(\rho V \cdot N)}{g} (-V) - \rho N \right] ds = \int_{R_i}^{R_E} \left[\rho_E \frac{V_E^2}{g} \left(\frac{\sin \alpha_E \cos \theta_E}{\sin(\theta_E + \alpha_E)} \right) \right] 2\pi R dR$$

+ Thrust due to pressure at exit
+ Thrust due to centerbody or base

$$= \left[\frac{R_E^2}{2} - \frac{R_i^2}{2} \right] 2\pi \frac{\rho_E V_E^2}{g} \left(\frac{\sin \alpha_E \cos \theta_E}{\sin(\theta_E + \alpha_E)} \right) + F_p + F_B$$

$$= P_c A_{th} C_F$$

Using the perfect gas equation, the thrust coefficient becomes

$$C_F = \frac{P_E}{P_c} \epsilon_E \left[\gamma \frac{M_E \cos \theta_E}{\sin(\theta_E + \alpha_E)} \right] + \frac{P_E}{P_c} \epsilon_E \text{ for } P_{base} = P_{ambient} = 0 \quad (2)$$

P_c = chamber pressure
 P_E = exit pressure

The nozzle angle θ_i plus the Prandl-Meyer turning angle ν_i are equal to $(\theta + \nu)$ at the exit.

$$\theta_i = (\theta_e + \nu_e) - \nu_i \text{ where } \nu \text{ is evaluated from}$$

$$\nu = \sqrt{\frac{\gamma+1}{\gamma-1}} \tan^{-1} \sqrt{\frac{\gamma-1}{\gamma+1}} (M^2 - 1) - \tan^{-1} \sqrt{M^2 - 1} \quad (3)$$

R_E can be determined for a given throat area (or thrust, chamber pressure and expansion ratio) and lip radius, R_L . Therefore, for a selected nozzle length L_E , the angle $(\theta_E + \alpha_E)$ can be found from

$$\theta_E + \alpha_E = \tan^{-1} \frac{R_E - R_L}{L_E} \quad (4)$$

The Mach No. at the exit can then be determined by solving for M_E in Eq. (1) and the thrust coefficient is calculated from Eq. (2). Nozzle efficiency is found by dividing this thrust coefficient by the ideal thrust coefficient

$$C_{F_{ideal}} = \sqrt{\frac{2\gamma^2}{\gamma-1} \left(\frac{2}{\gamma+1}\right)^{\frac{\gamma+1}{\gamma-1}} \left[1 - \frac{P_E}{P_C}\right]^{\frac{\gamma-1}{\gamma}}} + \frac{P_E}{P_C} \epsilon_E$$

4.2.4.2 TWO-DIMENSIONAL FORCED-DEFLECTION NOZZLE

Equations (1) through (4) for the two-dimensional nozzle are identical to those just presented except that the length of an element of mass flow through the nozzle is now just W instead of $2\pi R$ (and remembering that area ratio is still defined as A_{exit}/A_{throat}).

4.2.4.3 EFFECT OF NOZZLE LENGTH ON THRUST COEFFICIENT

Since an arbitrary nozzle length must be chosen to calculate the angle $(\theta_E + \alpha_E)$, the effect of this parameter on the nozzle efficiency must be investigated. The above equations were used to determine nozzle efficiency of the two-dimensional nozzle for a $\gamma = 1.23$ (liquid oxygen/liquid hydrogen), and a range of nozzle lengths. Length will be shown as percent length of a 15° wedge nozzle, ie.,

$$\frac{L \times 100}{L_{wedge}} = \text{Percent length} = \delta$$

$$L = \frac{W_{throat} (\epsilon - 1)}{\tan 15^\circ} \delta \quad \text{where } W_{throat} = \text{throat width}$$

Figure 44 shows the effect of percent length on the geometrical efficiency of the nozzle. As expansion ratio increases, a greater length is required to obtain a given efficiency. The forced-deflection nozzles can be designed to a much shorter length than the bell and conical nozzles

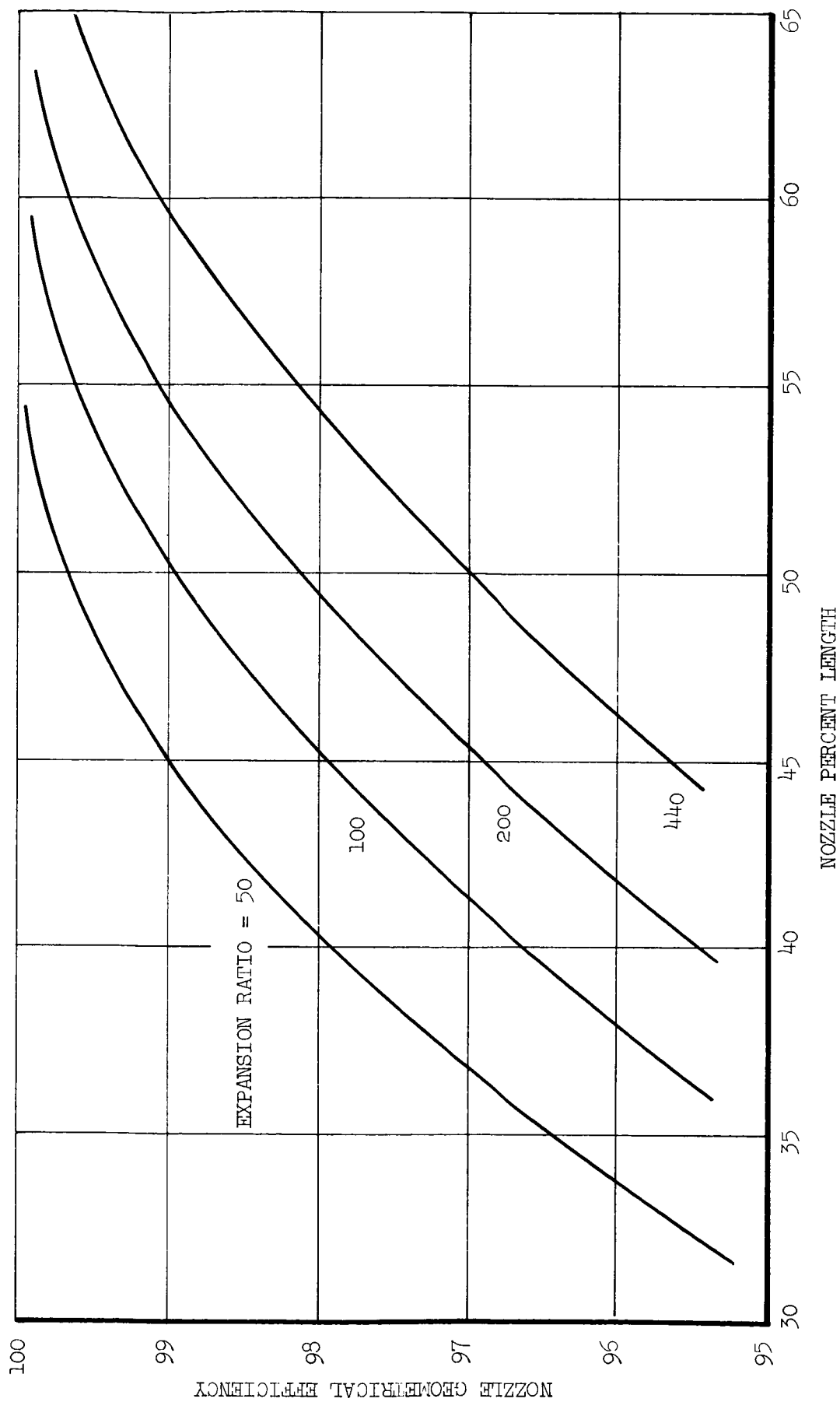


FIGURE 44. Effect of Length on Efficiency of Forced-Deflection Two-Dimensional Nozzles

for the same geometrical losses. The exchange of nozzle efficiency, and nozzle and vehicle inert weights with nozzle length, was considered in the evaluation of the various engine/vehicle systems.

Variation of exit Mach No. and exit divergence angle are shown in Figures 45 and 46 for a range in expansion ratio. As expansion ratio increases from 50 to 440, percent length to achieve $\eta_{CF} = 99\%$ increases from 48 to 63, and the nozzle exit angle decreases about two degrees.

4.2.4.4 BELL AND CONICAL NOZZLES

Flow divergence at the exit of the conical nozzle has been given in many references. Conical nozzle thrust coefficient efficiency can be closely approximated by $\eta_{CF} = 1 - \frac{\cos \theta}{2}$ where θ is the exit half angle. Bell geometrical losses were taken from Reference 3 and are presented in Figure 47.

4.2.5 CYCLE LOSSES

A pump fed engine system was selected over a pressure fed system since it will result in lighter tankage and propulsion weight for the vehicle systems we are considering. In order to include the effect of turbine power requirements in the optimization of P_c , the preliminary design of a turbopump for 110,000 pounds thrust, chamber pressure of 400 psia, and pressure losses representative of the systems considered, was established.

The turbopump preliminary design was conducted for liquid oxygen/liquid hydrogen propellants. Speed (rpm) of each pump was set by the suction specific speed which was assumed from state-of-the-art values to be 40,000 and 60,000 for the oxidizer and fuel pumps, respectively. The further assumption of 30 feet and 250 feet net-positive-suction-head for the oxidizer and fuel pumps resulted in allowable speeds of 14,200 rpm and 60,000 rpm. Thus, the two impellers either have to be geared or run by separate turbines. The choice of separate turbines in series was used in the design.

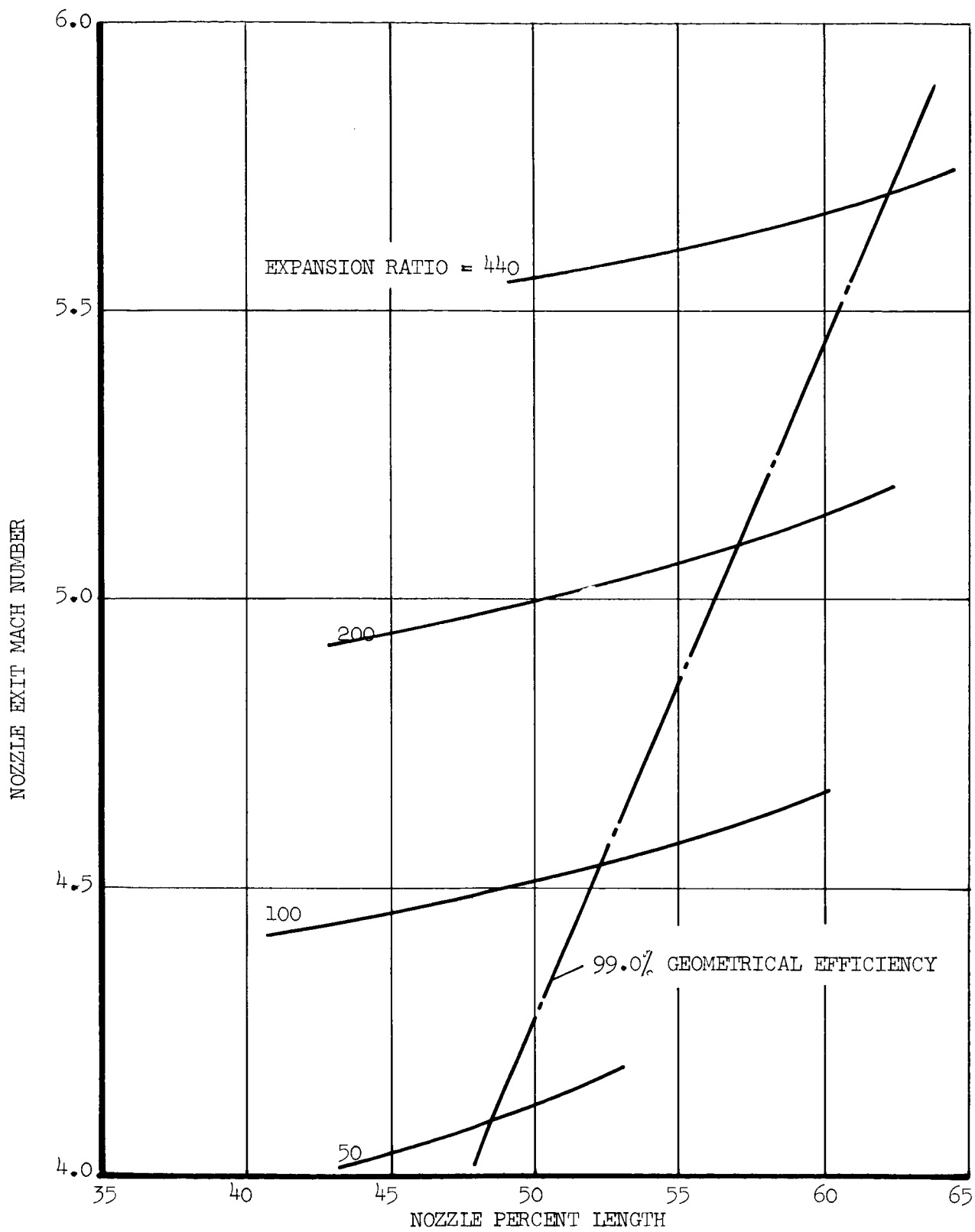


FIGURE 45. Nozzle Exit Mach Number

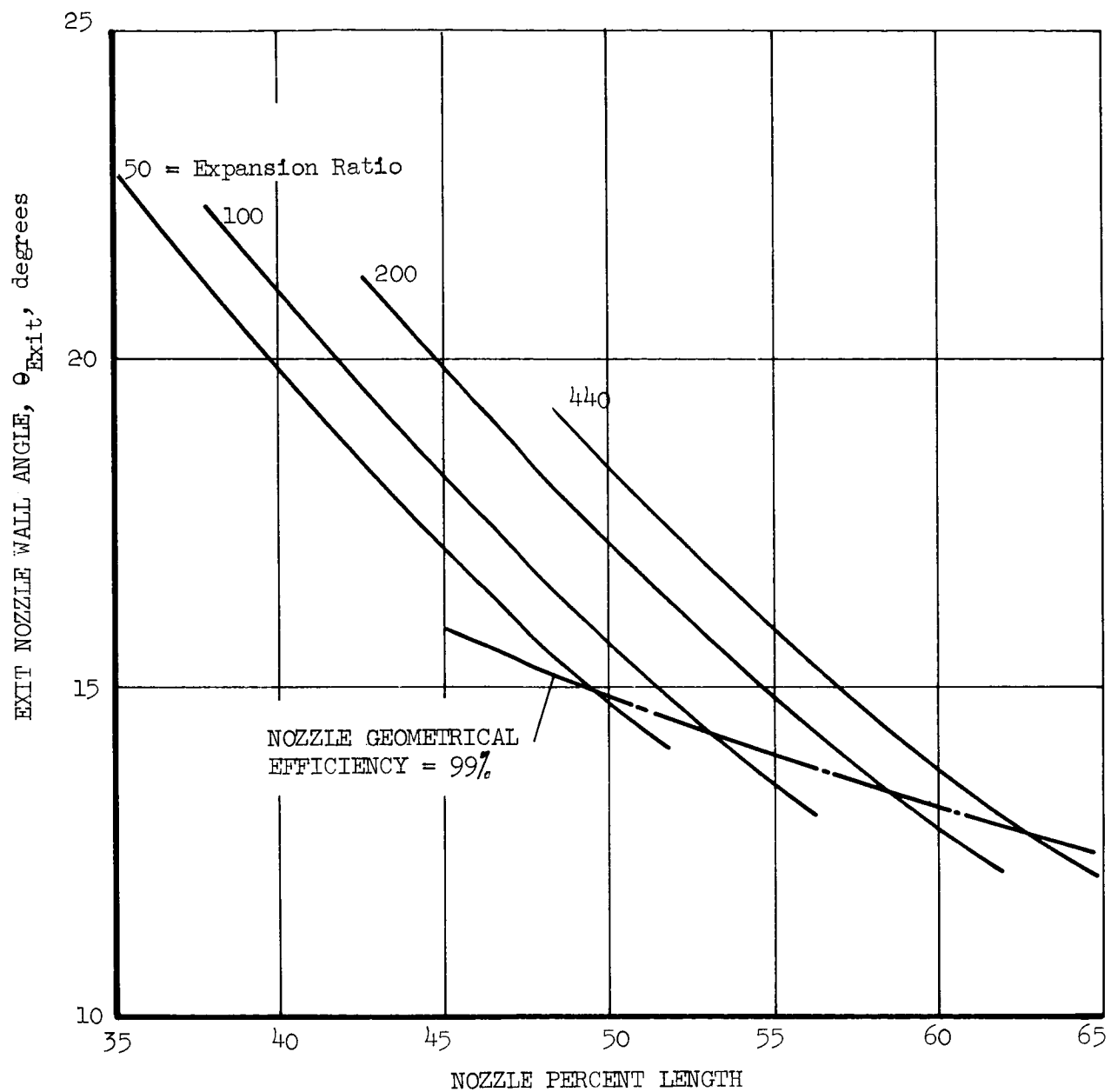


FIGURE 46. Nozzle Exit Wall Angle

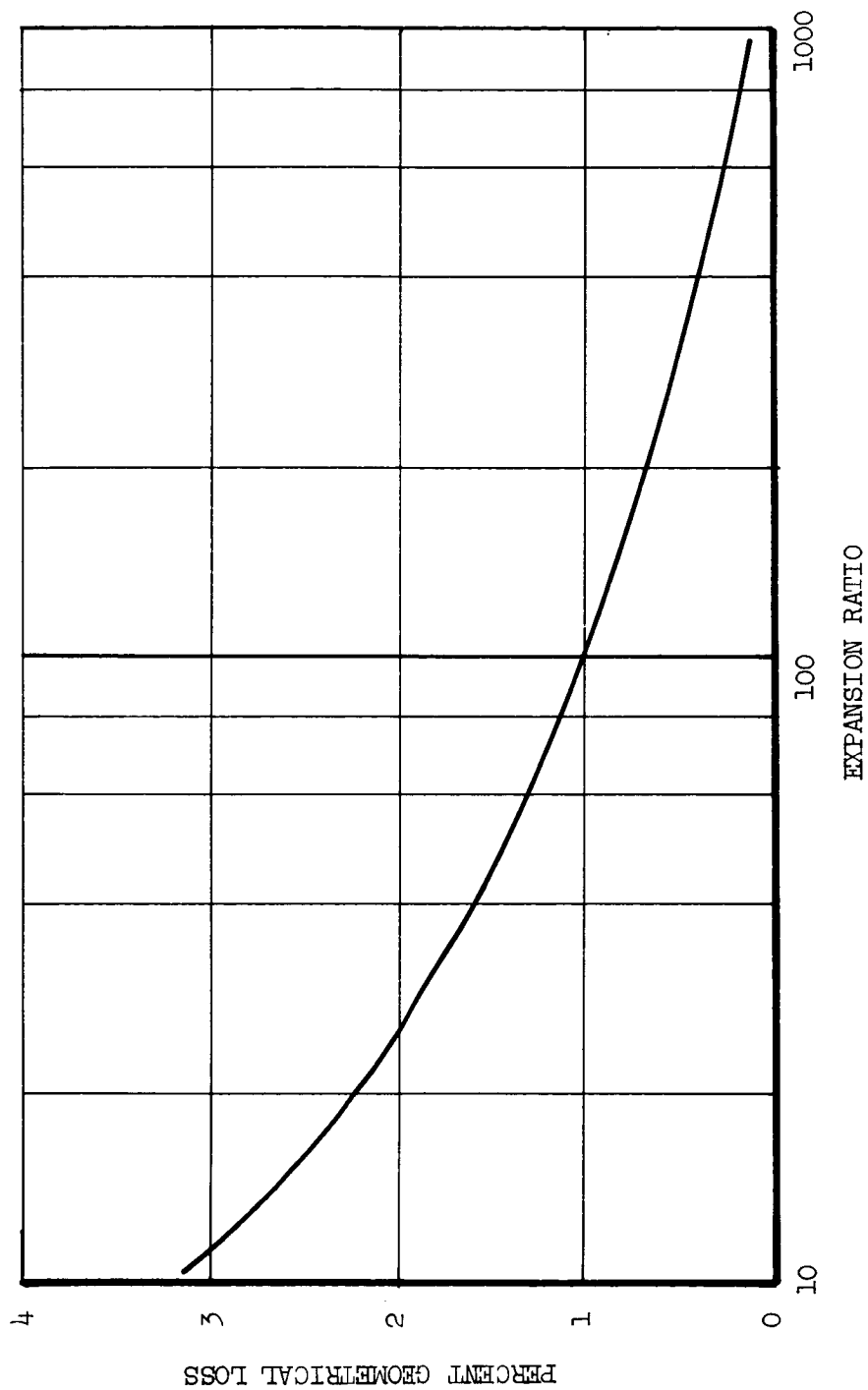


FIGURE 47. Geometrical Losses of Bell Nozzles

Impeller tip speeds of 245 feet per second and 1060 feet per second are required for the desired chamber pressure and a head coefficient of .60. Consideration of inducer flow coefficient required to obtain the assumed suction specific speed, and sufficient impeller hub-tip ratio for good vane design, required a compromise in allowable speeds and head coefficient. Resulting turbine efficiencies were 52 percent (fuel) and 32 percent (oxidizer), and the two pumps had efficiencies of 60 percent. The oxidizer turbine has a relatively low efficiency due to its required operation at a velocity ratio, u_p/c_j , of .07 which is far from optimum for the two-stage velocity compounded turbine used here.

Turbine flow required at 1350°F inlet temperature and the given thrust level, chamber pressure, and resulting efficiencies, was 2.25 pounds per second or about 1.0 percent of the total engine flow rate. Since the turbine flow was not assumed to contribute axial thrust, the resulting cycle loss was 1.0 percent and was scaled directly with chamber pressure for pressures other than the chamber pressure (400 psia) which was used in the design.

4.3. ENGINE WEIGHTS

Propulsion system weights were determined from empirically derived equations for turbopumps, gas generators, valves and lines, and conventional "can" type chambers and bell nozzles. Weights for the forced-deflection nozzle, toroidal type chamber, and uncooled chamber and manifolds were determined from design studies.

4.3.1 TURBOPUMPS

Turbopump weight has been shown to follow the equation,

$$W_{p_{ox,fuel}} = K \frac{\dot{w} P_D}{S_s^{1.35} NPSH^{1.2}} \quad (\text{Reference 9})$$

Where K = constant depending on pump configuration
(i.e., axial, centrifugal, geared, single shaft, etc.)

\dot{w} = pump flow rate, lb/sec

P_D = pump discharge pressure, psia

$$S_s = \text{suction specific speed} = \frac{N(\text{rpm}) \sqrt{Q(\text{gpm})}}{(\text{NPSH})^{.75}}$$

NPSH = net-positive-suction-head, ft

The constants K, were determined for the centrifugal-pump/series-turbine configuration discussed in Section 4.3.4. The parameters are shown in the table below:

Parameters	K	P_D	S_s	NPSH, ft
Fuel pump LH_2	28.2×10^6	$1.6 P_c$	60,000	250
Oxidizer pump LO_2	9.25×10^4	$1.5 P_c$	40,000	30

Turbopump weight for the liquid oxygen/liquid hydrogen engines was reduced to:

$$W_{TP} = \dot{w}_{\text{Total}} P_c \frac{1.41 \times 10^{-3}}{1 + \frac{1}{MR}} + \frac{1.68 \times 10^{-2}}{1 + M.R.}$$

where: $\dot{w}_{\text{Total}} = \frac{F}{I_{sp}}$, M.R. = propellant mixture ratio.

$$W_{TP} = W_{P_{ox}} + W_{P_{fuel}}$$

4.3.2. GAS GENERATORS

Gas generator weight was computed from the equation:

$$W_{gg} = 5.55 \times 10^{-4} \dot{w}_{\text{tot}}^{.523} P_c^{1.27}$$

4.3.3. CONVENTIONAL ENGINE WEIGHTS

Weights for the conventional engine system including pumps, lines and valves, gas generator, chamber, injector and nozzle, are shown in Figure 48 with variable chamber pressure, expansion ratio and thrust level. The nozzle is regeneratively-cooled to an expansion ratio of 15 and has a radiation-cooled extension downstream of that section. The nozzle extension has an average thickness of 0.06 inches in all cases.

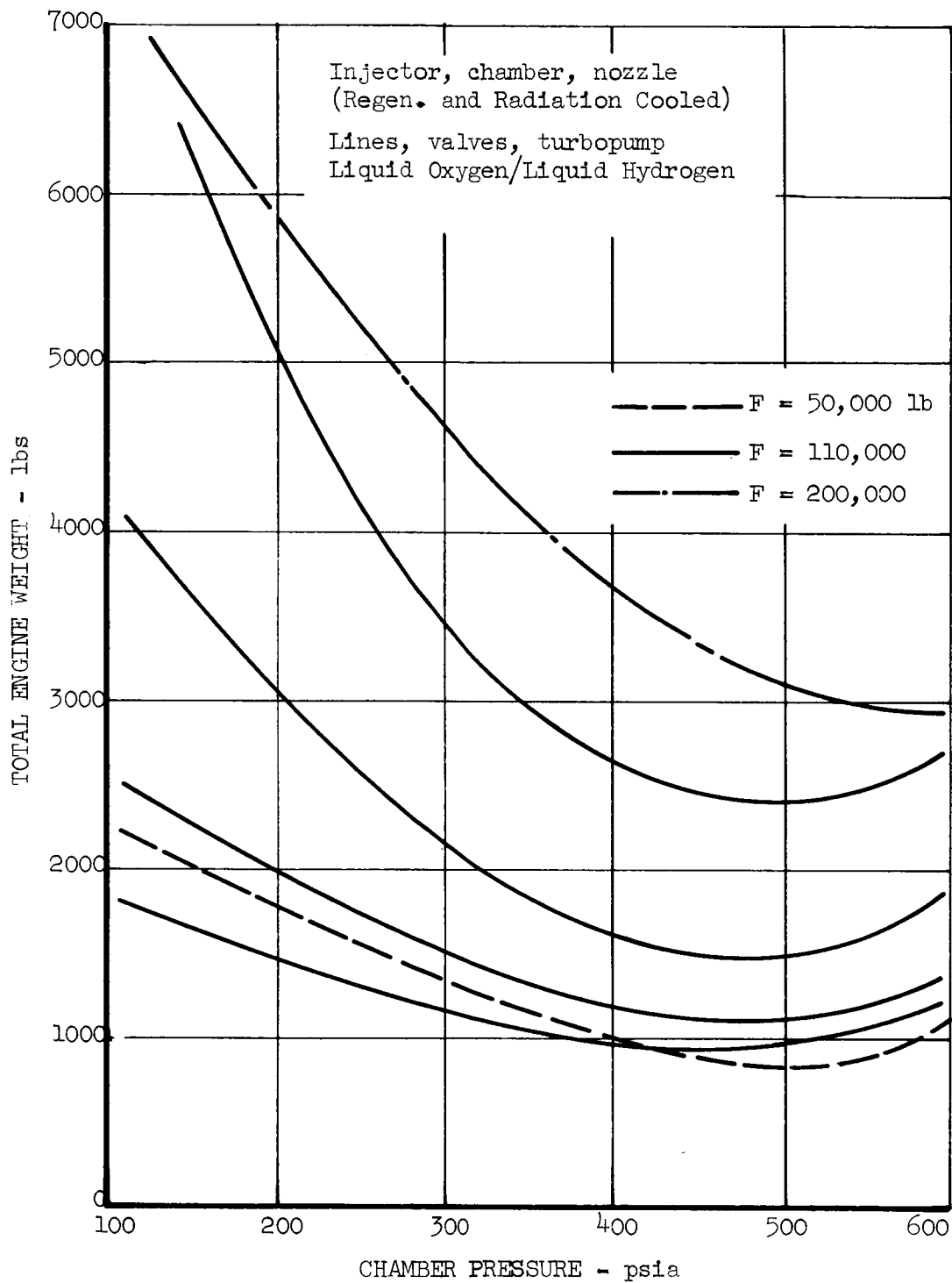


FIGURE 48. Conventional Engine Weight

4.3.4 FORCED-DEFLECTION ENGINE WEIGHTS

Weight of the forced-deflection engine, including pumps, lines and valves, gas generator, toroidal chamber, injector, and nozzle is shown in Figure 49. Weight is given for only one thrust level for this case since it was determined that with the conventional vehicle, and for the escape mission considered, approximately 110,000 pounds of thrust gives maximum payload.

4.3.5 SMALL NOZZLE CONCEPT-ENGINE WEIGHTS

The detailed structural design and weight analysis of the uncooled engine is discussed later in this section.

4.3.6 TRAJECTORY CONSIDERATIONS

In optimizing the engine thrust for the desired mission, a trade-off of propulsion weight versus velocity requirement to overcome gravity losses is needed. Data from computer-simulated trajectories for a 300 n.m. orbit escape was used to plot change in characteristic velocity (ΔV) versus thrust-to-weight ratio of the vehicle (Figure 50). The curve indicates that the losses due to gravity forces decrease rapidly at thrust-to-weight ratios in the order of .3 to .5, thus one might expect optimum thrust-to-weight of the engine/vehicle system to fall in this range.

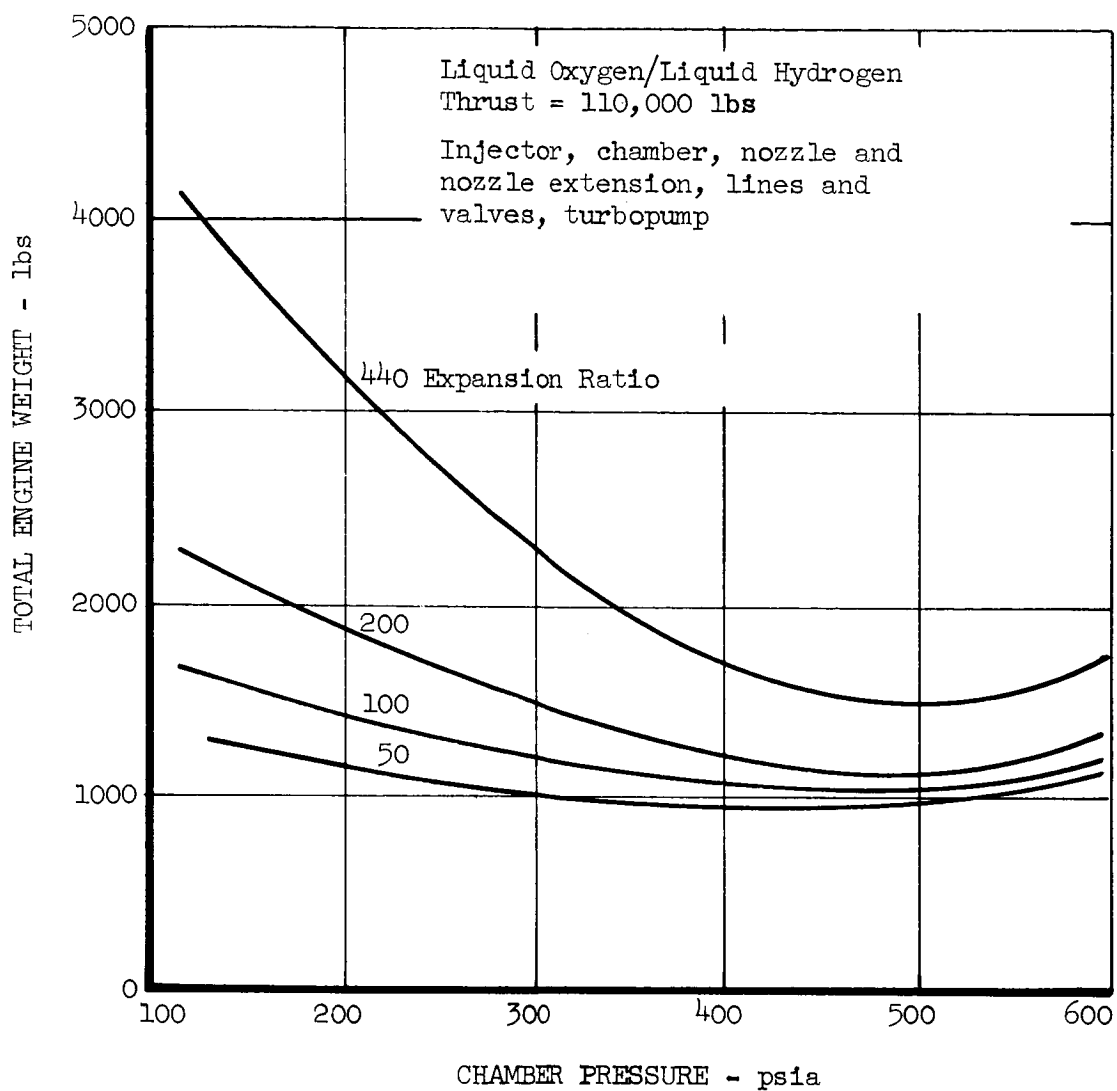


FIGURE 49. Forced-Deflection Engine Weight

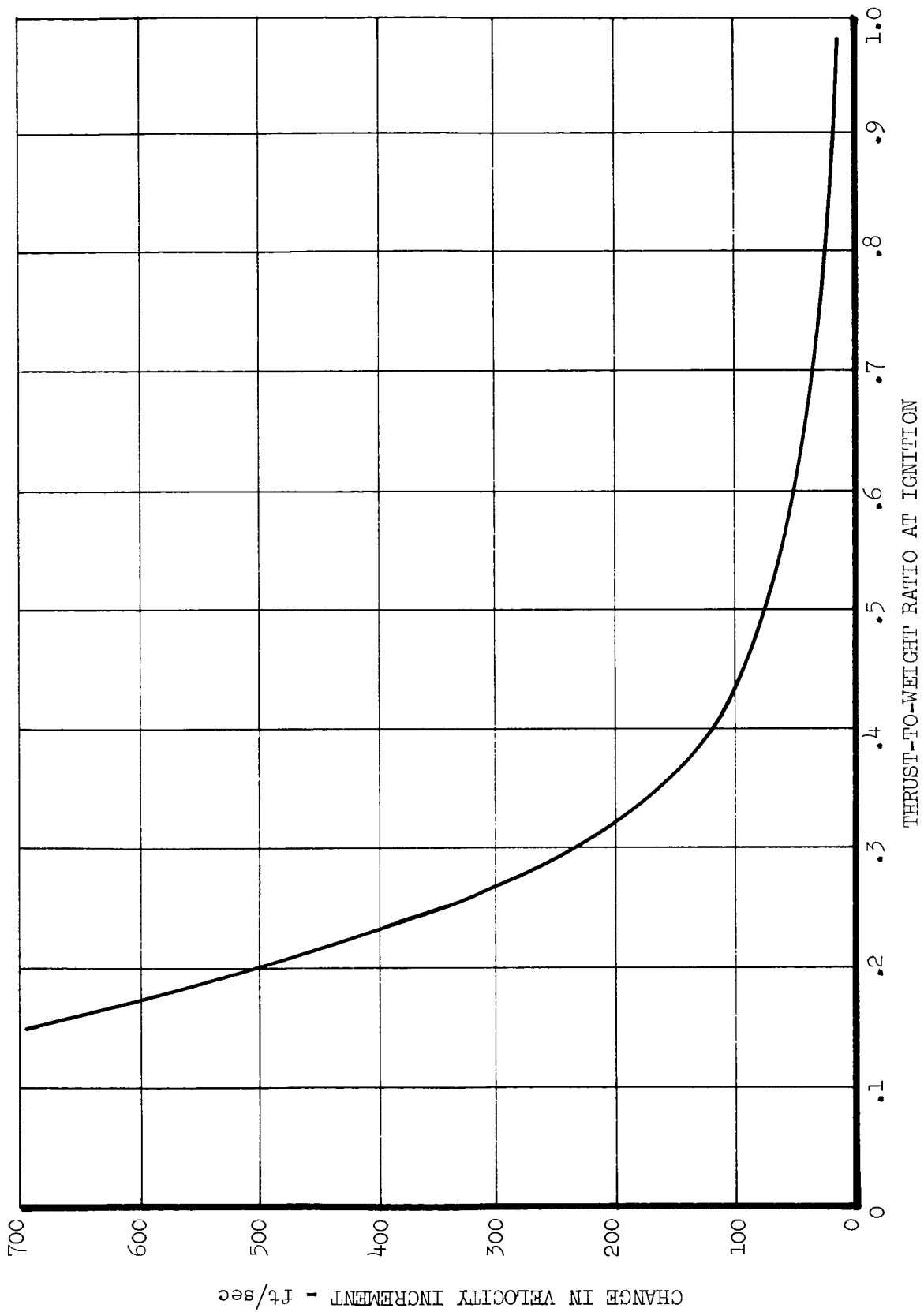


FIGURE 50. Change in Velocity Requirement Due to Gravitational Effects

4.4

VEHICLE STRUCTURAL AND WEIGHT ANALYSIS

The following paragraphs outline the assumptions and criteria used in the structural and weight analysis of the vehicles. Although pressure stabilized tankage was designed for several of the vehicles, final comparisons were made utilizing free-standing structure for all vehicles. The structural analysis is therefore based on stringer-frame-skin cylindrical tank sections and forward and aft structures, tensile load designed tank heads, and monocoque transition sections or skirts (Figure 51).

4.4.1

SIZING

Propellant weights were obtained from $W_{\text{prop}} = W_{\text{gross}} \left[1 - \frac{1}{e \frac{\Delta V}{g I_s}} \right]$,

and tank volumes were calculated using 1.0 percent outage, 3.0 percent ullage, and propellant densities of:

liquid oxygen	= 71.2 lb/ft ³
liquid hydrogen	= 4.36 "
hydrogen peroxide	= 91.8 "
diborane	= 25.9 "
payload	= 50 "

Tank diameters of the second and third stages of the vehicles were set by using zero length cylinders and 1.4:1 elliptical heads for the oxidizer tank. When this procedure resulted in excessive structure weight due to high tank length/diameter ratio, the effect of "off-loading" the oxidizer tank was investigated.

4.4.2

STRUCTURAL DESIGN

Techniques and equations used in determining the stress, size and weight of the vehicle structural components are outlined in the following paragraphs. Where pertinent, references are given for equations or constants which have been used in the analysis. Nomenclature of vehicle elements is shown in Figure 51

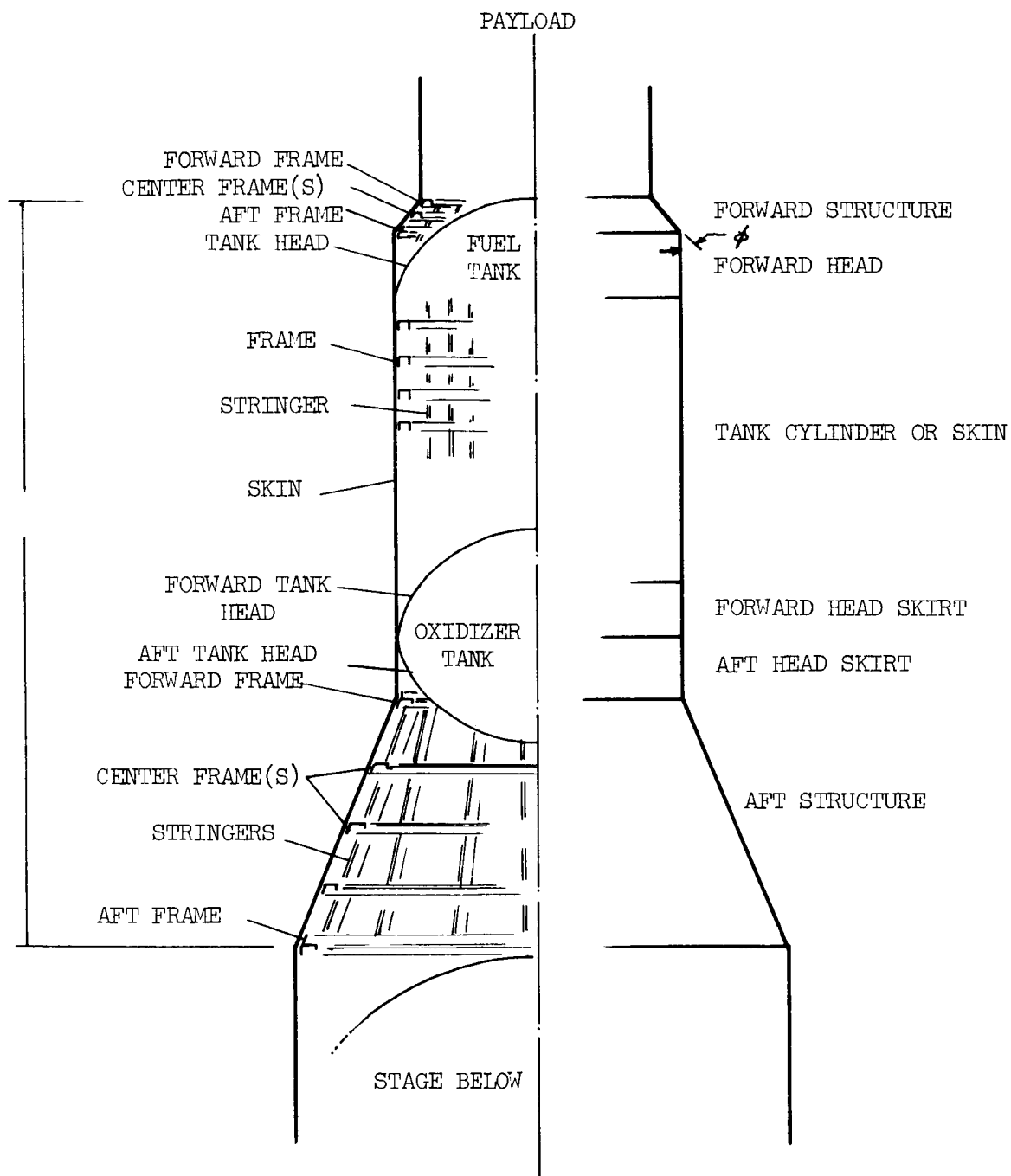


FIGURE 51. Vehicle Nomenclature

1. Forward Structure

A. Stringers

$$\text{Compressive load} = q_c = \frac{1}{\cos \phi} \left[\frac{M_1}{\pi R_1^2} + \frac{P_1}{\pi D_1} \right]$$

M = bending moment

P = axial load

R = vehicle radius

D = vehicle diameter

Required stringer area =

$$A_{st} = \frac{\pi D_{12} q_{c_{ult}}}{F_c}, \text{ where } D_{12} = \frac{D_1 + D_2}{2}$$

$$q_{c_{ult}} = 1.4 q_c$$

F_c = allowable ultimate compressive stress of material

= 35,000 psi for 7075 aluminum (structure)

= 30,000 psi for 2024 aluminum (skin)

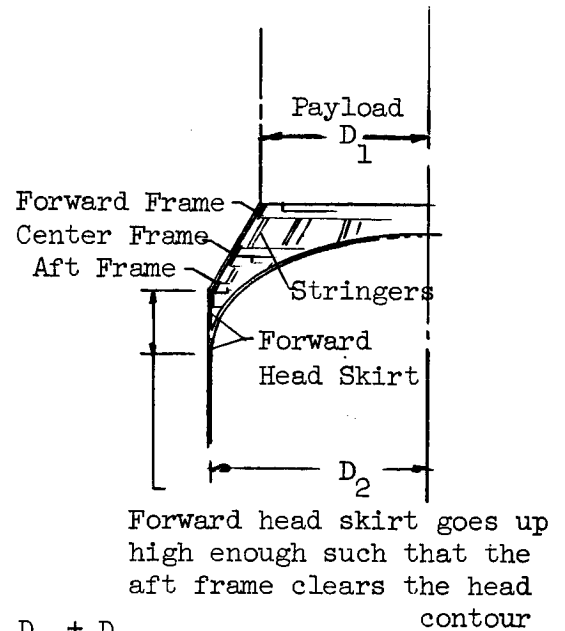
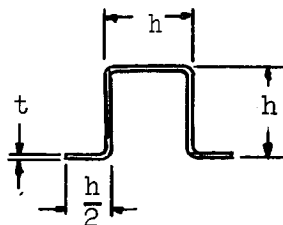
Weight Stringers =

$$A_{st} \times L_{st} \times \rho_{mat'l}$$

L_{st} = stringer length

$\rho_{mat'l}$ = density of material

For preliminary sizing purposes, all stringers were assumed to be "hat" sections with the geometry as shown below



The radius of gyration for this section =

$$\rho = \sqrt{\frac{I}{A}} = \left[\frac{\frac{2th^3}{12} + \left(\frac{h}{2}\right)^2 2ht}{4ht} \right] = .41h$$

Therefore, after stringer depth, h , is assumed for the section, the column allowable is determined from Figure 52 by taking $\frac{L}{\rho\sqrt{c}} = \frac{L}{\rho}$ for fixed ends. The column length, L , is determined from the optimum frame spacing = $.115 D_{12}$ (Page 79, Reference 10). If the allowable from Figure 52 is greater than the allowable stress assumed (35,000 psi for 7075), the column is stable. If it is smaller, a greater depth must be taken in order to increase the allowable stress.

b. Forward Frame

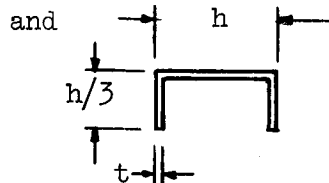
$$q_{1ult} = \left[\frac{M_1}{\pi R_1^2} + \frac{P_1}{\pi D_1} \right] 1.4$$

$$q_1' = \frac{q_{1ult} (R_2 - R_1)}{L} = \text{compressive load on frame due to "kick" load}$$

The critical compressive stress on the frame =

$$q_{1cr}' = \frac{3EI}{R_c^3}, \text{ where } R_c = \text{radius to the centroid of the frame section}$$

Taking a frame section as shown below,

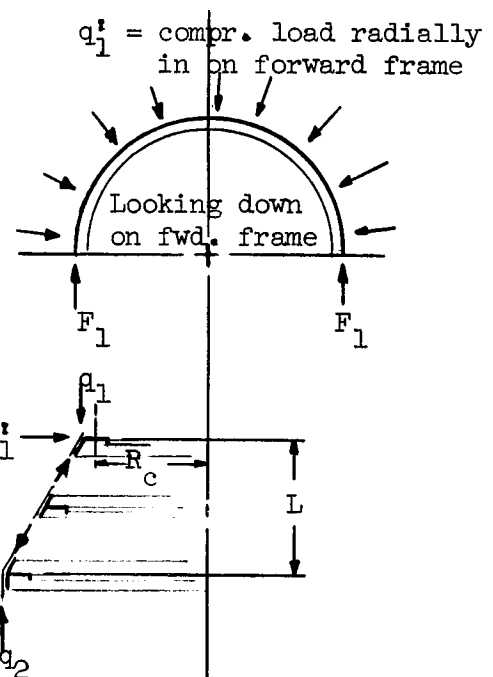


$$I_F = \frac{th^3}{4}$$

$$A_F = \frac{5}{3} ht$$

Then, assuming a height h ,

$$t_{cr} = \frac{4q_1' R_c^3}{3 E h^3} = \text{critical web thickness}$$



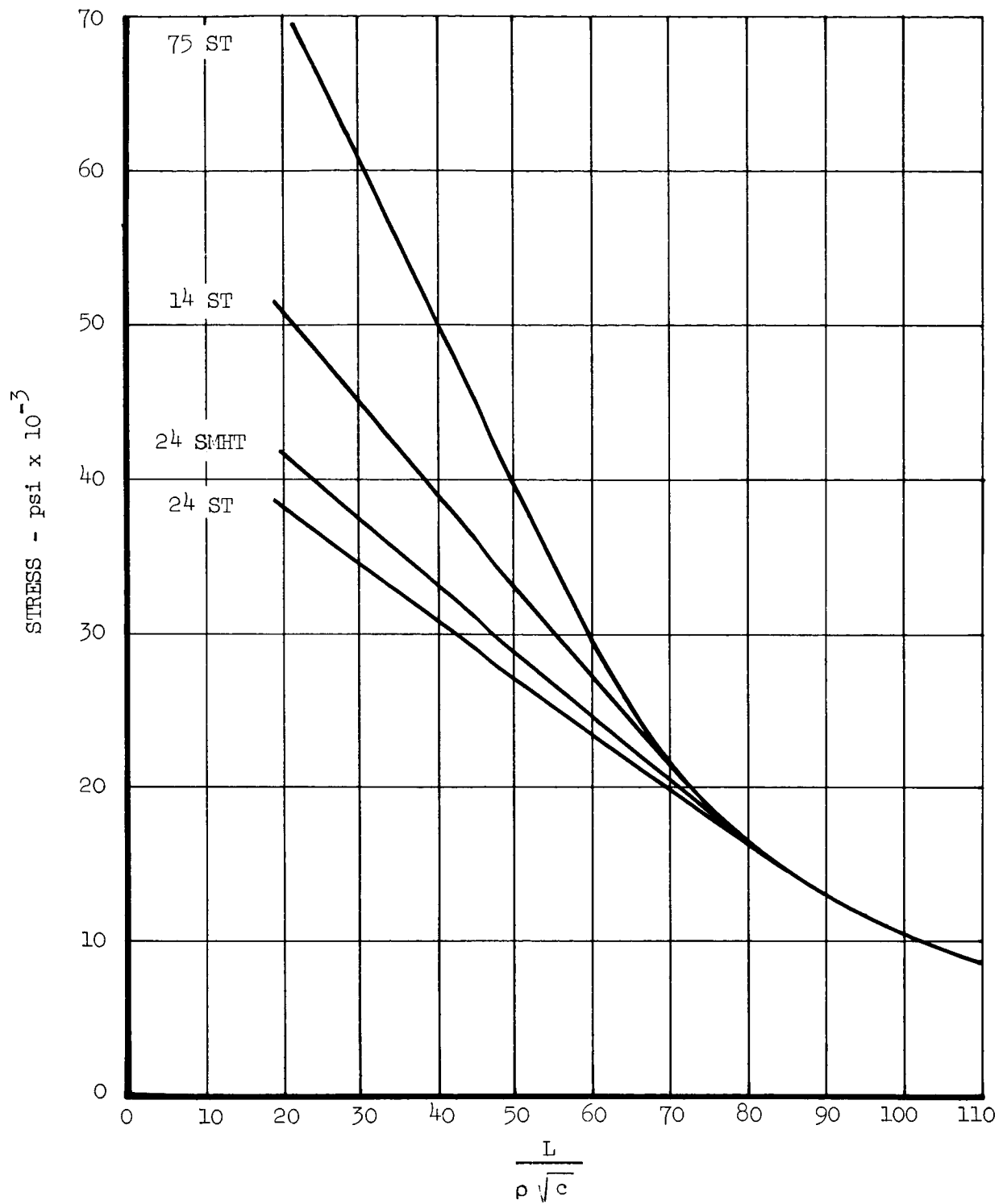


FIGURE 52. Design Column Curves for Extruded Shapes

The reactions due to the shear at the fittings will be

$$R_{Fl_{ult}} = \frac{1.4 W_{pl} \times (\text{traverse g's}), \text{ and the compressive stress in the}}{\text{No. fittings}}$$

$$f_c = \frac{Mc}{I_F} + \frac{Pax}{A_F} = \text{allowable stress}$$

W_{pl} = Payload Weight

$$P_{ax} = F_l + K_{axial} R_{Fl}$$

$$M = K_{\text{bend}} R_{\text{Fl}} R_c$$

where $K_{\text{bend}} = .066$
 $K_{\text{axial}} = 1.275$
 No. fittings = 8

} -- for the loading conditions chosen as reasonable for
 this application

The frame thickness required to resist this stress is calculated from f_c and the fact that $I_F = \frac{t_f h^3}{4}$, and $A_F = \frac{5}{3} h t_f$.

Total required frame thickness is therefore $t_{cr} + t_f$, and frame area is dictated by the assumed h and this total thickness. There obviously is a trade-off of weight as h increases, however as h becomes greater, the possibility of crippling of the ring would have to be investigated in the actual design of the frame.

$$\text{Weight fwd. frame} = D_{12} A_f \frac{\pi}{f_{\text{tot}}} \times \rho_{\text{mat'l}}$$

c. Center Frame

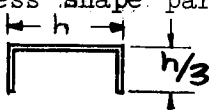
Required frame cross sectional area to resist instability failure
is

$$A_F = \sqrt{\frac{C_f M D_{12}^2}{K_4 L E}} \quad (\text{Reference 10, page 74})$$

$$C_f = \text{dimensionless coefficient} = \frac{1}{16,000} \quad (\text{Reference 10, page 67})$$

M = bend. mom. at the frame

K_4 = dimensionless shape parameter = 5.24 for



$$L = .115 D_{12} = \text{optimum frame spacing} \quad (\text{Reference 10, page 79})$$

E = modulus of elasticity

$$\text{Weight center frame} = A_F \pi D_{12} \times \rho_{\text{mat}} l$$

d. Aft Frame

$$q_{2\text{ult}} = \left[\frac{M_2}{\pi R_2^2} + \frac{P_2}{\pi D_2} \right] 1.4 = \text{compressive frame load,}$$

and the tensile load in the frame is

$$q_2' = \frac{q_{2\text{ult}} L}{R_1 - R_2} \quad \text{where } L \text{ is the axial length of the forward structure}$$

The tensile force is $F_2 = q_2' R_2$, and the required frame area is $A_F = \frac{F_2}{F}$ where

F is the allowable stress.

$$\text{Weight aft frame} = \pi D_2 A_F \rho_{\text{mat}} l$$

e. Skin

The shear load resisted by the skin is

$$V = 1.4 W_{pl} \times (\text{traverse g's})$$

For a shear resistant web the equation giving allowable critical buckling stress in

the skin is

$$F_{s_{cr}} = K_s E \left(\frac{t}{b}\right)^2 \quad (\text{Reference 11, page 393})$$

K_s is a function of $\frac{b^2}{Rt}$, and $\frac{a}{b}$, where

b = stringer spacing

a = frame spacing

R = radius from center line of vehicle to skin

$$K_s \approx 4.5 \text{ for } \frac{b^2}{Rt} \leq 4, \frac{a}{b} > 5 \quad (\text{Reference 11, page 396, 397})$$

Assume a skin thickness, t , near minimum gage, take $b = 2h$ from the stringer analysis 1.a, and calculate $F_{s_{cr}}$. The internal shear stress in the skin is

$$f_s = \frac{2V}{\pi D_{12} \times t}$$

For a semi-tension field web, the allowable shear stress, F_{sw} , is taken from curve (Reference 11, page 410) at the calculated ratio of $\frac{f_s}{F_{s_{cr}}}$. The web margin will

then be

$$M = \frac{f_s}{F_{sw}} - 1$$

The skin thickness is then iterated to achieve the desired margin.

$$\text{Weight skin} = \pi D_{12} L \times t \times \rho_{mat} \times 1$$

2. Fuel Tank

a. Forward Head

The design pressure of the tank sections are calculated from the static tank pressure plus the acceleration head of the propellants at the given section,

$$P_D = 1.4 P_{\text{tank}} + \frac{\rho_{\text{prop.}} \times \text{head} \times \text{axial acc.}}{144}, \text{ where } P_{\text{tank}} = \text{static tank pressure}$$

The tank wall thickness is

$$t_w = \frac{P_D R_{\text{Head}}}{2 \sigma_t}$$

where R_{head} is the radius of the elliptical head, i.e.,

$$R_{\text{head}} = 1.4 R_2 \text{ for a } 1.4:1 \text{ head } (R_2 = \text{tank cylinder radius})$$

$$\sigma_t = \text{allowable tensile stress}$$

The surface area of the elliptical head can be calculated from the k factors given in Figure 53.

$$A_{\text{ellipsoid}} = k A_{\text{sphere}} \text{ where the major diameter of the ellipsoid} = \text{sphere dia.}$$

$$A_{\text{head}} = k \frac{2}{3} \pi r^2$$

$$\text{Weight fwd. head} = t_w \times A_{\text{head}} \times \rho_{\text{mat}} \cdot l$$

b. Cylinder Skin

$$\text{Cylinder wall thickness} = t_w = \frac{P R_2}{\sigma} = t_{\text{skin}}$$

$$\text{Weight cylinder} = t_w \times \pi \times D_2 \times L_{\text{tank}} \times \rho_{\text{mat}} \cdot l$$

c. Forward Head Skirt (Monocoque)

$$q_{\text{ult}} = 1.4 \left[\frac{M}{\pi R_2^2} + \frac{P}{\pi D_2} \right], \text{ and wall thickness is}$$

$$t = \frac{R_2^{.612}}{2.24 E^{.388}} [q_{\text{ult}}]^{.388}$$

The thickness equation was developed from data presented in Reference 12 - Figure 7, and is valid within the range $60 < \frac{R}{t} < 3000$. Weight fwd. head skirt = $t \times$

$$A_{\text{skirt}} \times \rho_{\text{mat}} \cdot l$$

d. Stringers

$$q_c = \left[\frac{M}{\pi R_2^2} + \frac{P}{\pi D_2} \right],$$

if the stringers had to carry all the load, then

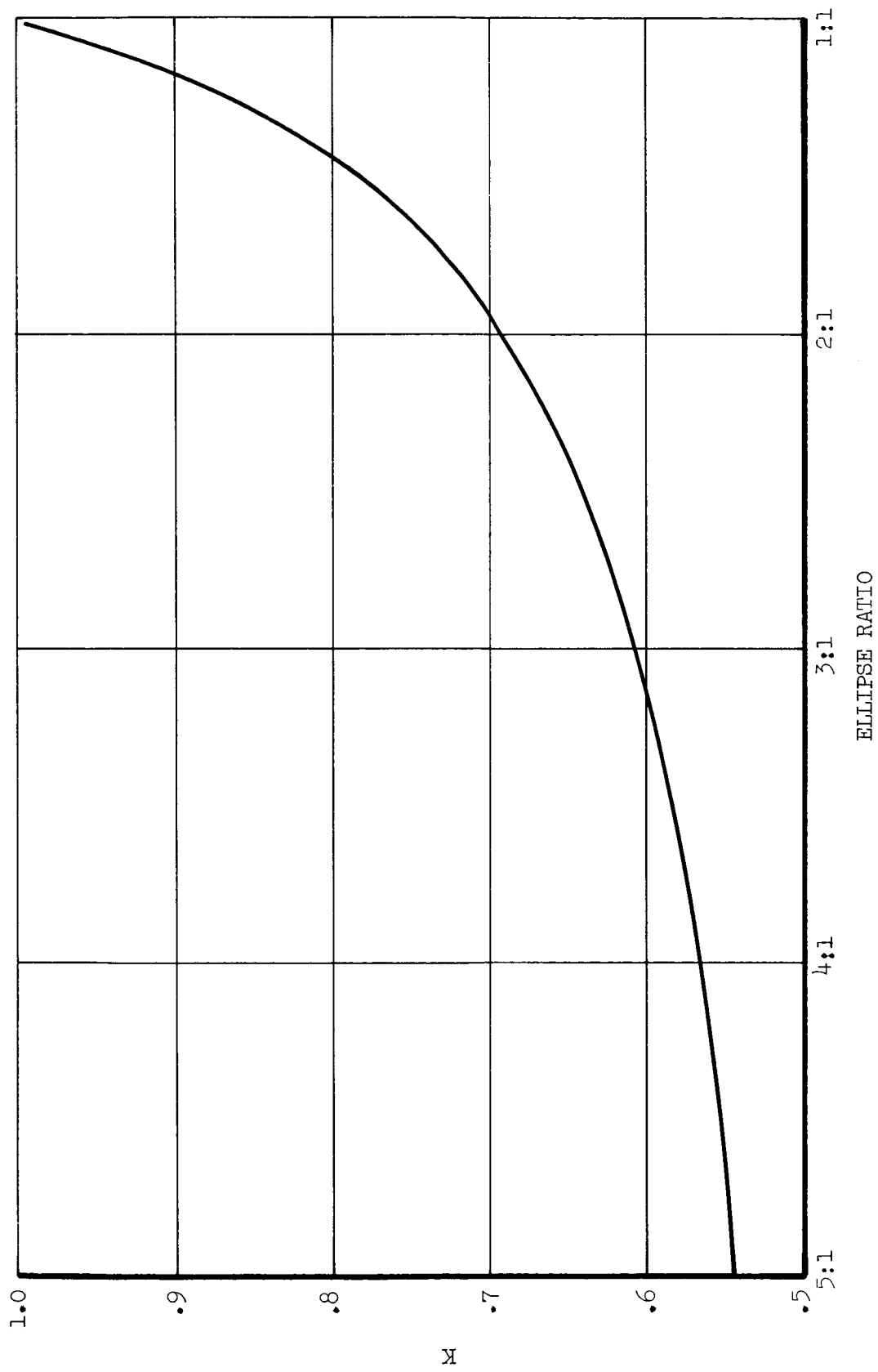


FIGURE 53. Tankhead Surface Area

$$A'_{st} = \frac{\pi D_2^2 q_{ult}}{f_c}$$

However, the skin carries some load, and from past experience, a better estimate of the stringer area is

$$A_{est} = .85 A'_{st}$$

The equivalent skin thickness of the stringer = $t'_{st} = \frac{A_{est}}{D}$

and gross tensile stress =

$$\frac{P_{tank} R_2}{2(t'_{st} + t_{skin})} = \left(\frac{P}{A} \right)_{gross}$$

where t_{skin} is taken from 2.b..

For combined stringer-skin-frame type structure, the stringer tensile stress is 40 percent of the gross tensile stress (Reference 13, page A16.6). Therefore, stringer tensile load is

$$q_{t_{skin}} = t'_{st} \times \left(\frac{P}{A} \right)_{gross} \times .40$$

Compressive stress in the skin is

$$q_{c_{st}} = \frac{.3 E t_{skin}^2}{R_2}$$

$$\text{Net } q_{c_{st_{ult}}} = \left[q_c - q_{c_{skin}} - q_{t_{st}} \right] \times 1.4$$

Then the stringer area is

$$A_{st} = \frac{\pi D_2^2 q_{c_{st_{ult}}}}{f_c}$$

This value is compared with A_{est} and iterated until the values are equal.

Weight stringers = $A_{st} \times L_{st} \times \rho_{mat} \times 1$

e. Frames

$$q_c = \left[\frac{M}{\pi R_2^2} + \frac{P}{\pi D_2} \right]$$

Tensile load resulting from the tank internal pressure, P_s , is

$$q_t = \frac{P_s R_2}{2}$$

Net $q_{c_{ult}}$ = $1.4 [q_c - q_t]$, and the equivalent bending moment

is $M' = \pi R_2^2 \times \text{Net } q_{c_{ult}}$.

The frame area is found by the same procedure as used in l.c. by setting $M' = M$. Frame spacing = $L_f = .115 D_2$, and no. frames = $\frac{L_{\text{cylinder}}}{L_f} + 1$

Total weight of frames = $A_f \times \pi D_2 \times N_f \times \rho_{\text{mat}} l$

3. Oxidizer Tank

a. Forward Head Skirt

$$q_c = \frac{M}{\pi R_2^2} + \frac{P}{\pi D_2}$$

$$q_t = \frac{P R_t}{2} = \text{tensile load due to internal pressure}$$

$$q_{c_{net_{ult}}} = [q_c - q_t] \quad 1.4$$

$$t = \frac{R^{.612}}{2.24 E^{.388}} [q_{c_{net_{ult}}}]^{.388}$$

$$\text{Weight fwd. Head Skirt} = A_{\text{skirt}} \times t \times \rho_{\text{mat}} l$$

b. Aft Head Skirt

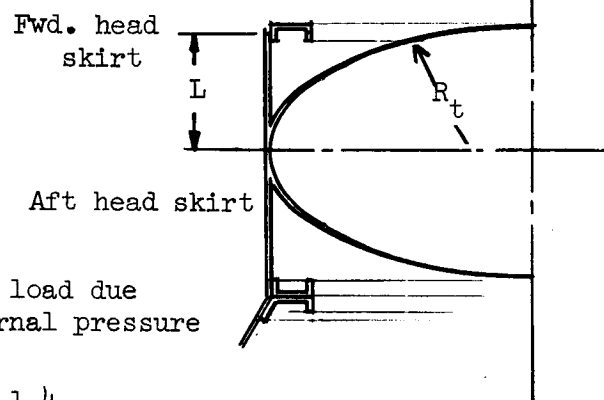
Similar to 3a except $q_t = 0$

c. Forward Head, Aft Head

Similar to 2a

4. Aft Structure

Analysis of forward and aft frames, center frames, stringers, and skin is the same as was shown for the Forward Structure (1).



4.5 CONVENTIONAL VEHICLE (LIQUID OXYGEN/LIQUID HYDROGEN PROPELLANTS)

4.5.1 GENERAL DESCRIPTION

As mentioned earlier in the report, the conventional vehicle is conventional in that it does not utilize integrated or unique propulsion or structure. The vehicle is free standing, consisting mostly of aluminum structure and skin. The propulsion system consists of a gas-generator driven turbopump, conventional can type chamber, and partially regeneratively cooled 80 percent bell type nozzle with a large radiation-cooled extension.

4.5.2 PROPULSION ANALYSIS

The chamber pressure, expansion ratio, and thrust of the conventional vehicle were optimized to give maximum payload for the escape-from-orbit mission. In addition, the effects of changing the velocity increment, cycle losses, recombination performance, and nozzle extension thickness on the optimum engine parameters were investigated for this system. Vacuum performance, nozzle losses, cycle losses, and engine weights were computed by the methods discussed in the previous sections of this report.

4.5.2.1 OPTIMIZATION OF THRUST, CHAMBER PRESSURE, AND EXPANSION RATIO

In the optimization of engine parameters, payload weight was calculated from the equation

$$W_{pl} = W_o - W_{prop} - W_{tankage} - W_{eng} - W_{interstage}$$

where W_{pl} = payload weight

W_o = stage gross weight = 240,000 pounds

$$W_{prop} = \text{propellant weight} = W_o \left[1 - \frac{1}{R_3} \right] = W_o \left[1 - \frac{1}{e^{\Delta V / g I_s}} \right]$$

$$W_{tankage} = \text{tankage, pressurization and insulation weight} = K_1 W_{oxidizer} + K_2 W_{fuel} + K_3 W_{prop} (\text{press.}) + K_4 W_{prop} (\text{insul.})$$

W_{eng} = engine weight = $f(P_c, \epsilon, \text{Thrust})$

$$W_{interstage} = \text{interstage weight} = K_5 \times \left[\text{nozzle length} \right]$$

Velocity increment, ΔV , was taken as 10,000 feet per second plus a $\Delta(\Delta V)$ taken from Figure 50 for the particular thrust-to-weight ratio. Specific impulse, I_s , is a function of theoretical performance at the particular P_c and ϵ , and nozzle losses associated with those values of P_c , ϵ and thrust. Values of the structural weight constants K_1 , K_2 , K_3 , K_4 and K_5 were developed in the structural analysis and had the following values for the conventional vehicle:

$$\begin{array}{rcl} K_1 & = & .0170 \\ K_2 & = & .178 \\ K_3 & = & .01 \\ K_4 & = & .003 \end{array} \left. \vphantom{\begin{array}{rcl} K_1 \\ K_2 \\ K_3 \\ K_4 \end{array}} \right\} \text{-- } \text{LO}_2/\text{LH}_2 \text{ Mixture Ratio} = 6.0$$

$$K_5 = 19 \text{ pounds/inch}$$

Ranges in chamber pressure from 150 psia to 600 psia, in expansion ratio from 50 to 400, and in thrust from 50,000 pounds to 200,000 pounds were considered in the study.

Results are shown in Figure 54, 55 and 56 for the three thrust levels. As thrust increases, the optimum chamber pressure becomes larger and the optimum expansion ratio becomes smaller; thus tending to keep the engine size or weight relatively constant. The points of optimum payload for each thrust level were plotted in Figure 57 where optimum thrust is seen to be approximately 125,000 pounds.

The optimum engine parameters for the conventional vehicle, interpolating between the thrust levels plotted in Figure 57, were 125,000 pounds thrust, chamber pressure of 520 psia and expansion ratio of 220.

4.5.3 EFFECT OF CHANGING ASSUMPTIONS ON OPTIMUM ENGINE

4.5.3.1 VELOCITY INCREMENT

Velocity increments of 4000 feet per second and 1000 feet per second were used in the optimization study to determine if the engine which was optimized for $\Delta V = 10,000$ was near optimum for lower energy missions. Results are presented in Figure 58 where percent of optimum payload for each ΔV is plotted versus chamber

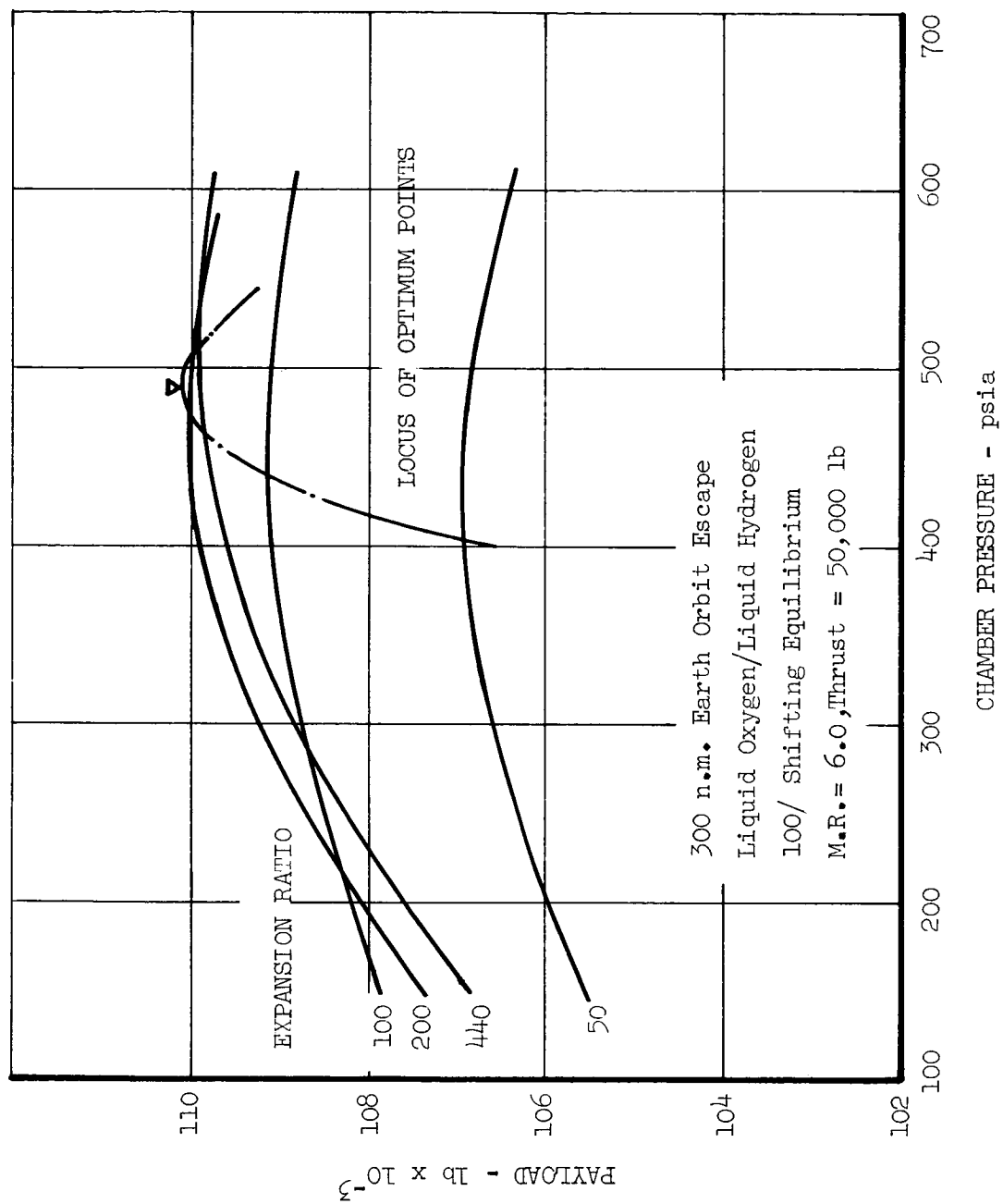


FIGURE 54. Effect of Engine Parameters on Performance of Conventional Vehicle

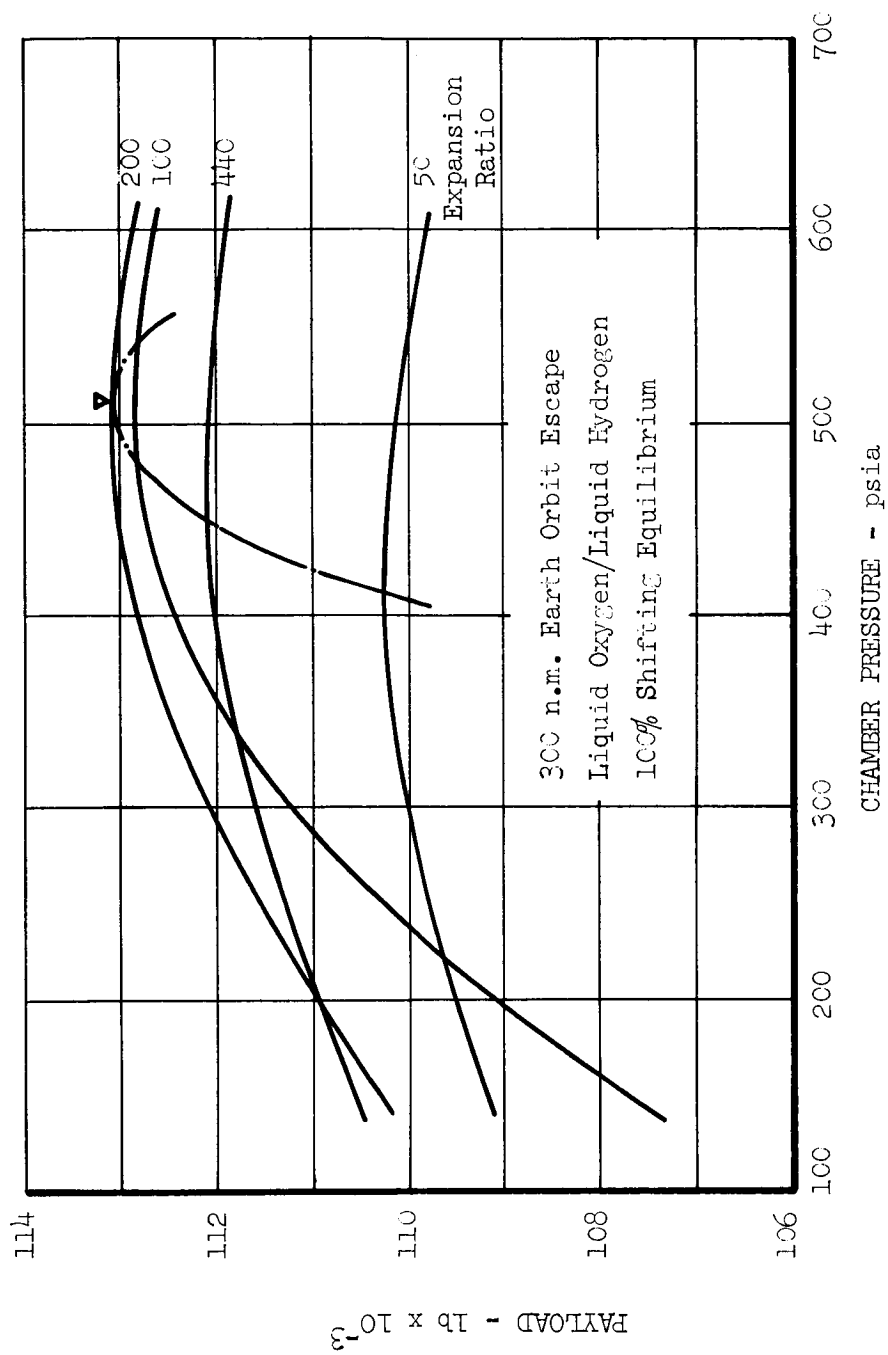


FIGURE 55. Effect of Chamber Pressure and Expansion Ratio on Performance of Conventional Vehicle

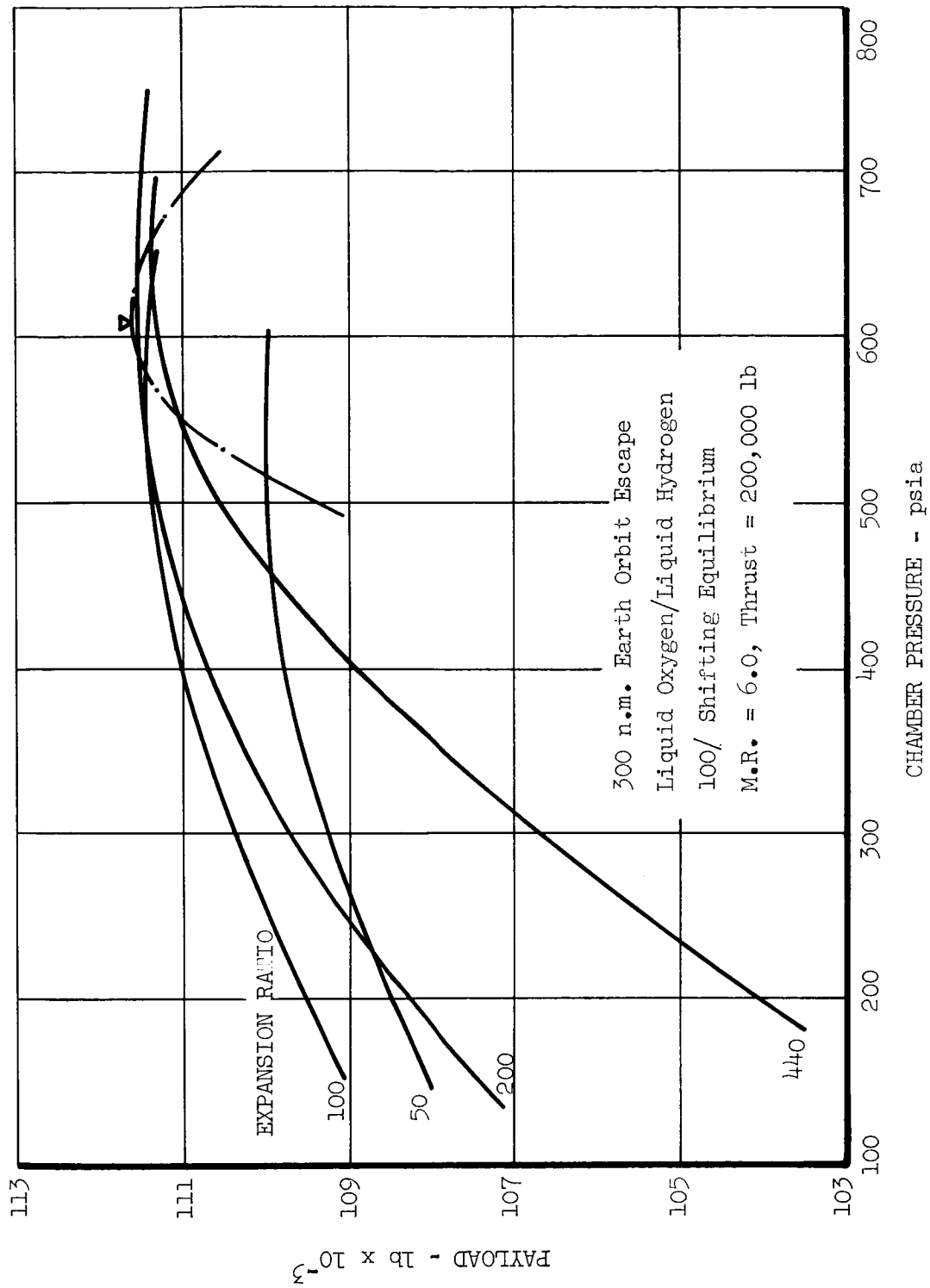


FIGURE 56. Effect of Engine Parameters on Performance of Conventional Vehicle

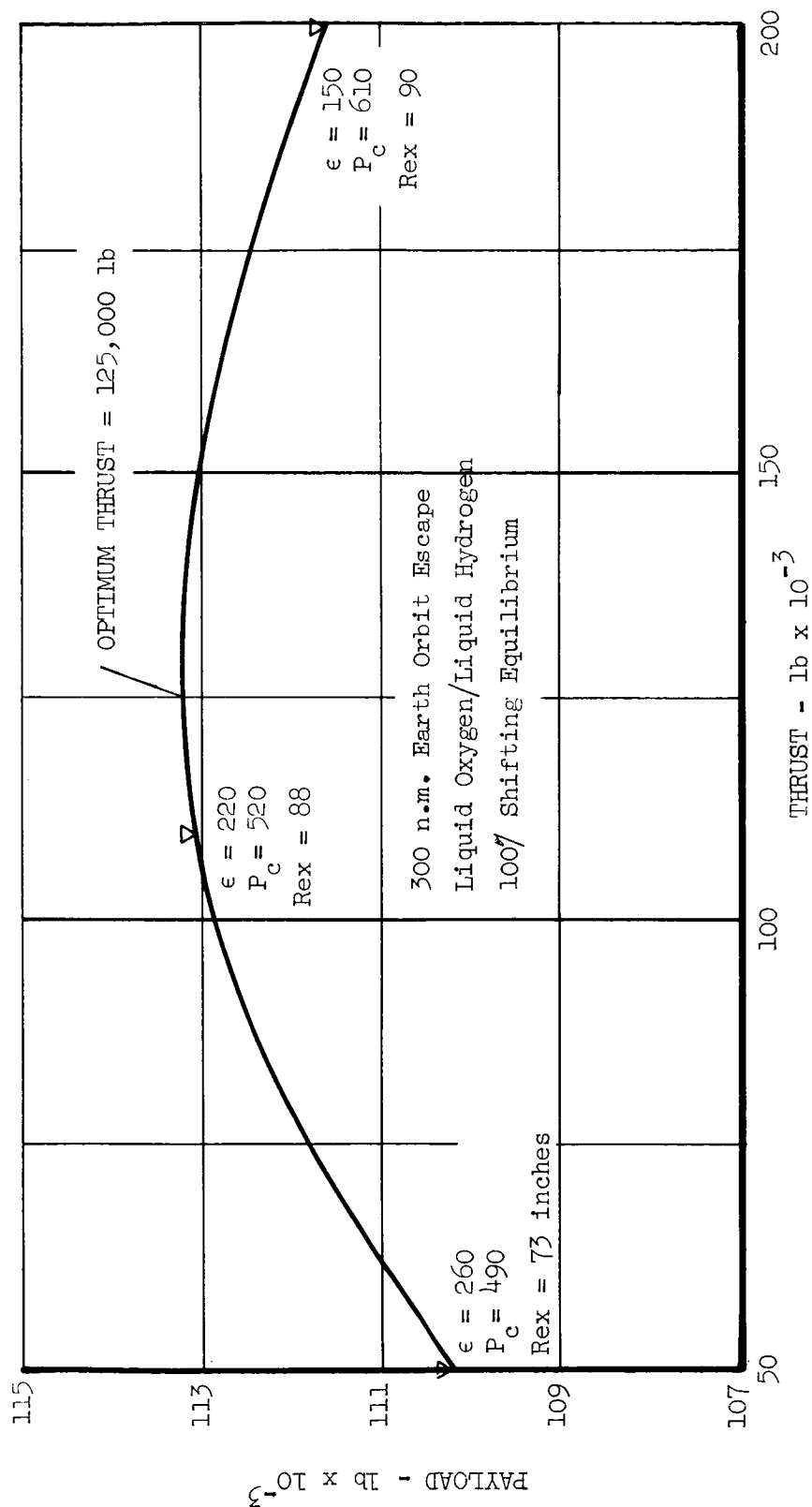


FIGURE 57. Effect of Thrust on Performance of Conventional Vehicle

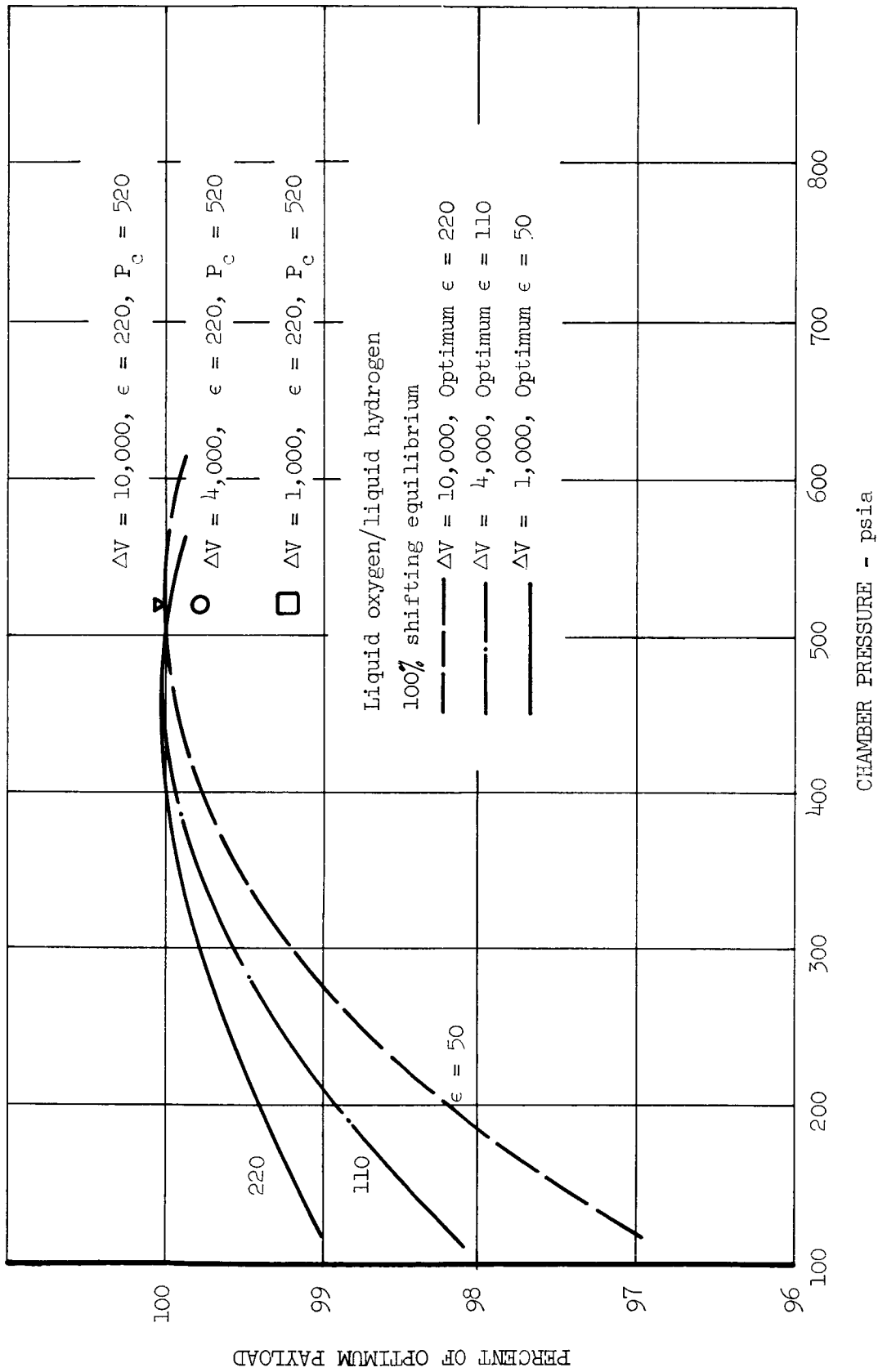


FIGURE 58. Effect of Velocity Increment on Selection of Engine Parameters

pressure. The parameters selected at $\Delta V = 10,000$ provide 99.8 percent of optimum payload for the same vehicle with $\Delta V = 4000$ and 99.2 percent of optimum payload if $\Delta V = 1000$.

It is interesting to note that optimum expansion ratio becomes less as ΔV decreases, thus de-emphasizing the importance of performance. This trend can also be seen from the exchange factor of burnout weight with performance,

$$\frac{\Delta W_{bo}}{W_{bo}} = \frac{\Delta V}{g I_s} \quad \frac{\Delta I_s}{I_s}$$

4.5.3.2 CYCLE LOSSES

To determine how important cycle losses were in selecting the optimum parameters for the conventional engine, cycle losses were reduced by 50 percent. Results are shown in Figure 59. Due to the reduced turbine flow requirements, optimum chamber pressure increases from 515 psia to 535 psia and expansion ratio is increased to about 230 from 220. Therefore, the effect of increasing cycle efficiency is very small in this upper stage application compared with the effect seen in large booster engines where optimum chamber pressures (and total cycle losses) are four to five times higher.

4.5.3.3 EQUILIBRIUM PERFORMANCE

The engine was optimized using 100 percent frozen propellant performance. As shown in Figure 60, optimum expansion ratio and chamber pressure are higher than those found with shifting performance. Also, payload has decreased to about 95 percent of optimum payload for 100 percent shifting performance. Therefore, as indicated earlier in the study, the choice of recombination energy level is not only important in selecting the best engine operating conditions, but the choice also influences payload capability.

4.5.3.4 RADIATION COOLED NOZZLE THICKNESS

Although the stress analysis conducted on the radiation cooled skirt of the small nozzle concept showed that average skirt thickness would be in the order of .04 to .06 inches, this average thickness was perturbed to determine its effect on optimum area ratio for the conventional engine. Results are given in Figure 61.

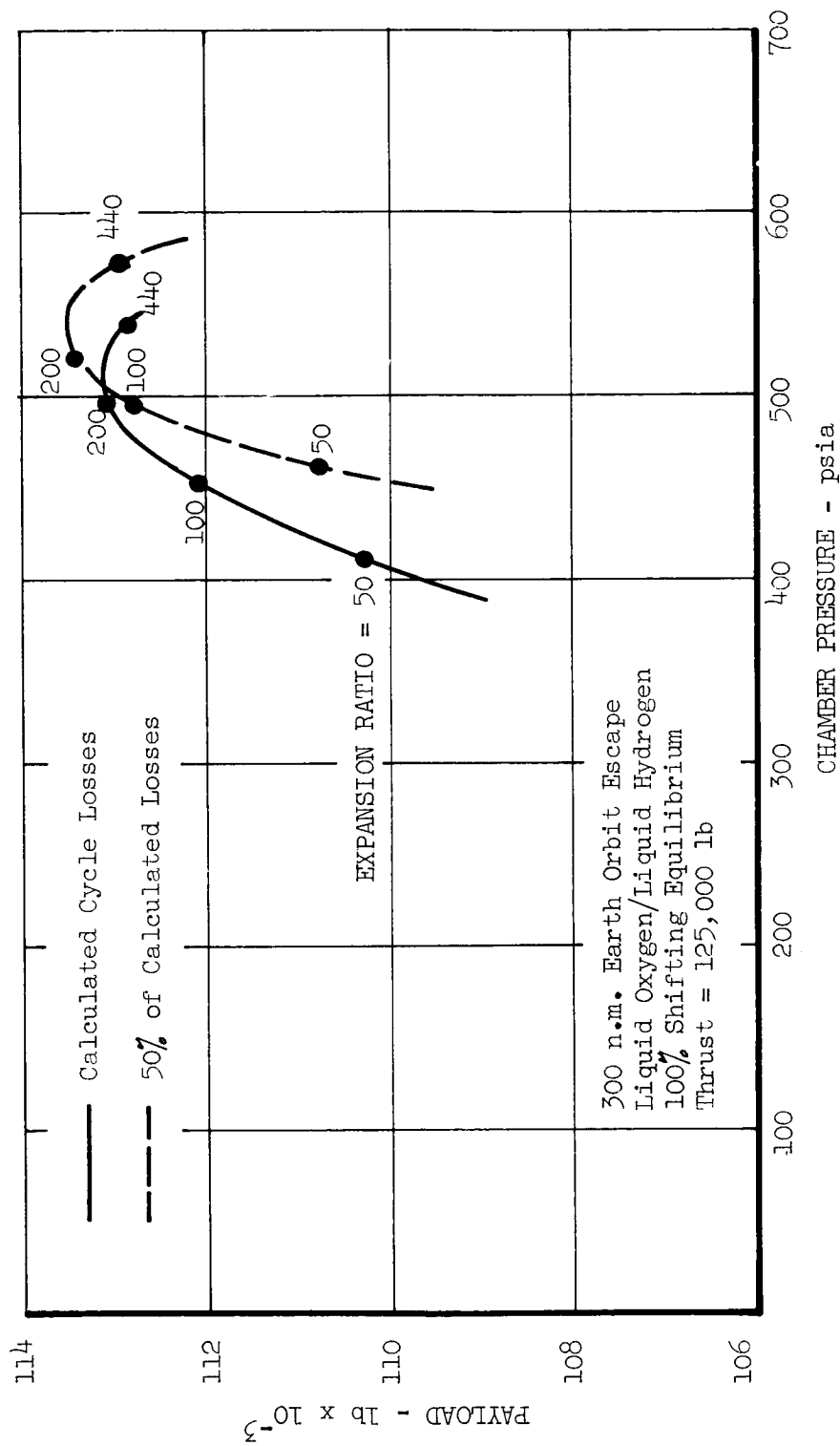


FIGURE 59. Effect of Cycle Losses on Selection of Engine Parameters

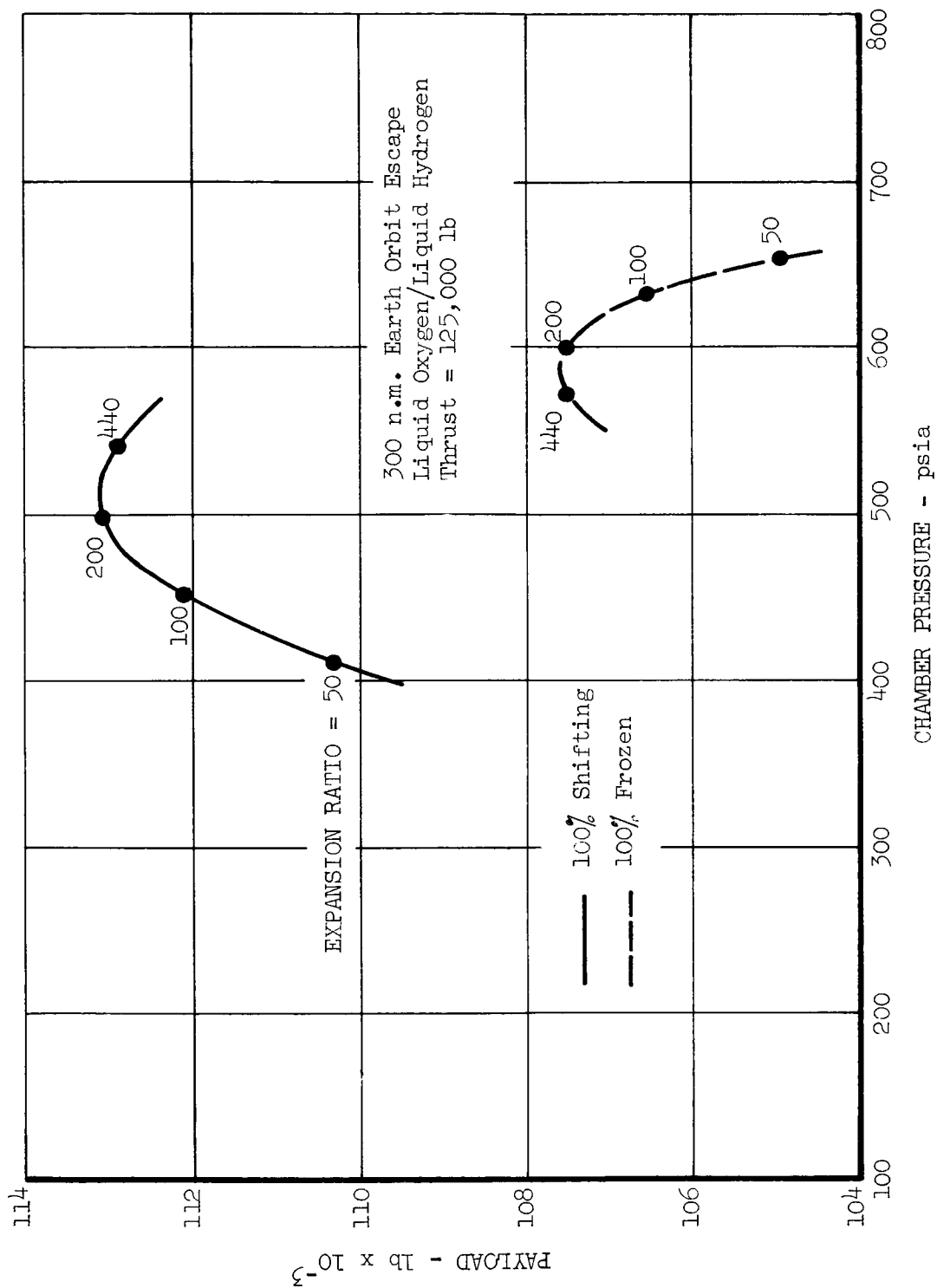


FIGURE 60. Effect of Equilibrium Performance on
Selection of Engine Parameters

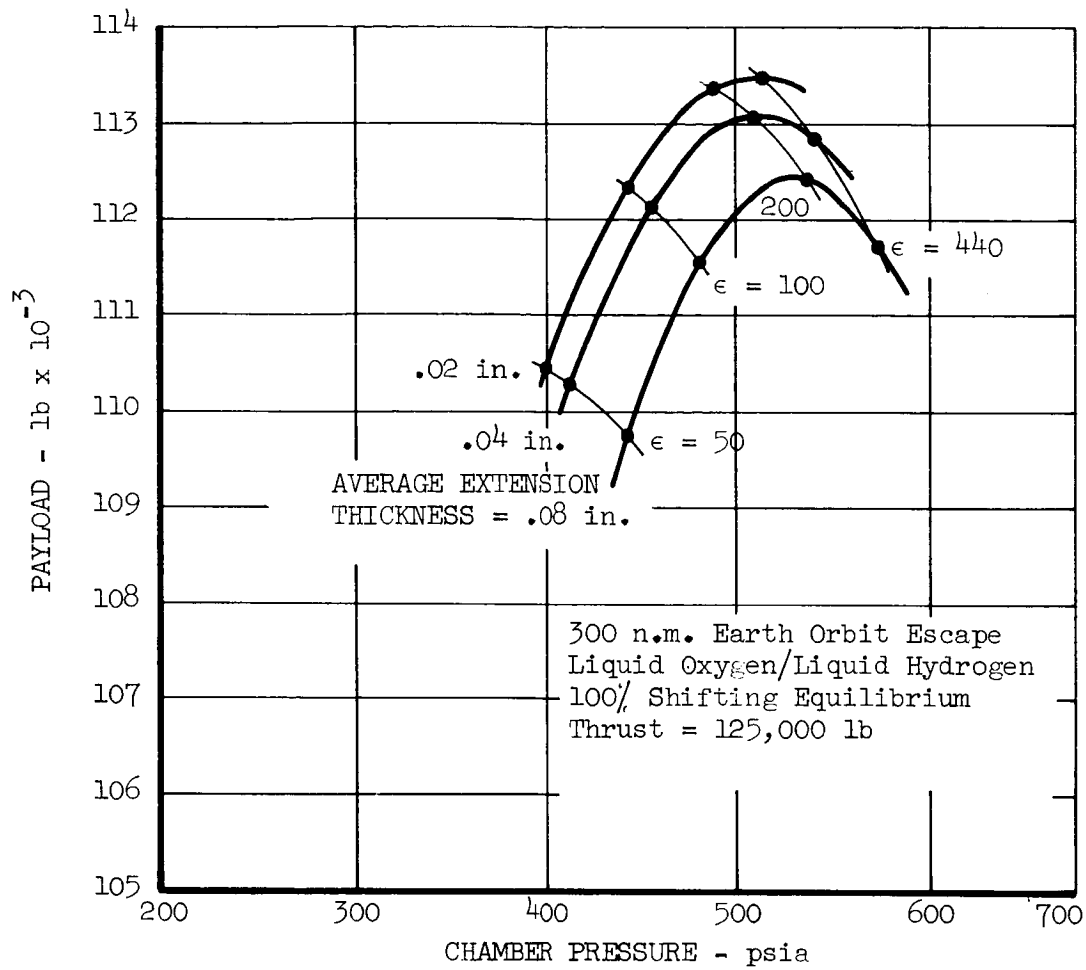


FIGURE 61. Effect of Nozzle Extension Thickness
Selection of Engine Parameters

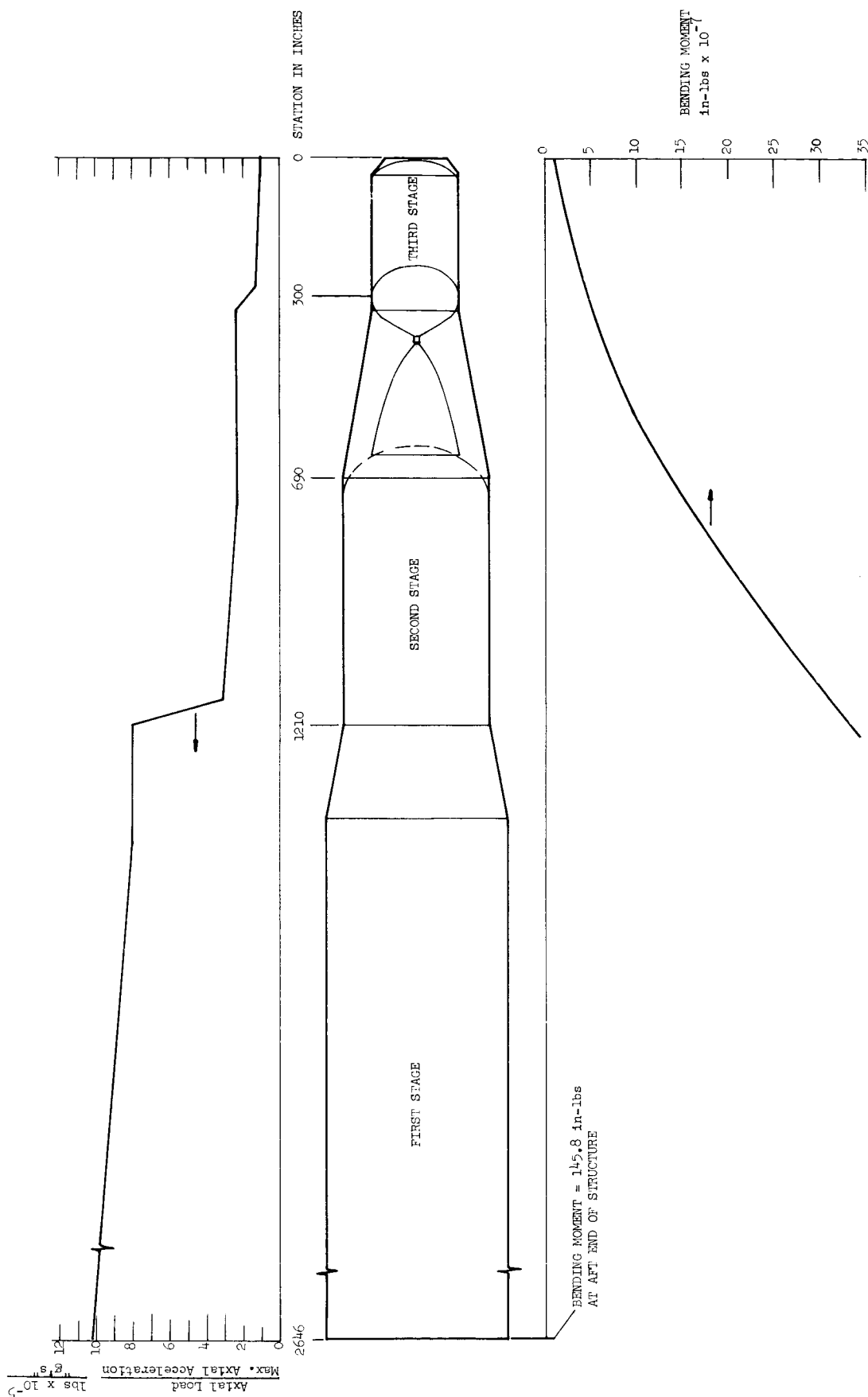


FIGURE 62. Conventional LO_2/LH_2 Vehicle

As the skirt gets heavier, the optimum engine gets smaller, i.e., P_c increases and ϵ decreases. However, the payload capability is not significantly different even where skirt thickness has been doubled from .04 to .08.

4.5.4 SELECTED ENGINE CONFIGURATION

The selected parameters and geometry for the conventional engine are listed below. The nozzle is regeneratively cooled to expansion ratio of 15:1.

Thrust	125,000 pounds
Chamber Pressure	520 psia
Expansion Ratio	220:1
Theor. Vac. Engine Impulse (Shifting)	479.8 sec.
Mixture Ratio	6.0

Losses - Percent

Drag	1.90
Geometry	.56
Cycle	1.30

Actual Engine Impulse	462.0 sec.
Nozzle Exit Radius	87 inches
Nozzle Length	260 inches

Total Engine Weight

Injector, Chamber, Regen. Cooled Nozzle Section, Radiation Cooled Nozzle Extension, Turbopump, Lines and Valves, Gas-Generator	1494 pounds
---	-------------

4.5.5 VEHICLE ANALYSIS

The vehicle structure was sized, stressed, and weighed according to the procedure outlined in the STRUCTURAL ANALYSIS section.

The tank diameters of both the second and third stages of the conventional vehicle were set by using zero length cylinders and 1.4:1 elliptical heads for the oxidizer tank. Resultant over-all tankage length to diameter (L/D) ratios for the two stages are 1.9 for the third stage and 2.1 for the second stage. Vehicle geometry is shown in Figure 62.

$$\text{Relative Payload Wt} = 240,000 - (W_{\text{eng}} + W_{\text{structure}} + W_{\text{prop}})_{3i} +$$

$$\frac{W_{\text{structure}_{1\text{conv}}} - W_{\text{structure}_{1i}}}{R_2 R_3} +$$

$$\frac{W_{\text{structure}_{2\text{conv}}} - W_{\text{structure}_{2i}}}{R_3}$$

where i denotes the vehicle being compared with the conventional vehicle.

The first and second stage structural weights are different for all of the vehicles due to change in bending moments caused by changes in the third stage configuration. These changes in bending moments can be seen in the bending moment diagrams presented for each of the evaluated vehicles.

Since this method was used throughout, the relative payload of the evaluated vehicles will be discussed in Section 4.11, "RELATIVE PERFORMANCE OF VEHICLE CONCEPTS."

4.6 CONVENTIONAL VEHICLE (HYDROGEN PEROXIDE/DIBORANE PROPELLANTS)

Propulsion analysis and vehicle structural weight calculations were also performed using the propellant combination of $\text{H}_2\text{O}_2/\text{B}_2\text{H}_6$ in the conventional vehicle configuration. The vehicle geometry and load diagrams are given in Figure 63.

4.6.1 ENGINE CONFIGURATION

Thrust	125,000 pounds
Chamber Pressure	525 psia
Expansion Ratio	220:1
Theor. Vac. Specific Impulse (Shifting)	
Mixture Ratio = 1.83	433 sec
Losses - percent	
Drag 1.80	
Geometry .60	
Cycle 1.00	
Actual Engine Impulse	419 sec
Nozzle Exit Radius	88 inches

The shear and bending moment diagrams presented in Figure 62 were used to size structural elements of the vehicle. A weight breakdown of the tankage and structure is given in the following table.

Conventional Vehicle Weight Breakdown (Weight in Pounds)

Third Stage

Fwd Structure	434
Pressurization System	1183
Fuel Tank	
Fwd. Head Skirt	464
Fwd. Head	216
Skin	882
Frames	203
Stringers	1365
Oxidizer Tank	
Fwd. Head Skirt	495
Fwd. Closure	239
Aft Closure	292
Aft Head Skirt	680
Engine Mount	200
Insulation	355
Interstage Structure	6830

4.5.6 VEHICLE PAYLOAD

Relative payload of the evaluated vehicles was obtained by using the conventional vehicle as a reference. Payload weight of the third stage of each configuration was calculated using third stage gross weight of 240,000 pounds, and subtracting from this propellant weight and the inert weights of the third stage propulsion and structure. Then, using the conventional vehicle first and second stage weights as a reference, delta inert weights of the first and second stages were divided by the appropriate stage mass ratios (R) and subtracted from the third stage payload weight.

This can be expressed in equation form as:

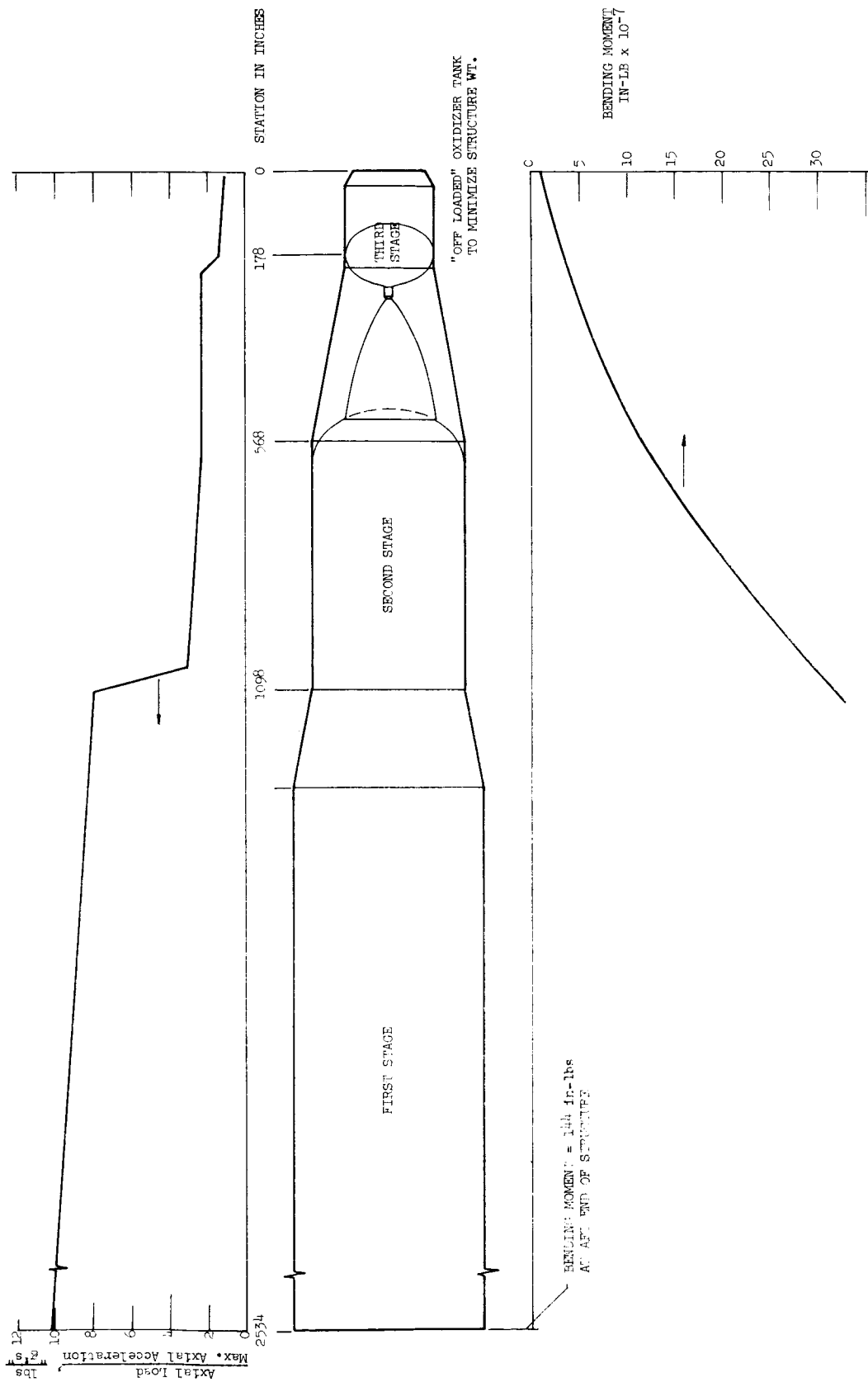


FIGURE 33. Conventional H_2O_2/B_2H_6 Vehicle

Nozzle Length	246 inches
Total Engine Weight	
Injector, Chamber, Regen. cooled	
Nozzle Section, Radiation cooled	
Nozzle Extension, Turbopump	
Lines and Valves, Gas-Generator	1516 pounds

4.6.2 CONVENTIONAL VEHICLE WEIGHT BREAKDOWN (WEIGHT IN POUNDS)

Third Stage

Fwd. Structure	363
Pressurization System	600
Fuel Tank	
Fwd. Head Skirt	448
Fwd. Head	208
Skin	483
Frames	60
Stringers	355
Oxidizer Tank	
Fwd. Head Skirt	327
Fwd. Closure	233
Aft Closure	273
Aft Head Skirt	582
Engine Mount	200
Insulation	180
Interstage Structure	5900

4.7 INTEGRATED NOZZLE/TANKHEAD VEHICLE (LIQUID OXYGEN/LIQUID HYDROGEN PROPELLANT)

4.7.1 GENERAL DESCRIPTION

This vehicle has a large forced-deflection nozzle integrated with the tankhead of the stage below. When separating, the tank is vented, the nozzle separated from the tank by a peripheral-shaped charge, and the interstage, which is in two halves, is blown free of the nozzle. A sketch of the separation is shown in Figure 64. Both free-standing and pressure-stabilized designs were completed for this configuration; the free-standing structure resulted in a higher payload capability for the integrated vehicle.

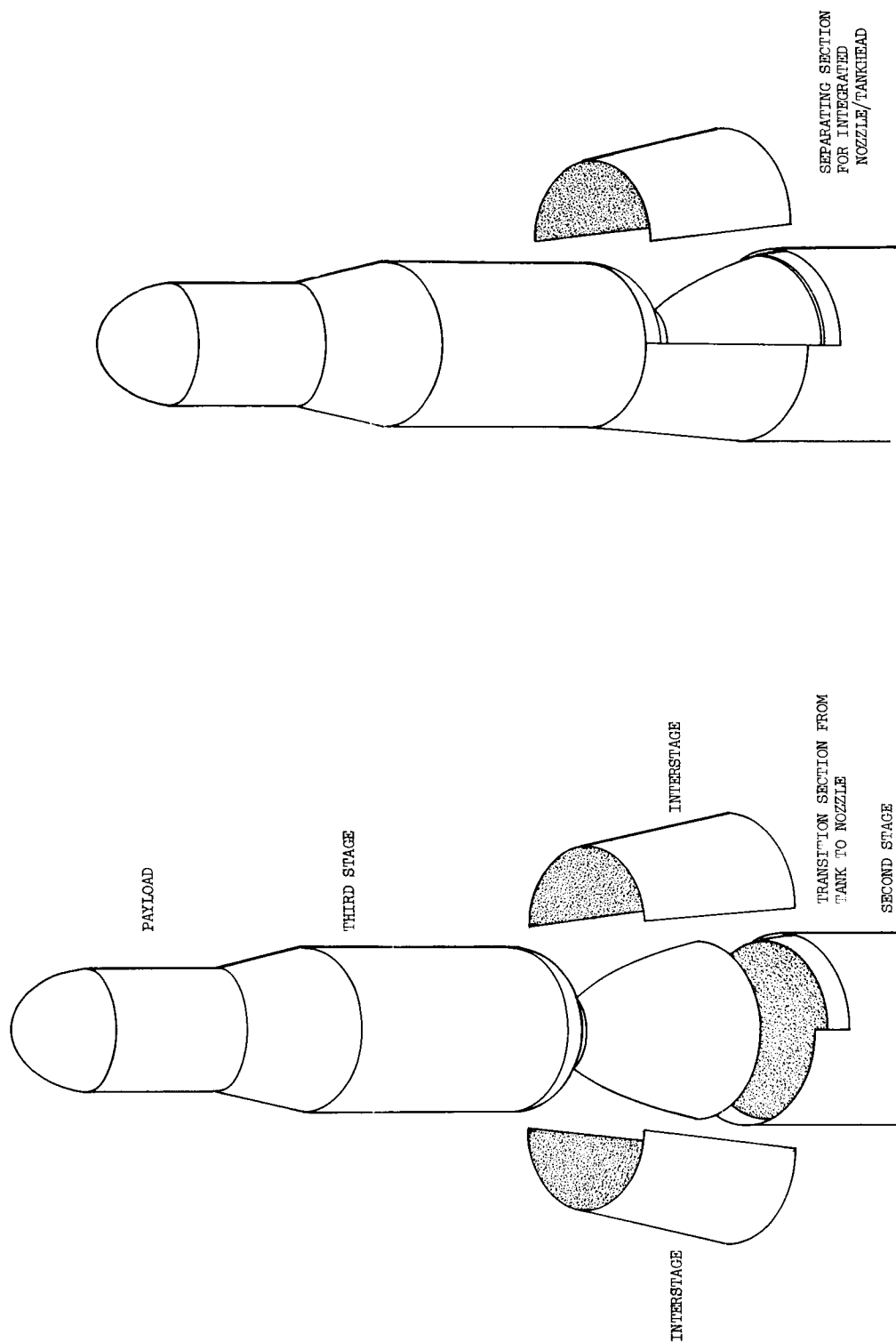


FIGURE 64. Separation Technique for the Integrated Vehicle

In conventional vehicle design, the propulsion system can be optimized relatively independently of the vehicle structure except for nozzle length-inter-stage considerations. When the nozzle and tank are integrated either the optimum nozzle geometry sets the tank geometry or the optimum tank geometry sets the nozzle geometry. In the practical case, some compromise would have to be reached between propulsion efficiency of the third stage and inert weight of the second stage for the vehicle configuration considered here.

4.7.2 PROPULSION AND VEHICLE ANALYSIS

Initially, the third stage propulsion system was optimized by assuming (1) nozzle geometry was not restricted by the stage below, (2) that the only structural weight penalty incurred in the second stage was interstage weight, (3) tank pressure dictated the nozzle thickness (.065 in.), and (4) thrust was 125,000 pounds - the value which had been found to be optimum for the conventional vehicle. Results of this study (Figure 65) indicated that optimum engine parameters were $P_c = 500$ psia and $\epsilon = 200$.

Nozzle exit radius was 100 inches for the optimum point. A second stage vehicle having a diameter of 244 inches was designed for this nozzle configuration. Comparison of the second stage structural weights of this vehicle with the structural weights of the second stage of the conventional vehicle indicate that this tankage geometry is far from optimum (7300 pounds weight difference). Therefore, another second stage was designed having the same diameter as the conventional second stage (320 inches).

Geometry and load diagrams of this configuration are given in Figure 66. The moments are much smaller than for the 244 inch stage due to the decreased lengths and the total structural weight is 10,800 pounds lighter than the 244 inch diameter stage. Structural details are shown in Figure 67.

4.7.3 ENGINE CONFIGURATION

Thrust	125,000 pounds
Chamber Pressure	500 psia
Expansion Ratio	440:1
Theor. Vac. Specific Impulse (Shifting)	485.7 sec
Mixture Ratio = 6.0	
Losses - percent	
Drag	2.15
Geometry	.50
SGC 206 FR-1 Cycle	1.10

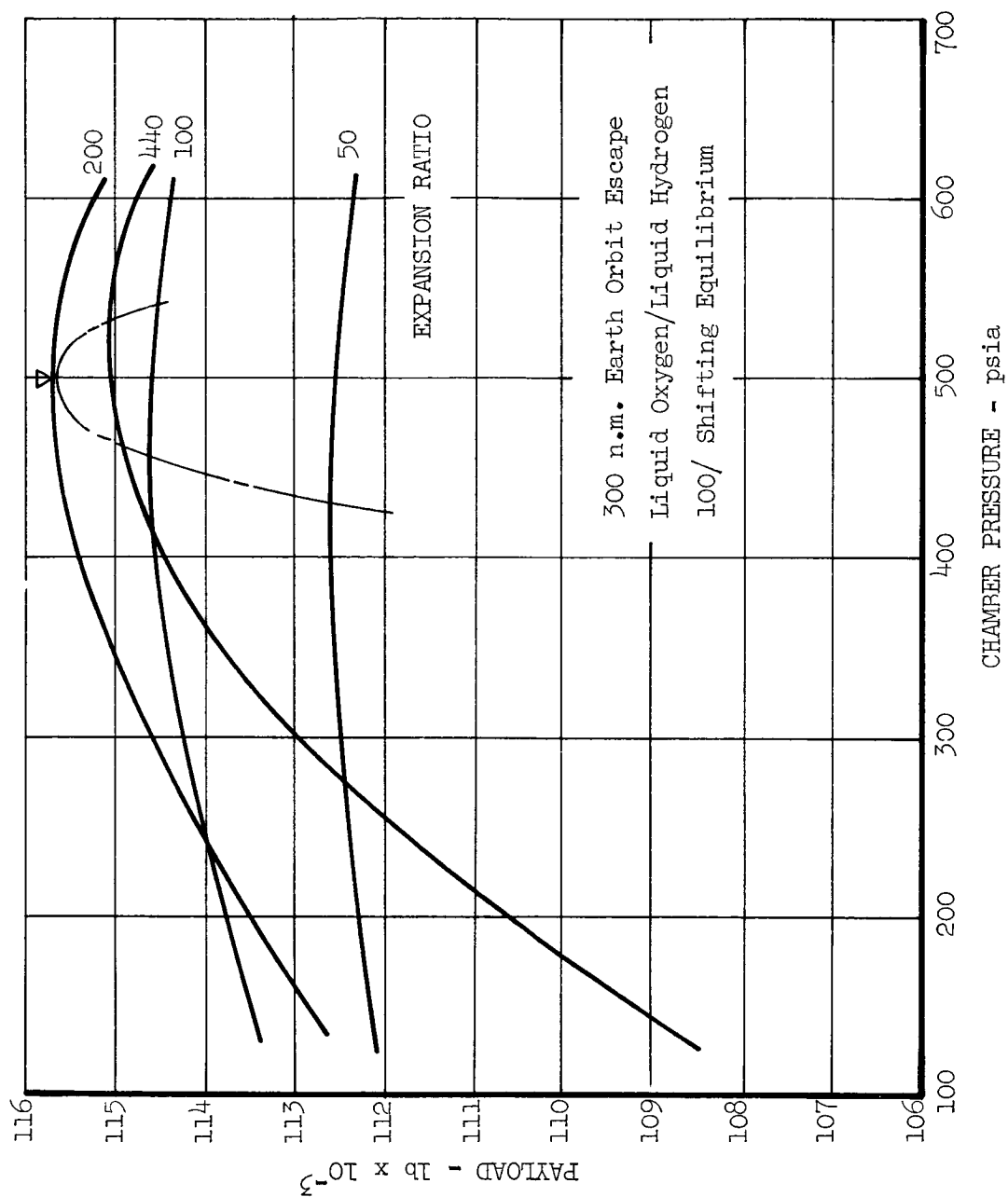


FIGURE 65. Effect of Forced-Deflection Engine Parameters on Payload Performance

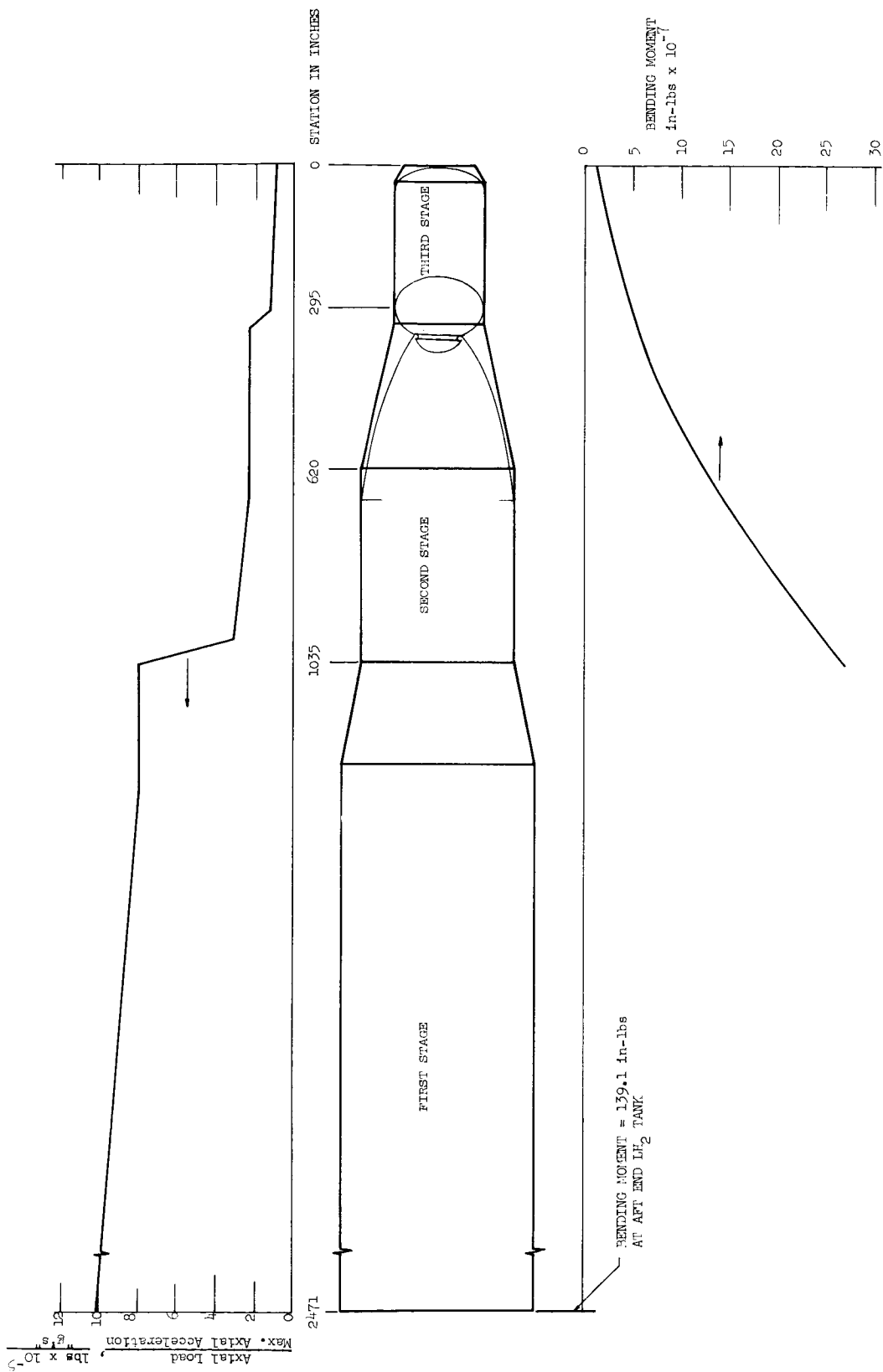
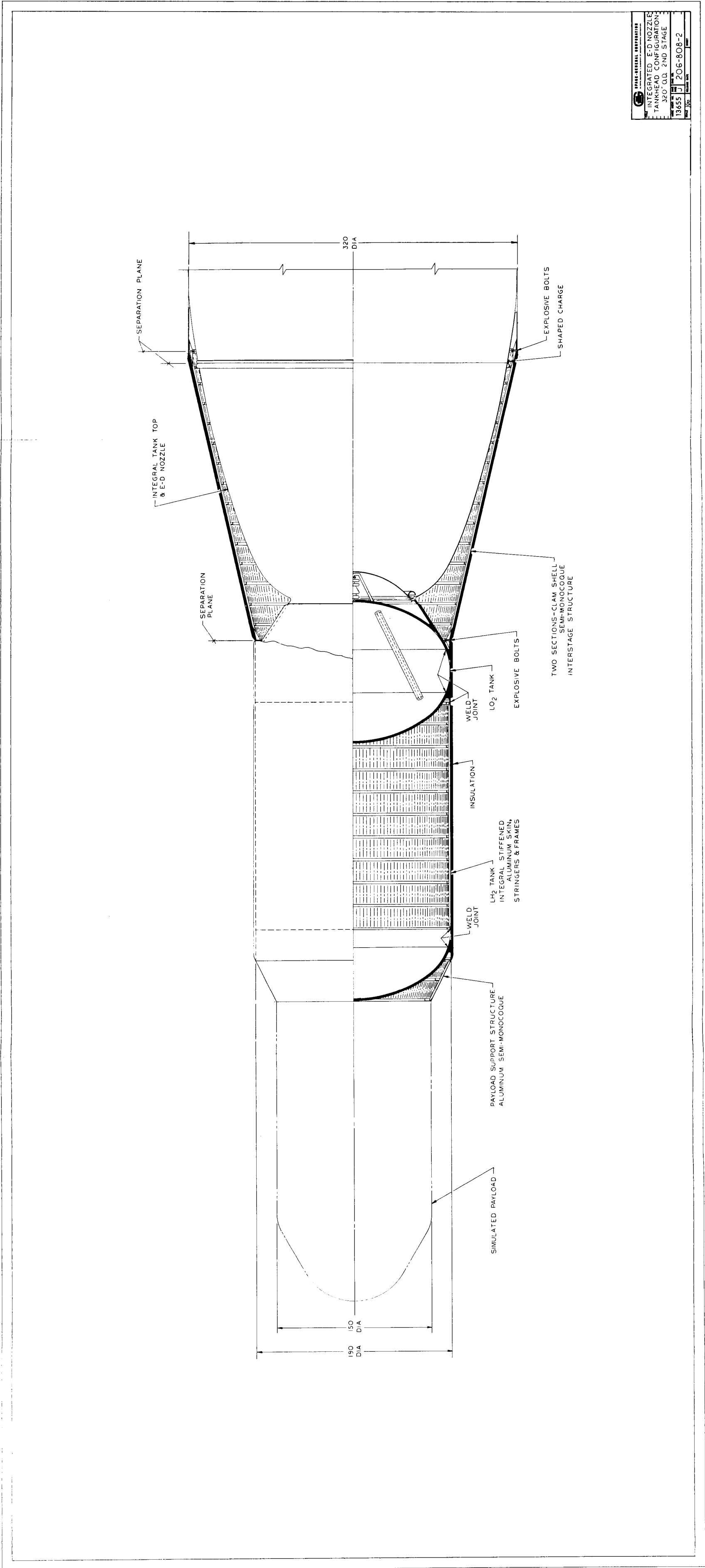


FIGURE 66. Integrated LO₂/LH₂ Vehicle



Actual Specific Impulse	468.0 sec
Base Radius to Lip	75 inches
Nozzle Exit Radius	150 inches
Nozzle Length	244 inches
Engine Weight	
Injector, Chamber, Regen. cooled nozzle section, Radiation cooled nozzle/tankhead extension, Turbo- pump, lines and valves, Gas- generator, Centerbody	3346 pounds
(the nozzle/tankhead weight is 2200 pounds)	

4.7.4 INTEGRATED VEHICLE WEIGHT BREAKDOWN (WEIGHT IN POUNDS)

Third Stage

Fwd. Structure	434
Pressurization System	1170
Fuel Tank	
Fwd. Head Skirt	464
Fwd. Head	201
Skin	824
Frames	190
Stringers	1275
Oxidizer Tank	
Fwd. Head Skirt	487
Fwd. Closure	235
Aft Closure	287
Aft Head Skirt	673
Engine Mount	500
Insulation	351
Interstage Structure	5930

4.7.5 PRESSURIZED TANKAGE DESIGN

Since the integrated nozzle/tankhead may dictate the use of titanium in the second stage, the possibility of using pressure-stabilized second stage tankage was investigated to take advantage of the high tensile strength/density

ratio of the material. Tank pressure was increased until the internal load was equal to the total external load due to bending and axial compression; i.e.,

$$\frac{PR}{2} = \frac{M}{\pi R^2} + \frac{P}{2 \pi R}$$

where P = tank pressure

M = ult. bending moment

π = ult. axial load

The study showed that although there is a savings in second stage weight under the pressure stabilized condition, the increase in nozzle/bulkhead weight (due to the increased tank pressure from 30 psia to 90 psia), which is carried along with the third stage, results in a net loss in payload. Therefore, relative payload of the integrated configuration was compared using structurally stabilized tankage.

4.7.6 RELATIVE PAYLOAD

Relative payload of this configuration is discussed in Section 4.11.

4.8 SMALL NOZZLE ENGINE CONCEPT (LIQUID OXYGEN/LIQUID HYDROGEN PROPELLANTS)

Early efforts on the small nozzle, or small throat, engine concept are summarized in the Section, Vehicle Conceptual Study. Although the original concept of integrating many very small nozzles with tankage or structure was not competitive with the conventional vehicle from the performance standpoint, the concept does appear competitive in large annular two-dimensional nozzles. This concept makes use of very narrow throat widths which would probably be impractical with ablative or regenerative cooling methods. Since nozzle length is a function of throat width, the small nozzle concept permits large area ratios with minimum interstage length and weight.

The geometrical configuration of this engine concept is presented in Figure 68. It has a central turbopump with dual discharges on both the oxidizer and fuel pumps which feed a toroidal distribution manifold. Eight sets of propellant lines come from this manifold to uncooled chambers and manifolds which feed the two-dimensional forced deflection nozzle.

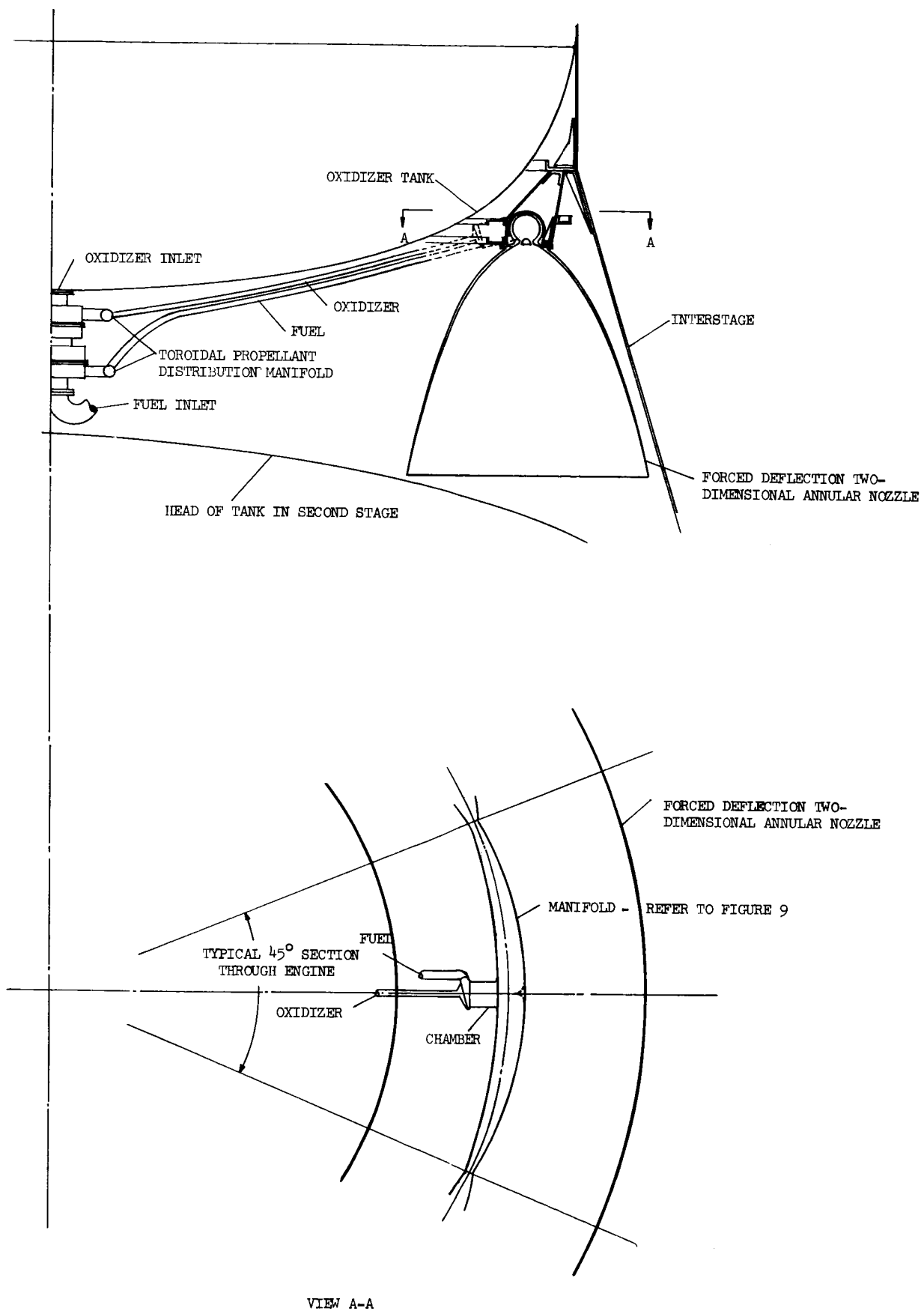


FIGURE 68. Small Nozzle Concept - Geometry of Engine System

4.8.1 PROPULSION ANALYSIS

Frictional drag in the two-dimensional forced deflection nozzle is shown in Figure 69. Conical and bell nozzle drag is also shown in Figure 69 for comparison with the two-dimensional nozzle. However, simply showing expansion ratio and throat width does not really present an equitable comparison between the nozzle types due to the fact that nozzle length has not been taken into account. It can be shown that the ratio of throat width of a two-dimensional 15° half-angle wedge nozzle to the throat radius of a 15° three-dimensional nozzle is

$$\frac{W_{th\ 15^\circ}}{R_{th\ 15^\circ}} = \frac{L_{2-d\ 15^\circ}}{L_{3-d\ 15^\circ} (\sqrt{\epsilon + 1})}$$

Figure 70 shows that two-dimensional forced-deflection nozzle length is about 50 percent of 15° wedge nozzle length for the same thrust coefficient efficiency. Conventional bell nozzles are approximately 70 percent of 15° conical nozzle length at this same expansion ratio and efficiency. Therefore, the ratio of two-dimensional forced-deflection throat width to bell throat radius is

$$\frac{W_{th\ f-d}}{R_{th\ bell}} = \frac{.70}{.50} \frac{1}{(\sqrt{\epsilon + 1})} \quad \text{for equal nozzle lengths}$$

$$\frac{1.4}{(\sqrt{\epsilon + 1})} \left(\frac{L_{f-d}}{L_{bell}} \right) \quad \text{for arbitrary ratio of nozzle lengths}$$

It is now possible to compare drag for the two nozzle types at, for example, $\epsilon = 200$, and with the two-dimensional nozzle length 30 percent as long as the bell. Arbitrarily choosing the bell throat radius as 5 inches, the throat width of the two-dimensional nozzle for this case becomes 0.139 inches. Thus drag (from Figure 69) is 2.4 percent for the conical nozzle and 2.9 percent for the two-dimensional nozzle. For a rough estimate as to the interstage weight trade-off with impulse loss due to the difference in drag, assume that; ΔV is 10,000 ft per sec, nominal stage burnout weight is 120,000 lb, bell nozzle specific impulse is 460 sec, and interstage weighs 20 lb per inch. Then the change in burnout weight due to impulse change is,

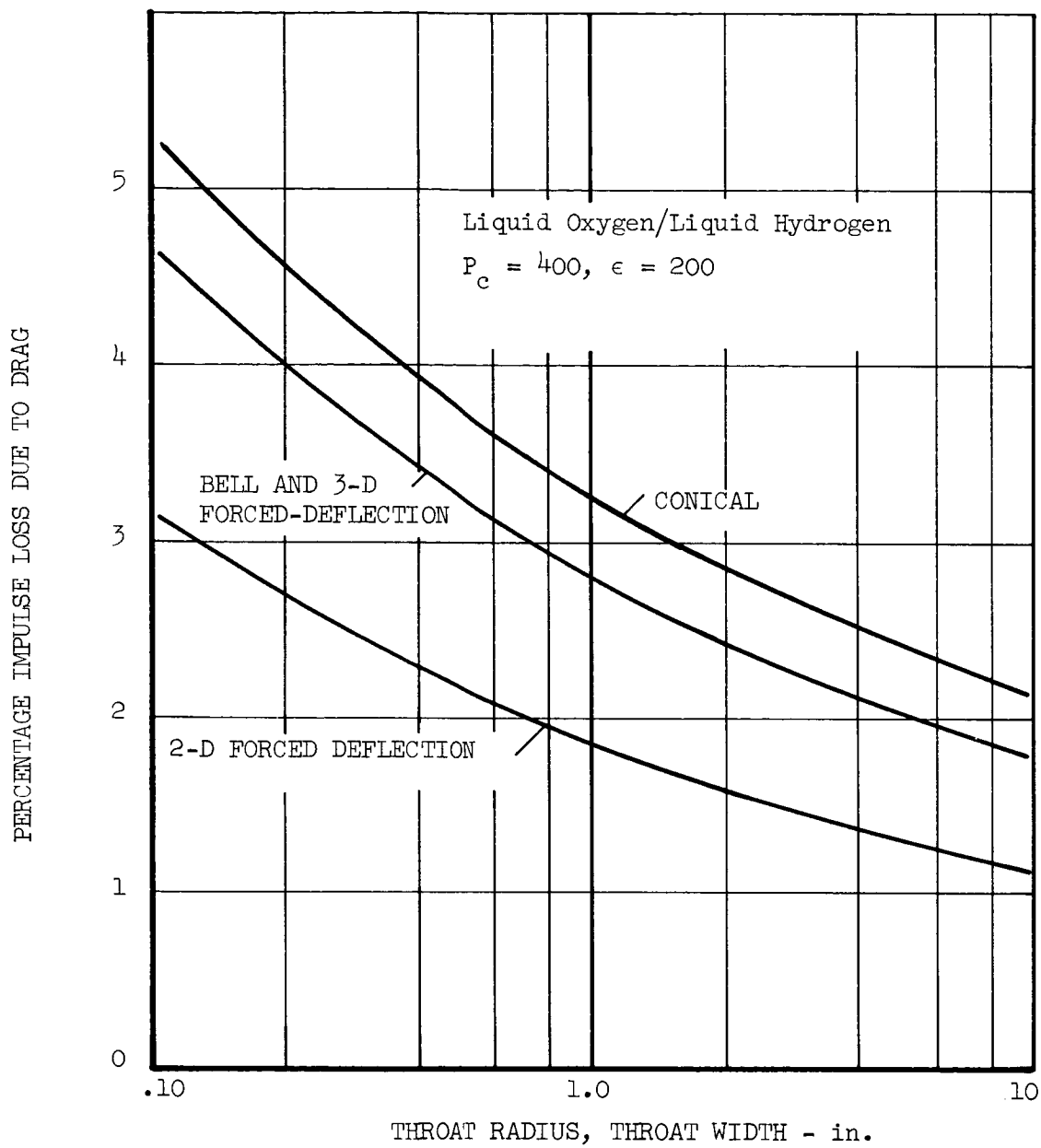


FIGURE 69. Nozzle Frictional Drag Losses

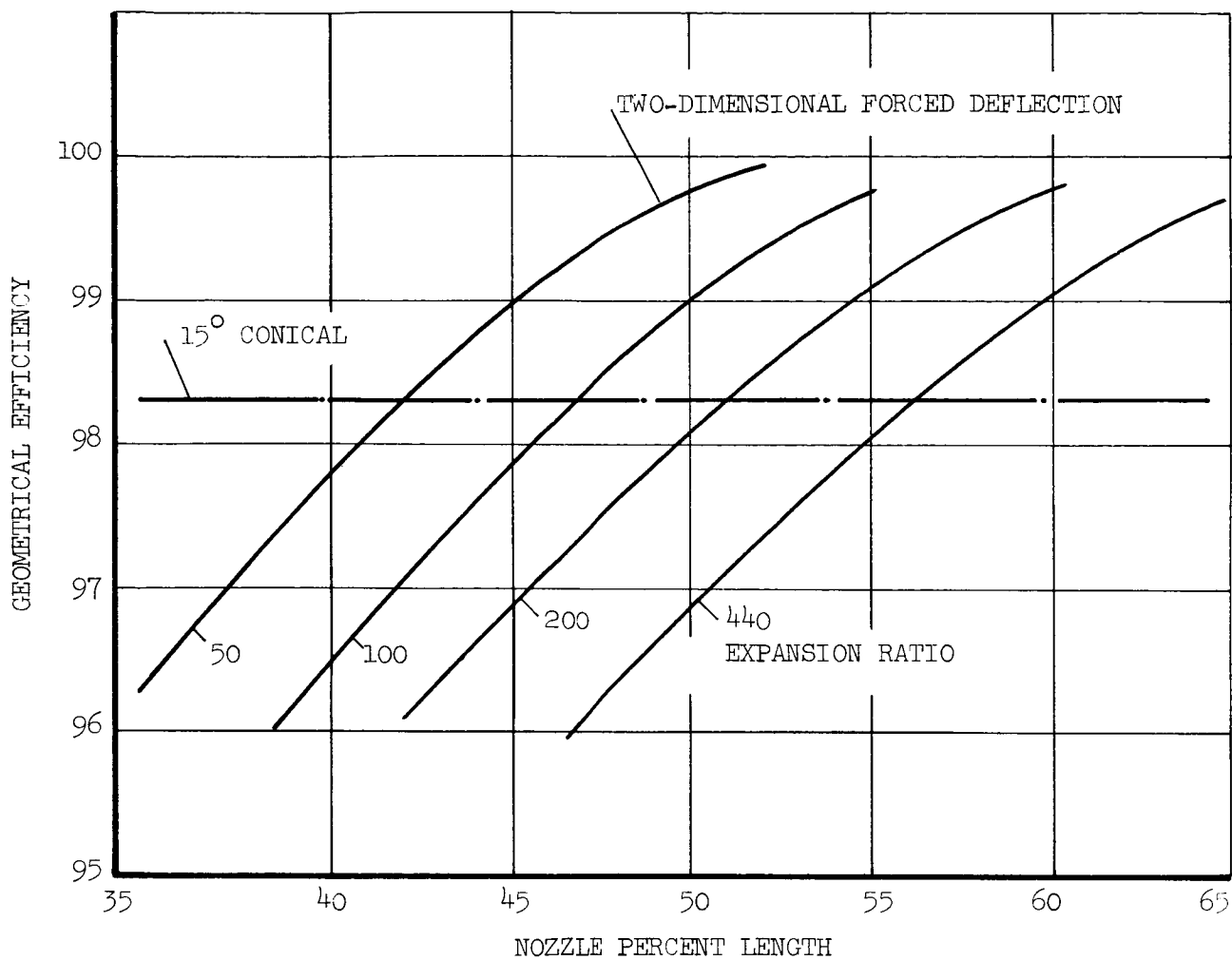


FIGURE 70. Effect of Percent Length on Efficiency of F-D Nozzle

$$\Delta W_{bo_impulse} = \frac{W_{bo} \Delta V}{g I_s} \Delta I_s = \frac{120,000 \times 10,000}{32.2 \times 460 \times 460} \times$$

$$(.005 \times 46) = 406 \text{ lb.}$$

The bell nozzle length is

$$L = \frac{r_{th} (\sqrt{\epsilon - 1})}{.268} (.7) = \frac{5 (\sqrt{200 - 1})}{.268} (.7) = 172 \text{ inches}$$

and the two-dimensional nozzle length is $.30 \times 172 = 52$ inches. Thus, the difference in interstage length is 120 inches, and difference in interstage weight will be 2400 pounds. This interstage is jettisoned with the stage below so it must be divided by the mass ratio of the stage we are considering to convert it to equivalent burnout weight, i.e.,

$$\Delta W_{bo_interstage} = \frac{2400}{\left(\frac{\Delta V}{g I_s}\right)_e} = \frac{2400}{1.96} = 1220 \text{ pounds}$$

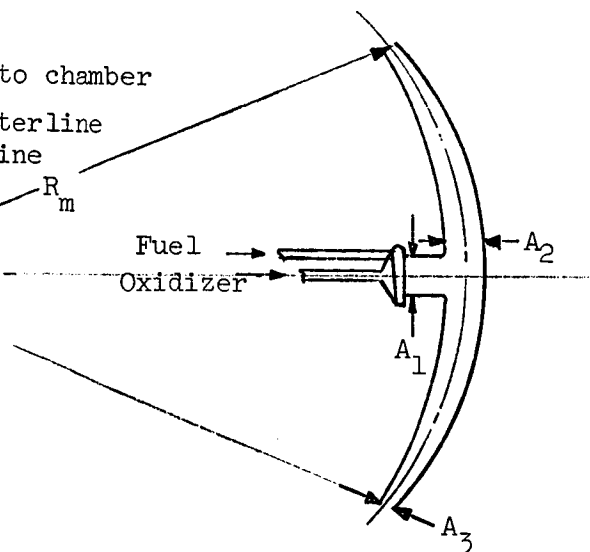
Or for this simplified example, the change in nozzle configuration appears to have given us an increase in burnout weight of about 814 pounds. The reduction in interstage length will also reduce the bending moments in the preceding stages and favorably affect the fabrication, transportation, and operational characteristics of the vehicle.

However, other factors such as weight of this new engine configuration, reduced stage weights due to reduced bending moments, and propellant weight changes imposed by fuel cooling requirements must be taken into account.

4.8.2 CHAMBER AND MANIFOLD SIZING

The geometrical configuration of the individual chamber and manifolds is shown in the sketch below. The required flow areas and Mach Number, in the chamber and manifold were established from a study of existing chamber contraction ratios, and existing axial turbine manifolds.

- A_1 = chamber area
 A_2 = manifold area adjacent to chamber
 R_m = radius from vehicle centerline to the manifold centerline
 A_{th} = required throat area at the given chamber pressure, thrust, and thrust coefficient



It was found from studying the geometry of existing rocket chambers that a flow Mach Number of .30 to .50 would exist adjacent to the injector if uniform axial flow could be assumed at that section (actually it is more reasonable to speak of injector to throat contraction ratio). For ratio of specific heats of 1.23 and Mach Number of .35 the ratio of injector to throat area is approximately 1.8. Then the chamber area becomes

$$A_1 = 1.8 A_{th} = 1.8 \frac{F}{P_c C_F N} \approx \frac{F}{P_c N}$$

where N = number of chambers

F = total engine thrust

C_F = thrust coefficient

P_c = chamber pressure

A check of the Injection Density, $\frac{\text{Injector Area}}{\text{Weight flow rate}}$, for this injector area gives

$$\frac{A_{inj}}{\dot{w}} = \frac{A_1}{\dot{w}} = \frac{\frac{F}{P_c N}}{\frac{F}{I_s N}} = \frac{I_s}{P_c} \approx \begin{cases} \frac{450}{500} = .9 \\ \frac{450}{200} = 2.25 \end{cases}$$

Injectors for both high energy cryogenics and storables have successfully operated within the range of A_{inj}/w of 1 to 4, therefore this chamber sizing criterion should afford good combustion performance.

Considering the flow in the hot gas manifold to be similar to that in axial turbine manifolds, low total pressure losses should be achieved at Mach numbers in the manifold of .25 to .35. Therefore, a Mach number of .35 was selected for sizing the manifold flow areas. The area, A_2 , then is equal to one-half of A_1 and diminishes to some minimum cross-sectional area A_3 at the ends of the manifold.

4.8.3 STRESS ANALYSIS

The chambers and manifolds of the small nozzle engine operate at a wall temperature of 4000°F , therefore requiring a material which has adequate strength at this temperature. A review of current high temperature metal data was conducted and the most promising metal turned out to be tungsten. Strength characteristics are given in Figure 71. To date no erosion resistant surface coating is available for tungsten at 4000°F . Therefore, in the structural analysis of the high temperature components of the uncooled engine, tungsten properties from Figure 71 were used as being representative of state-of-the-art material technology, but with a hypothetical surface coating to resist erosion. The effect of state-of-the-art increases in material strength properties on weight of the uncooled engine was investigated to indicate potential advantages of the concept.

Two methods of transferring thrust loads from the skirt to the thrust structure were studied. In the first method the thrust loads are taken from the skirt through the hot gas manifold to the thrust structure; the thrust is taken directly from the skirt to the thrust structure in the second method. The stress analysis for the two methods is outlined in the following paragraphs.

I. THRUST TAKEN THROUGH MANIFOLD

The stress model and free body diagrams are given in Figure 72.

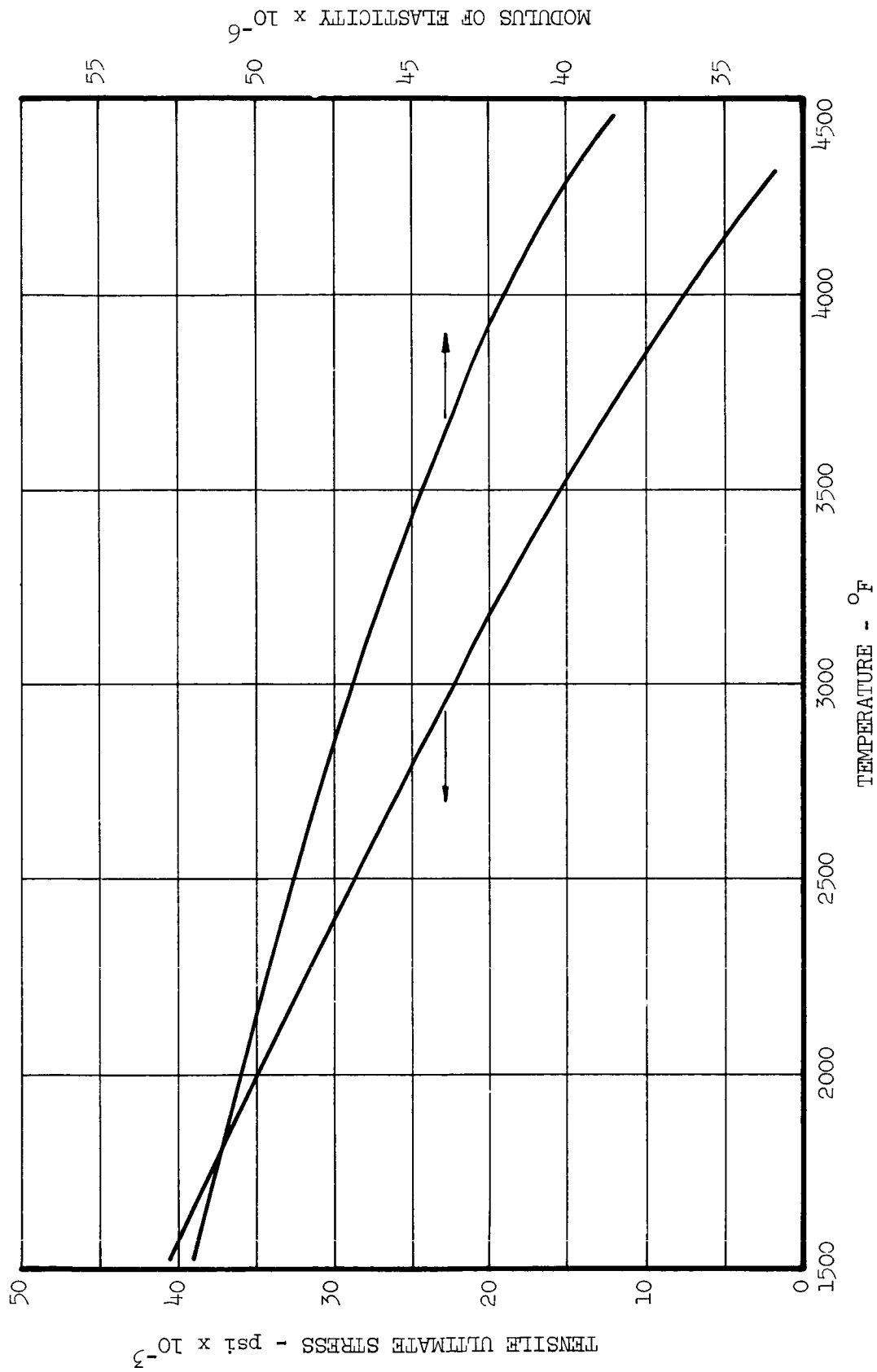
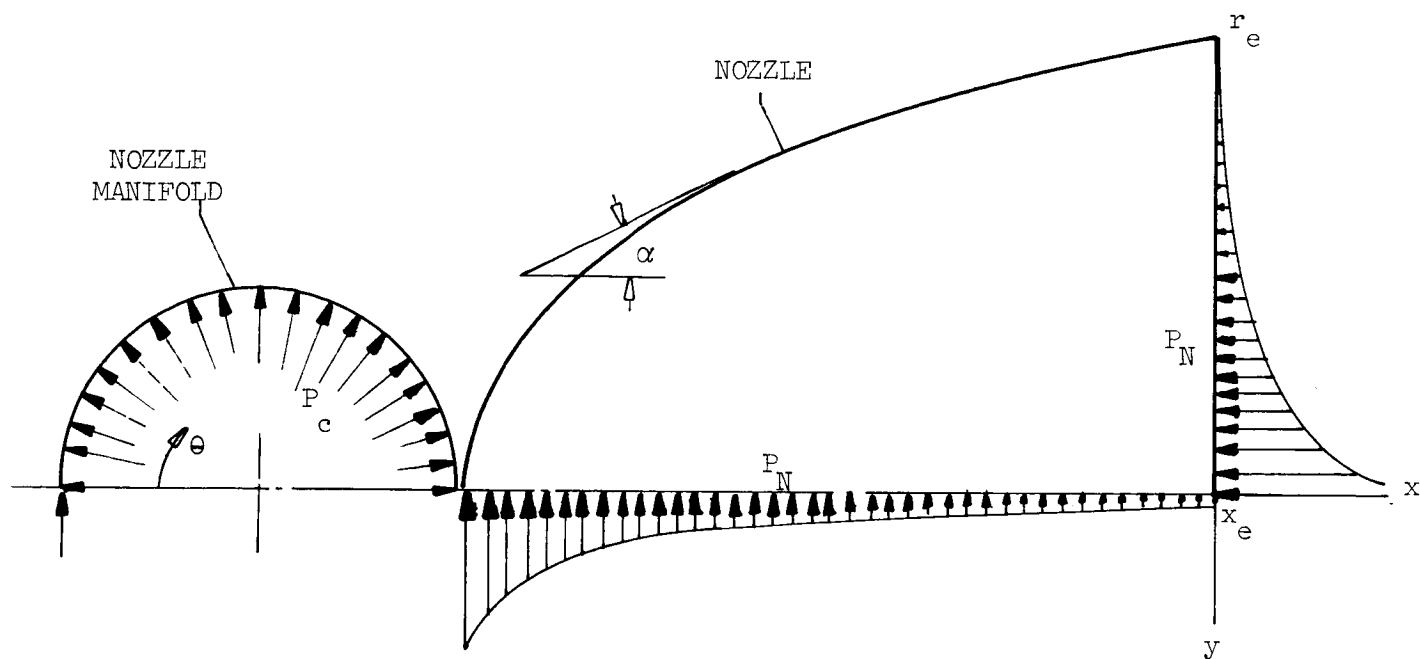
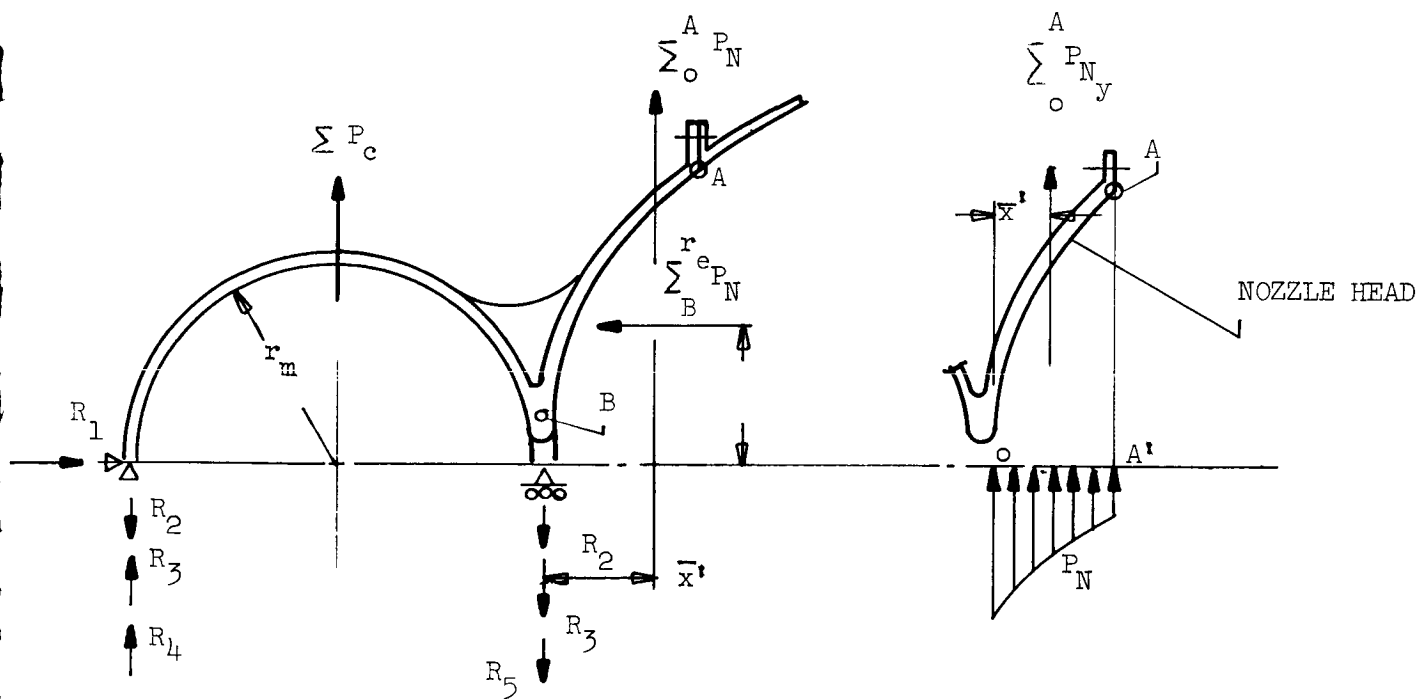


FIGURE 71. Strength Properties of Manifold Material



STRESS MODEL



FREE BODY DIAGRAM

FIGURE 72. Stress Model and Free Body Diagrams for for Manifold Configuration 2

$$R_1 = \int_0^r e P_N dy = \frac{1}{2} \quad (\text{thrust/inch of manifold})$$

$$R_2 = \frac{1}{2} \int_0^\pi P_c \sin \theta r_m d\theta = P_c r_m \quad (\text{tensile force in manifold})$$

$$R_3 = \frac{\sum_0^r e P_N \bar{y}}{2 r_m} \quad (\text{reaction from moment due to thrust})$$

$$R_4 = \frac{\bar{x}' \sum_0^{A'} P_N}{2 r_m} \quad \text{where } \bar{y} = \frac{\int_0^r e P_N y dy}{\sum_0^r e P_N}$$

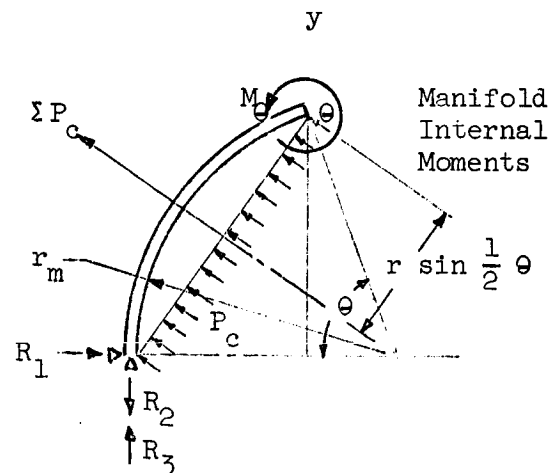
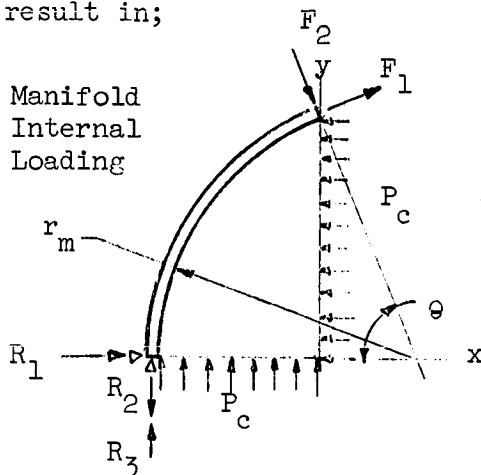
$$R_5 = \sum_0^{A'} P_N \left(1 + \frac{\bar{x}'}{2 r_m} \right)$$

It was assumed that $\sum P_{Ny}$ is reacted by hoop tension in the nozzle skirt, therefore

$$R_4 = R_5 = 0.$$

(1) Manifold Design

From the manifold internal loading shown below, the summation of forces in x and y directions and the summation of moments at a given section result in;



$$F_1 = P_c r_m - R_3 \cos \theta - R_1 \sin \theta$$

$$M_\theta = r_m [R_1 \sin \theta - R_3 (1 - \cos \theta)]$$

Since the ring has an elastic resistance to bending, a redundant moment must also be taken into account which is

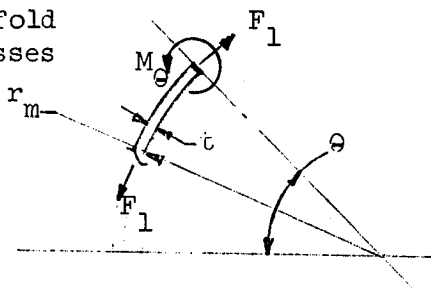
$$M_o = R_2 - \frac{2 R_1}{\pi}$$

Therefore the total moment is $M_\theta + M_o = M_T$.

The bending and tensile stresses due to M_T and F_1 (using the moment of inertia

$I = \frac{t^3}{12}$) are:

Manifold
Stresses



$$f_B = \frac{1}{t} \left\{ \frac{6 r_m}{t^2} [R_1 \sin \theta - R_3 (1 - \cos \theta)] + \frac{R_3}{r_m} - \frac{2 R_1}{\pi r_m} \right\}$$

$$f_T = \frac{1}{t} (P_c r_m - R_3 \cos \theta - R_1 \sin \theta)$$

and for combined bending and tension

$$R_B + R_T = 1$$

$$\frac{f_B}{F_B} + \frac{f_T}{F_T} = 1 \text{ where } F_B + F_T = F = \text{Design stress}$$

The manifold thickness can now be shown to be

$$t = \frac{B + \sqrt{B^2 + 24 r_m A F}}{2F}$$

$$\text{where } A = R_1 \sin \theta - R_3 (1 - \cos \theta) + \frac{R_3}{r_m} - \frac{2 R_1}{\pi r_m}$$

Summation of forces in the x direction gives,

$$F_7 = \frac{\int_A^r e P_N dy + \int_y^A P_N dy}{\cos x} = \frac{e}{\cos \alpha}$$

Summation of moments gives,

$$M_7 = \int_A^r e P_N dy (y_A - y) + \int_y^A P_N y dy + \int_x^{A'} P_N x dx = M$$

For combined compression and bending,

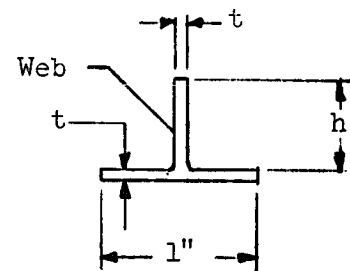
$$R_B + R_C = 1$$

$$\frac{A}{t \cos \alpha F} + \frac{\pm 6 M}{t^2 F} = 1$$

$$t = \frac{A \pm \sqrt{A^2 \pm 24 \cos^2 \alpha FM}}{2 \cos \alpha F} \quad \text{with no web}$$

If the thickness, t, becomes excessive a web of thickness t and height h can be used in which case

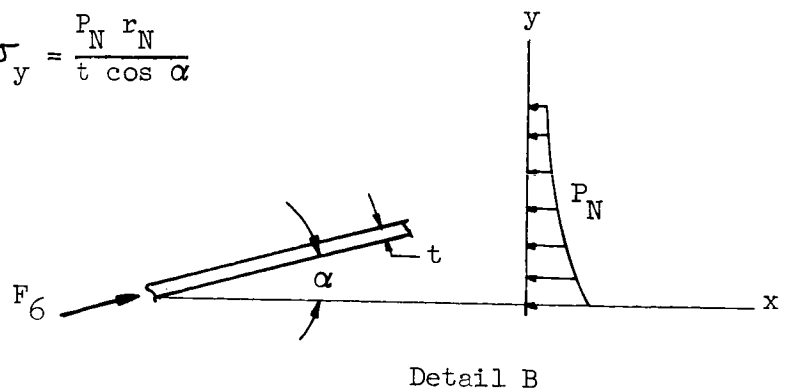
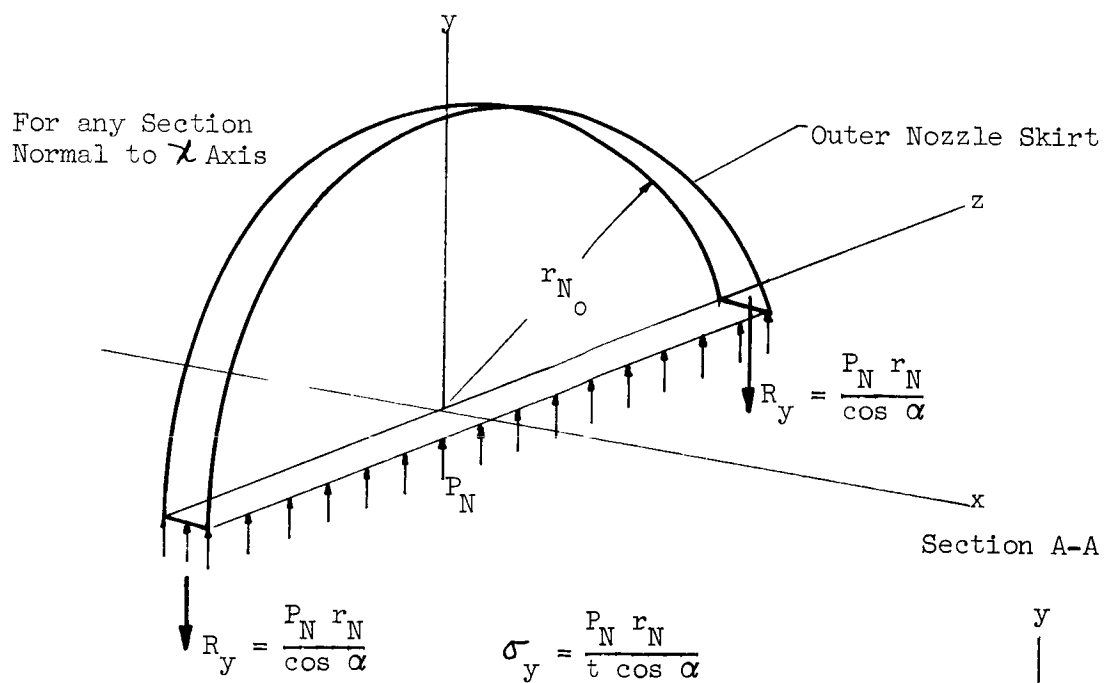
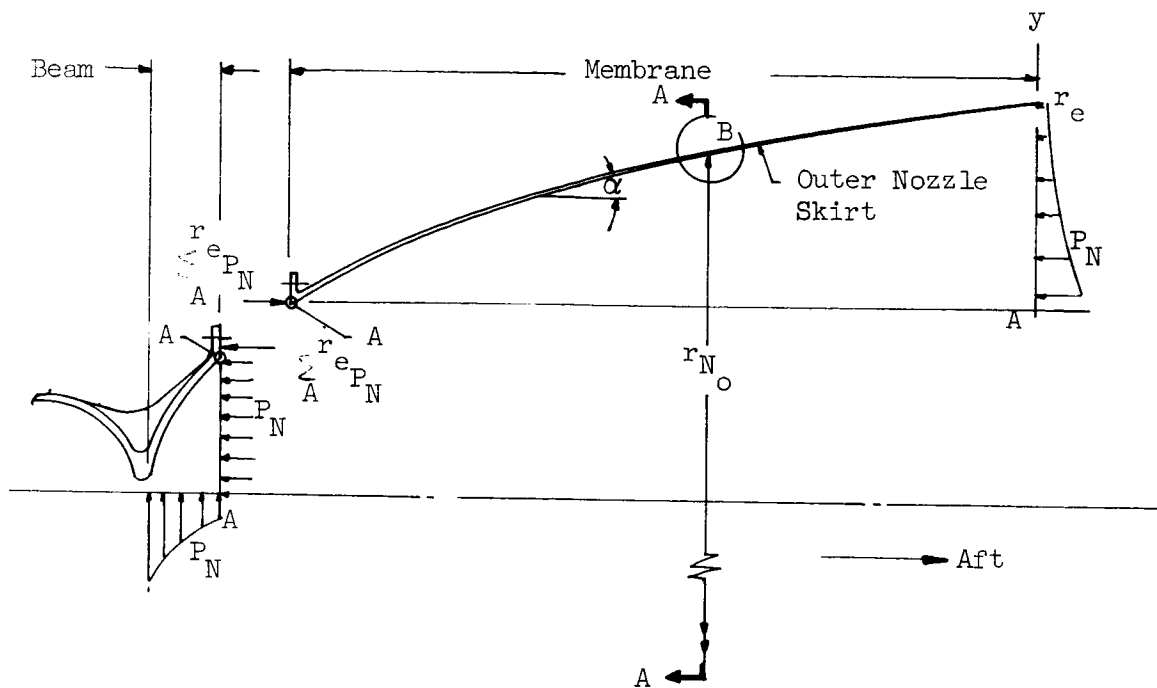
$$t = \frac{.4 h^2 A + 12 M (h+1) \cos \alpha F}{4 (h+1) \cos \alpha F h^2}$$



(3) Nozzle Skirt Design

The outer nozzle skirt (shown on the following page) is designed as a membrane from the flange to the exit section. Summation of forces in the y direction are reacted by hoop tension. The compressive stress

NOZZLE SKIRT



$$\sigma'_6 = \frac{F_6}{t} = \frac{\int_0^{r_N} P_N dy}{t \cos \alpha},$$

is increased due to the hoop tension to

$$\sigma_6 = \frac{\int_0^{r_N} P_N dy}{t \cos \alpha} + \frac{P_N r_{N_0} \mu}{t \cos \alpha}$$

where μ is Poisson's Ratio. Critical buckling stress in the skirt can be calculated from

$$\sigma_{cr} = \frac{C E t \cos \alpha}{r_{N_0}} = C' E \quad (\text{Figure 73 and 74})$$

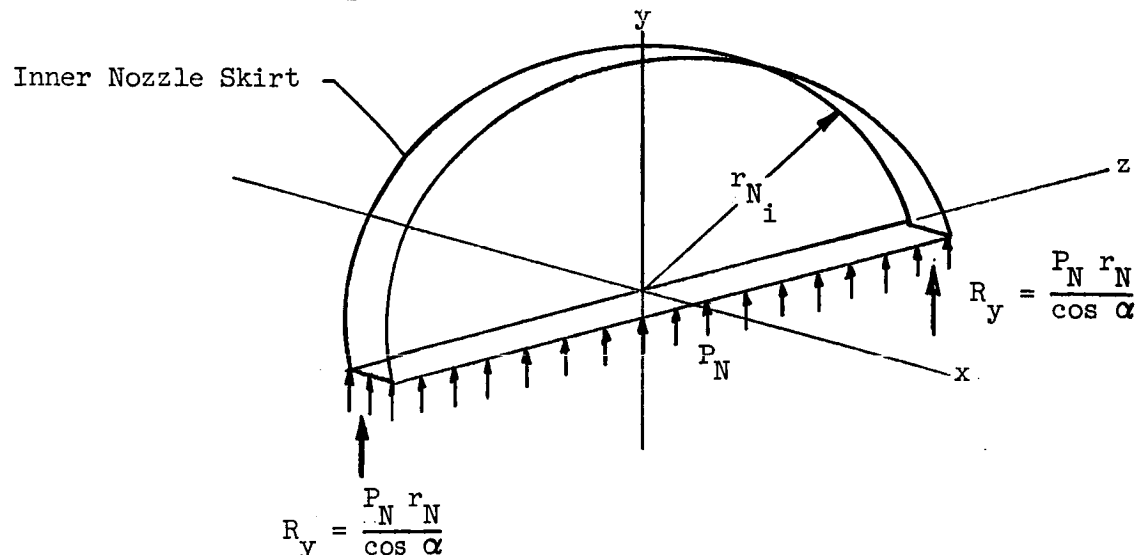
$$\text{where } C' \text{ is approximately } = 8 \left(\frac{r_{N_0}}{t \cos \alpha} \right)^{-1.58}$$

for the range we are interested in (Figure 74)

For design purposes σ_6 is equated to σ_{cr} and solved for nozzle thickness.

Then the greater of this thickness and thickness calculated from $t = \frac{P_N r_N}{F \cos \alpha}$, is used for determining skirt weight.

The reaction $R_y = \frac{P_N r_N}{\cos \alpha}$ is in the opposite direction on the inner nozzle skirt thus putting the skirt in compression rather than tension.



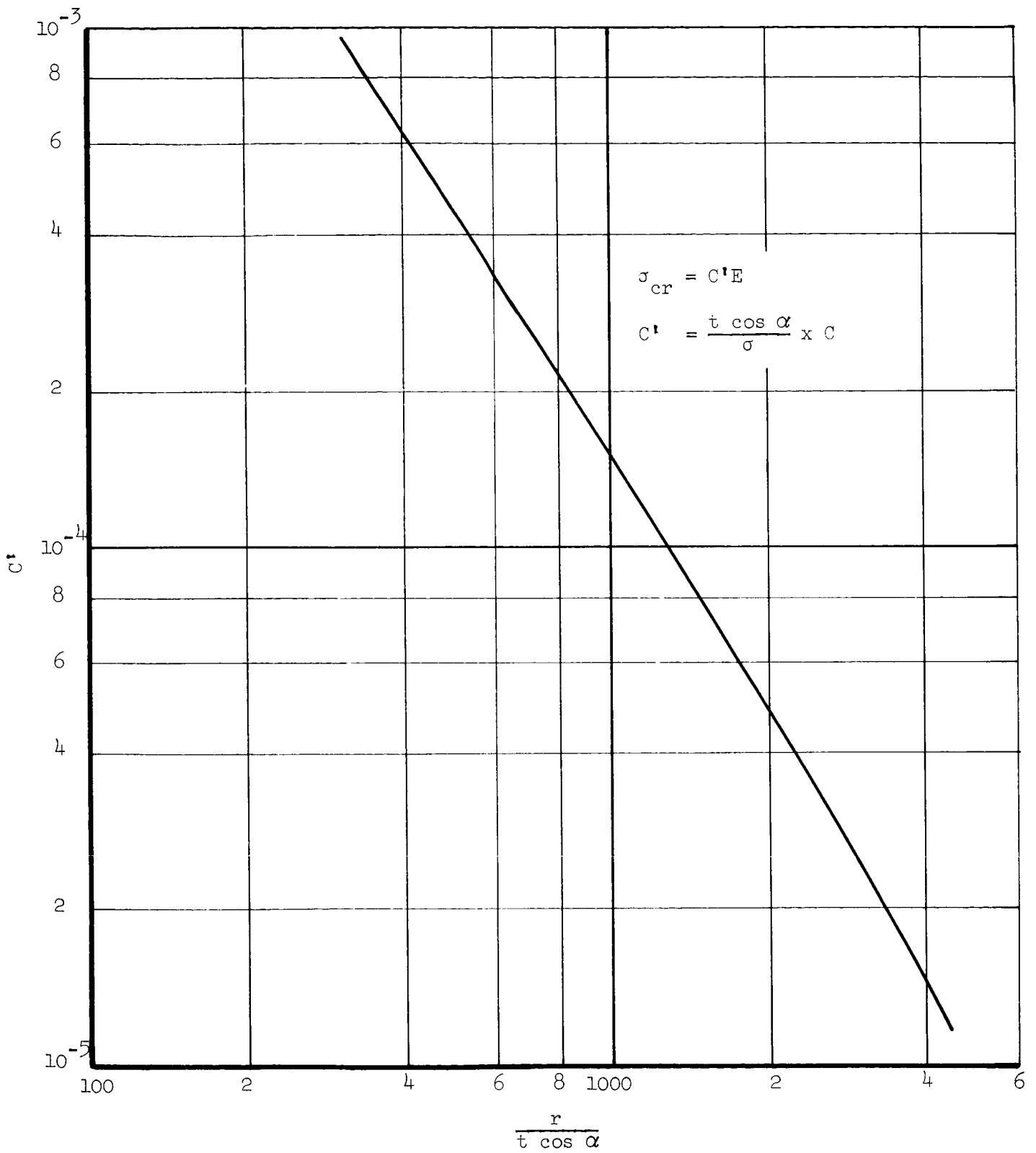


FIGURE 73. Buckling Coefficient of a Compressed Cone
(NACA TN 3783)

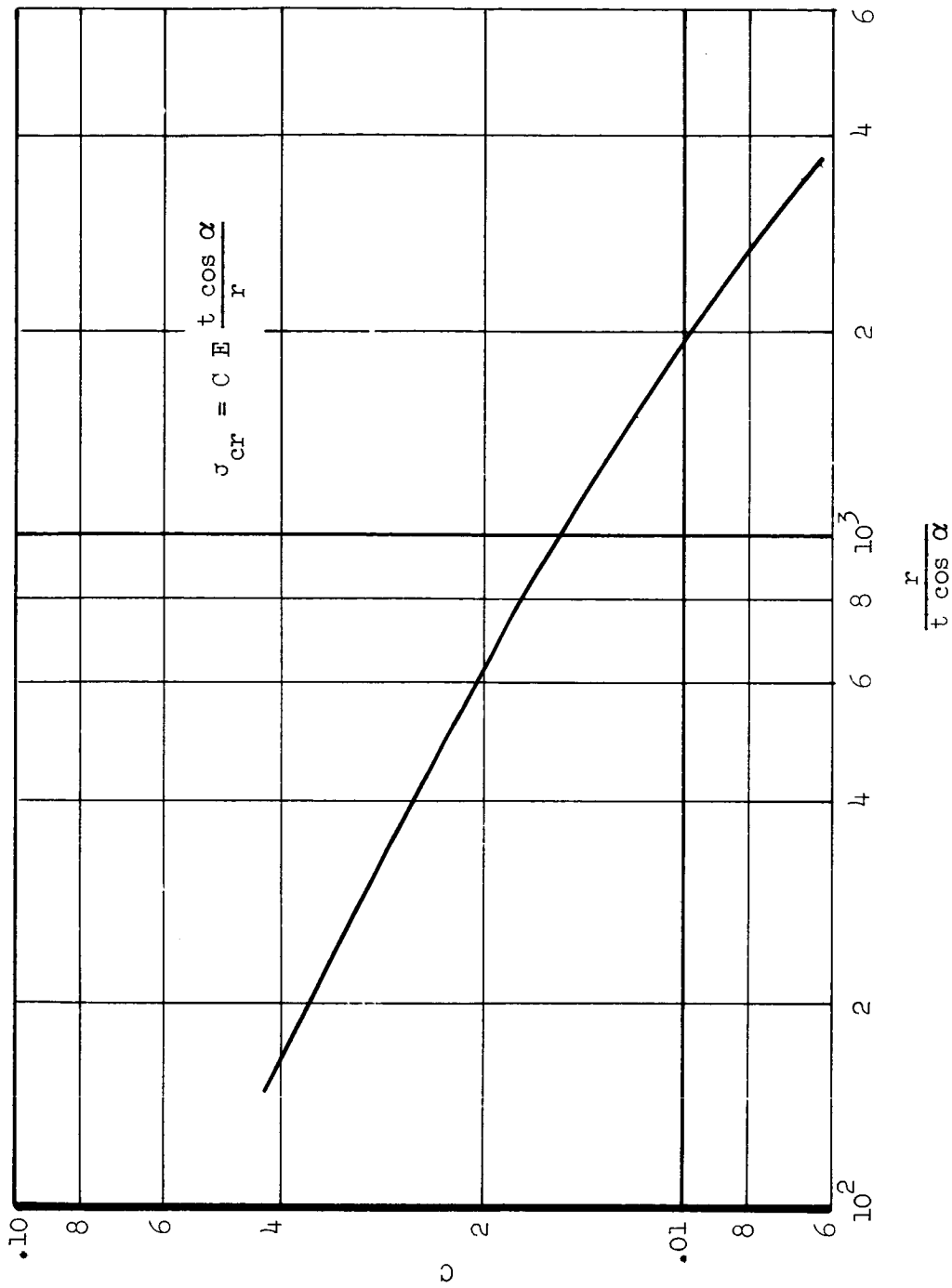


FIGURE 74. Buckling Coefficient

The force F_6 for the inner nozzle skirt has a compressive stress

$$\sigma_6' = \frac{\int_y^{r_N} P_N dy}{t \cos \alpha}$$

which is relieved by the normal compressive stress such that

$$\sigma_6 = \left[\frac{\int_y^{r_N} P_N dy}{t \cos \alpha} - \frac{P_N r_{N_i} \mu}{t \cos \alpha} \right]$$

The critical buckling stress is

$$\sigma_{cr} = \frac{C E t \cos \alpha}{r_{N_i}} = C' E$$

where C' is the same as in the outer skirt.

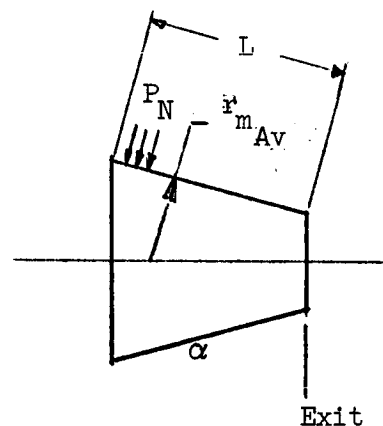
Equating σ_6 to σ_{cr}

$$t_2 = \frac{r_{N_i}^{.612}}{2.24 \cos \alpha E^{.388}} \left[\int_y^{r_e} P_N dy - P_N r_{N_i} \mu \right]^{.388}$$

Critical buckling pressure for the inner skirt (or cone) is

$$P_{cr} = \frac{.75 E t^{3/2}}{L (r_{N_i \text{ av.}})^{3/2}} \quad (\text{Reference 14})$$

where $r_{N_i \text{ av.}} = \text{Average } RN_i / \cos \alpha$



where: $K P_c$ is an equivalent pressure across the beam and e is the centerbody length being considered.

Thus the thickness of the centerbody is

$$t = 1.73 d \left(\frac{K P_c}{F} \right)^{1/2}$$

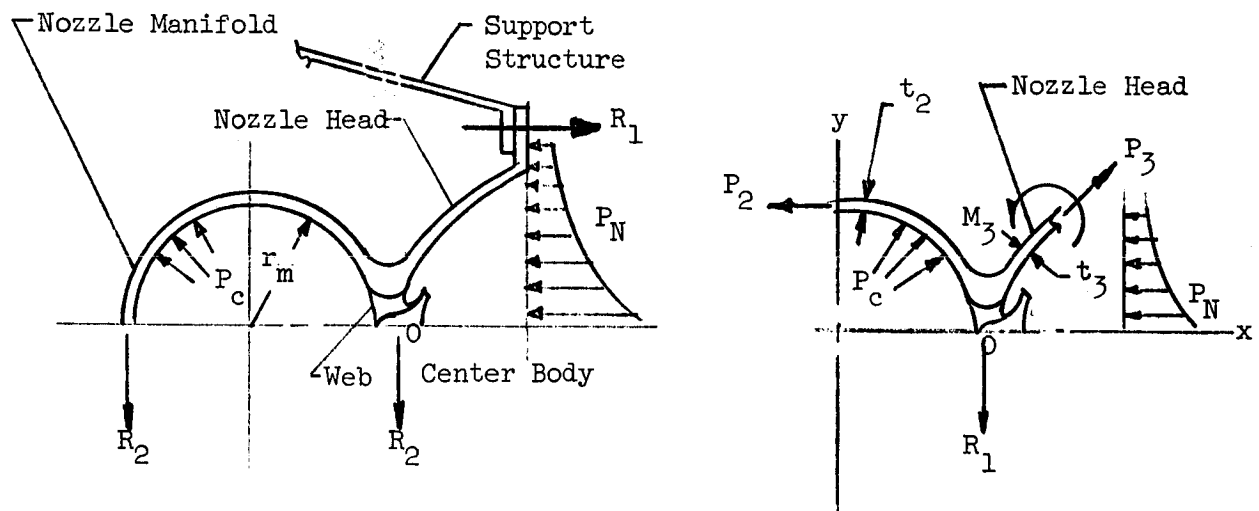
Chamber Design

The chamber is designed to simple hoop tension, i.e., chamber wall thickness

$$t = \frac{P_c R}{F}$$

II. THRUST FORCES TAKEN DIRECTLY INTO THRUST STRUCTURE

The stress model and free body diagram for the configuration are shown below.



The reactions R_1 and R_2 are identical with the similar reactions in the case where thrust loads are carried through the manifold, i.e.,

$$R_1 = \int_0^{r_e} P_N dy$$

$$R_2 = P_c r_m$$

The manifold wall load $P_2 = P_c r_m$ and skirt head load $P_3 = \int_0^y P_N dy$, and the moment $M_3 = \int_0^y P_N dy$. Thus the manifold wall thickness, t_2 , is determined by hoop tension, i.e.,

$$t_2 = \frac{P_c r_m}{F}$$

The head thickness t_3 is dictated by combined bending and tensile loads,

$$t_3 = \frac{P_3 + \sqrt{P_3^2 + 24 \cos^2 \alpha F M_3}}{2 \cos \alpha F}$$

Calculations of weights for the uncooled engine indicated that it weighs more per pound of thrust than conventional engines. Factors which contribute to the heavier weight are (1) the requirement of high temperature materials such as tungsten which has a density of .70 pounds per cubic inch compared to typical conventional engine material which has densities on the order of .30 pounds per cubic inch, (2) weight characteristics of distributed chambers compared to a single can-type chamber, and (3) the relatively heavy thrust structure. Due to the heavier weight, optimum thrust level for the uncooled type engine will be less than the 125,000 pounds found optimum for the conventional engine. The geometry of the liquid oxygen/liquid hydrogen (uncooled) engine was set by (1) considerations of the vehicle for which it was designed (190 inch diameter), (2) the engine parameters selected as being close to optimum for the configuration, and (3) the manifold and chamber sizing criteria discussed earlier.

As the diameter of the manifold changes, the throat width changes for a given thrust, i.e., as manifold diameter increases;

- (a) Throat width decreases, skirt width and length decrease, interstage length decreases, and frictional drag increases.
- (b) Manifold weight and plumbing weight increase.

Thus, there are performance and weight trade-offs which would determine an optimum manifold diameter. Although a complete optimization was not performed, both the engine parameters and geometry were selected from these considerations. The parameters selected for the uncooled engine were 90,000 pounds thrust, 400 psia chamber pressure, and expansion ratio of 200:1. Manifold diameter was set at 160 inches which dictated a throat width of .125 inches for 90,000 pounds thrust. Nozzle skirt length is 54 inches and total exit width is 53 inches. The contour is given in Figure 75.

Engine weight was determined for the configuration (I) taking the thrust load through the manifold, and for the configuration (II) taking the thrust load directly into the thrust structure from the skirt.

Location of the flange joint between the tungsten head and radiative cooled skirt was determined by properties of the radiation cooled skirt material

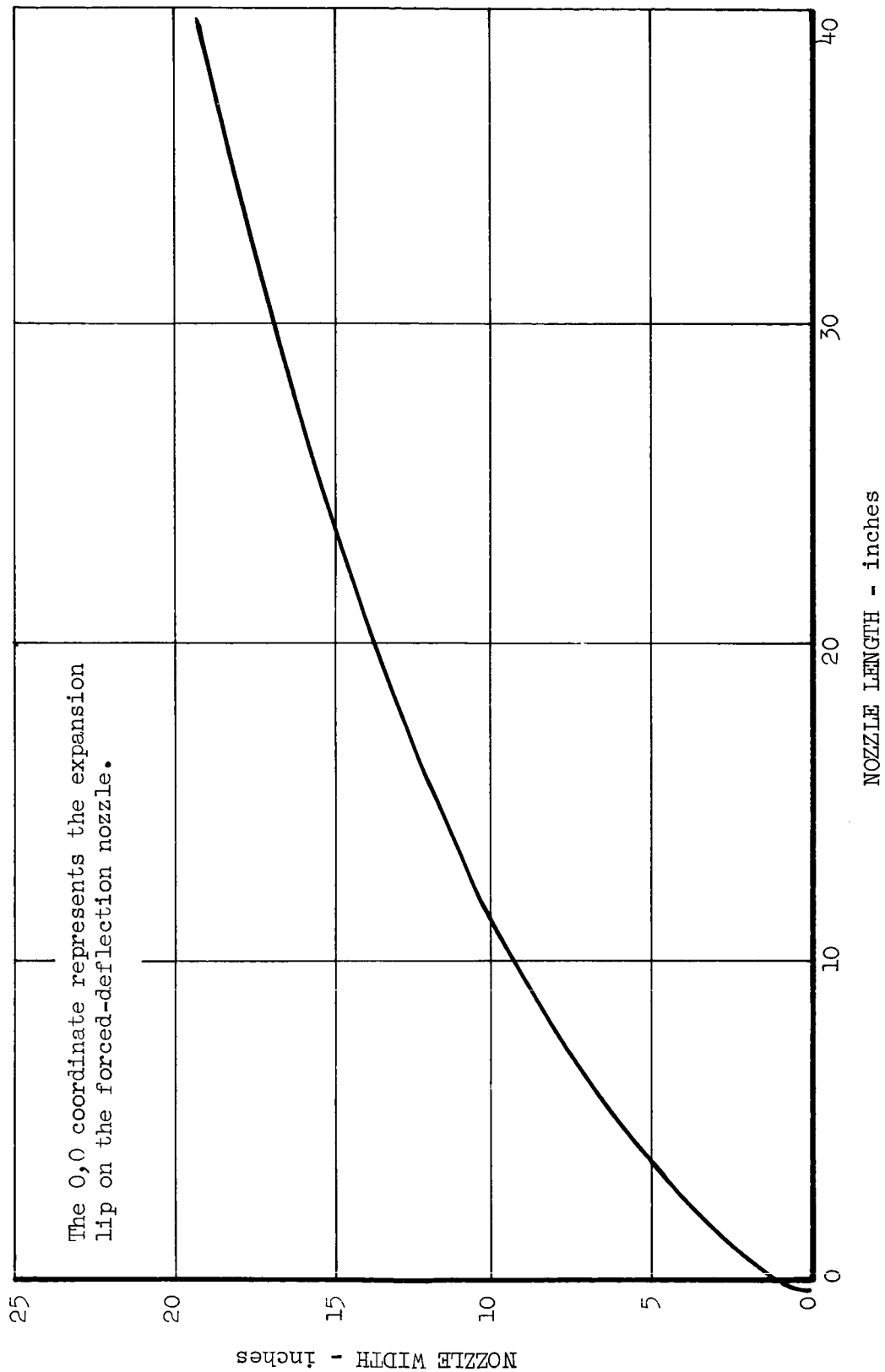


FIGURE 75. Two-Dimensional Nozzle Contour

and the change in wall temperature as the flange is moved away from the throat. As the flange moves away from the throat, more of the skirt material is tungsten and the nozzle becomes heavier. The properties for the radiation skirt are given in Figure 76.. It can be seen that the ultimate and yield stress both drop off rapidly at around 1400°F, therefore the flange joint was placed at the location with 1400°F wall temperature or a radius of 1.75 inches. Since the thrust loads are taken out at the flange in configuration II, it would be desirable to have the flange at or near the location of the resultant thrust force,

$$\bar{y} = \frac{\int_0^{r_e} P_N y \, dy}{P_N}, \text{ in order to reduce the moment loads on the head}$$

section which acts as a beam. The location of \bar{y} for the 200:1 nozzle was calculated to be 1.97 inches, or very close to the location dictated by temperature considerations.

Weight calculations, which utilized the geometry and component thickness as discussed in the preceding paragraphs, resulted in the weight breakdown as given in the following table.

<u>Configuration</u>	<u>Component</u>	<u>Weight - lbs</u>
(I)	Thrust loads	1485
	carried through	
	Manifold	442
	Struts	120
	Centerbody	330
	Nozzle Skirt	775
	Chamber	247
	Thrust Structure	<u>330</u>
	TOTAL	3709
(II)	Thrust loads	502
	taken directly into	
	thrust structure	560
	Struts	59
	Centerbody	218
	Nozzle Skirt	755
	Chamber	247
	Thrust Structure	<u>681</u>
	TOTAL	3022

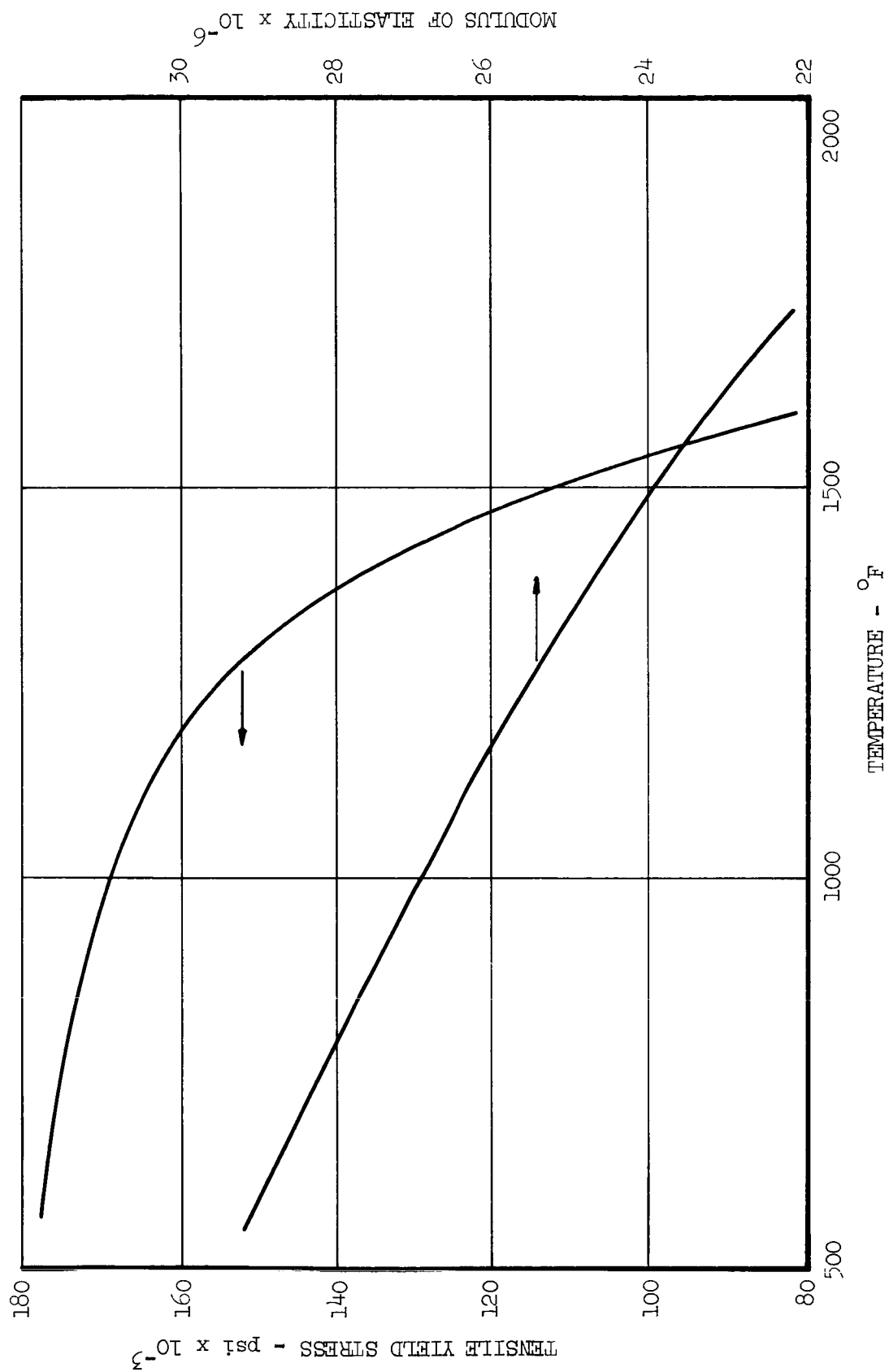


FIGURE 76. Properties of Rene 41 Skirt Material

As shown in the table, the most obvious differences in weight for the two configurations are in the manifolds and thrust structure.

Scale drawings of the manifolds in Figures 77 and 78 show end sections and mean sections through the manifold. Configuration I is very heavy in the area next to the centerbody and around the manifold since it takes the bending and compression loads of the thrust and the tensile loads due to chamber pressure. Configuration II is thicker next to the flange since it carries the thrust from the throat section to the flange like a cantilevered beam. However, as the drawings show, Configuration II is much lighter in the manifold section since thrust loads are not transferred through the manifold.

Thrust structure for both configurations is shown in Figure 79. Two additional frames and about twice as much skin are required for configuration II which takes thrust loads from both sides of the manifold.

For the engine parameters evaluated, the second configuration is about 19 percent lighter using the current materials technology available with tungsten (Figure 71). If state-of-the-art advances afford 200 percent and 400 percent increases in strength to density ratio of the high temperature materials, uncooled engine weight for this case will be reduced from 3022 pounds to 2400 pounds and 1835 pounds, respectively.

4.8.5 ENGINE CONFIGURATION

The selected parameters and geometry for the annular two-dimensional forced-deflection nozzle and engine are listed below.

Thrust	90,000 pounds
Chamber Pressure	400 psia
Expansion Ratio	200:1
Theor. Vac. Specific Impulse (Shifting)	464.2 sec
Mixture Ratio = 3.0	
Losses - Percent	
Drag	3.00
Geometry	.50
Cycle	1.00

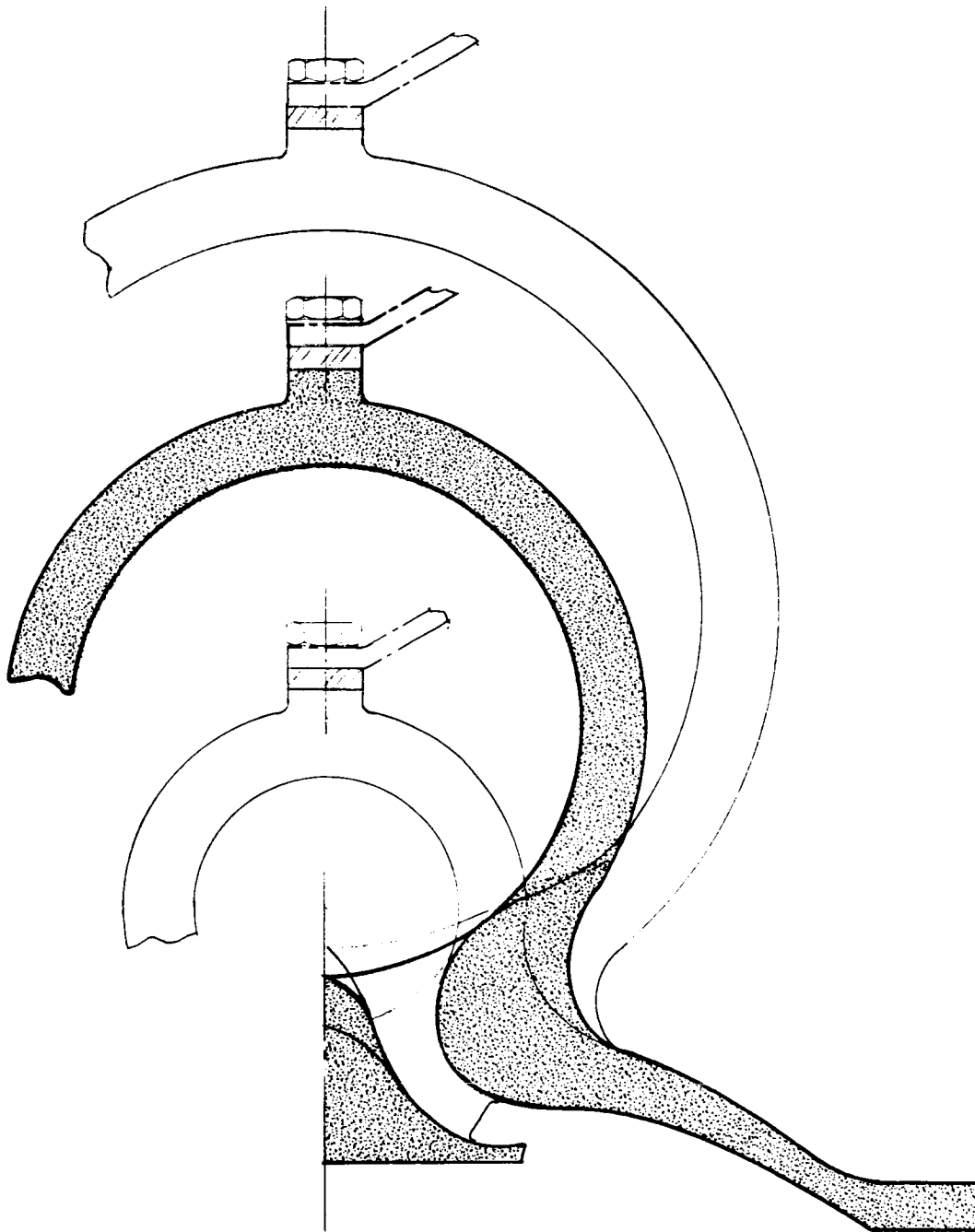


FIGURE 77. Manifold Configuration I

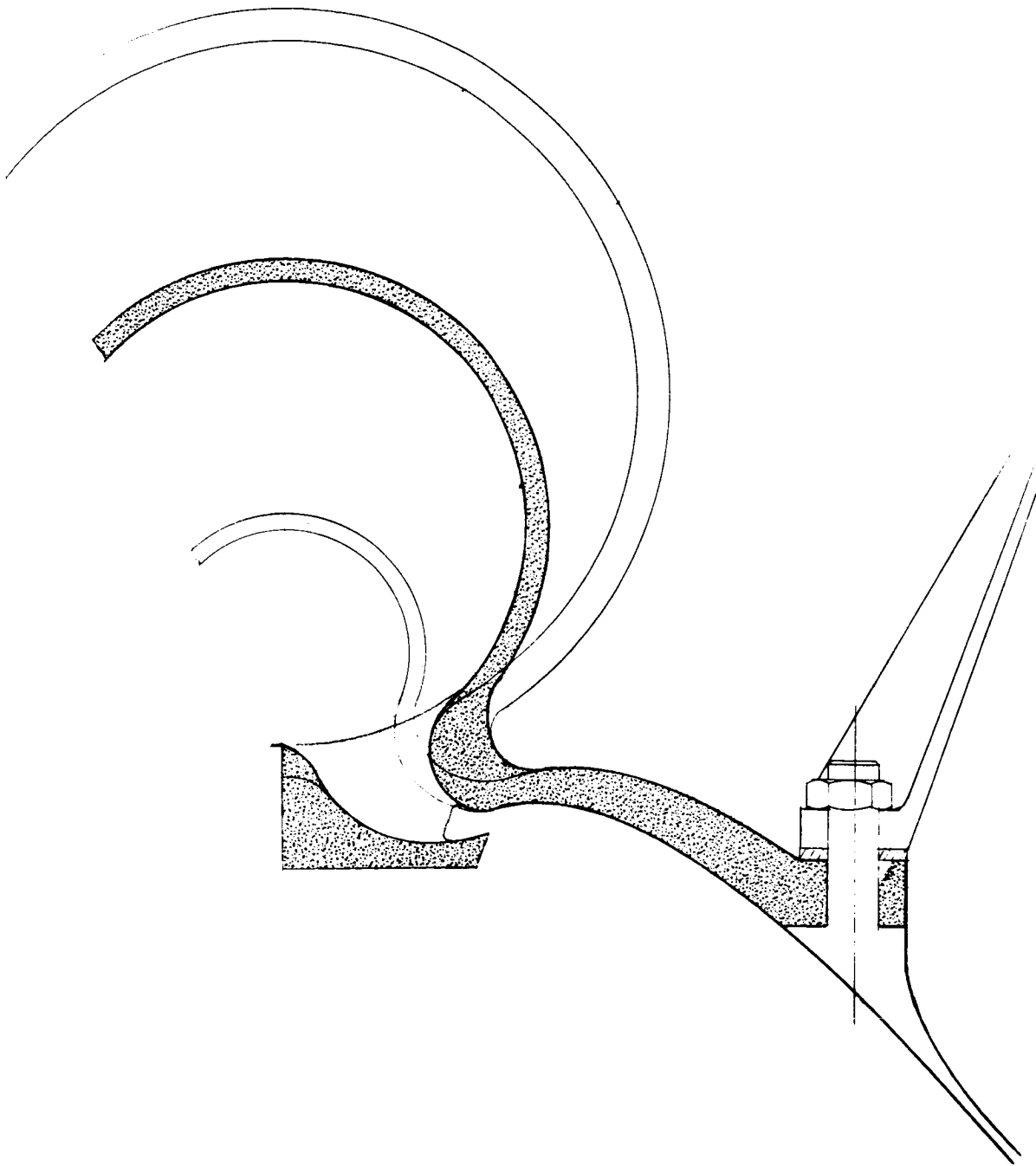
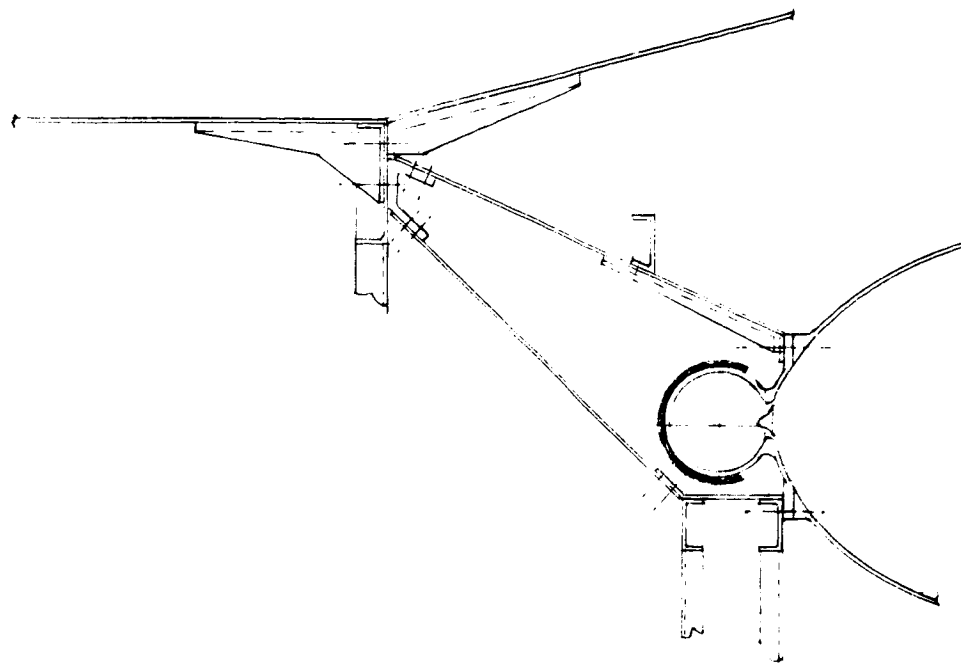
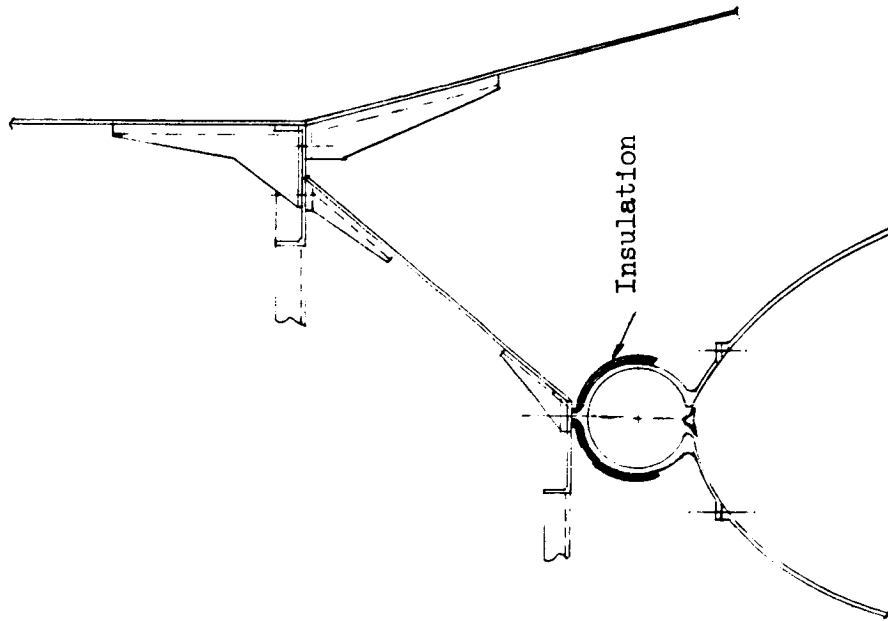


FIGURE 78. Manifold Configuration II



Manifold Configuration II



Manifold Configuration I

FIGURE 79. Small Nozzle Concept - Thrust Structure

Actual Engine Impulse	443.0 sec
Manifold Radius	80 inches
Centerbody Width	2.5 inches
Throat Width	.125 inches
Nozzle Exit Width (total)	53 inches
Nozzle Exit Length	54 inches
Total Engine Weight (excluding thrust structure)	2813 pounds

4.8.6 VEHICLE ANALYSIS

The tank diameter of the third stage vehicle was set at 104 inches using an elliptic head ratio of 2.0. Propellant volume and radius of the vehicle are greater than required for the conventional vehicle due to the decrease in mixture ratio from 6.0 to 3.0 and the attendant bulk density decrease from 22.40 pounds per cubic foot to 14.95 pounds per cubic foot. Tankage length to diameter ratio is 2.2:1. Second stage geometry is the same as the conventional second stage except for the difference in the interstage.

Shear and bending moment diagrams presented in Figure 80 were used to size structural elements of the vehicle.

VEHICLE WEIGHT BREAKDOWN (WEIGHT IN POUNDS)

Third Stage

Fwd. Structure	422
Pressurization System	1820
Fuel Tank	
Fwd. Head Skirt	263
Fwd. Head	313
Skin	1750
Frames	272
Stringers	2060
Oxidizer Tank	
Fwd. Head Skirt	475
Fwd. Closure	362
Aft Closure	415
Aft Head Skirt	760

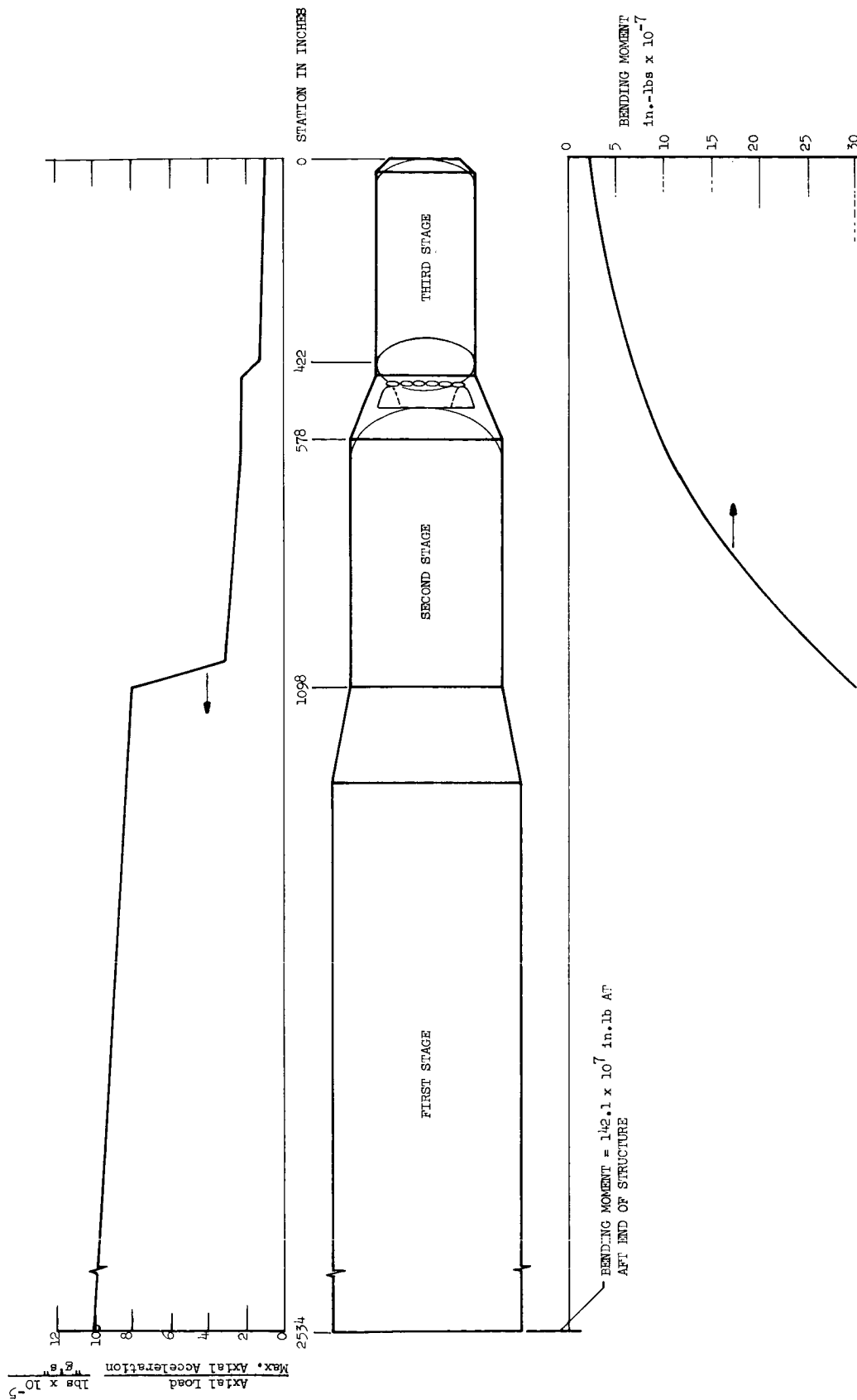


FIGURE 80. Small Nozzle Concept Vehicle (LO_2/LH_2)

Engine Mount	681
Insulation	614
Interstage Structure	2880

4.8.7 VEHICLE PAYLOAD

Payload of the uncooled-engine vehicle is discussed in the section "PAYLOAD COMPARISON OF THE EVALUATED VEHICLES".

4.9 SMALL THROAT ENGINE CONCEPT (HYDROGEN PEROXIDE/DIBORANE PROPELLANTS)

A vehicle utilizing the small throat concept and the storable propellant combinations of H_2O_2/B_2H_6 was designed. The geometry and loading diagrams of the vehicle are given in Figure 81.

4.9.1 ENGINE CONFIGURATION

Thrust	90,000 pounds
Chamber Pressure	400 psia
Expansion Ratio	220:1
Theor. Vac. Specific Impulse	
Mixture Ratio = 1.83:1	432 sec
Losses - percent	
Drag	2.97
Geometry	.50
Cycle	1.00
Actual Engine Impulse	414 sec.
Manifold Radius	80 inches
Centerbody Width	2.5 inches
Throat Width	.107 inches
Nozzle Exit Width (total)	50 inches
Nozzle Exit Length	51 inches
Total Engine Weight	2420 pounds

4.9.2 VEHICLE WEIGHT BREAKDOWN (WEIGHT IN POUNDS)

Third Stage

Fwd. Structure	378
Pressurization System	596

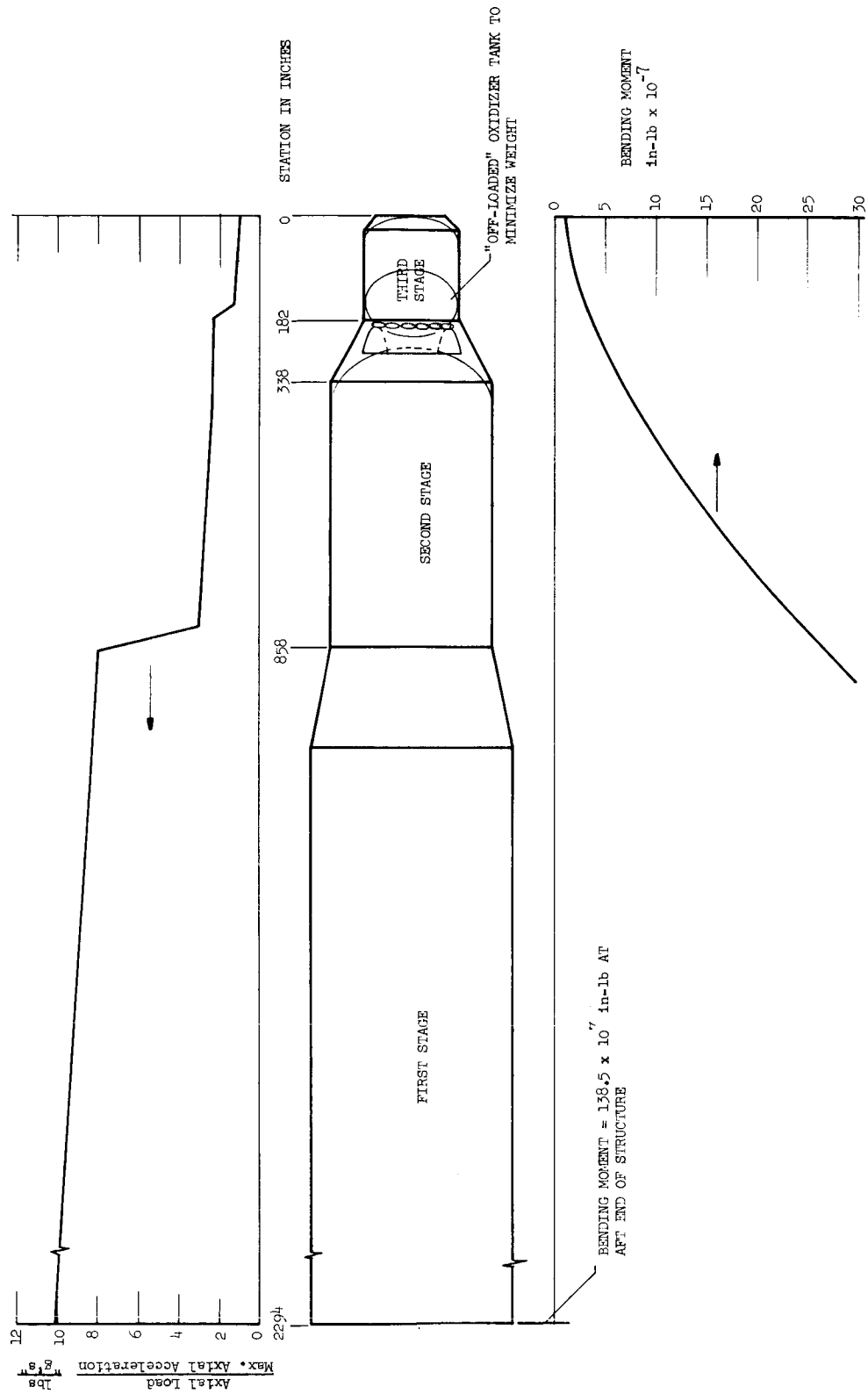


FIG RE 81. Small Nozzle Concept Vehicle (H_2O_2/B_2H_6)

Thus, thickness from this equation is

$$t_1 = \left(r_{N_i \text{ av}} \right)^{.6} \left[\frac{P_N L}{.75E} \right]^{.4}$$

and for design purposes the greater of t_1 and t_2 is used.

Centerbody Strut Design

Taking the average thickness of the strut as \bar{t} , the moment of inertia

$$I_{\text{strut}} = \frac{c^3 \bar{t}}{12 \sin \beta} \quad \text{and} \quad \text{Area}_{\text{strut}} = \frac{\bar{t} c}{\sin \beta}$$

The bending stress from M_θ is

$$f_B = \frac{6 D r_m \sin \beta}{c^2 \bar{t}} \left\{ \left[R_1 \sin \theta - R_3 (1 - \cos \theta) + \frac{R_3}{r_m} - \frac{2R_1}{\pi r_m} \right] \right\}$$

and the tensile stress is

$$f_T = \frac{D \sin \beta}{c t F} (R_2 + R_3)$$

Combining the bending and tensile stresses

and taking the allowable stress level = $F = F_B = F_T$,

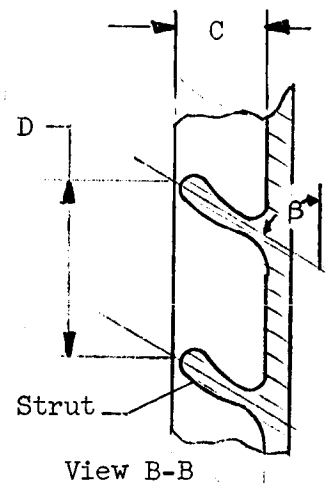
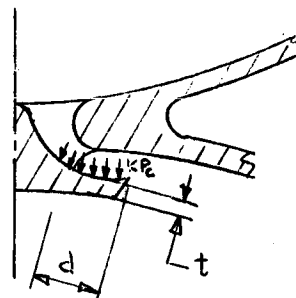
the thickness of the strut is

$$\bar{t} = \frac{D \sin \beta}{F} \left\{ \frac{R_2 + R_3}{c} + \frac{6 r_m}{c^2} \left[R_1 \sin \theta - R_3 (1 - \cos \theta) + \frac{R_3}{r_m} - \frac{2R_1}{\pi r_m} \right] \right\}$$

Centerbody Design

The pressure of the exiting gases place a bending stress on the centerbody of

$$f_b = \frac{\frac{K P_c d^2 e}{2} + \frac{t}{2}}{\frac{t^3 e}{12}}$$



Fuel Tank	
Fwd. Head Skirt	455
Fwd. Head	211
Skin	490
Frames	62
Stringers	360
Oxidizer Tank	
Fwd. Head Skirt	332
Fwd. Closure	236
Aft Closure	277
Aft Head Skirt	590
Engine Mount	681
Insulation	180
Interstage Structure	2395

4.10 EFFECTS OF THE THIRD STAGE CONFIGURATION ON FIRST AND SECOND STAGE STRUCTURE WEIGHT

The effects of changing the third stage configurations (i.e., going from conventional to the integrated concept) on the structural loads in the boost stages of the vehicles was very important to the relative advantages of the evaluated concepts. Bending and axial load determination and structure weight calculations were completed for the boost stages of each vehicle. These results are presented in Table IV and Figure 82. For the purposes of payload comparison, the first and second stage structure and interstage weights of the conventional liquid oxygen/liquid hydrogen vehicle were used as a reference, and differences between the weights of this configuration and the other configurations, ΔW structure, were used to calculate the ΔW_{pl} which is presented in Table IV. The term ΔW_{pl} is the ΔW structure of the particular element divided by the appropriate mass ratio(s) to correct it to third stage payload weight. The following trends were results of the detailed structural and weight analysis (see Section 4.4).

- Varying the third stage engine length not only changes interstage length, but also changes the bending loads and

TABLE IV
SUMMARY OF EVALUATED VEHICLES

CONFIGURATION		CONVENTIONAL LO_2/LH_2	SMALL NOZZLE LO_2/LH_2	INTEGRATED LO_2/LH_2	CONVENTIONAL $\text{H}_2\text{O}_2/\text{B}_2\text{H}_6$	SMALL NOZZLE $\text{H}_2\text{O}_2/\text{B}_2\text{H}_6$
Thrust	lbs	125,000	90,000	125,000	125,000	90,000
Chamber Pressure	psia	520	400	500	525	400
Expansion Ratio		220	200	440	220	220
Nozzle Exit Radius	in.	87	50 (width)	150	88	54 (width)
Nozzle Length	in.	260	54	244	246	58
$\frac{\dot{W}_{\text{ox}}}{\dot{W}_{\text{fuel}}}$, Bulk Density		6, 22.4	3, 14.9	6, 22.4	1.83, 48.2	1.83, 48.2
Engine Impulse	sec*	462	443	468	419	414
Velocity Increment	ft/sec	10,065	10,140	10,065	10,065	10,140
Propellant Weight	lbs	117,900	121,900	116,700	126,100	127,600
Vehicle Length	in.	2646	2534	2471	2524	2294
ΔW_{pl3}						
First Stage Tankage			133	249	76	254
Contributed from First and Second Stage Structure elements			94	155	43	149
Second Inter-stage			537	1830	302	1050
TOTAL	lbs		1940	461	438	2065
Tank., Structure, Insul., Inert			2704	2695	859	3518
Press., Mount						
Engine System		7018	9807	7091	3650	4163
TOTAL	lbs	1494		3346	1516	
Third Stage Payload -	lbs	8512		10,437	5166	
Relative Payload	% *	113588	95.3	115,558	109,593	96.5
		100.0		102.0	96.6	
Relative Payload	***	95.1	95.0			

* 100% shifting equilibrium propellant performance

*** 100% frozen propellant performance

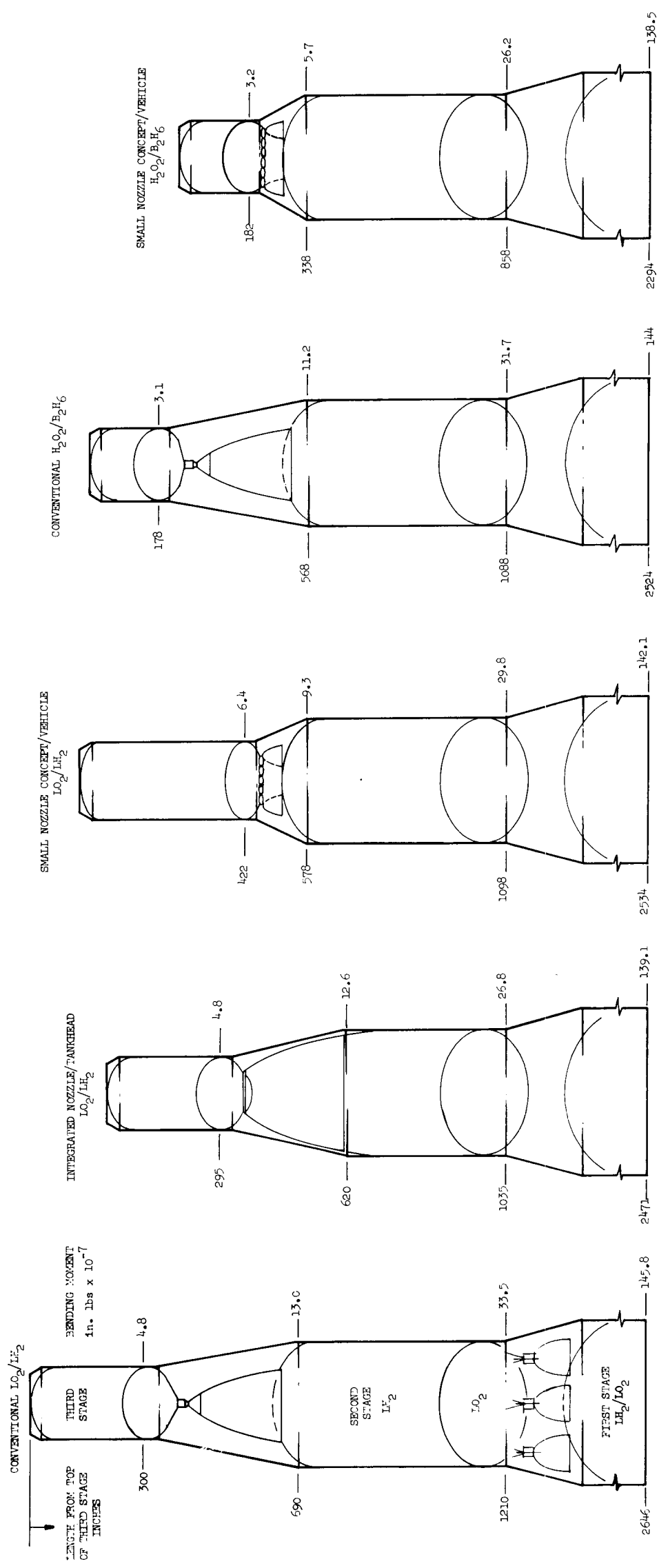


FIGURE 82. Configurations of the Evaluated Vehicles

frustrum cone angle of the interstage structure (Figure 82). Weight per axial length of the second interstage was plotted in Figure 83 for the different vehicles. It can be seen that if the forward and aft diameters of the two joined stages are held constant to minimize tankage structure, a reduction in length does not bring the interstage weight down proportionately with this length change since the cone angle increases as the length is decreased.

Another interesting factor brought out by the structural analysis and detailed design study was the relationship between the bending loads imposed on the stage, and the stage weight. Percent of the reference stage weight was plotted versus percent of the reference bending moment calculated at the base of the fuel tank. It was determined from the detailed design study that approximately sixty percent of the vehicle tankage and structural weight is contributed by elements dependent on bending loads and that the bending load is approximately sixty percent of the total load imposed on these structural elements. Therefore, as the curve in Figure 84 indicates, a decrease in bending moment, (related to changes in the third stage configuration in this case) of ten percent brings about a decrease in tankage and structural weight of about 3.6 percent.

It can be seen from Table IV that differences in second stage tankage and structure weights are significant for some of the configurations and must be included in determining the payload capability of the vehicles.

However, changes in bending moment in the first stage due to changes in third stage geometrical configuration are very small (Figure 82) and the corresponding payload contributions from these changes are also small (Table IV).

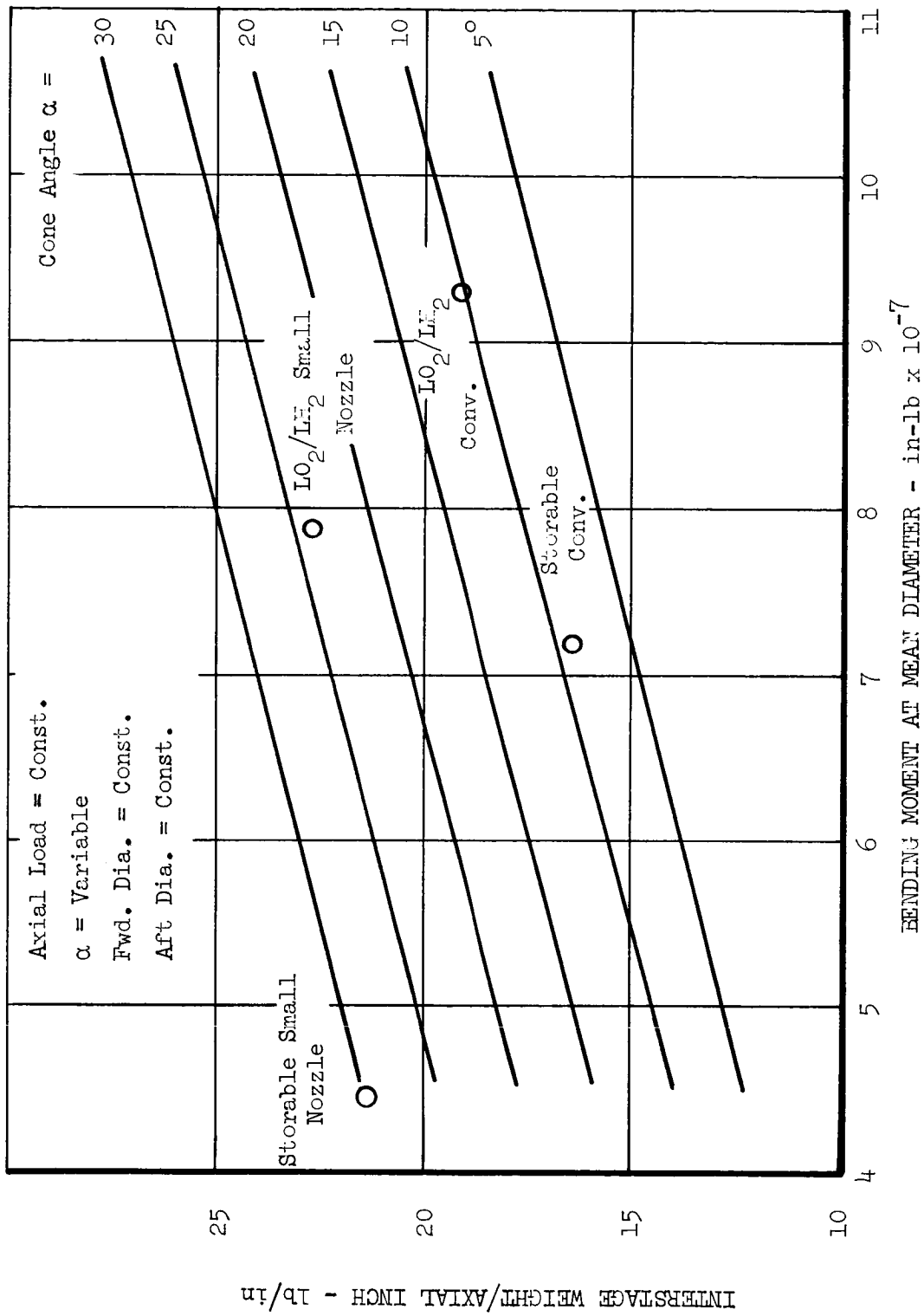


FIGURE 83. Effect of Bending Moment and Cone Angle on Interstage Weight

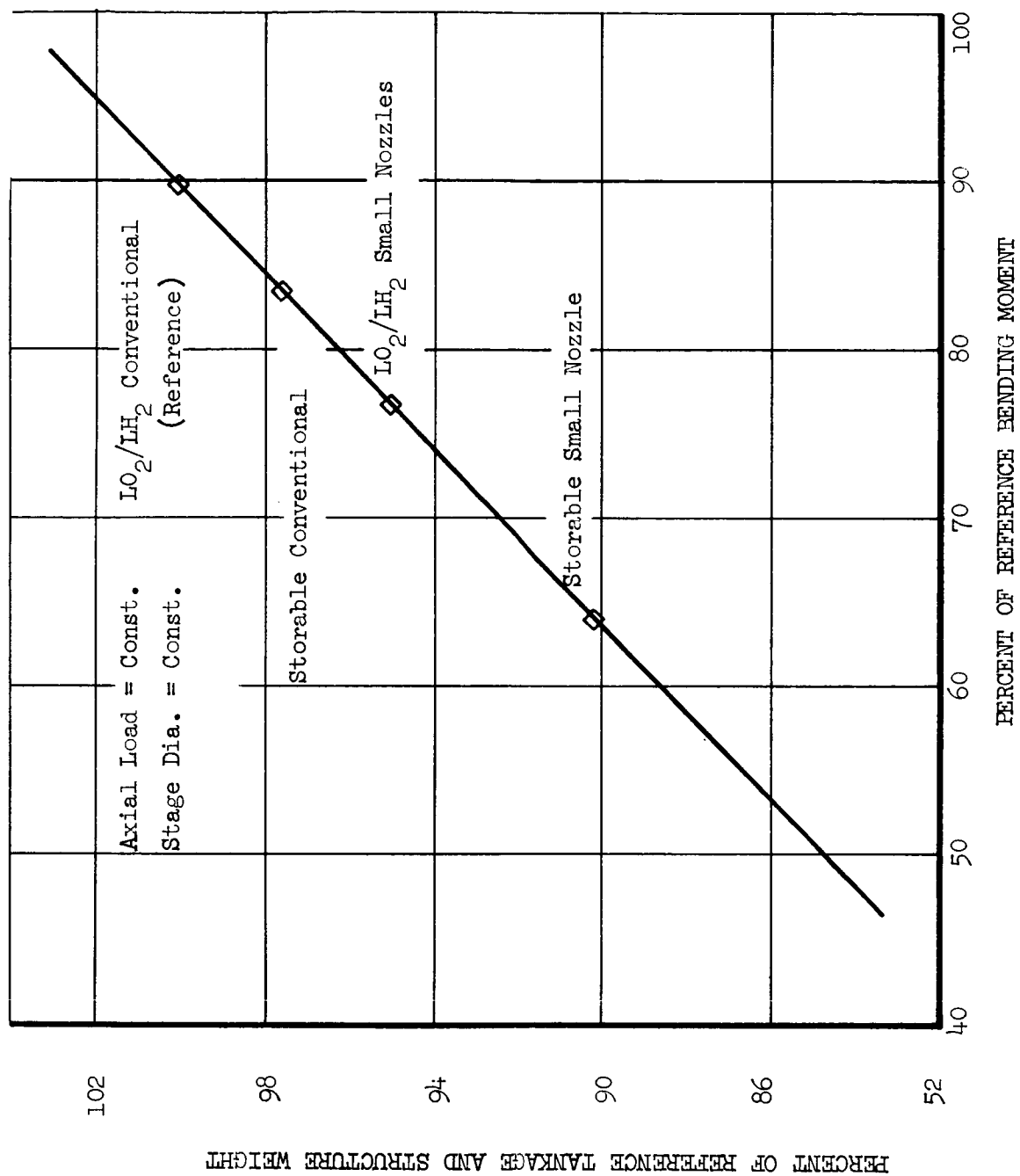


FIGURE 84. Effect of Bending Moment on Tankage and Structure Weight

4.11 PAYLOAD COMPARISON OF THE EVALUATED VEHICLES

Payload for the reference and integrated vehicle configurations is summarized in the table below.

Configuration	Conventional LO ₂ /LH ₂	Small Nozzle Concept LO ₂ /LH ₂	Integrated Nozzle/Tank LO ₂ /LH ₂	Conven- tional H ₂ O ₂ /B ₂ H ₆	Small Nozzle Concept H ₂ O ₂ /B ₂ H ₆
Payload - lb 100% Shifting	113,588	108,184	115,558	109,593	109,334
Relative Payload-% 100% Shifting	100.0	95.3	102.0	96.6	96.5
Relative Payload-% 100% Frozen	95.1	95.0			

4.11.1 LIQUID OXYGEN/LIQUID HYDROGEN PROPELLANTS

4.11.1.1 INTEGRATED VEHICLE

The integrated nozzle/tankhead vehicle has a two percent payload advantage over the conventional vehicle. Although the gross payload increase due to higher specific impulse and savings in first and second stage structure weights amounted to about 4000 pounds, a much heavier integrated tankhead/nozzle now carried with the third stage makes the propulsion system about 1800 pounds heavier than the conventional propulsion system. The net payload advantage is therefore limited to about 2200 pounds or two percent.

4.11.1.2 SMALL NOZZLE CONCEPT

The small nozzle concept/vehicle has limited payload capability with this propellant combination due to the non-optimum mixture ratio for shifting equilibrium performance. In going from mixture ratio of 6.0 to 3.0, the propellant weight is increased 3600 pounds and the propellant bulk density is decreased considerably. In addition, the propulsion system weight is 1300 pounds higher than for the conventional system. These disadvantages are partially offset by decreased first and second stage weights, however, the net payload for the concept is 96 percent of the conventional vehicle payload.

When 100 percent frozen equilibrium performance is assumed, the mixture ratio is not as "off-optimum" and payload is nearly equal for the conventional and small nozzle vehicles.

4.11.2 HYDROGEN PEROXIDE/DIBORANE PROPELLANTS

4.11.2.1 CONVENTIONAL VEHICLE

A very interesting point brought out by the study was the payload capability of this propellant combination relative to the high energy cryogenic system. Even if some reasonable estimates of combustion efficiency are introduced, the payload capability of this storable combination merits further investigation.

4.11.2.2 SMALL NOZZLE VEHICLE

The small nozzle vehicle configuration has lower specific impulse than the conventional vehicle and a heavier engine, however, reductions in first and second stage tankage, structure, and interstage weights bring the net payload to very near that provided by the conventional vehicle. In addition, the length of this vehicle is 20 feet shorter than the conventional vehicle length.

Section 5

EXPERIMENTAL PROGRAM

INTRODUCTION AND SUMMARY

Objectives of the experimental program were twofold. The first objective was to determine nozzle drag losses at two Reynolds Numbers, thereby making possible the correlation of measured losses with the theoretical methods of prediction. The second objective was to substantiate the predicted difference in drag for two-dimensional and three-dimensional nozzles. These test objectives were selected as being both meaningful to the evaluation of the small nozzle concept, and valuable to the general technology of nozzle performance prediction.

Two nozzles were designed at Space-General and subsequently fabricated and tested at the facilities of the Fluidyne Engineering Corporation. The nozzles tested were (1) a 15° half angle conical nozzle with expansion ratio of 65:1 and throat area of one square inch, and (2) a two-dimensional forced-deflection nozzle with throat area of one square inch (throat width = .054 inches) and expansion ratio of 65:1. The nozzles were run at various pressure ratios and at two different chamber pressures (i.e., two different Reynolds Numbers). Each model had over 100 static pressure taps downstream of the throat. The frictional force in the nozzle was calculated from the thrust coefficient determined from force balance readings and the thrust coefficient obtained from the integral of wall pressure and area. Results of the experimental study are summarized in the following table.

Configuration	Throat Reynolds Number/ft	Chamber Pressure psia	Static Thrust Coefficient C_{T_F}	Measured Drag Loss ΔC_{T_a}	Predicted Drag Loss ΔC_{T_p}	Computed Experimental Error ΔC_{T_e}
15° Conical Nozzle	4.2×10^7	135	0.974	0.004	.0150	$\pm .001$
	1.46×10^7	45	0.974	0.005	.019	$\pm .001$
2-D Forced- Deflection Nozzle	4.12×10^7	135	0.972	0.028	.014	$\pm .0035$
	1.47×10^7	45	0.971	0.022	.0174	$\pm .0035$

The thrust loss due to drag predicted by the modified Frankl-Voishel equation (Reference 7) and the computed experimental error are also given in the table. Since, theoretically, nozzle frictional drag is inversely proportional to the Reynolds Number, nozzle drag should increase as Reynolds Number (or chamber pressure) is decreased. The experimental data indicate that for the forced-deflection nozzle, the measured drag does not show this predicted trend with Reynolds Number. However, there was evidence during the test that unanticipated flow variations (See Section 5.4.2) were obtained in the two-dimensional nozzle when the chamber pressure was varied from 45 to 135 psia (at the same pressure ratio) and this phenomenon might possibly have caused the drag to differ from the expected trend. Magnitude of the measured drag for this nozzle was found to be about 20 to 80 percent higher than the predicted value for the high and low Reynolds Numbers, respectively.

The measured drag data for the conical nozzle exhibit the predicted trend with Reynolds Number, but the drag is only about 25 percent of the predicted drag at each Reynolds Number.

Since the same equations were used for predicting the drag for each nozzle, and assuming the same flow phenomena are being dealt with, it seems unlikely that the equations would predict drag values four times too high for the conical nozzle and half the correct value for the two-dimensional nozzle.* It appears to be more probable that the errors in instrumentation, recording, data reduction, and analysis may have reduced the accuracy of determining the actual frictional forces in the nozzle below that predicted by error analysis and below the accuracy which might be expected from a review of the excellent reproducibility of data evidenced in the test program. This conclusion is further supported by the boundary layer probe data which were

* Spalding and Chi, AIAA Journal, pg 2160, 1963, show the root mean square of $\left(\frac{C_{f \text{ experimental}}}{C_{f \text{ theoretical}}} - 1 \right)$ for 22 data sources, as calculated by the Frankl-Voishel Equation, to be 28 percent.

obtained for each nozzle in the test program. Predicted boundary layer thickness for the two nozzles is shown below.

Configuration	Throat Reynolds Number/foot	Predicted Exit B.L. Thickness, δ in.
15° Conical Nozzle	4.2×10^7	.27
	1.46×10^7	.34
2-d Forced-Deflection Nozzle	4.22×10^7	.25
	1.47×10^7	.31

The rake data indicated that free stream total pressure was obtained at .30 to .40 inches from the wall for the conical nozzle, and .25 to .35 inches for the forced deflection nozzle, and the boundary layer was thicker at the low chamber pressures as would be expected from the theory. The fact that the measured boundary layer was even thicker for the conical nozzle than for the two-dimensional nozzle is further evidence that the measured nozzle frictional losses should be suspected.

Although painstaking efforts were put forth under this program to insure sufficient accuracy in the instrumentation and reduction of data, it appears that additional experimental effort* is necessary (preferably after further refinement of techniques and facilities) before sound conclusions can be drawn concerning correlation of theoretical and experimental frictional losses in nozzles.

* A continuation of the experimental effort initiated under this contract has been conducted by Aerojet and will be reported in the Aerojet-General Corporation Report, AGC NAS-7-136-01F, March, 1964, "Study of High Effective Area Ratio Nozzles for Spacecraft Engines.

5.1 DISCUSSION OF TEST PROGRAM

This test program was undertaken to determine the static thrust characteristics of two high area ratio exhaust nozzle configurations. Both configurations were tested at various Reynolds numbers in the fully expanded flow region.

Basic articles were a 15° conical nozzle and a two-dimensional forced-deflection nozzle, both having nominal area ratios of 65:1. Model aerodynamic lines and boundary layer probe lines were specified by Space-General, and design, fabrication, and tests were performed by FluidDyne.

Nozzle thrust was determined both from force-balance data and from integration of the measured wall pressures. The difference between these two thrust determinations isolates the boundary layer friction loss. Measurements were also made of nozzle flow coefficient and boundary layer pressure profiles.

The variation in Reynolds number level corresponded to the lowest and highest values at which sufficiently reliable data could be obtained. The highest Reynolds number was limited primarily by the pressure differential across the rubber seal in the force-balance system, and the lower limit was dictated by the lowest model total pressure which would still allow full expansion of the nozzle flow. Reynolds numbers attained thus differed by a factor of 3:1.

An analysis was made of the probable experimental error in determining the skin friction drag. The probable error in the case of the conical model was found to be 0.20% of the ideal exhaust thrust. The two-dimensional model was installed downstream of an inlet diffuser which guided the flow uniformly from the small cylindrical seal to the large rectangular entrance to the model. This necessitated different analysis procedure in which the momentum flux into the model had to be evaluated separately. The additional uncertainty in the entering momentum flux calculation increased the probable inaccuracy in the friction drag coefficient for the two-dimensional model to 0.67%.

5.2 FACILITY AND MODEL DESCRIPTION

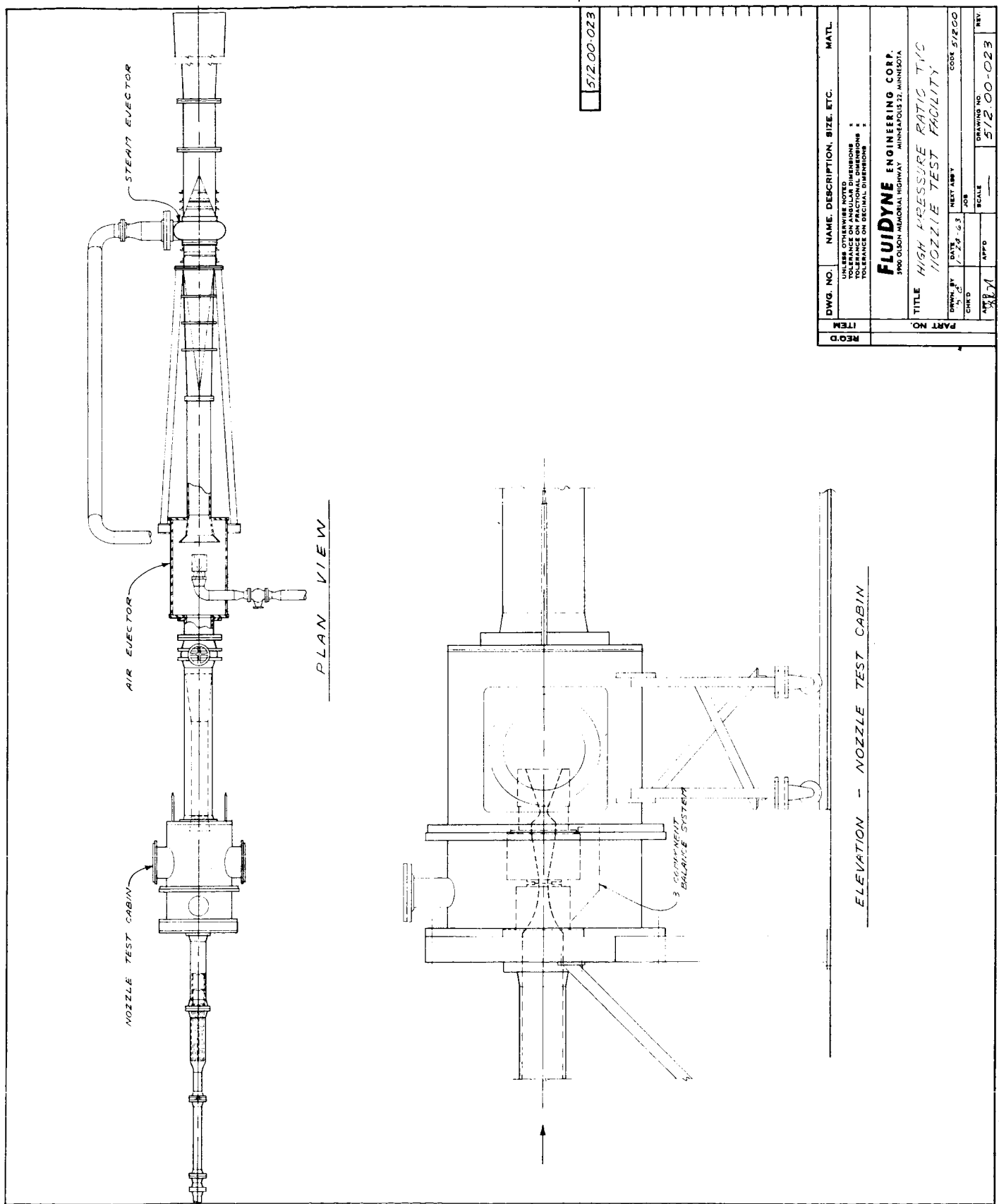
5.2.1 FACILITY DESCRIPTION

The model tests were performed at FluidDyne's Elk River Aerodynamics Laboratory. Static thrust data were obtained in Channel 8, a cold-flow axisymmetric free-jet thrust stand specially designed for high pressure-ratio operation (Figure 85). Photographs showing the test area and models installed in the facility are presented in Figure 86.

High pressure air from the facility storage system (2370 cu. ft. at 500 psi) was throttled, metered, and discharged through the model into the test chamber. Model total pressure for the present tests was controlled to either 45 or 130 psia, to provide a 3:1 variation in Reynolds number. Tests at lower pressures between 20 and 45 psia disclosed that insufficient facility pressure ratio was available to fully expand the internal flow in the nozzle models. Test chamber pressure (ambient to the model) was controlled by throttling the flow as it exhausted to atmosphere through the second-throat diffuser. A conical flow pickup was used for the conical model tests, and a square pickup followed by the cylindrical diffuser was used with the 2-D model. Low test cell pressures are maintained by a two-stage (air followed by steam) ejector.

The Channel 8 data consisted of measurements of balance forces, nozzle contour static pressures, air flow rates, model total pressure, test chamber pressure, and inlet pressure measurements necessary to calculate the nozzle thrust from the balance force. Facility stations are defined schematically in Figure 87.

The force balance, instrumented to measure the axial thrust vector, was mounted within the test chamber as shown in Figure 85. This balance was structurally isolated from the inlet air ducting by means of a thin rubber membrane seal. The force on the model assembly downstream of the seal was transmitted via the balance strain gage elements to a digital readout system. The mechanical details of the seal and inlet ducting can be seen in Figure 88.



REC'D	ITEM	DWG. NO.	NAME, DESCRIPTION, SIZE, ETC.	MATL.
			UNLESS OTHERWISE NOTED DIMENSIONS ARE IN INCHES TOLERANCE ON FRACTIONAL DIMENSIONS ± TOLERANCE ON DECIMAL DIMENSIONS ±	
FLUIDYNE ENGINEERING CORP. 3900 OLSON MEMORIAL HIGHWAY MINNEAPOLIS 22, MINNESOTA				
PART NO. TITLE HIGH PRESSURE RATIO TVC NOZZLE TEST FACILITY				
DESIGNED BY H. C.		DATE 1/24/63	TEST APP'Y JOB	CODE 51200
CHECKED H. C.		APP'D H. C.	SCALE —	DRAWING NO. 512.00-023
THIS DRAWING AND THE INFORMATION IT CONTAINS ARE THE PROPERTY OF THE FLUIDYNE ENGINEERING CORPORATION. IT IS NOT TO BE COPIED OR REPRODUCED IN ANY MANNER WITHOUT THE WRITTEN PERMISSION OF THE CORPORATION.				

FIGURE 85. High Area Ratio Nozzle Test Facility

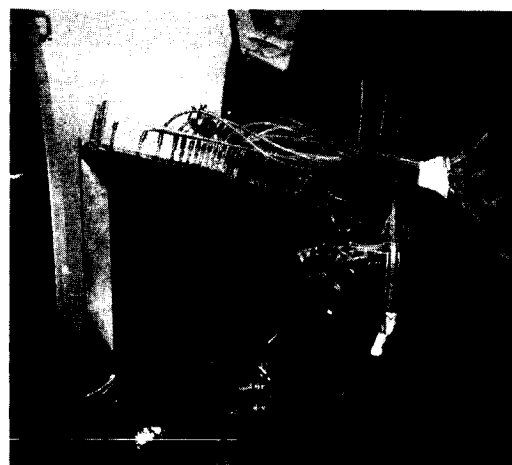
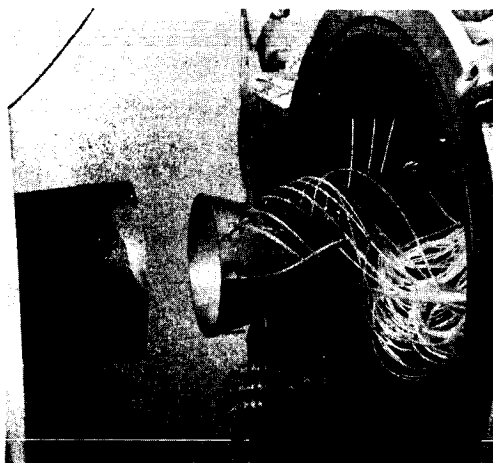
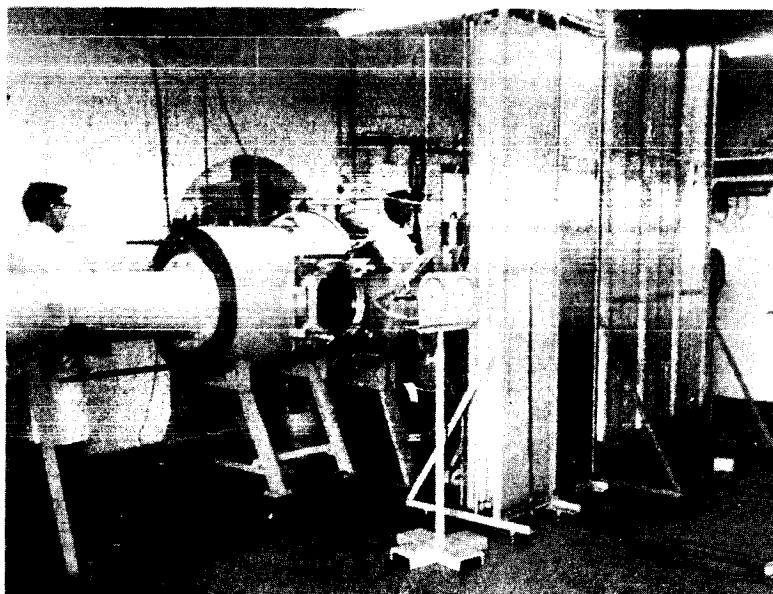
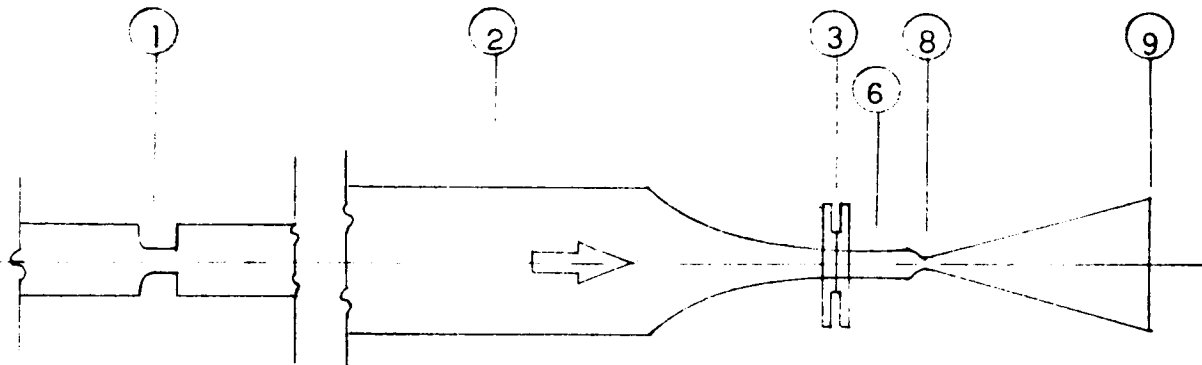


FIGURE 86. Photographs of Test Area and Installed Models

FLUIDDYNE ENGINEERING CORPORATION



- ① ASME Metering Orifice
- ② Facility Stagnation Chamber
- ③ Flexible Seal Station
- ⑥ Model Inlet Chamber
- ⑧ Model Throat Station
- ⑨ Model Exit Station

FIGURE 87. Station Definition for Channel 8 Static Thrust Facility

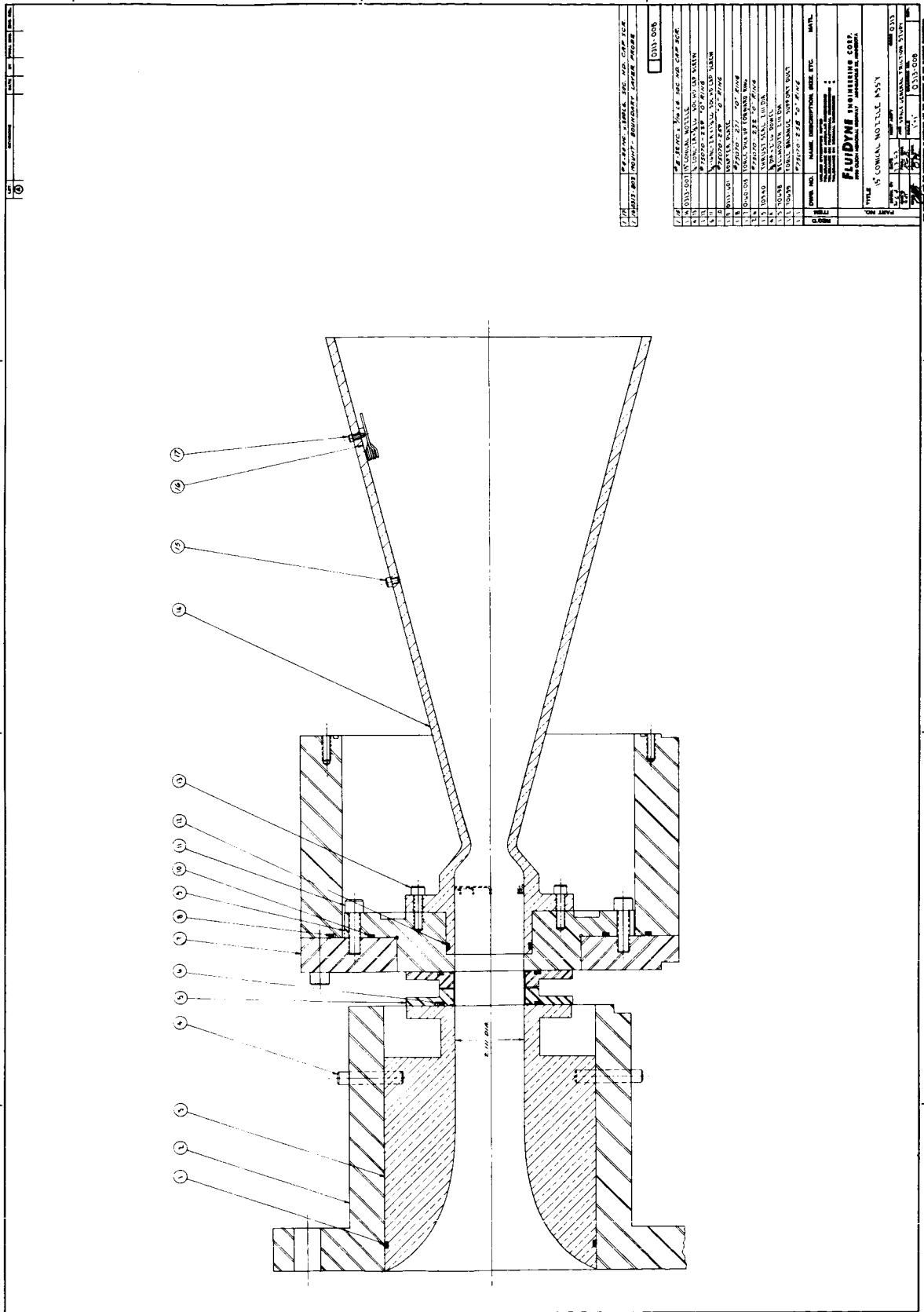


FIGURE 88. Assembly of Space-General Conical Nozzle in FluidDyne Channel 8

Various other items of test hardware such as mercury and silicon fluid manometers, precision pressure gauges, and electronic readout equipment were available for the test measurements.

A typical test was conducted as follows: the model pressure was set by throttling to the desired value, and the nozzle pressure ratio was regulated by controlling the test cell pressure with a downstream valve. When pressures were stabilized, the force-balance readout recording system was started. Force readings in counts were recorded on Teledeltos tape at one second intervals. After approximately 5 seconds, polaroid photographs were simultaneously taken of the pressure gauges and manometer boards, and the readout tape was electronically marked. The air flow was then shut down and the photographs and "counts" from the readout tape were recorded and filed.

5.2.2 MODEL DESCRIPTION

Nozzle aerodynamic lines and boundary layer probe lines were specified by Space-General and the models were designed and fabricated by Fluidyne. Inspected model dimensions and pressure tap locations are presented in Figure 89. The two basic configurations were as listed below.

A convergent-divergent 15° conical nozzle with a geometric area ratio, $\epsilon = 65$ was the first model tested. Instrumentation consisted of total and boundary layer pressure rakes in the inlet, detailed in Figure 89, and static pressure taps located on the inlet and shroud contours as tabulated in Figure 90. Installation of the 15° conical nozzle in the test facility is shown in Figure 86.

A two-dimensional forced-deflection nozzle (Figure 91) denoted 2-D F-D nozzle, was also tested. The "dynamic" area ratio for parallel out-flow was $\epsilon = 65$, and the geometric area ratio was $\epsilon = 88$. Contour pressure taps were installed in the model inlet, shroud, and centerbody as shown in Figures 92, 93, and 94. Locations of the inlet total pressure rakes are detailed in Figure 94. A thin ($1/16$ ") plate was machined to fit the shroud contour in the vertical plane. The nozzle with plate installed, designated

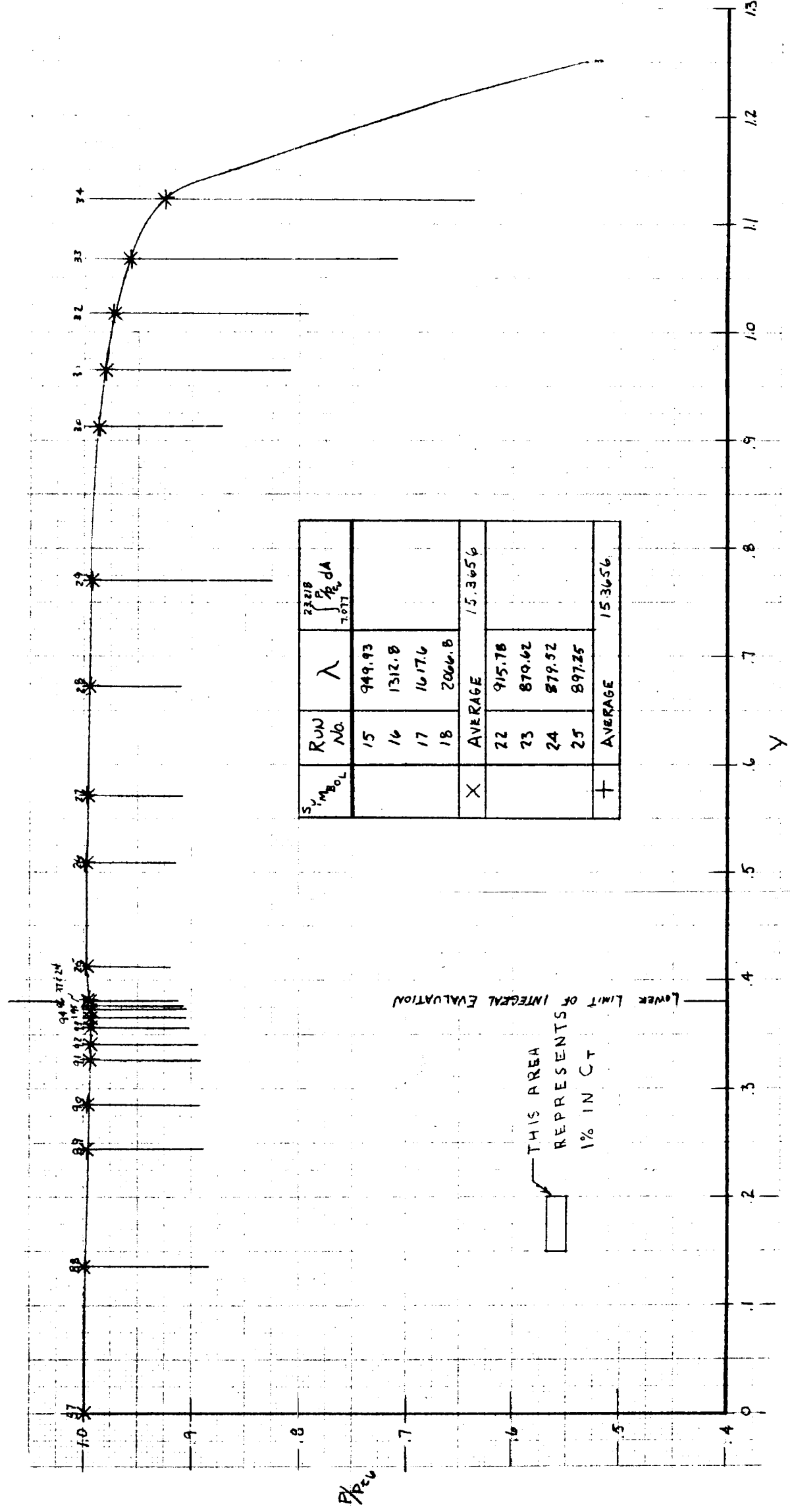
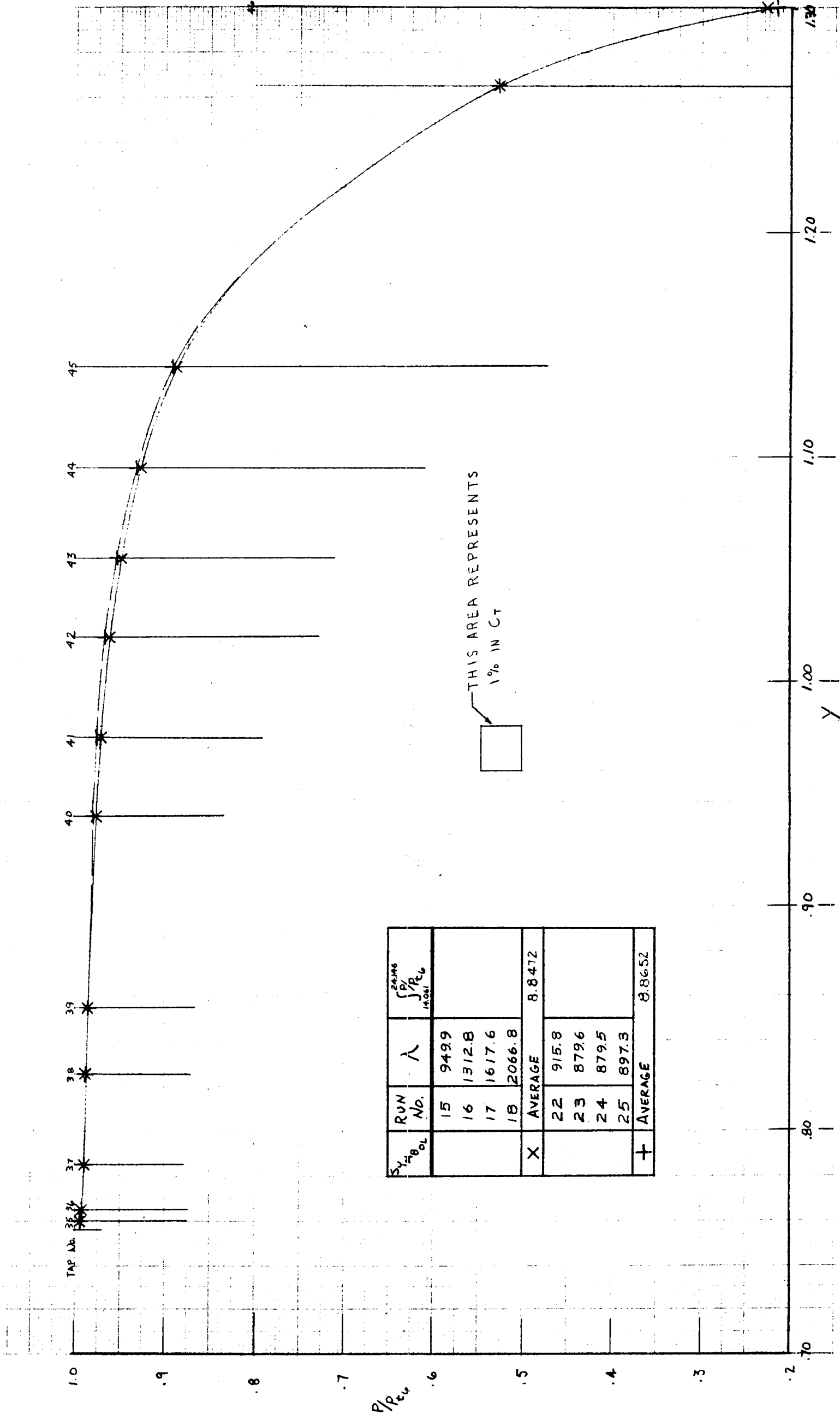


FIGURE 110. Shroud Pressure Distribution, 2-D Nozzle



SHROUD PRESSURE DISTRIBUTION (2 of 2)
 15° CONICAL NOZZLE, $\epsilon = 65$
 CHANNEL 8 DATE: 8-22-63
 9-10, 11-63

THIS AREA REPRESENTS
 1% IN C_T

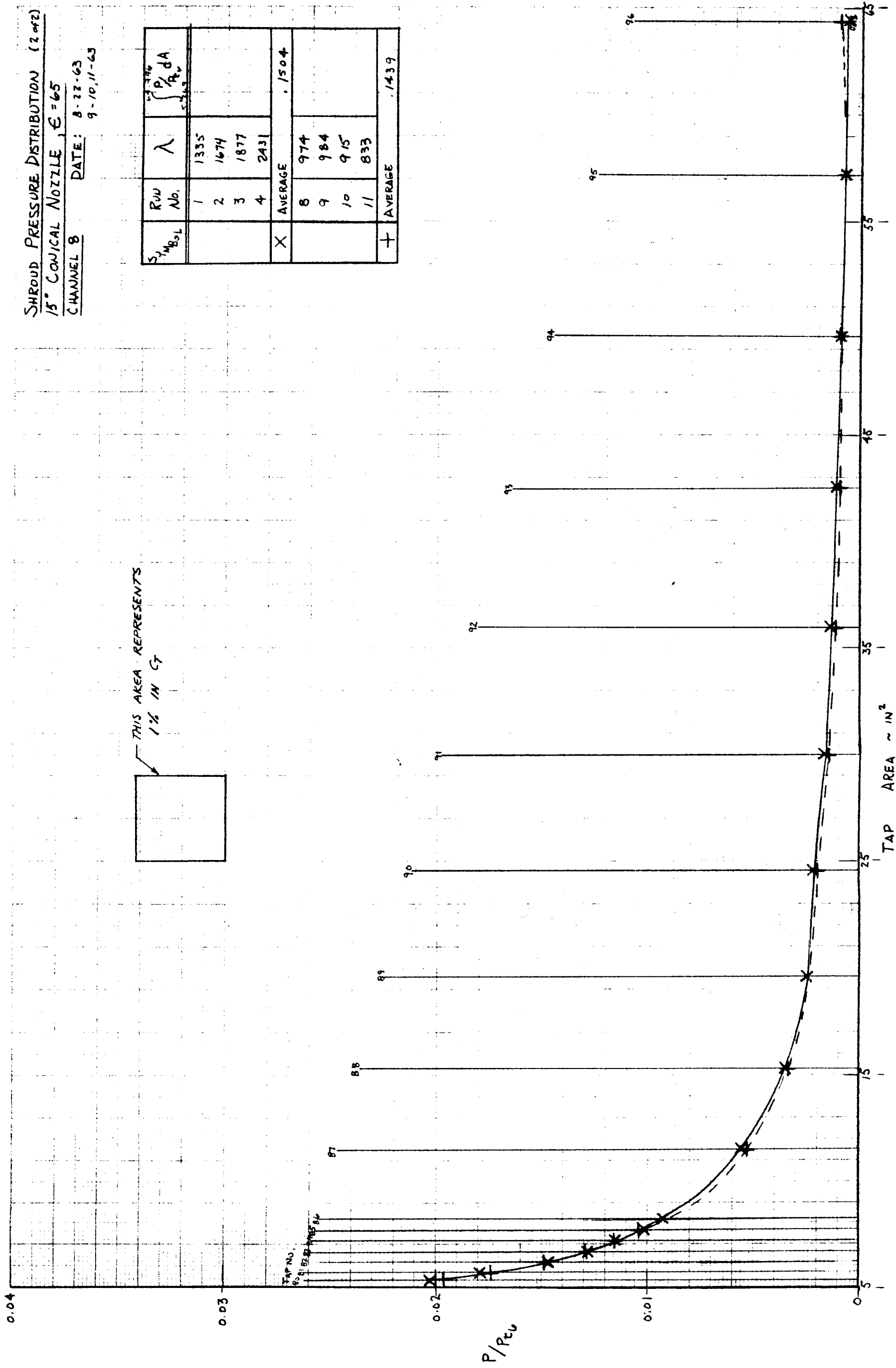
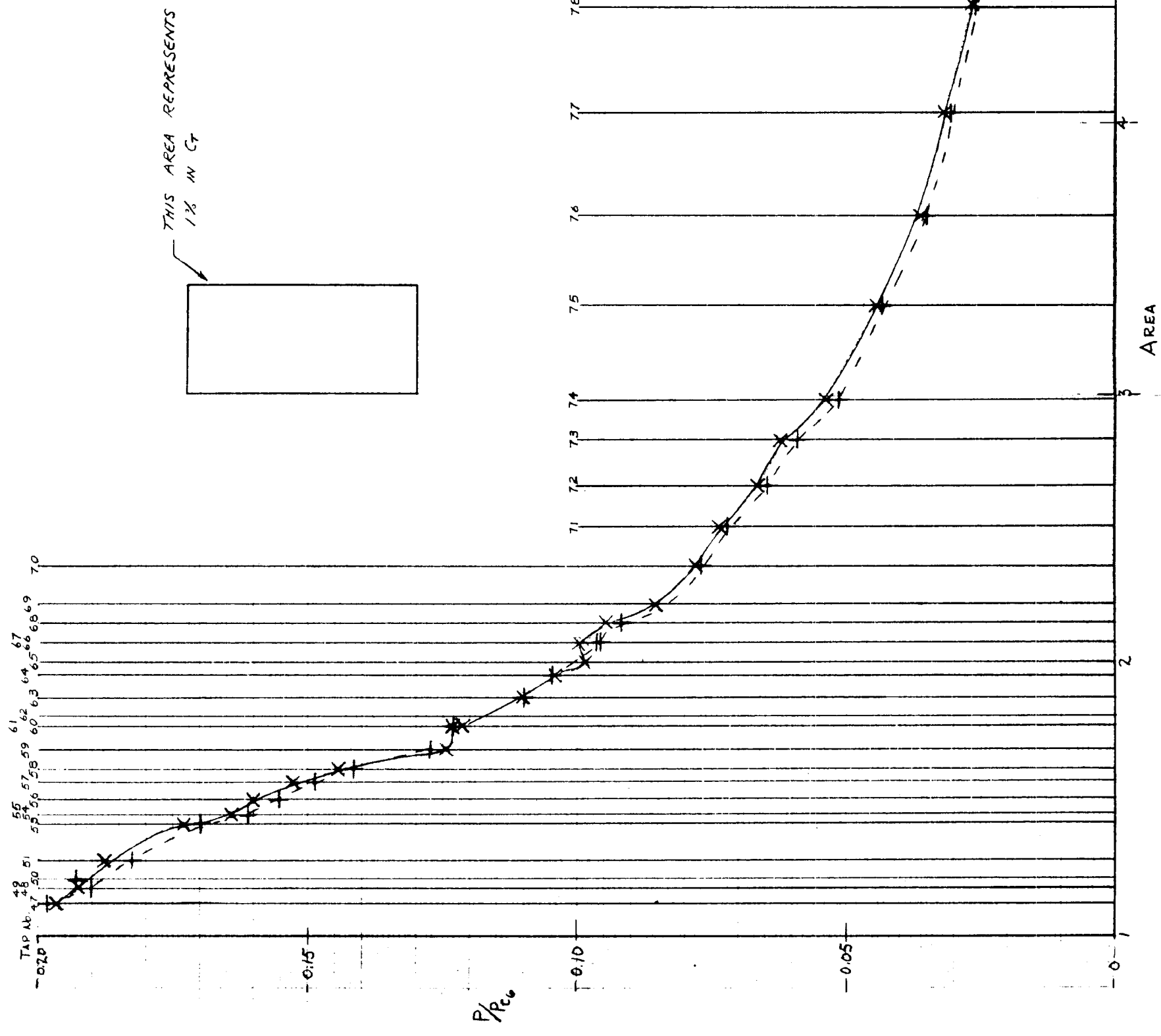


FIGURE 104. Conical Nozzle Pressure Distribution

SHROUD PRESSURE DISTRIBUTION (1 of 2)
 15° CONICAL NOZZLE, $\epsilon = 65$
 CHANNEL 8 DATE: 8-22-63
 9-10, 11-63

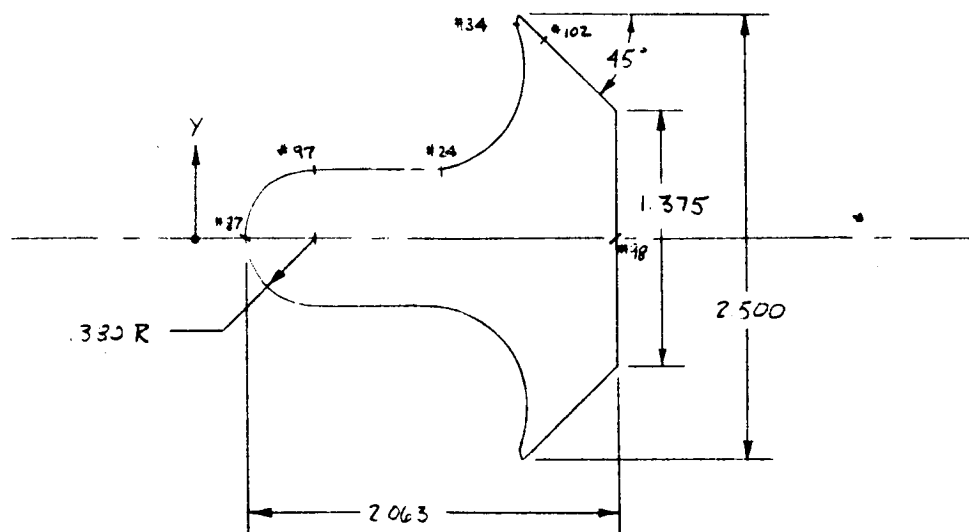


SYMBOL	ROW No.	λ	$\int \frac{P}{P_0} dA$
	1	1335	
	2	1674	
	3	1877	
	4	2431	
X	AVERAGE		.2798
	8	974	
	9	984	
	10	915	
	11	833	
+	AVERAGE		2736

FIGURE 103. Conical Nozzle Pressure Distribution

TAP NO.	X(in.)	R(in.)	Θ°	Area(in. ²)
18	17.398	1.056	0	3.503
19	16.901	1.056	10	3.503
20	16.421	1.056	20	3.503
21	15.948	1.056	30	3.503
22	15.897	1.054	40	3.490
23	15.883	1.0535	50	3.487
24	15.791	1.039	60	3.391
25	15.769	1.034	70	3.359
26	15.724	1.0185	80	3.259
27	15.660	.989	90	3.073
28	15.642	.977	100	2.999
29	15.588	.935	110	2.746
30	15.532	.887	120	2.469
31	15.489	.850	130	2.267
32	15.441	.809	140	2.056
33	15.385	.762	150	1.822
34	15.394	.769	330	1.858
35	15.306	.695	170	1.517
36	15.242	.648	180	1.319
37	15.247	.652	0	1.333
38	15.177	.613	200	1.180
39	15.114	.591	210	1.097
40	15.050	.574	220	1.035
41	14.937	.564	230	.999
42	14.937	.564	240	.999
43	14.940	.564	60	.999
44	14.956	.564	260	.999
45	14.843	.574	270	1.022
46	14.801	.580	280	1.057
47	14.753	.597	290	1.118
48	14.698	.612	300	1.175
49	14.699	.612	120	1.175
50	14.664	.621	320	1.210
51	14.599	.638	330	1.279
52	-	-	-	-
53	14.478	.671	350	1.414
54	14.448	.679	0	1.448
55	14.454	.678	180	1.442
56	14.400	.692	20	1.504
57	14.347	.707	30	1.568
58	14.308	.717	40	1.615
59	14.251	.733	50	1.686
60	14.183	.751	60	1.772
61	14.181	.752	240	1.772
62	14.152	.759	80	1.810
63	14.099	.773	90	1.877
64	14.035	.790	100	1.961
65	13.997	.700	110	2.011
66	13.948	.814	120	2.082
67	13.950	.813	300	2.082
68	13.895	.828	140	2.154
69	13.846	.841	150	2.222
70	13.749	.867	160	2.362
71	13.649	.894	170	2.511
72	13.549	.920	180	2.659
73	13.443	.949	190	2.829
74	13.351	.973	200	2.974
75	13.150	1.027	210	3.314
76	12.956	1.079	220	3.658
77	12.752	1.134	230	4.040
78	12.555	1.187	240	4.426
79	12.348	1.242	250	4.846
80	12.151	1.295	260	5.269
81	11.956	1.347	270	5.700
82	11.750	1.402	280	6.175
83	11.550	1.456	290	6.660
84	11.352	1.509	300	7.154
85	11.154	1.562	310	7.665
86	10.952	1.616	320	8.204
87	9.850	1.911	330	11.473
88	8.750	2.206	340	15.288
89	7.659	2.498	350	19.604
90	6.547	2.796	0	24.560
91	5.448	3.090	10	29.996
92	4.350	3.384	20	35.976
93	3.248	3.679	30	42.522
94	2.152	3.973	40	49.589
95	1.052	4.267	50	57.200
96	0.084	4.527	60	64.383

FIGURE 90. 15° Conical Nozzle - Pressure Tap Locations



CONTOUR TAPS		
TAP NO.	Y	Z
24	.381	1.14
25	.412	1.64
26	.509	2.14
27	.572	3.14
28	.673	3.64
29	.771	4.14
30	.913	4.88
31	.965	5.14
32	1.018	5.64
33	1.068	6.14
34	1.123	7.14
87	0	1.64
88	.135	1.74
89	.245	1.84
90	.285	1.94
91	.326	5.04
92	.341	5.14
93	.357	5.24
94	.364	5.34
95	.373	5.44
96	.377	5.54
97	.381	5.64
BASE TAPS		
TAP NO.	Y	Z
98	0	4.644
99	.160	4.644
100	.470	4.644
101	.780	4.644
102	1.100	4.644

FIGURE 93. 2-D Forced-Deflection Nozzle Centerbody

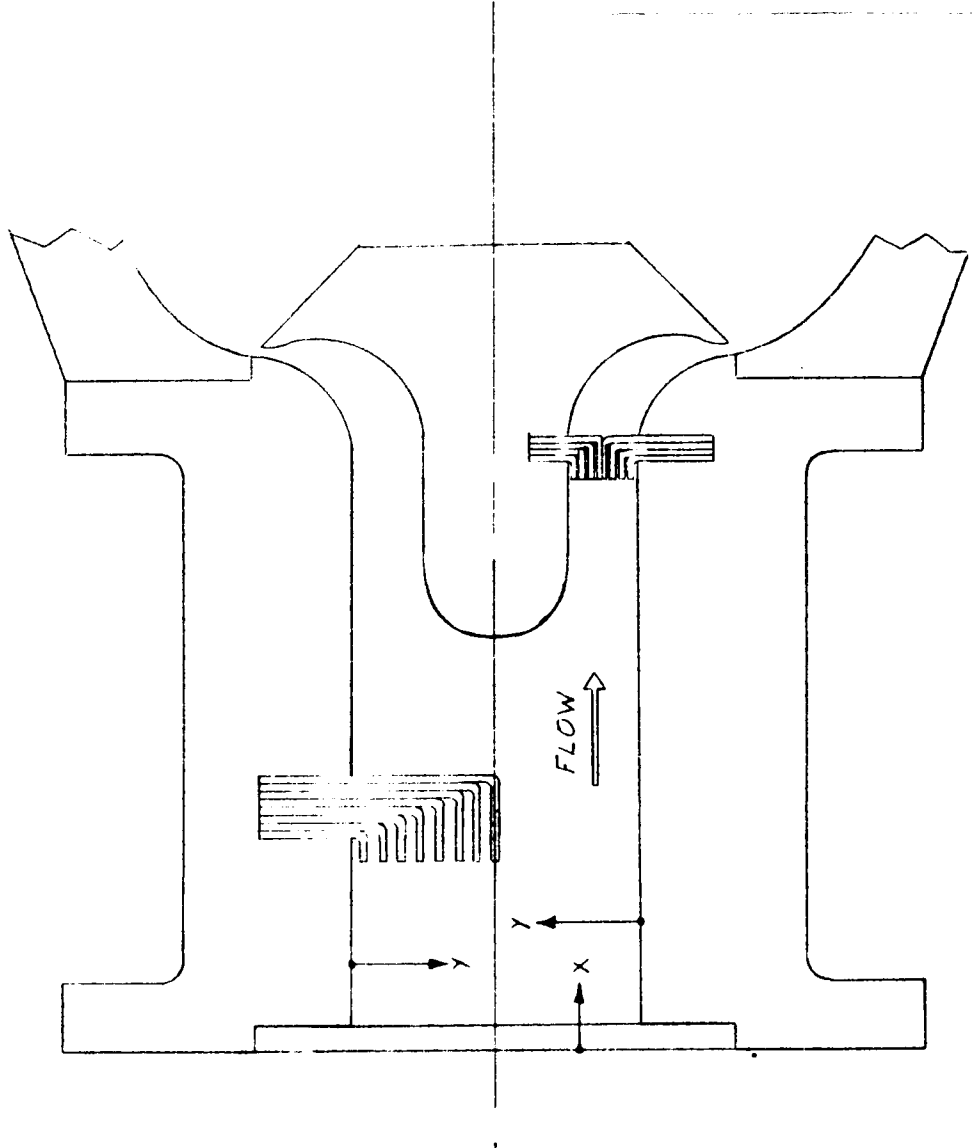


FIGURE 94. 2-D Forced-Deflection Nozzle Total and Boundary Layer Pressure Tap Locations

TAP NO.	X	Y	Z
1	2.985	.355	4.590
2		.320	
3		.275	
4		.225	
5	1.000	.060	4.630
6		.160	
7		.260	
8		.360	
9		.460	
10		.560	
11		.650	
12		.730	
13	1.096	.260	2.630
14		.580	
15		.770	
16	1.103	.260	.088
17		.570	
18		.770	
19	2.966	.155	4.910
20		.105	
21		.055	
22		.025	

NOTE: Z MEASURED FROM RIGHT SIDEWALL LOOKING UPSTREAM

"2-D F-D sidewall friction configuration," is shown in Figure 95, as are partial assemblies of the nozzle.

A boundary layer probe, detailed in Figure 96, was fabricated for use with both the conical and 2-D F-D configurations. Typical installation of the probe is shown in Figure 91. This probe was positioned at nominal area ratios of 20, 40, and 65 (exit).

5.3 DATA ANALYSIS PROCEDURES

The description of the data reduction and analysis procedures used for this study includes a presentation and discussion of the formulas and basic principles involved. A detailed set of calculations for a typical series of tests is included as Figure 97. The following discussion of data analysis procedures may be more easily understood by simultaneously referring to these sample calculations.

5.3.1 THRUST COEFFICIENT AND FRICTION LOSS

The thrust coefficient of an exhaust nozzle is defined as the ratio of the measured exhaust thrust, $mv + (P_e - P_a) A_e$, of the mass flow to the ideal exhaust thrust of the same actual mass flow. The general formula may be derived from momentum principles:

$$C_{TF} = \frac{(\text{Entering stream thrust}) + (\text{Forces on the stream tube to the exit}) - (\text{Ambient pressure} \times \text{exit area})}{\frac{W_a}{g} v_i}$$

Using the terminology of this study, C_{TF} is defined as follows:

$$C_{TF} = \frac{F_3 - F_D - P_a A_e}{\frac{W_a}{g} v_i}$$

The term F_3 (the entering stream thrust) was evaluated using the actual area at station 3, the metered weight flow, measured static pressure, and one-dimension-flow tables. For the configurations tested the inlet flow was not one-dimensional, since a thin boundary layer was developed in the contraction

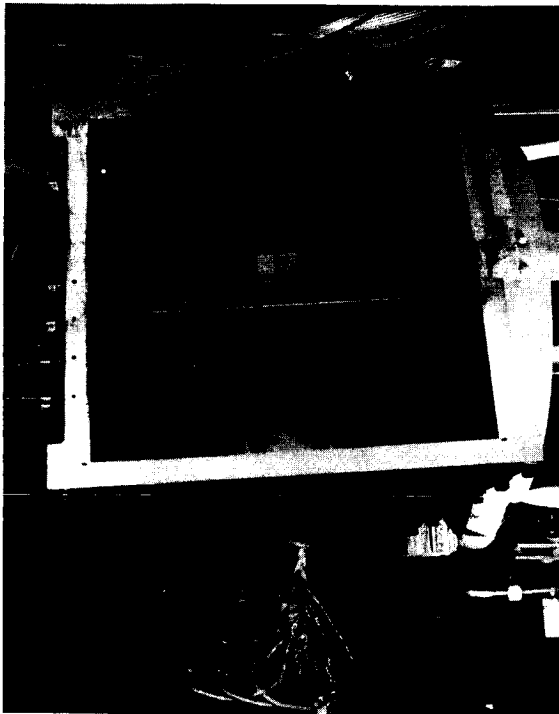
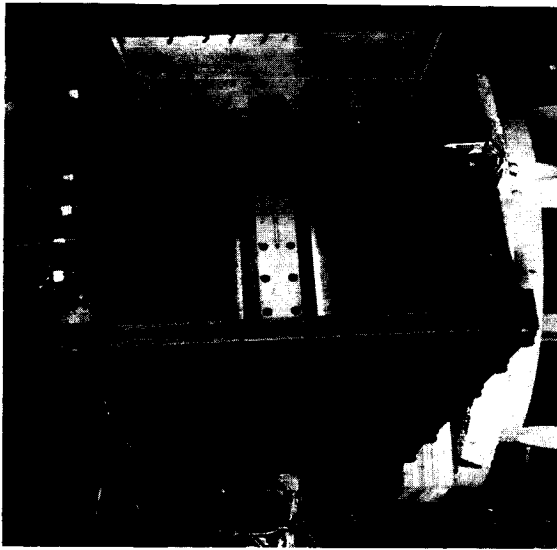
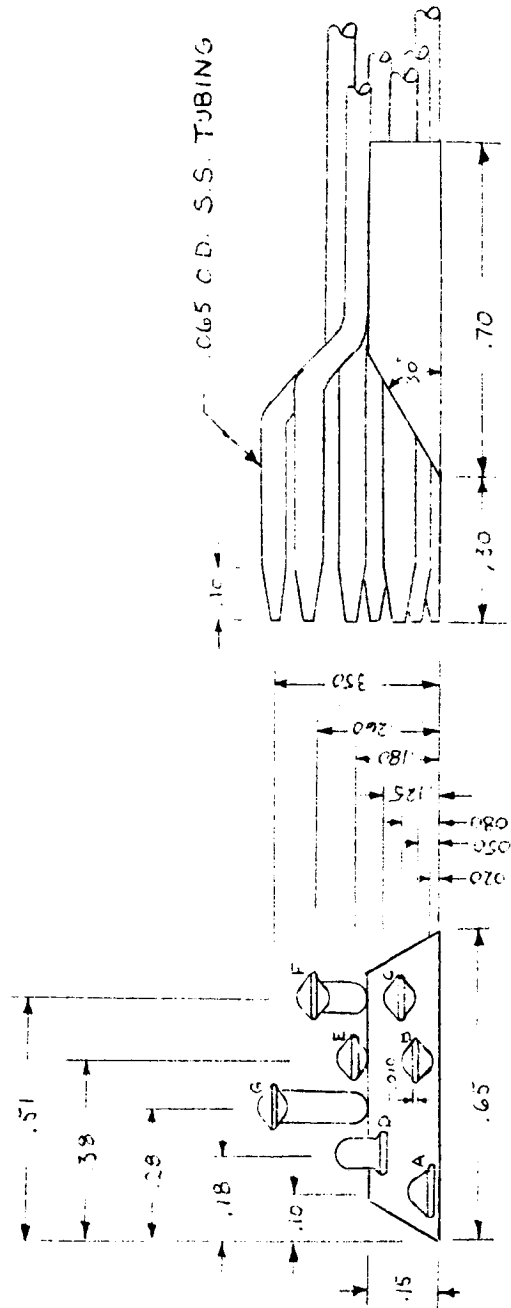


FIGURE 95. Photographs of 2-D Forced-Deflection Nozzle



ALL DIMENSIONS IN INCHES
2 1/2" SCALE

FIGURE 96. Boundary Layer Probe

RUN DATE 8-22-63

$$K_1 = \frac{C_{D1} M_1 A_1}{A_3} = .993(5318) \frac{A_1}{A_3} = .07585$$

$$K_2 = C_{D1} A_1 = .993 A_1 = .4991$$

$$K_3 = \frac{C_{D1} A_1}{A_8} = .993 \frac{A_1}{A_8} = .4991$$

$$A_1 = .5027 \text{ in}^2$$

$$A_3 = 3.500 \text{ in}^2$$

$$A_8 = 1.000 \text{ in}^2$$

$$A_9 = 64.996 \text{ in}^2$$

$$C_2 \rightarrow 370.90 \quad 369.00 \quad 368.00 \quad 366.50$$

$$K_{20} \rightarrow .006686 \quad .6684 \quad .6683 \quad .6682$$

$$A_3 = 3.500 \text{ in}^2$$

$$A_8 = 1.000 \text{ in}^2$$

$$A_9 = 64.996 \text{ in}^2$$

No.	NAME	OPERATION	UNITS	RUN NO. 1	RUN NO. 2	RUN NO. 3	RUN NO. 4
1	Nominal Test M						
2	Barometer Pressure		Hga	-0-	-0-	-0-	-0-
3	P _{t,1}	From Data Sheet	psia	29.04	29.05	29.04	29.05
4	P _{t,2}	From Data Sheet	psia	256.56	257.07	256.76	257.27
5	P ₃	From Data Sheet	psia	129.21	129.12	129.06	128.97
6	P _{t,6}	From Data Sheet	psia	126.65	126.57	126.50	126.42
7	P _a	From Data Sheet	psia	129.21	129.12	129.06	128.97
8	M _{3,1-D}	From Data Sheet	psia	.097	.077	.069	.053
9	P ₃ /P _{t,3}	From Flow Tables for \dot{m}		.1537	.1541	.1540	.1544
10	P/P ₃	From Flow Tables for \dot{m}		1.0389	1.0391	1.0391	1.0393
11	F _{3,1-D}	$A_3 \times 5 \times 10$	lbs	460.51	460.31	460.06	459.86
12	P _{t,3} Eff	$5/9$	psia	1335.2	1674.3	1876.7	2431.1
13		From Data Sheet		1.6918	1.6995	1.7033	1.7112
14	$\frac{m V_L}{P_{t,6} A_8}$	From Graph for		216.62	218.05	218.28	219.72
15	$\frac{W_a}{g} V_L$	$K_2 \times 3 \times 14$	lbs	.9910	.9937	.9929	.9956
16	C _{D8}	$K_3 \times 3/16$					

No.	NAME	OPERATION	UNITS	RUN NO. 1	RUN NO. 2	RUN NO. 3	RUN NO. 4
17	H ₂ O	Balance Force, C ₂ x K ₂₀	lbs	247.98	246.64	245.93	244.90
18	P _a A ₃	⑦ x A ₃	lbs	.34	.27	.24	.19
19	H	⑪ - ⑪⑦ - ⑪③	lbs	212.19	213.40	214.14	214.77
20	C _{T,1-D}	⑲ / ⑮		.9795	.9787	.9799	.9775
21	P _a A ₉	⑦ A ₉	lbs	6.30	5.00	4.48	3.44
22	$(1+M^2) \frac{P_a}{P_{a,9}}$	⑲ + ⑳	lbs	218.49	218.40	218.62	218.21
23	C _{D8} F ₈ P _{t,6}	K ₂ x ③	lbs	128.05	128.30	128.15	128.40
24	f _{9,1-D}	⑳ / ⑳		1.7063	1.7023	1.7060	1.6995
$C_{TF} = \frac{F_3 - H_2 - P_{a,3}}{\frac{W_a}{g} V_i}$				$\bar{f}_{9,1-D} = 1.7035 \pm 0.20\%$			
25	$\frac{(1+M^2)}{(1+M^2)_{1-D}}$	From Inlet Press. Dist. and Graph. Integration		.9971			
26	F ₃	⑪ x ⑳	lbs	459.17	458.97	458.72	458.52
27	ΔF ₃	⑪ - ⑳	lbs	-1.34			
28	Δ C _T	㉑ / ⑮		-.0062	-.0062	-.0062	-.0061
29	C _{TF}	㉑ - ㉑		.9733	.9725	.9737	.9714

$\bar{f}_9 = 1.6988$

FIGURE 97. Sample Thrust Calculations - 15° Conical Nozzle
Thrust Data - High R_N

upstream of the seal. The entering stream thrust was integrated to account for these boundary layer effects, Figure 98; the one-dimensional stream thrust was then corrected accordingly.

The basic quantities measured during typical Channel 8 runs were P_{T1} , P_3 , P_a , P_{T6} , P_{T2} , and H_{2O} . A mass flow function was then computed for station 3, where \dot{m}_3 is tabulated as a function of Mach number in Reference 15.

$$\dot{m}_3 = g \sqrt{\frac{\gamma}{R}} \times M \left[1 + \frac{\gamma-1}{2} M^2 \right]^{1/2} = \frac{W_a \sqrt{T_t}}{P_3 A_3}$$

Since
$$W_a = \frac{.5318 P_{t1} A_1 C_{D1}}{\sqrt{T_t}}$$

\dot{m}_3 could be calculated for each run directly in terms of constants and measured values:

$$\dot{m}_3 = \frac{.5318 C_{D1} P_{t1} A_1}{P_3 A_3}$$

P_3 was then calculated from the dimensionless stream thrust (f/P) obtained from one-dimensional-flow tables (Reference 15) using the above \dot{m}_3 as a parameter.

$$F = (f/P_3 \times P_3 \times A_3) \text{ where } f/P_3 = (1 + M_3^2)$$

The ideal momentum of the actual mass flow ($\frac{W_a}{g} v_i$) is a function only of the actual flow and operating pressure ratio. For convenience, accurate curves of

$$\frac{m_i v_i}{P_{t6} A_8}$$

as a function of γ are available. The denominator of C_{TF} was then evaluated using

$$\frac{m_i v_i}{P_{t6} A_8}$$

for the test and the metering nozzle data:

$$\frac{W_a}{g} v_i = C_{D8} P_{t6} A_8 \frac{m_i v_i}{P_{t6} A_8} = C_{D1} P_{t1} A_1 \eta$$

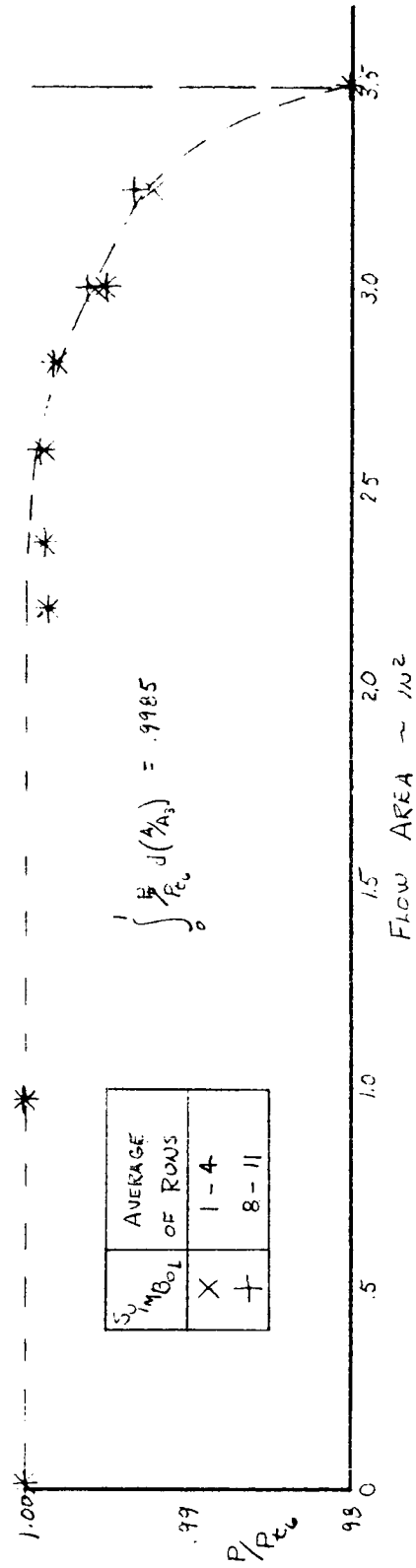
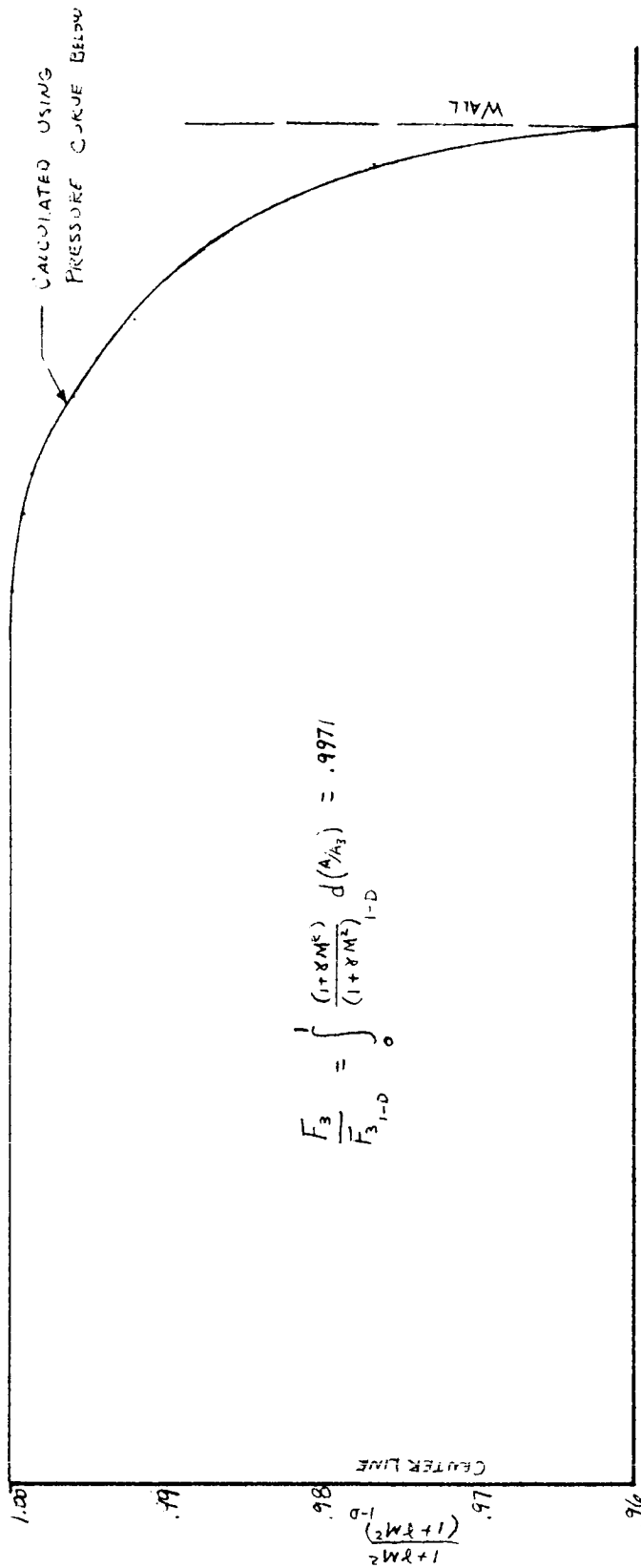
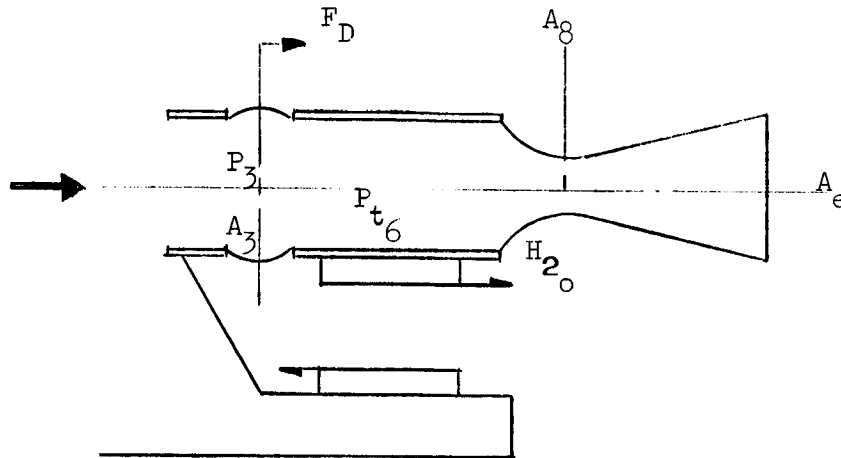


FIGURE 98. Inlet Momentum Integration, 15° Conical Nozzle

The second term in the numerator of the expression for C_{TF} is F_D , the interior contour drag force. The balance system does not measure this term directly, but instead values of H_{2O} are obtained which include all forces acting on the model assembly downstream of the seals.



By summing forces from the above figure

$$F_D = H_{2O} + P_a (A_3 - A_e)$$

Thus:

$$C_{TF} = \frac{F_3 - H_{2O} - P_a A_3}{\frac{W_a}{g} v_i}$$

Thrust coefficients were also evaluated from the pressure-area forces as determined by integration of the pressure distribution on the nozzle contours.

$$C_{TP} = \frac{F_3 - \sum \int P \, dA - P_a A_e}{\frac{W_a}{g} v_i} = \frac{F_3 - \sum \int P \, dA - P_a A_e}{C_{D8} A_8 P_{t6} \eta}$$

$$C_{TP} = \frac{F_3/P_{t6} - \sum \int P/P_{t6} \, dA - A_e}{C_{D8} A_8 \eta}$$

C_{T_P} does not include friction forces, thus the thrust loss due to friction is

$$\Delta C_{T_f} = C_{T_P} - C_{T_F}$$

5.3.2 DISCHARGE COEFFICIENT

Discharge coefficients for the model were calculated using a choked ASME long-radius metering nozzle as a standard (Reference 16). Continuity gave the following equation for the model discharge coefficient.

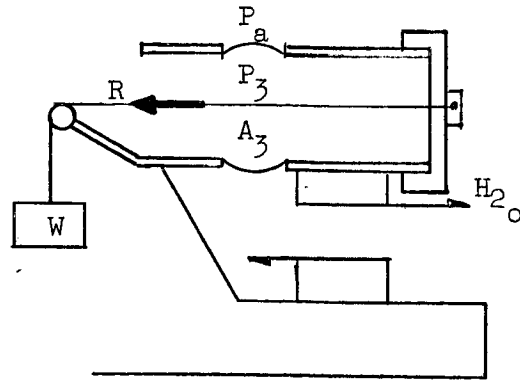
$$C_{D_8} = \frac{0.993 A_1 P_{t_1}}{P_{t_6} A_8}$$

where 0.993 is the discharge coefficient of the ASME nozzle at a typical pipe Reynolds number for this program.

5.3.3 BALANCE CALIBRATION

The seal used to separate the nozzle and balance assembly from the inlet duct is a simple pressure-tight expansion joint consisting of a thin rubber membrane lying over a small gap between two metal plates. If the deflection under load can be kept low, the stretch in the thin rubber seal will also be low, and the tensile forces across the seal can be incorporated into the balance calibration. Two problems associated with seals of this type are: (1) the difficulty in matching the diameter of the seal to the inlet duct diameter and (2) the possibility of forcing the thin rubber membrane into the gap between the two plates with high integral operating pressures. The combination of these two factors requires that the seal and balance assembly must be calibrated in place under simulated operating conditions to include the effect of the seal as it varies with axial deflection (load) and internal pressure.

The calibration set-up is shown in the sketch.



The calibration rig consisted of a rigid beam attached to the force balance pick-up ring. This beam assembly also sealed the duct to allow pressurization. Attached to the end of the beam, parallel to the tunnel centerline, was a wire running upstream over a pulley arrangement to the horizontal weight basket. The balance was calibrated under simulated conditions as follows. The inlet duct was pressurized to test values of seal station differential pressure (ΔP_3). The balance was then given a series of reverse loads by means of the weight-pulley setup to simulate the range of resultant loads applied to the balance during model tests. From the sketch, summing horizontal forces, we obtain

$$H_{2O} = (\Delta P_3) A_3 - R.$$

The resultant balance load is readout on an electronic digital readout system, the calibration giving the relation between the net balance load and the readout counts.

The balance load (H_{2O}) may then be represented as the product of a calibration constant (K_{2O} , lb/count) and the readout counts (c_2). Hence the final calibration is plotted as K_{2O} vs counts for various values of (ΔP_3).

NOTATION

A	Cross-Section Area, in ²
C ₂	Horizontal Balance Readout, Counts
C _D	Discharge Coefficient, Dimensionless
C _T	Static Thrust Coefficient, Dimensionless
ΔC _T	Thrust Coefficient Decrement, Dimensionless
D	Diameter, in.
f/p	Stream Thrust Per Unit Area Function, Dimensionless
F	Stream Thrust, lb
g	Gravitational Constant, ft/sec ²
H	Horizontal Thrust Component, lb
H _{2o}	Horizontal Balance Force, lb
K	Constants Used in Data Reduction
K _{2o}	Horizontal Force Constant, lb/count
	Characteristic Length, ft
M	Mach Number, Dimensionless
η	$\frac{m_i v_i}{P_{t6} A_i}$ Non-Dimensional Ideal Thrust
m	Mass Flow Rate, slugs/sec
\dot{m}	Mass Flow Function °R ^{1/2} /sec
P	Pressure, Static Unless Otherwise Specified by Subscript, psia.
R	Gas Constant, 1716.3 ft ² /sec ² °R
R	Radius, in.
R _N	Reynolds Number, Dimensionless

r	Radial Location from Model Centerline, in.
T	Temperature, °R
V	Velocity, ft/sec
W	Weight Flow Rate, lb/sec
X	Axial Coordinate, in.
Y	Vertical Coordinate, in.
y	Distance Perpendicular to Nozzle Contour, in.
δ	Boundary Layer Thickness, in.
ϵ	Nozzle Geometric Area Ratio, Dimensionless
λ	Nozzle Pressure Ratio, Dimensionless
γ	Ratio of Specific Heats, Dimensionless, 1.4 for Air
θ	Meridian Angle Measured Clockwise Looking Upstream

Subscripts

a	Ambient or Actual
b	Base
des	Design
e	Exit
Eff	Effective
f	Friction
F	Force
i	Ideal
P	Pressure
t	Total Conditions
W	Wall
1	Metering Nozzle Station
2	Facility Stagnation Chamber
3	Flexible Seal Station
6	Model Inlet Station
8	Model Throat Station
9	Model Exit Station

5.4 DISCUSSION OF RESULTS

5.4.1 15° CONICAL NOZZLE

Static thrust coefficients, evaluated both from direct force measurements and integration of the pressure distributions on the nozzle contours, are presented in Figure 99. Since all data points were in the fully expanded flow region (constant exit stream thrust) the thrust curves shown were calculated using the average exit stream thrust parameter, \bar{F}_9 , and the effective design area ratio,

$$\frac{A_E}{C_{D8} A_8 C_{T_{Max}}}$$

The maximum $C_{T_{Max}}$ is indicated on the curve by a tic mark at design pressure ratio (corresponding to the effective design area ratio). Absolute levels of the thrust curves calculated from the force data were identical at both Reynolds number conditions with $C_{T_{F_{des}}} = 0.974$. Frictional thrust loss, obtained as the difference between the pressure and force performance curves, increased slightly with decreasing R_N from $\Delta C_{T_f} = 0.4$ to 0.5. Design thrust performance is summarized in Table V, and a test schedule is listed in Figure 100.

Increased boundary layer thickness at the throat at low R_N is evidenced by a 0.3 drop in discharge coefficient from $C_{D8} = 0.993$ to 0.990 (Figure 101).

Pressure distributions on the nozzle contour are presented in Figures 102, 103 and 104. Pressure ratios on the divergent shroud contour were generally lower at the low R_N . The sensitivity of thrust coefficient to the pressure area integrations is noted on each of the pressure distribution plots.

The boundary layer was surveyed at three positions in the conical shroud for each R_N level, using the wedge boundary layer probe shown in Figure 96. Resulting pressure profiles are presented in Figure 105. As a check, a conventional small-blockage total pressure rake was fabricated and

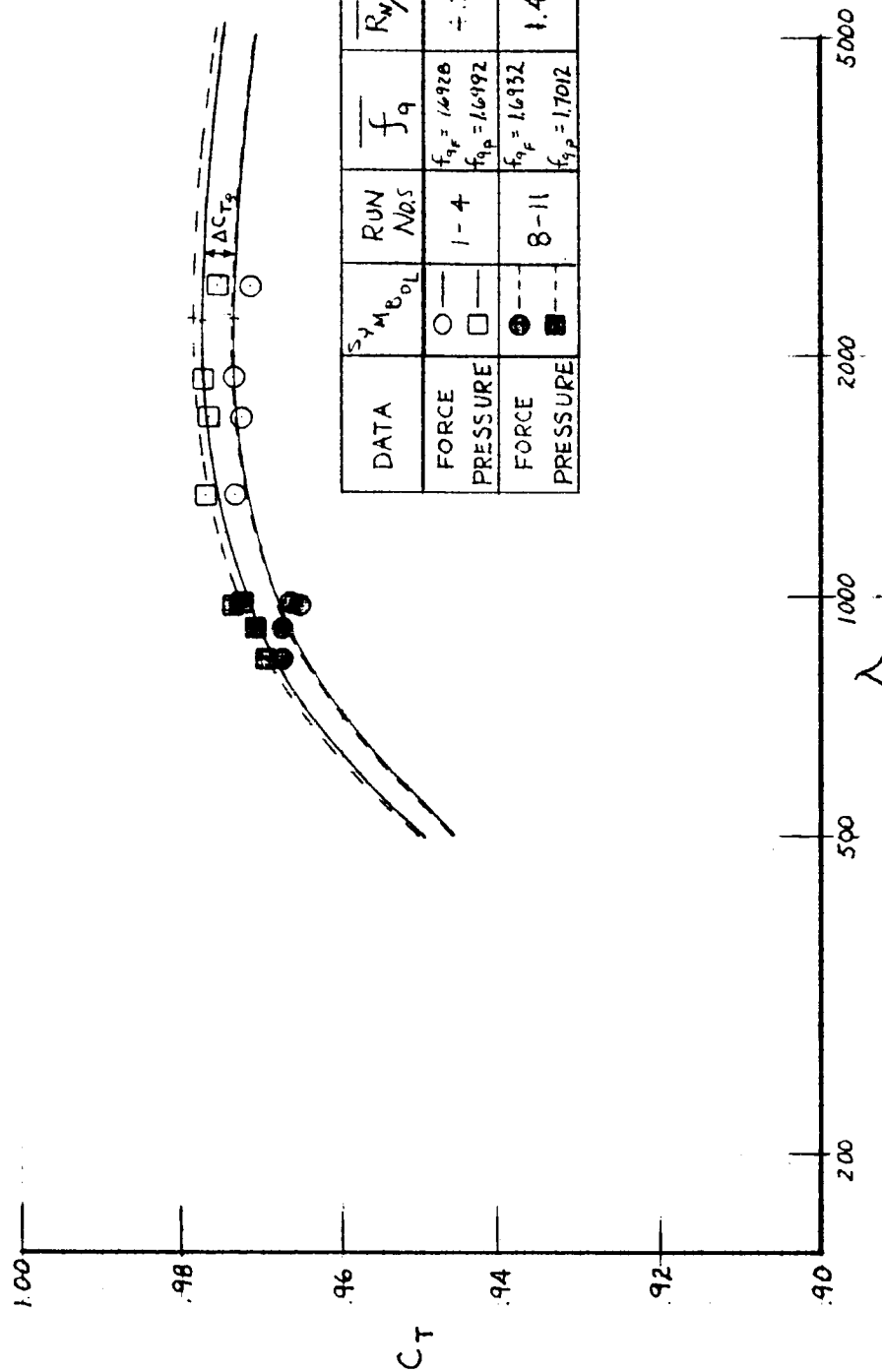


FIGURE 99. Static Thrust Coefficients, 15° Conical Nozzle

TABLE V
PERFORMANCE SUMMARY

CONFIGURATION	$R_{N/\lambda}$ (ft ⁻¹)	$\frac{A_E}{C_{D8} A_8 C_{TMAX.}}$	$\lambda_{des.}$	C_{TF} at $\lambda_{des.}$	ΔC_{Tf} at $\lambda_{des.}$
15° Conical Nozzle	4.20 x 10 ⁷	67.23	2211	0.974	0.004
	1.46 x 10 ⁷	67.42	2222	0.974	0.005
2-D F-D Nozzle	4.22 x 10 ⁷	90.76	3400	0.972	0.028
	1.47 x 10 ⁷	94.07	3579	0.971	0.022

FLUIDDYNE ENGINEERING CORPORATION

TEST CONFIGURATION: 15° CONICAL NOZZLE

<u>RUN NO.</u>	<u>λ</u>	<u>$R_{N/1} \times 10^{-7} (\text{ft}^{-1})$</u>	<u>ϵ</u>	<u>COMMENTS</u>
1	1335	4.20		Force and Contour Pressure Data
2	1674	4.20		
3	1877	4.20		
4	2431	4.20		
5	1450	4.20	20	Boundary Layer Survey Data
6	1466	4.20	40	
7	1574	4.20	65	
8	974	1.46		Force and Contour Pressure Data
9	984	1.46		
10	915	1.46		
11	833	1.46		
12	727	1.46	20	Boundary Layer Survey Data
13	1007	1.46	40	
14	790	1.46	65	

TEST CONFIGURATION: 2-D F-D NOZZLE

15	950	4.22		Force and Contour Pressure Data
16	1313	4.21		
17	1618	4.21		
18a	2067	4.22		
18b	2281	4.15		Sidewall Friction Configuration, Force Data
18c	2494	4.14		
19	1968	4.21	20	Boundary Layer Survey Data
20	1856	4.21	40	
21	694	4.21	65	
22	916	1.49		Force and Contour Pressure Data
23	880	1.46		
24	880	1.46		
25	897	1.49		
26	723	1.45	20	Boundary Layer Survey Data
27	830	1.46	40	
28	787	1.46	65	

FIGURE 100. Channel 8 Test Schedule

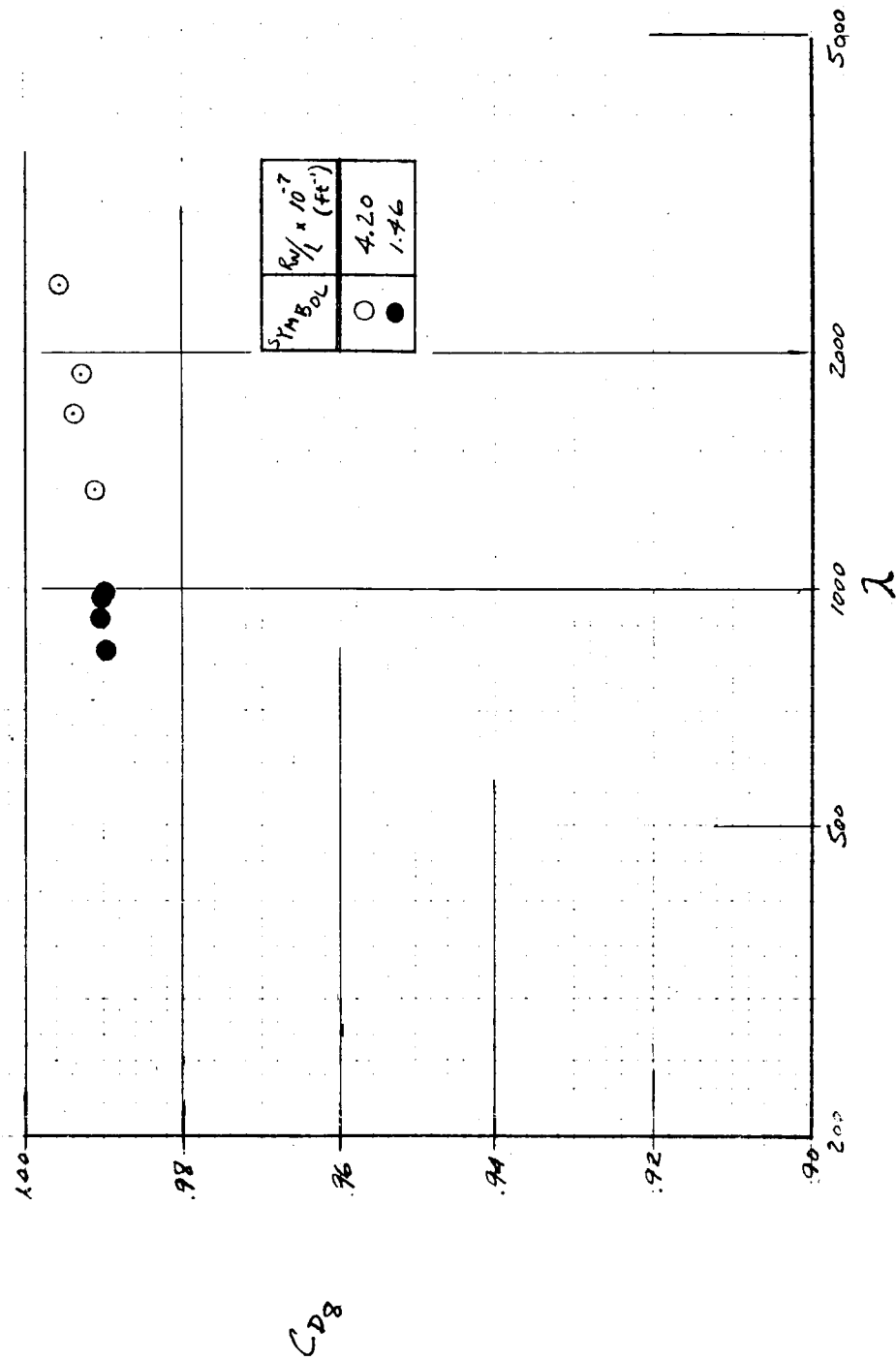


FIGURE 101. Discharge Coefficients, 15° Conical Nozzle

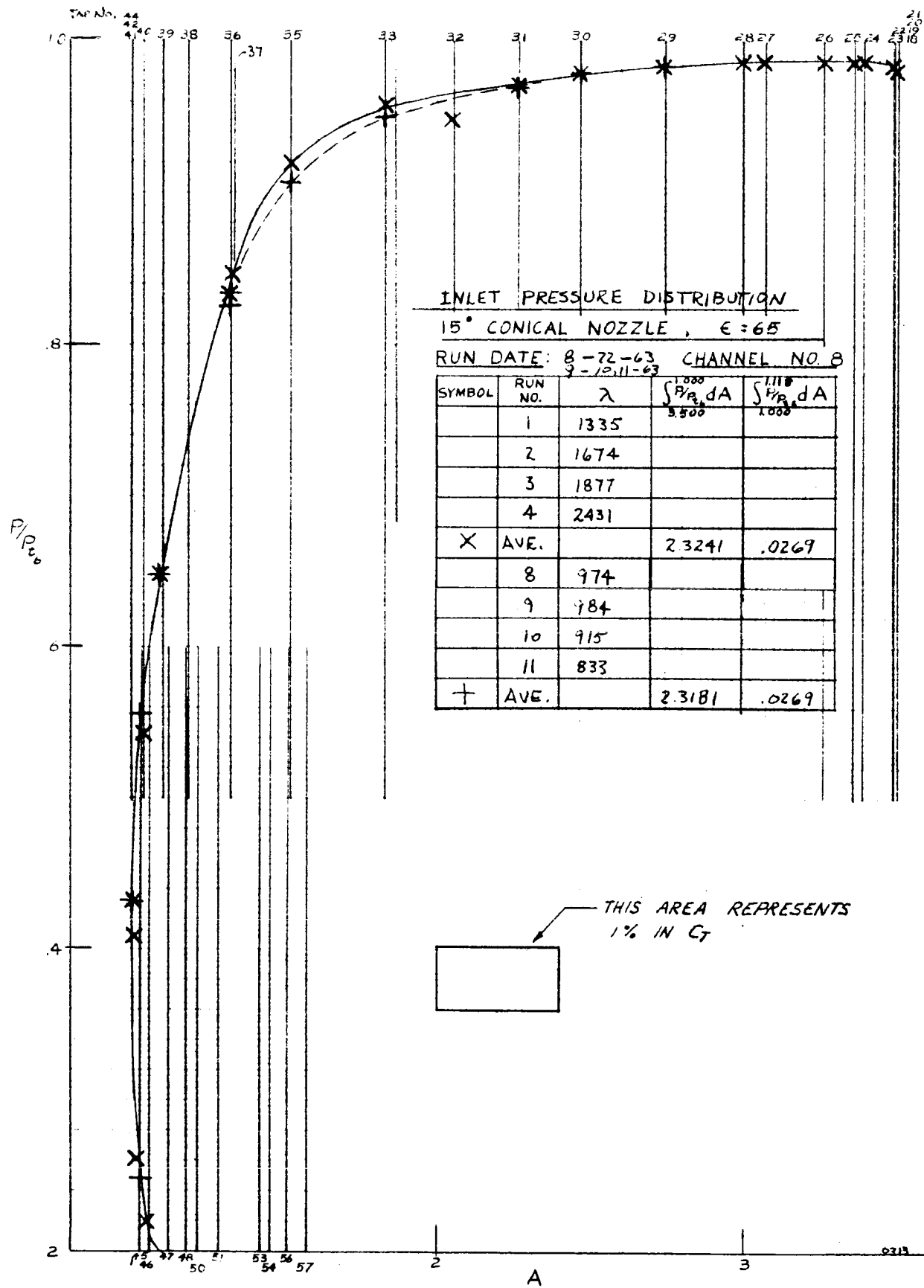


FIGURE 102. Conical Nozzle Pressure Distribution

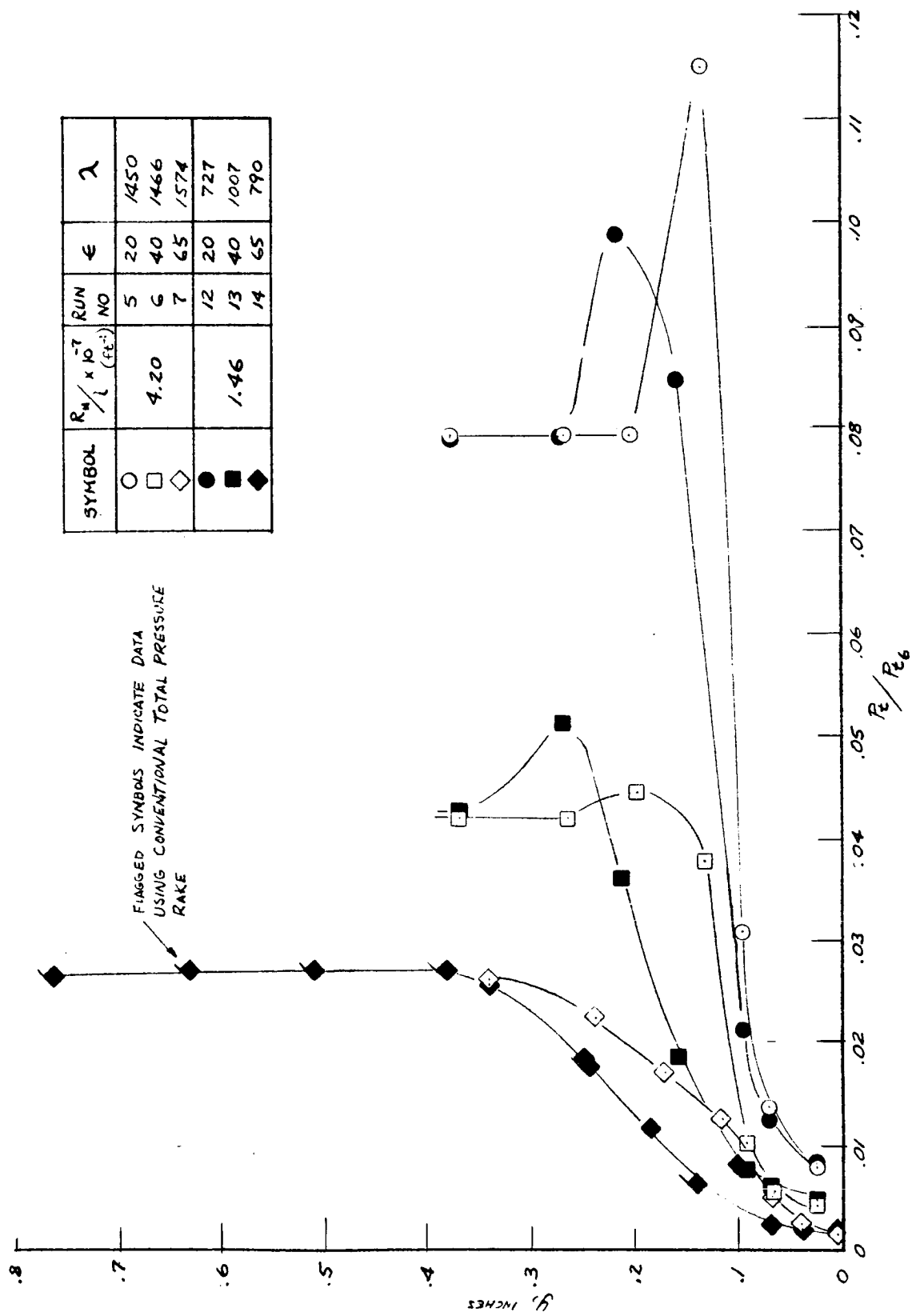


FIGURE 105. Boundary Layer Surveys

used at the exit, resulting in substantiation of the wedge probe data at the nozzle exit and extending the survey to $Y = 0.76$ inches as shown in Figure 105. The exit pressure profile indicates a nominal boundary layer thickness $\delta = 0.35$ for low R_N and $\delta = 0.30$ for high R_N .

5.4.2 TWO-DIMENSIONAL FORCED DEFLECTION NOZZLE

Thrust performance of the 2-D F-D nozzle as shown in Figure 106 indicated a design $C_{T_F} = 0.972$ for the high R_N flow condition, which was within 0.1 of the value obtained for the lower R_N condition. It was noted, however, that two different flow conditions existed in the nozzle depending on Reynolds number level. The flow for the high R_N condition was closed at the nozzle exit (i.e., completely filling the nozzle exit area). This flow pattern resulted in centerbody base pressures considerably less than ambient, as shown in Figure 107, while the base pressure at low R_N was greater than ambient.

The sketch in Figure 107 shows the two distinct flow regimes: flow in two "layers" separated by a base cavity or void, and coalescing flow where the two jets combine to fill the exit area. An indication of the first flow regime is given by the lampblack streaks visible on the model sidewall in Figure 95. Lampblack patterns at the high R_N condition indicated the flow field closed near the nozzle exit. Similar flow patterns have been observed in annular-flow forced-deflection models, e.g., Reference 17. A "two-dimensional" nozzle introduces an added complication, however, depending on whether the flow closes upstream or downstream of the sidewall exits. Further complication arises from the possibility of a disturbance from the second-throat diffuser propagating upstream into the open base cavity; see Reference 18.

The low R_N data (semi-open symbols, Figure 106) was therefore corrected for the base pressure difference in Figure 107, i.e., the thrust performance comparison is based on the closed-flow condition for both R_N levels. This correction resulted in lowering C_{T_F} by about 1.7%. Frictional thrust losses were considerably higher than observed for the conical nozzle, being $\Delta C_{T_F} = 2.2\%$ and 2.8% for the low and high R_N , respectively.

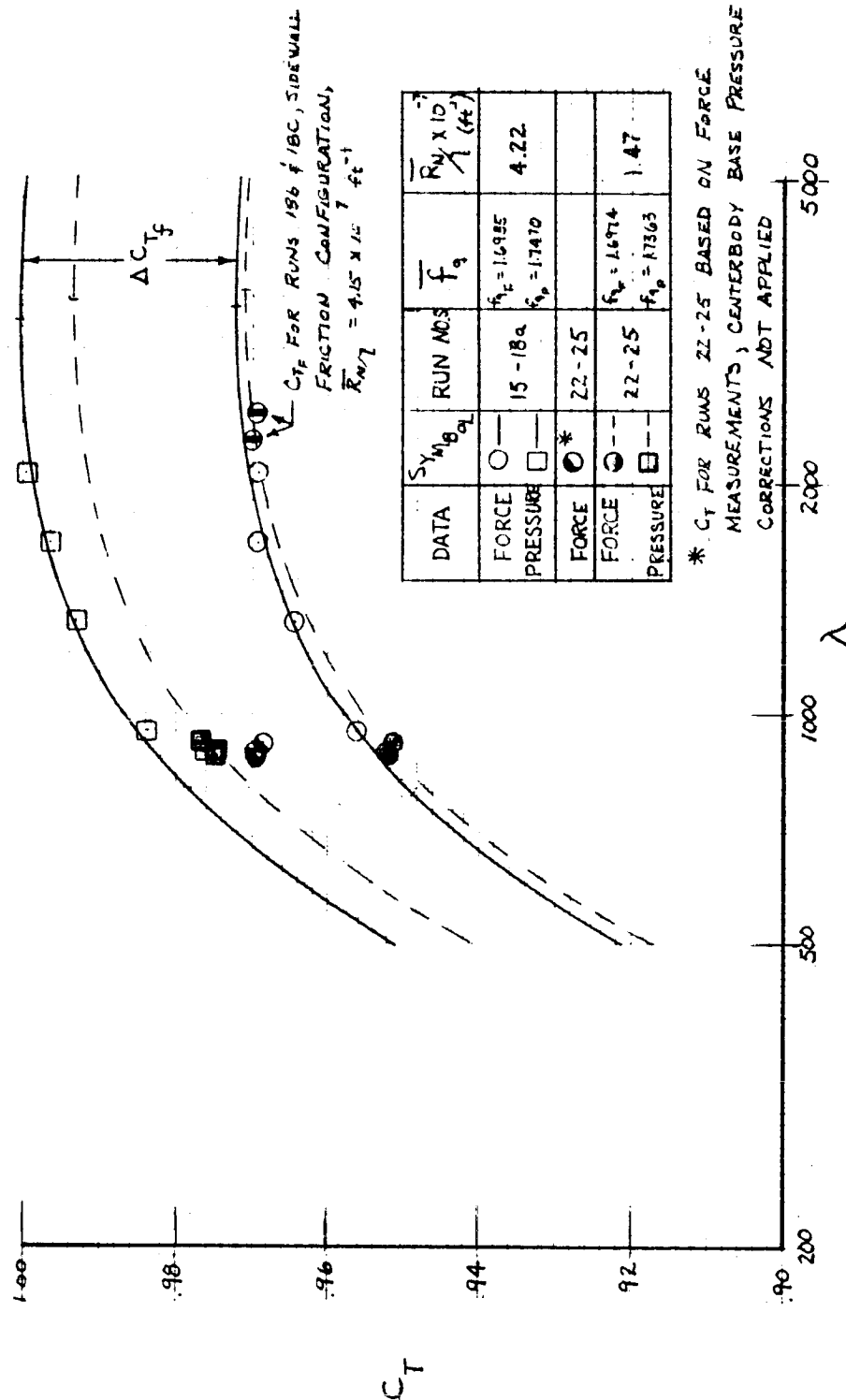


FIGURE 106. Static Thrust Coefficients, 2-D Nozzle

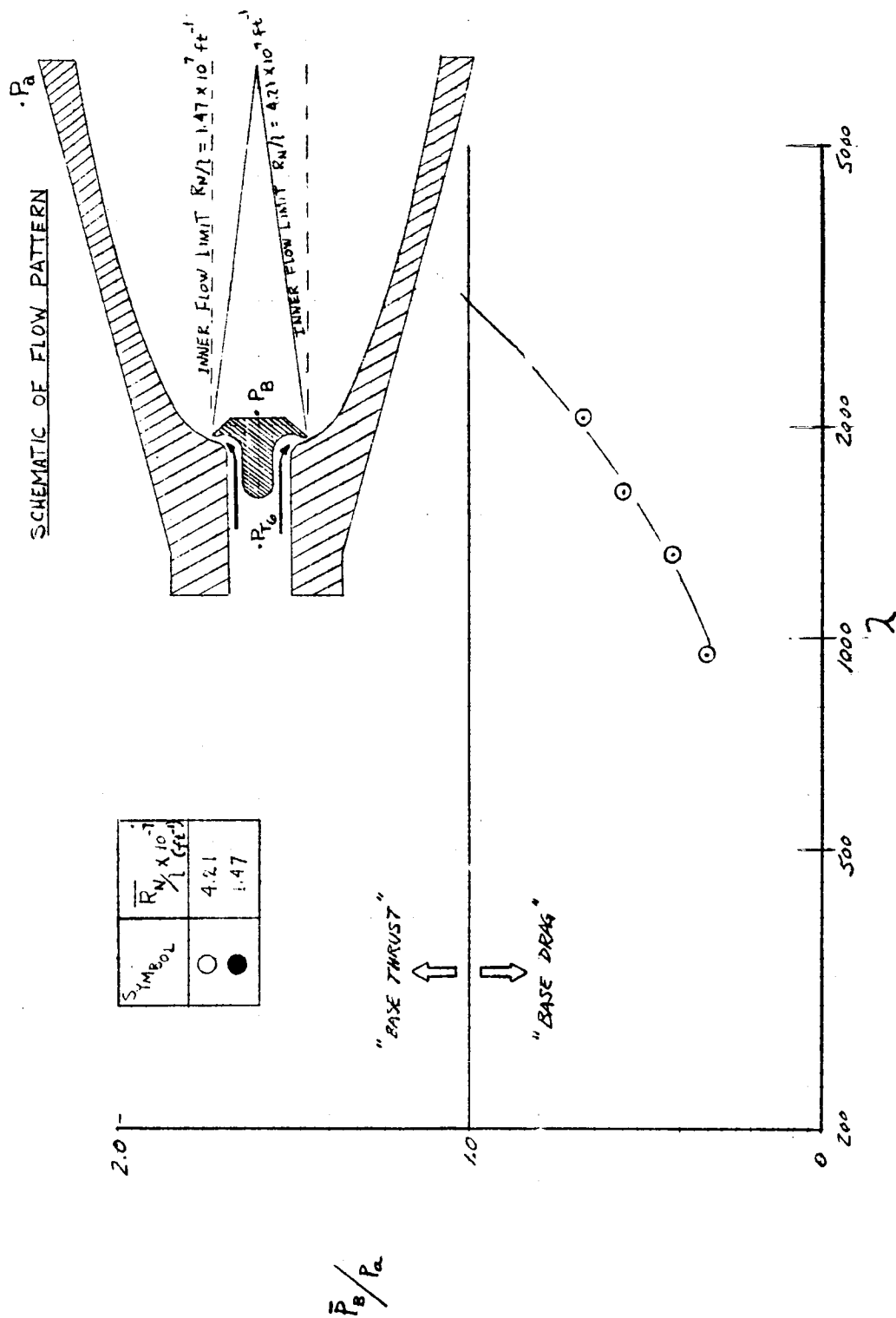


FIGURE 107. Centerbody Base Pressures, 2-D Nozzle

Force data for the sidewall friction configuration (Figure 106) agreed within experimental accuracy with the basic nozzle data.

Discharge coefficients for the 2-D nozzle are presented in Figure 108. As might be expected, considering the large perimeter to area ratio of the throat, the discharge coefficient was significantly reduced, from $C_{Dg} = 0.980$ for high R_N to 0.960 for low Reynolds number conditions. Further evidence of this substantial change in effective throat area can be seen in the nozzle pressure distributions. Figure 109 shows the pressure level in the inlet to be higher for the low R_N condition while downstream of the throat the pressure level is lower. This change in pressure level with R_N is considerably larger than observed for the conical nozzle. Pressure distributions for other portions of the nozzle are presented in Figures 110, 111, 112, and 113.

The pressure distribution curves in the throat region were drawn with the aid of one-dimensional pressure versus area calculations.

The boundary layer in the shroud was surveyed at three specified locations (Figure 114). Pressure profiles at the nozzle exit indicate a nominal boundary layer thickness $\delta = 0.35''$ for both R_N conditions.

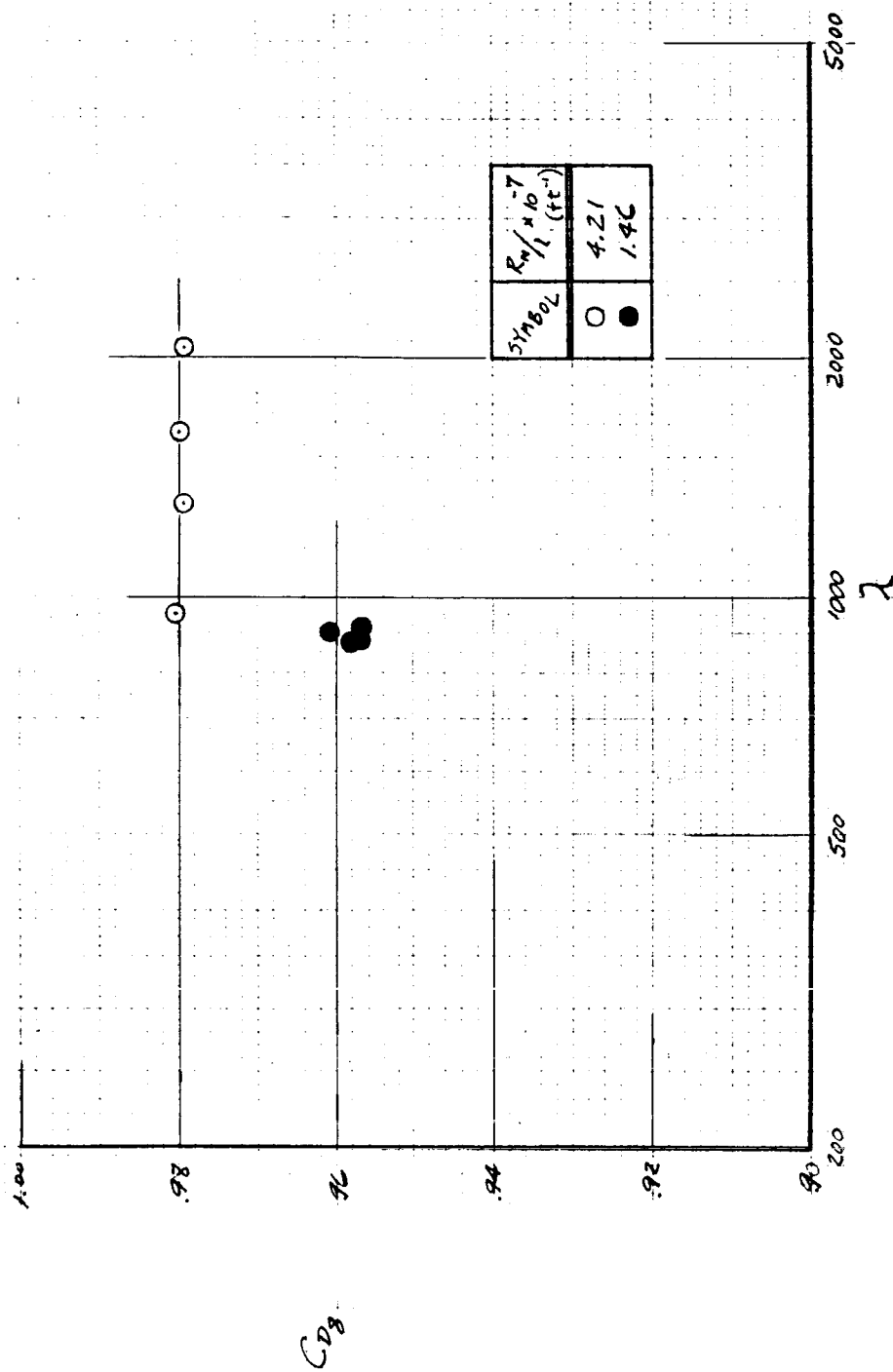


FIGURE 108. Discharge Coefficients, 2-D Nozzle

SYMBOL	RUN NO.	λ	$\int_0^{23.218} \frac{P}{P_{t0}} dA$
	15	949.93	
	16	1312.8	
	17	1617.6	
	18a	2066.9	
X	AVG.		.0076
	22	915.78	
	23	879.62	
	24	879.52	
	25	897.25	
+	AVG.		.0353

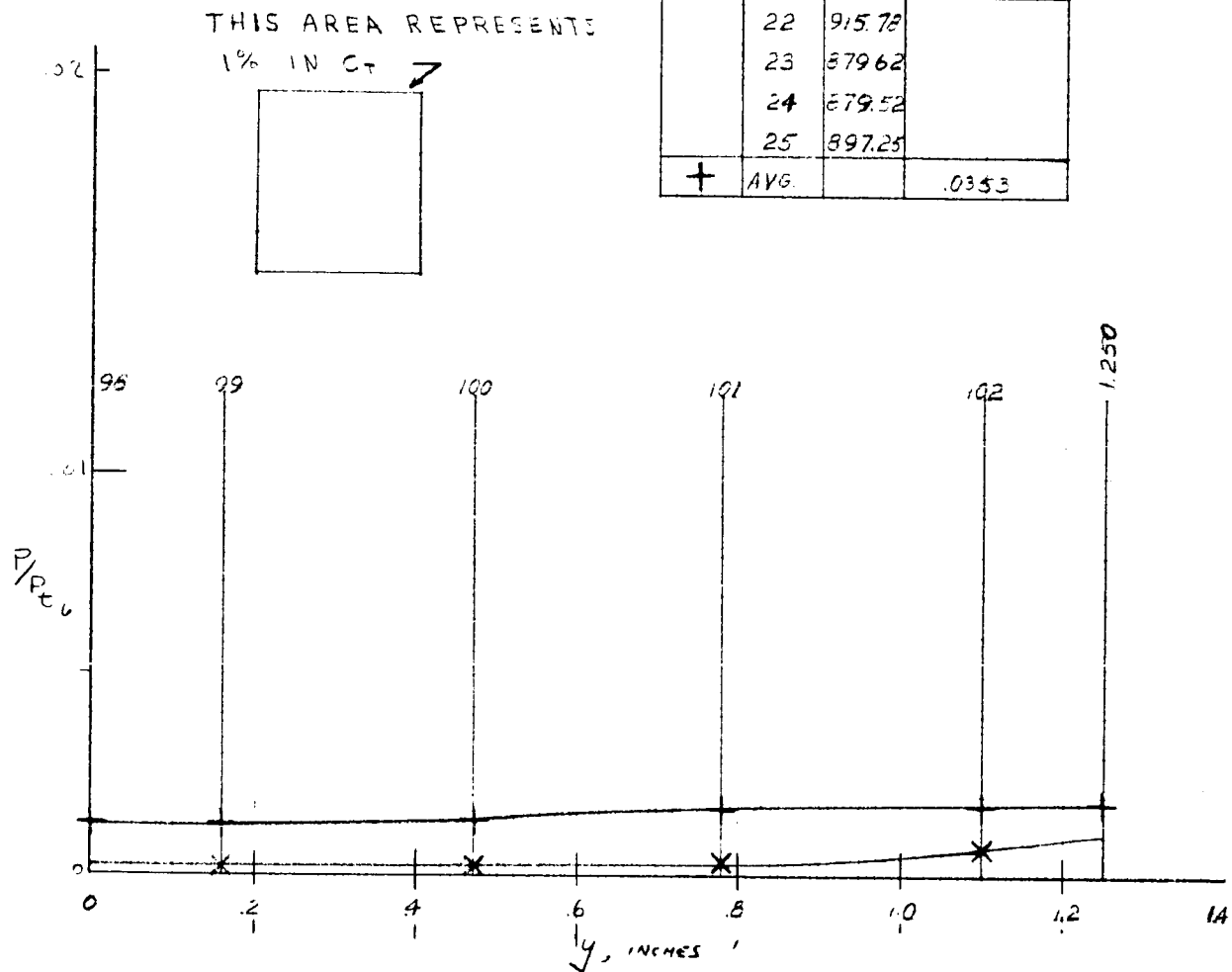


FIGURE 111. Shroud Pressure Distribution, 2-D Nozzle

SHROUD PRESSURE DISTRIBUTION
2-D F-D NOZZLE
CHANNEL 8 DATE: 8-29-63, 9-11-63

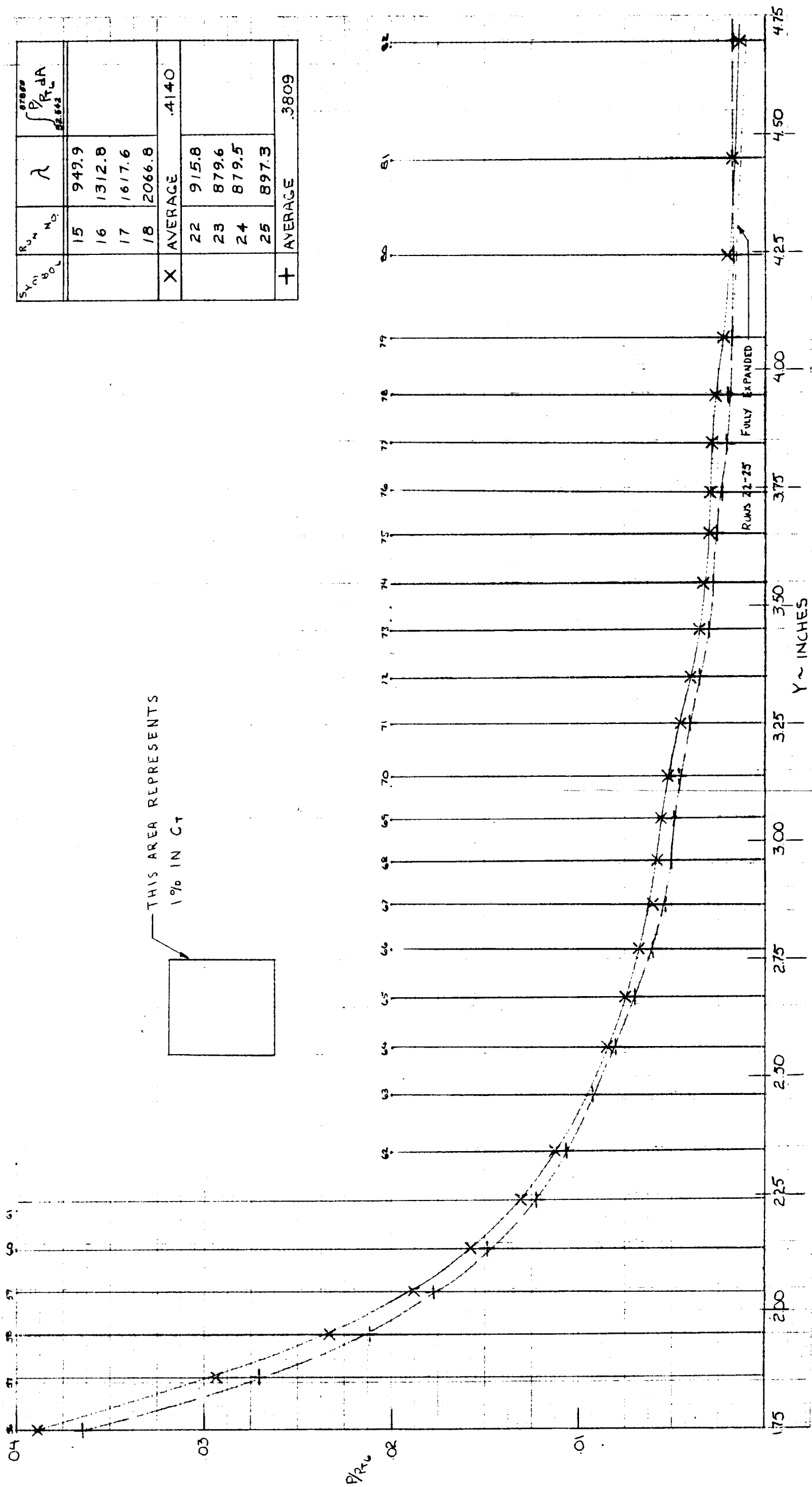
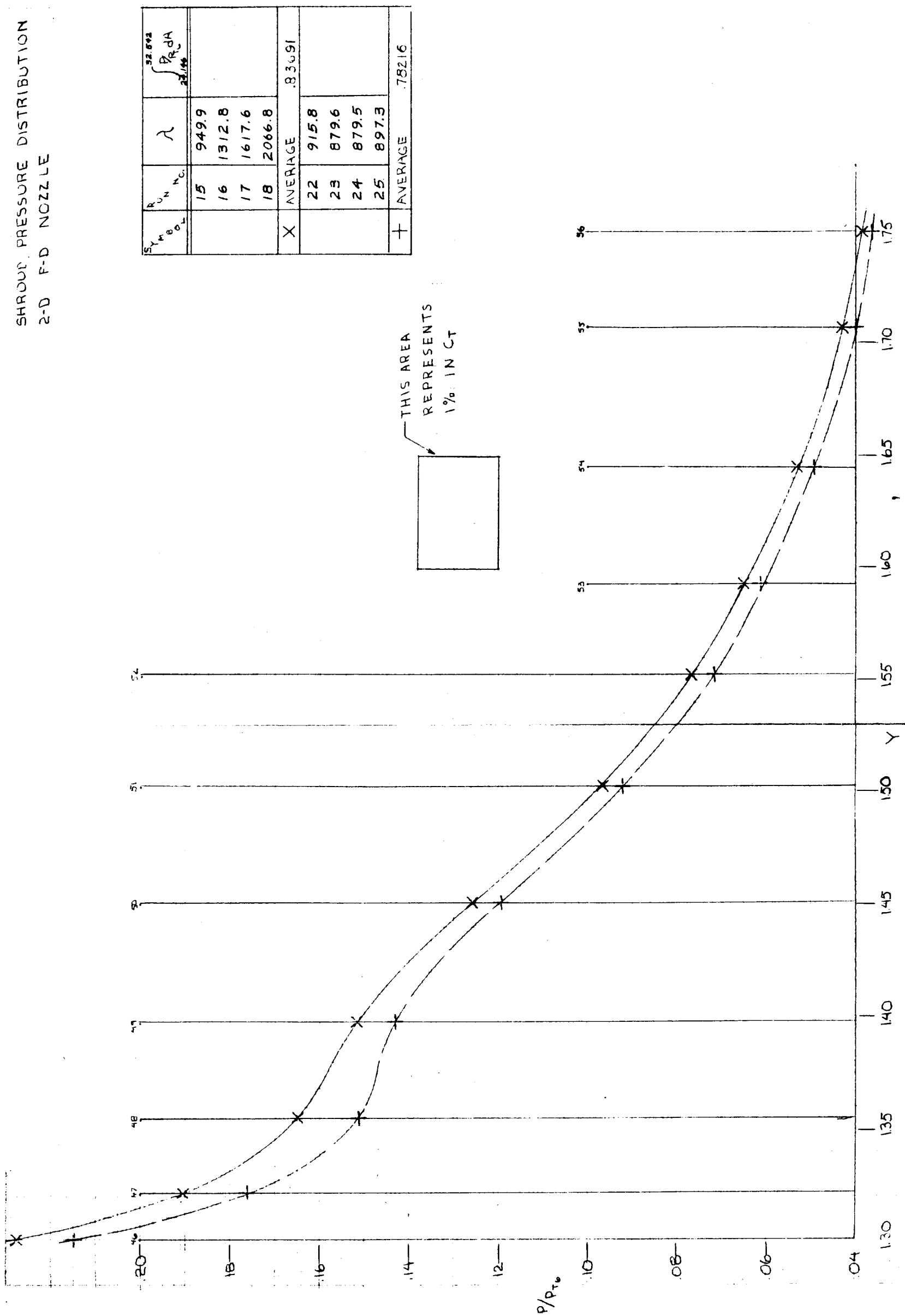


FIGURE 113. Shroud Pressure Distribution, 2-D Nozzle

SHROUD PRESSURE DISTRIBUTION
2-D F-D NOZZLE



$S_{Y_{1/8} \theta_L}$	$R_{UN} N_C$	λ	$\int_{23.14}^{52.642} P_{cDA}$
	15	949.9	
	16	1312.8	
	17	1617.6	
	18	2066.8	
X	AVERAGE	.83691	
	22	915.8	
	23	879.6	
	24	879.5	
	25	897.3	
+	AVERAGE	.78216	

FIGURE 112. Shroud Pressure Distribution, 2-D Nozzle

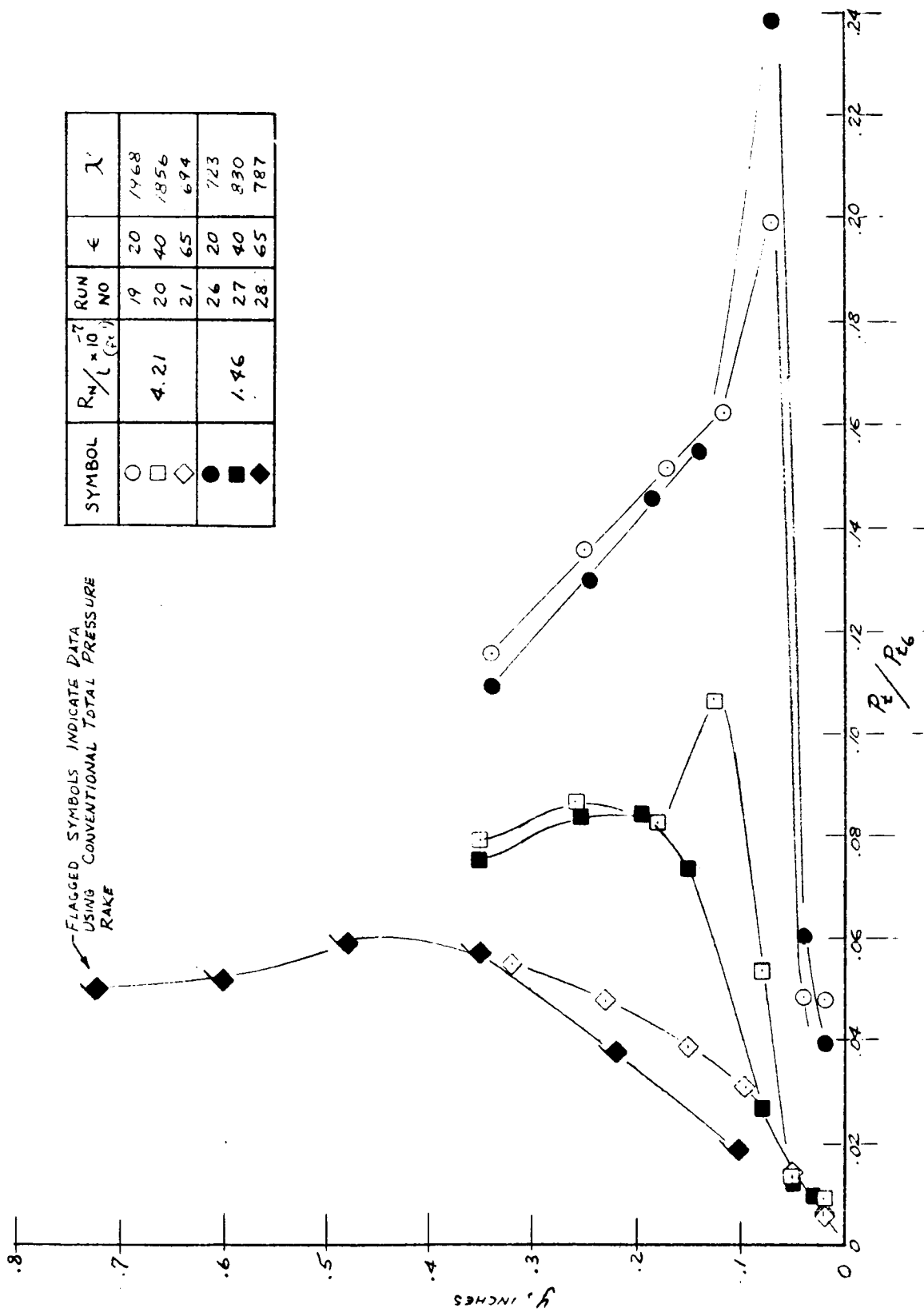


FIGURE 114. Boundary Layer Survey, 2-D Nozzle

REFERENCES

1. Sievers, Tomazic, Kinney, NASA-TR-111, Theoretical Performance of Hydrogen-Oxygen Rocket Thrust Chamber, 1961.
2. Olsen, Recombination and Condensation Processes in High Area Ratio Nozzle, ARS Journal, May 1962.
3. Third Quarterly Report, Study of High Effective Area Ratio Nozzles for Spacecraft Engine, Contract NAS 7-136, Aerojet-General, Sacramento, 1962.
4. K.N.C. Brae, Atomic Recombination in Nozzles: Methods of Analysis for Flows with Complicated Chemistry, Univ. of Southampton, 1961.
5. Rubesin, Maydew, Varga, NACA TN 2305, An Analytical and Experimental Investigation of the Skin Friction of the Turbulent Boundary Layer on a Flat Plate, 1951.
6. Tromblay, Rocketdyne ADM 61-83, Calculation of Friction Drag in Rocket Nozzles and Demonstration of the Effect on Specific Impulse, 1961.
7. Persh and Lee, Navord Report 4200, A Method for Calculating Turbulent Boundary Layer Development in Supersonic and Hypersonic Nozzles including the Effects of Heat Transfer, 1956.
8. Elliot, Bartz, Silver, JPL Tech. Report No. 32-387, Calculations of Turbulent Boundary Layer Growth in Axisymmetric Nozzles, 1963.
9. Koelle, Handbook of Astronautical Engineering, McGraw-Hill, 1961.
10. Shanley, F.R., Weight-Strength Analysis of Aircraft Structures, Dover, 1960.
11. Perry, D.J., Aircraft Structures, McGraw-Hill, 1950.
12. Gerard and Becker, NACA TN 3783, Handbook of Curved Plates and Shells, 1957.
13. Bruhn, E.F., Analysis and Design of Aircraft Structures, Tri-State, 1958.
14. Roark, R.J., Formulas for Stress and Strain, McGraw-Hill, 1954.

REFERENCES - cont'd.

15. Kennedy, E.C., Sonheim, D.W., and Barnes, A.M., New Mach Number Tables for Internal Ramjet Flow Analysis, Convair Ordnance Aerophysics Laboratory Memorandum 50, April 1952.
16. Supplement to ASME Power Test Codes Chapter 4. Flow Measurement, Instruments and Apparatus Part 5 - Measurement of Quantity of Materials. P.T.C. 19.5;4, 1959.
17. Monson, D.R., Thornberg, G.H., and Myers, M.C., Cold-Flow Model Tests of Segmented Forced-Deflection Rocket Nozzles Incorporating Ambient Base Bleed and Injection Thrust Vector Control, Phase I and II. Fluidyne Project 0249, Aerojet-General Corporation P.O. E-290585 (LRP), March 1963, Confidential.
18. AEDC TDR-62-196, Zero Secondary Flow Ejector-Diffuser Performance Using Annular Nozzles, January 1963.